# Durham E-Theses

## *Three-dimensional unsteady flow in the oscillating turbine blade row*

Huang, Xiuquan

**How to cite:**

Huang, Xiuquan (2006) *Three-dimensional unsteady flow in the oscillating turbine blade row*, Durham theses, Durham University. Available at Durham E-Theses Online: http://etheses.dur.ac.uk/2328/

**Use policy**

The full-text may be used and/or reproduced, and given to third parties in any format or medium, without prior permission or charge, for personal research or study, educational, or not-for-profit purposes provided that:

- a full bibliographic reference is made to the original source
- a link is made to the metadata record in Durham E-Theses
- the full-text is not changed in any way

The full-text must not be sold in any format or medium without the formal permission of the copyright holders.

Please consult the full Durham E-Theses policy for further details.

Academic Support Office, Durham University, University Office, Old Elvet, Durham DH1 3HP
e-mail: e-theses.admin@dur.ac.uk Tel: +44 0191 334 6107
http://etheses.dur.ac.uk

# THREE-DIMENSIONAL UNSTEADY FLOW IN OSCILLATING TURBINE BLADE ROW

**Xiuquan Huang**

School of Engineering

University of Durham

**The copyright of this thesis rests with the author or the university to which it was submitted. No quotation from it, or information derived from it may be published without the prior written consent of the author or university, and any information derived from it should be acknowledged.**

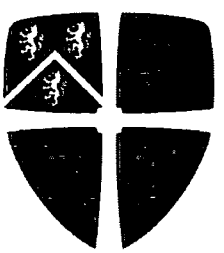

A thesis submitted to University of Durham

for the degree of Doctor of Philosophy

July 2006

1 1 OCT 2006

# Declaration

I declare that no material presented within this thesis has been submitted towards a degree or qualification at this or any other university

Signiture: 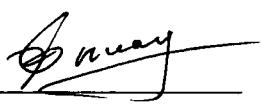

date: 7th July 2006

**Copyright**© July 2006 by Xiuquan Huang

The copyright of this thesis rests with the author. No quotation from it should be published in any format, including electronic and the internet, without the author's prior written consent. Any information derived from it should be acknowledged appropriately.

# Acknowledgements

I would like to express my deepest appreciation to Prof. Li He, who offered me the study opportunity, provided continual guidance, was patient with my progress and supplied consistent financial support in the last three and half years. Being an excellent mentor and friend, Li has the greatest respect from me.

This work was partially sponsored by ALSTOM Power Ltd, and I would like to thank Dr. David Bell for his technical support throughout this project.

I would like to acknowledge help of the technicians within the School of Engineering, especially Mr. Allan Swann for manufacturing the test blades, Mr. Ian Glassford for constructing the linear turbine cascade and Mr. Colin Wintrip for his various assistance.

I would like to extend my thanks to Dr. Haidong Li, with whom I had valuable discussions. Dingxi, Vera, Orhan and Ying from the Unsteady Aerodynamics and Aeroelasticity Group are always friendly, encouraging and helpful.

Most of all, my thanks would go to my wife and parents, for their unconditional love and support.

# Abstract

This thesis documents an experimental and computational study of the unsteady flow around oscillating blades in low-pressure turbines, with emphasis on the three-dimensional flow behaviour, intra-row interaction effects, tip clearance flow and part-span shroud influence. The research vehicles were a linear low speed oscillating turbine test cascade and a realistic low-pressure steam turbine rotor/stage.

Systematic experimental measurements were conducted on the linear turbine cascade, which consists of seven, large scale, prismatic blades with the middle blade being driven to oscillate in a three-dimensional bending/flapping mode. Blades were instrumented with pressure tappings at six span-wise sections between 10% and 95% span to facilitate detailed three-dimensional steady and unsteady pressure measurements on the blade surface. Steady flow pressure was measured by using an inclined manometer bank, whilst the unsteady pressure measurements were obtained through off-board pressure transducers. The measured unsteady pressure was superposed to construct tuned cascade flutter data using a technique named the influence coefficient method. This study produced the first known set of 3D flutter data for tuned turbine cascade.

On the computational side, a state-of-the-art, single-passage, three-dimensional, time-marching, Navier-Stokes flow solver has been adopted. The computational solutions of the linear cascade flow exhibits a consistently high level of agreement with the experimental data, which corroborates the experimental findings on the one hand and acts to validate the present flow solver on the other hand. The results, from several aspects, suggest a strong three-dimensional nature of the unsteady aerodynamic response to the blade first-bending/flapping and clearly demonstrate the inadequacies of the currently widely used two-dimensional and quasi-three-dimensional methods.

The validated computational method has been later applied to the realistic low pressure turbine configurations. It was found that accurate flutter predictions require three-dimensional, multi-row flow solvers including tip clearance modelling.

**Keywords**: low-pressure turbine, blade flutter, CFD, aeroelastic testing, part-span shrouds, three-dimensional flow, intra-row interaction, tip clearance flow.

# Contents


**1 Introduction** **1**

1.1 General Background . . . . . 1

1.2 Description of Flutter Characteristics and Parameters . . . . . 5

1.3 Motivation and Objectives . . . . . 9

1.4 Overview of This Thesis . . . . . 11

**2 Review of the Literature** **12**

2.1 Experimental Investigations . . . . . 12

2.1.1 Blade Oscillating Schemes . . . . . 12

2.1.1.1 Free Flutter Tests . . . . . 12

2.1.1.2 Controlled Flutter Tests . . . . . 14

2.1.2 Experimental Facilities . . . . . 15

2.1.2.1 High Speed Rotating Rigs . . . . . 15

2.1.2.2 Stationary Annular Cascades . . . . . 17

2.1.2.3 Linear Cascades . . . . . 19

2.2 Computational Methods . . . . . 24

2.2.1 Frequency Domain Methods . . . . . 24

2.2.2 Time Domain Methods . . . . . 27

2.3 Closing Remarks . . . . . 31

**3 Experimental Methods** **33**

3.1 Description of Test Facility . . . . . 33

3.1.1 Low Speed Wind Tunnel . . . . . 35

3.1.2 Working Section . . . . . 35

3.1.3 Blade Choice/Design . . . . . 36

3.1.4 Blade Oscillating Drive . . . . . 38

3.1.5 Blade Instrumentation . . . . . 40
3.1.6 Operational Conditions . . . . . 42
3.2 Data Acquisition and Reduction . . . . . 42
3.2.1 Data Acquisition . . . . . 42
3.2.2 Correction on Tubing Effects . . . . . 48
3.2.3 Influence Coefficient Method . . . . . 49
3.2.4 Aerodynamic Damping . . . . . 51
3.3 Experimental Errors and Repeatability . . . . . 52

**4 Computational Methods** **55**
4.1 Basic Flow Model . . . . . 55
4.2 Spatial Discretisation and Temporal Integration . . . . . 58
4.3 Boundary Conditions . . . . . 60

**5 Experimental and Computational Study of Turbine Cascade at Nominal Condition** **67**
5.1 Experimental Results . . . . . 67
5.1.1 Steady Flow Measurements . . . . . 67
5.1.2 Unsteady Flow Measurements . . . . . 70
5.1.2.1 Evaluation of Pitchwise Convergence and Linearity of Unsteady Response . . . . . 70
5.1.2.2 Tuned First Harmonic Pressure . . . . . 76
5.1.2.3 Aerodynamic Damping . . . . . 80
5.2 Computational Study . . . . . 81
5.2.1 Steady Flow Computations . . . . . 82
5.2.2 Unsteady Flow Predictions . . . . . 83
5.3 Summary . . . . . 101

**6 Influence of Upstream Stator on Rotor Flutter Stability** **103**
6.1 Description of Intra-Row Interaction . . . . . 103
6.2 Aerodynamic Work Calculation in Multiple-Disturbance Environment . 106
6.3 Results and Discussion . . . . . 108
6.3.1 Two-Dimensional Case . . . . . 109

6.3.1.1 Validation of the Single Passage Solver . . . . . 111
6.3.1.2 Overview of 2D Predictions . . . . . 112
6.3.1.3 Intra-Row Gap Effects (2D) . . . . . 113
6.3.2 Three-Dimensional Stage . . . . . 117
6.4 Summary . . . . . 118

**7 Influence of Tip Clearance on Oscillating Blade Flow 119**
7.1 Experimental Investigation . . . . . 119
7.1.1 Experimental Setup . . . . . 119
7.1.2 Steady Flow . . . . . 120
7.1.3 Unsteady Results . . . . . 122
7.1.3.1 Unsteady Pressure . . . . . 122
7.1.3.2 Aerodynamic Damping . . . . . 125
7.2 Computational Study . . . . . 128
7.2.1 Case One: Linear Turbine Cascade . . . . . 129
7.2.2 Case Two: LP Turbine Rotor . . . . . 135
7.3 Quasi-Steady Analysis . . . . . 140
7.4 Summary . . . . . 142

**8 Influence of Part-span Shrouds on Blade Aeroelastic Characteristics 144**
8.1 Part-Span Shrouded Linear Cascade . . . . . 145
8.1.1 Experimental Setup . . . . . 145
8.1.2 Numerical Modelling of Part-Span Shrouds . . . . . 146
8.1.3 Results and Discussion . . . . . 146
8.2 Part-Span Shrouded LP Turbine Rotor . . . . . 151
8.3 Summary . . . . . 154

**9 Conclusions and Recommendations for Future Work 156**
9.1 Conclusions . . . . . 156
9.1.1 Unsteady Flow around Oscillating Linear Turbine Blades . . . . 157
9.1.2 Prediction of the Realistic LP Steam Turbine Rotor . . . . . 158
9.2 Recommendations for Further Work . . . . . 159

**Bibliography 160**

**Appendix: Blade Profile Specification** **173**

# List of Figures


1.1 Collar's triangle of forces . . . . . 2
1.2 Campbell diagram . . . . . 3
1.3 Typical compressor map with blade flutter boundaries . . . . . 4
1.4 The definition of Mass Coefficient . . . . . 6
1.5 An interpretation of reduced frequency . . . . . 7
1.6 Blade row and isolated wing . . . . . 8
1.7 Nodal diameter pattern (3 NDs) . . . . . 9

2.1 Vogt and Fransson's annular sector cascade . . . . . 19
2.2 Bell and He's single blade facility . . . . . 23
2.3 Yang and He's compressor cascade . . . . . 23

3.1 Test facility . . . . . 34
3.2 Schematic of the low speed wind tunnel . . . . . 34
3.3 The working section (generated by SolidWorks) . . . . . 36
3.4 'Cut and Try' blade design procedure . . . . . 37
3.5 Blade profile and nomenclature . . . . . 37
3.6 The blade drive mechanism . . . . . 39
3.7 Locus of blade displacement delivered by the single bar crank . . . . . 39
3.8 Locations of blade surface pressure tappings . . . . . 40
3.9 Instrumented blade . . . . . 41
3.10 Sample pressure transducer response . . . . . 44
3.11 Schematic of the unsteady pressure acquisition system . . . . . 44
3.12 Raw and ensemble-averaged unsteady pressure signals at 70% span on the suction surface of blade 0, $K$=0.4 . . . . . 46
3.13 Measurement of the tubing transfer function, Yang (2004) . . . . . 49

3.14 Unsteady aerodynamic response in a travelling wave mode . . . . . 50
3.15 Influence coefficients in a cascade with one oscillating blade . . . . . 50
3.16 Repeatability and errors in the measurement of amplitude and phase angle of the first harmonic pressure response . . . . . 54

4.1 Single passage domain . . . . . 61
4.2 Bladerow interface treatment . . . . . 64

5.1 Steady flow blade surface pressure distributions at different spanwise sections on Blade -1 . . . . . 68
5.2 Steady flow blade surface pressure distributions at different spanwise sections on Blade 0 . . . . . 68
5.3 Steady flow blade surface pressure distributions at different spanwise sections on Blade 1 . . . . . 69
5.4 Comparison of blade surface pressure distributions at mid-span . . . . . 69
5.5 Experimental test for pitchwise convergence — unsteady pressure response on the five central blades due to the oscillation of blade 0 ($K$=0.4) 71
5.6 Experimental test for pitchwise convergence — aerodynamic damping contribution from the five central blades, ($K$=0.4, $\sigma_0$=0°) . . . . . 71
5.7 Experimental test for linearity — first harmonic pressure coefficient on the reference blade at two different oscillating amplitudes, ($K$=0.4) . . 74
5.8 Experimental test for linearity — relative amplitude of the second harmonic pressure coefficient on the reference blade, ($K$=0.2) . . . . . 75
5.9 Experimental test for linearity — relative amplitude of the second harmonic pressure coefficient on the reference blade, ($K$=0.4) . . . . . 75
5.10 Experimental test for linearity — relative amplitude of the second harmonic pressure coefficient on the reference blade, ($K$=0.6) . . . . . 76
5.11 Amplitude of the first harmonic pressure response ($K$=0.4, $\sigma_0$=−60°) . 77
5.12 Phase of the first harmonic pressure response ($K$=0.4, $\sigma_0$=−60°) . . . . 79
5.13 Global aerodynamic damping at three reduced frequencies . . . . . 80
5.14 3D Computational Mesh . . . . . 82
5.15 Mesh dependency study: steady blade surface pressure predictions . . . 82

5.16 Predicted and measured steady blade surface pressure distributions (Mesh 2) . . . . . 83
5.17 Aerodynamic damping prediction at nominal conditions, $\xi$ . . . . . 84
5.18 Predicted and measured amplitude of the first harmonic pressure (Mesh 2, $K$=0.2, $\sigma_0$=−90°) . . . . . 87
5.19 Predicted and measured phase angle of the first harmonic pressure (Mesh 2, $K$=0.2, $\sigma_0$=−90°) . . . . . 88
5.20 Predicted and measured amplitude of the first harmonic pressure (Mesh 2, $K$=0.2, $\sigma_0$=90°) . . . . . 89
5.21 Predicted and measured phase angle of the first harmonic pressure (Mesh 2, $K$=0.2, $\sigma_0$=90°) . . . . . 90
5.22 Predicted and measured amplitude of the first harmonic pressure (Mesh 2, $K$=0.4, $\sigma_0$=−60°) . . . . . 91
5.23 Predicted and measured phase angle of the first harmonic pressure (Mesh 2, $K$=0.4, $\sigma_0$=−60°) . . . . . 92
5.24 Predicted and measured amplitude of the first harmonic pressure (Mesh 2, $K$=0.4, $\sigma_0$=120°) . . . . . 93
5.25 Predicted and measured phase angle of the first harmonic pressure (Mesh 2, $K$=0.4, $\sigma_0$=120°) . . . . . 94
5.26 Predicted and measured amplitude of the first harmonic pressure (Mesh 2, $K$=0.6, $\sigma_0$=−45°) . . . . . 95
5.27 Predicted and measured phase angle of the first harmonic pressure (Mesh 2, $K$=0.6, $\sigma_0$=−45°) . . . . . 96
5.28 Predicted and measured amplitude of the first harmonic pressure (Mesh 2, $K$=0.6, $\sigma_0$=120°) . . . . . 97
5.29 Predicted and measured phase angle of the first harmonic pressure (Mesh 2, $K$=0.6, $\sigma_0$=120°) . . . . . 98
5.30 Aerodynamic damping variation along blade span, $\xi_{span}$, $K$=0.2 . . . . 99
5.31 Aerodynamic damping variation along blade span, $\xi_{span}$, $K$=0.4 . . . . 99
5.32 Aerodynamic damping variation along blade span, $\xi_{span}$, $K$=0.6 . . . . 100

6.1 Pressure signal decomposition . . . . . 107

6.2 Model LP stage . . . . . 108
6.3 Stator-rotor computational mesh (2D tip section) . . . . . 110
6.4 Spectra of unsteady axial forces on the rotor . . . . . 112
6.5 Forward travelling wave modes . . . . . 114
6.6 Backward travelling wave modes . . . . . 115
6.7 Computational mesh for the 3D LP steam turbine stage . . . . . 117
6.8 Predicted spanwise variation in local Loc-Dec for staged rotor and isolated rotor, 11 ND backward travelling wave mode . . . . . 118

7.1 Schematic of the blade tip clearance setting . . . . . 120
7.2 Steady pressure distribution with different tip clearances at 95% span . 121
7.3 Amplitude of first harmonic pressure at 95% span ($K$=0.4, $\sigma_0$=$-$60°) . 123
7.4 Phase angle of first harmonic pressure at 95% span ($K$=0.4, $\sigma_0$=$-$60°) 124
7.5 Local aerodynamic damping coefficient ($K$=0.4, $\sigma_0$=$-$60°) . . . . . 126
7.6 Measured aerodynamic damping coefficient at 95% span on the suction surface ($K$=0.4, $\sigma_0$=$-$60°) . . . . . 127
7.7 Variation of measured global aerodynamic damping coefficient with tip clearance ($K$=0.4, $\sigma_0$=$-$60°) . . . . . 127
7.8 Computational mesh for tip clearance flow calculations . . . . . 129
7.9 Blade surface steady pressure distribution . . . . . 130
7.10 Entropy $[exp(-\Delta S/R)]$ contours with secondary velocity vectors (left) and static pressure contours (right) at 80%$C_{ax}$ . . . . . 131
7.11 Predicted and measured amplitude (left) and phase angle (right) of first harmonic pressure at 95% span section . . . . . 133
7.12 Aerodynamic damping at 95% span on the suction surface . . . . . 134
7.13 Variation of global aerodynamic damping with tip clearance . . . . . 134
7.14 Computational mesh for model LP rotor with a tip clearance . . . . . 135
7.15 Steady flow blade surface pressure coefficient distribution at 98% span 136
7.16 Steady flow entropy $[exp(-\Delta S/R)]$ contours at 98% span . . . . . 137
7.17 Predicted spanwise variation in local total-to-total efficiency with and without tip clearance for the LP rotor . . . . . 137
7.18 Steady flow entropy $[exp(-\Delta S/R)]$ contours at 80%$C_{ax}$ . . . . . 138

7.19 Steady flow pressure contours at 80%$C_{ax}$ . . . . . 138
7.20 Predicted spanwise variation in local Loc-Dec with and without tip clearance for the LP rotor, 11 NDs backward travelling wave mode . . . . . 139
7.21 Oscillating turbine passage . . . . . 141
7.22 Blade tip at the minimum, mean and maximum displacements (axial view) 141

8.1 Part-span shrouded linear cascade . . . . . 145
8.2 Mesh used for part-span shroud calculation . . . . . 146
8.3 Effects of part-span shrouds on amplitude of the unsteady pressure response, left: experiment, right: calculation ($K$=0.4, $\sigma_0$=−60°) . . . . . 148
8.4 Effects of part-span shrouds on phase angle of the unsteady pressure response, left: experiment, right: calculation ($K$=0.4, $\sigma_0$=−60°) . . . . 149
8.5 Comparison between experiment and calculation (with part-span shrouds, $K$=0.4, $\sigma_0$=−60°) . . . . . 150
8.6 Computational mesh for model LP rotor with part-span shrouds . . . . 152
8.7 Predicted spanwise variation in local log-dec with and without with part-span shrouds for the LP rotor (shrouds located at 75% span) . . . . . 152
8.8 Predicted first harmonic pressure at 70% span . . . . . 153
8.9 Predicted first harmonic pressure at 80% span . . . . . 154
8.10 Predicted spanwise variation in local log-dec with and without with part-span shrouds for the LP rotor (shrouds located at 85% span) . . . . . 154

# List of Tables


2.1 Summary on 3D Experimental Studies . . . . . 31

2.2 Summary on Computational Methods . . . . . 32

3.1 Cascade properties . . . . . 38

3.2 Bending mode shape . . . . . 40

3.3 Axial location of tappings, $x/C_{ax}$ . . . . . 41

3.4 Summary of operational conditions . . . . . 42

3.5 Sampling rates . . . . . 45

3.6 Overall standard deviation in the measurement of $|C_{p1}|$ and $\phi_1$ . . . . . 53

4.1 Relation between Nodal Diameters, IBPAs and Passages . . . . . 61

5.1 Mesh dependency study . . . . . 81

6.1 Natural frequency & mode-shape (2D tip section) . . . . . 110

6.2 Summary for the forward travelling wave modes . . . . . 114

6.3 Summary for the backward travelling wave modes . . . . . 115

6.4 3D Predictions of Log-Dec ($\xi$) . . . . . 118

7.1 Predicted Log-Dec ($\xi$) of LP Rotor with and without tip clearance . . . 136

8.1 Part-span shroud specification . . . . . 145

8.2 Global aerodynamic damping coefficients for settings with and without part-span shrouds ($K$=0.4, $\sigma_0$=−60°) . . . . . 151

8.3 Predicted Log-Dec ($\xi$) of the model LP rotor with and without part-span shrouds . . . . . 153

# Nomenclature

### Roman Symbols

| | |
|---|---|
| $A$ | finite volume surface, $m^2$ |
| $a$ | speed of sound, $m/s$ |
| $A_n, B_n$ | Fourier coefficients |
| $A_{p,n}$ | amplitude of the $n^{th}$ harmonic pressure, $Pa$ |
| $A_x$ | local bending amplitude, non-dimensionalised with chord |
| $A_{x,tip}$ | bending amplitude at blade tip, non-dimensionalised with chord |
| $C$ | blade chord length, $m$ |
| $C_p$ | steady flow blade surface pressure coefficient, $C_p = \frac{P - P_2}{P_{01} - P_2}$ |
| $c_p$ | specific heat at constant pressure, $J/(kg \cdot K)$ |
| $C_{ax}$ | axial blade chord length, $m$ |
| $C_{mass}$ | Mass Coefficient |
| $C_{p,n}$ | amplitude of the $n^{th}$ harmonic pressure coefficient, $C_{p,n} = \frac{A_{p,n}}{(P_{01} - P_2) \cdot A_{x,tip}}$ |
| $D$ | displacement, $m$ |
| $e$ | internal energy, $J/kg$ |
| $f$ | frequency, $Hz$ |
| $F, G, H$ | inviscid fluxes |
| $h$ | blade height, $m$ |
| $K$ | reduced frequency, $K = \frac{\omega C}{V_{ref}}$ |
| $k$ | molecular thermal conductivity, $W/(m \cdot K)$ |
| $M$ | Mach number |
| $m$ | mass, $kg$ |
| $N_b$ | number of blades |
| $N_{fou}$ | order of Fourier series |

| | |
|---|---|
| $N_{pt}$ | number of perturbations |
| $P$ | pressure, Pa |
| $Pr$ | Prandtl number |
| $q$ | heat flux |
| $r$ | radial coordinate, $m$ |
| $Re$ | Reynolds number |
| $S$ | inviscid source term |
| $s$ | pitch length, $m$ |
| $T$ | temperature, $K$; time period, $s$ |
| $t$ | time, $s$ |
| $U$ | conservative flow variable vector |
| $u$ | absolute velocity, $m/s$ |
| $V_{ref}$ | reference velocity, $m/s$, $V_{ref} = \sqrt{\frac{2(P_{01} - P_2)}{\rho}}$ |
| $x$ | axial coordinate,$m$ |
| $\vec{n}$ | unit vector |

**Greek Symbols**

| | |
|---|---|
| $\alpha$ | blade inlet angle, *deg.* |
| $\beta$ | blade exit angle, *deg.* |
| $\delta$ | Logarithmic Decrement |
| $\gamma$ | specific heat ratio; stagger angle, *deg.* |
| $\mu$ | kinematic viscosity, $Pa \cdot s$ |
| $\Omega$ | rotor rotation angular speed, $rad/s$ |
| $\omega$ | angular velocity, $rad/s$ |
| $\phi$ | phase angle, *deg.* |
| $\pi$ | constant number '*pi*', $3.1415926\cdots$ |
| $\rho$ | density, $kg/m^3$ |
| $\sigma$ | inter-blade phase angle, *deg.* |
| $\tau$ | viscous stress; pseudo time |
| $\theta$ | tangential angular coordinate, $rad$ |
| $\xi$ | aerodynamic damping coefficient; logarithmic decrement |

**Subscripts**

| | |
|---|---|
| 0 | stagnation state; the reference blade |

| | |
|---|---|
| 1 | inlet; the first order |
| 2 | exit; the second order |
| $\theta$ | tangential direction |
| $ic$ | influence coefficient |
| $l$ | laminar |
| $mg$ | moving grid |
| $n$ | the $n^{th}$ order |
| $r$ | radial direction |
| $t$ | turbulent |
| $tip$ | blade tip |
| $to$ | torsion |
| $tw$ | travelling wave |
| $x$ | axial direction |

**Abbreviations**

| | |
|---|---|
| 2D | two dimensional |
| 3D | three dimensional |
| Cal. | calculation |
| CFD | computational fluid dynamics |
| EO | engine order |
| Exp. | experiment |
| FE | finite element |
| HCF | high cycle fatigue |
| IBPA | inter-blade phase angle |
| LE | leading edge |
| Log-Dec | logarithmic decrement |
| LP | low pressure |
| M.P. | multiple-passage |
| ND | nodal diameters |
| P.S. | pressure surface |
| S.P. | single-passage |
| S.S. | suction surface |
| TE | trailing edge |
| TipC | tip clearance |
| TTF | tubing transfer function |
| w/o | without |

# Chapter 1

# Introduction

## 1.1 General Background

The axial-flow turbomachine is currently the machine of choice for large scale applications, such as aeroengines and power plant turbines. The successful operation of a turbomachine is dependent not only upon its aerodynamic performance but also the aeroelastic stability of its rotating parts. However, the critical situation of the latter aspect is that engine blades continue to encounter flow induced vibration problems. Consequently, there is an urgent demand for better understanding of the mechanism, and an enhanced predictive capability, of blade aeroelasticity.

The study of aeroelasticity concerns the response of a non-rigid structure to its surrounding flow under the mutual interaction of aerodynamic, inertial and elastic forces. This mutual interaction has been famously depicted by Collar's triangle of forces, shown in Figure 1.1 (Collar, 1946). Based on the natures of excitations, the most common types of aeroelastic phenomena that concern the turbomachine designers can be classified into two categories: *forced response* and *flutter*. Forced response is defined as the vibration induced by time-periodic aerodynamic excitations, which are independent of the blade vibration and usually referred to as external excitations. Such excitations usually arise from the relative rotation of adjacent structures or inlet/exit distortions. Conversely, flutter is a self-excited aeroelastic instability phenomenon, in which the aerodynamic forces that sustain the blade oscillating motion are regarded as being dependent solely on that motion.

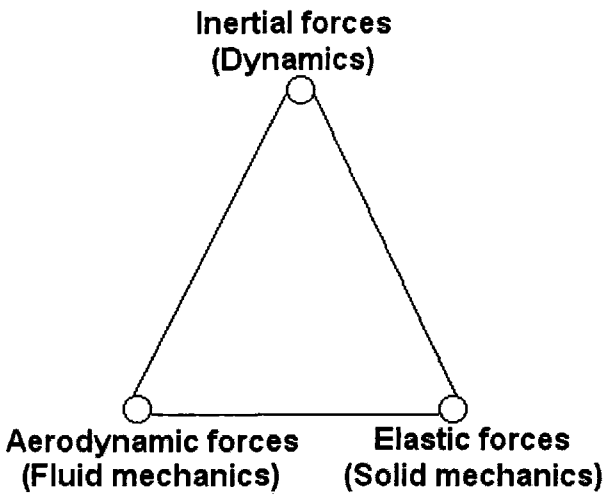


**Figure 1.1: Collar's triangle of forces**

Generally, forced response occurs at the so-called resonant conditions, in which the frequencies of time-periodic aerodynamic excitations are at or near the natural frequencies of the concerned rotor blades. To determine the frequencies at risk of forced response instabilities, a Campbell diagram, shown in Figure 1.2, is usually utilised in design practices. In this diagram, the bladed disk vibration mode frequencies are plotted against the rotational speed, together with the corresponding *engine orders* (EO — multiple of the rotor rotational frequency). The potential of force response exists where a vibration mode frequency line crosses an EO line. When forced response occurs, blades will experience excessive alternating stress levels and result in *high cycle fatigue* (HCF) if there is not enough damping (aerodynamic and/or mechanical). Forced response problems may appear in any part of the multistage turbomachines.

Given that the potential instabilities of force response are identified, preventative measures (e.g. shifting the structure mode frequencies) can be taken to avoid those resonant excitations during any design phase. In the case of power generation turbines, the standard design approach has been that blade fundamental mode frequencies should be shifted away from all EO frequencies below about eight times rotor rotational frequency and identifiable sources of EO excitation, such as the number of stationary vanes, number of vane segments, number of combustor chambers, etc (Scalzo et al., 1986). Thus, for power generation turbines continuously running at a constant speed through months and years, forced response may not be a main concern as long as an

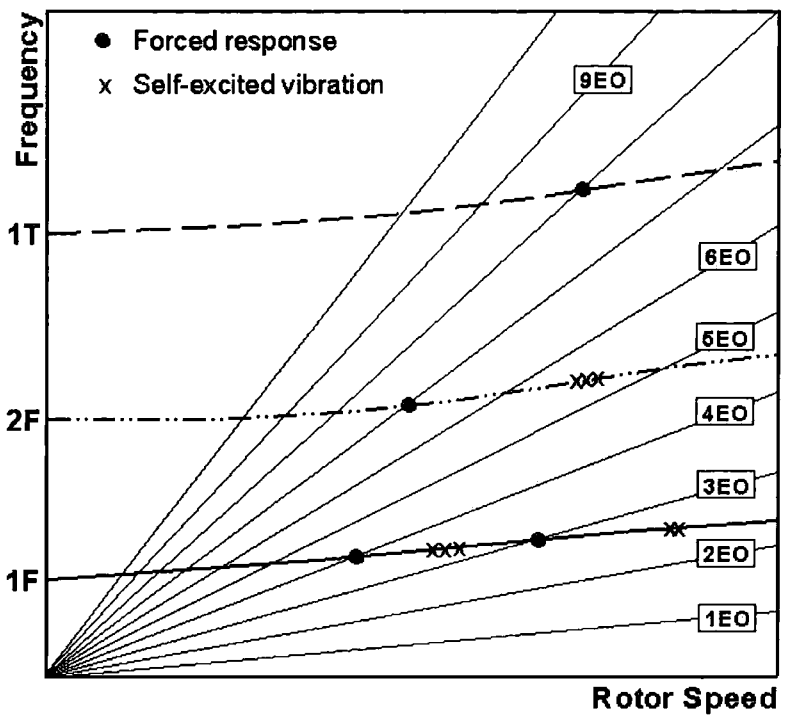


**Figure 1.2: Campbell diagram**

appropriate design is chosen to prevent resonant excitations at the normal operation condition. However, for aeroengines, which operate over a wide range of speeds and often go through transient procedures such as start-up and shut-down, it is inevitable to undergo some resonant conditions and, accordingly, forced response needs to be addressed.

By contrast, flutter occurs over a wide range of operational conditions at design and/or off-design points. This can be seen on a typical axial-flow compressor map with blade flutter boundaries, as shown in Figure 1.3. According to different aerodynamic conditions, the common flutter types have been designated as subsonic stall flutter, supersonic stall flutter, choke flutter and unstalled supersonic flutter. The subsonic stall flutter, occurring at a high pressure ratio and a low mass flow subject to high incidence, has the highest frequency of occurrence. This type of flutter is thought to be likely associated with the highly separated flow over the suction surface. Choke flutter occurs near the choke line, usually with high negative incidence values, and is less common. Most of flutters occur at off-design conditions, while the unstalled supersonic flutter

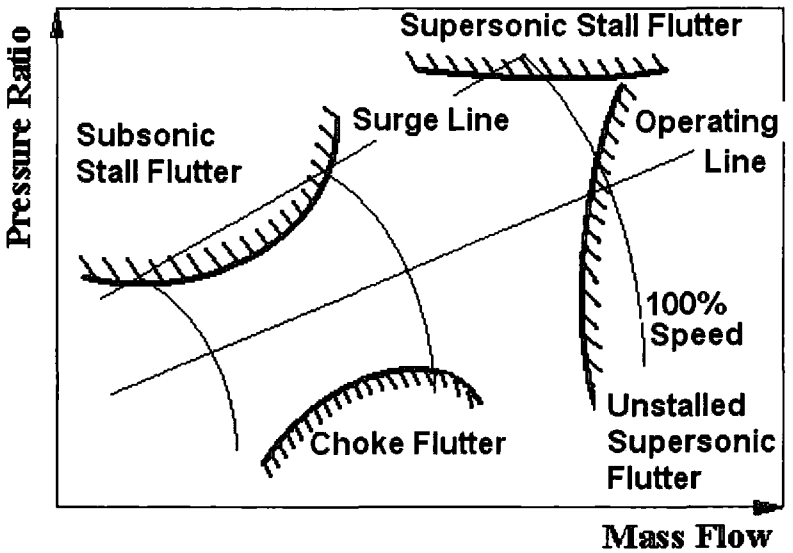


**Figure 1.3: Typical compressor map with blade flutter boundaries**

line crosses the operating line and this type of flutter needs to be examined at or near design point. The flutter mechanisms are far from well-understood and the aforementioned names are therefore only provisional. This is just as indicated by observations of Mikolajczak et al. (1975) and Stargardter (1977) that flow stall may not be essential for the so-called stall flutter. The mechanical failure associated with flutter is destructive and can result in loss of an entire blade and damage to others. Depending on the extent of individual instabilities, blade failure caused by flutter may be due to excessive stress developed in a few vibration periods or HCF in the case of limit cycle vibrations.

Current flutter design procedures still largely rely on empirical rules with reduced frequency, Mach number and incidence as the common design parameters. However, empirical rules are unreliable, especially when employed to designs with less similarity. More recently, *two-dimensional* (2D) or quasi *three-dimensional* (3D) *computational fluid dynamics* (CFD) has been incorporated into the flutter design system and this enables more accurate prediction of aeroelastic instability. For research and troubleshooting, fully three-dimensional CFD methods have been widely available.

Although the majority of past efforts directed at flutter has concentrated upon compressors, the seriousness of flutter has also been recognised in axial-flow turbines. Indeed, the design of last stage rotor blades in low-pressure (LP) steam turbines presents a

significant challenge in terms of aeroelastic design, due to their high aspect ratio, high operating pressure ratio and relatively low natural frequencies. This challenge will become more pressing in the future as the ongoing turbomachinery design is consistently driven towards being lighter, higher load and more efficient.

## 1.2 Description of Flutter Characteristics and Parameters

Blade flutter usually starts from an infinitesimal perturbation which can be excited either aerodynamically or mechanically. This type of perturbation is also characterised by a blade natural vibration mode. Once the blade vibration starts, it tends to induce unsteady aerodynamic forces which will in turn act upon the blade and drive the blade vibration either to attenuate or grow. This process is actually a dynamic interaction of the blade and its surrounding flow. Consequently, there exists energy exchange between the vibrating blade and the surrounding unsteady flow. Depending on the time-lag between the vibrating blade and the unsteady aerodynamic forces acting on it, the energy exchange may be positive (the blade absorbs energy from the flow), negative (the blade vibration dissipates energy to the flow) or zero (the energy exchange remains balanced) during a specific vibration cycle. If the blade absorbs energy from the flow, the initially small vibration will be amplified and the instability - flutter commences, often leading to blade failure due to lack of mechanical damping to dissipate the energy.

The aforementioned dynamic interaction between the vibrating blade and the unsteady flow is a mechanics/aerodynamics coupled problem. As has been well recognised, the coupling effects between the blade structural dynamics and the unsteady aerodynamics are largely dictated by the *Mass Coefficient*, a ratio between the mass of the blade and that of air/gas in the control volume (Figure 1.4):

$$C_{mass} = \frac{m}{\rho\pi(C/2)^2} \tag{1.1}$$

where $m$ is the mass per unit span of blade, $C$ the blade chord and $\rho$ the air/gas density in the control volume. Typical values of Mass Coefficient for conventional turbomachinery blades are much higher than those for aircraft wings. This indicates that, in turbomachinery, the aerodynamic forces remain much smaller than the inertial and elastic ones and do not considerably cause modal coupling during flutter. Furthermore,

the influence of the unsteady aerodynamic forces upon the blade vibration characteristics (mode shape and frequency) can be neglected during blade flutter. This forms the basis of the widely used *Energy Method* (Carta, 1967) based flutter prediction methods. Application of the Energy Method enables flutter predictions to be split up into two relatively independent constituents, i.e. structural and aerodynamic ones. On the structural side, the natural modes of blade vibration are taken into account and conventionally determined by employing a *finite element* (FE) method. While on the aerodynamic side, the blade vibration induced unsteady aerodynamic forces need to be predicted through the unsteady CFD analyses. Generally speaking, the computational load of a blade flutter prediction using the Energy Method is mostly confined to the aerodynamic side, i.e. the unsteady aerodynamic calculations.

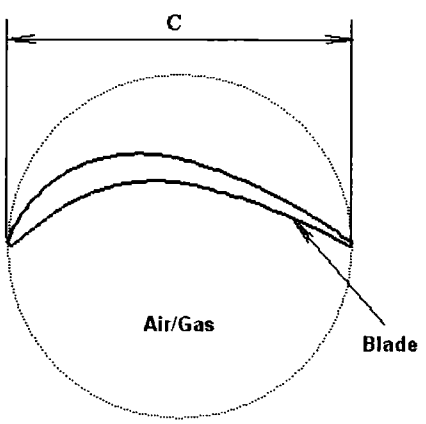


**Figure 1.4: The definition of Mass Coefficient**

To characterise the flow unsteadiness associated with the blade vibration, one non-dimensional parameter, termed the *reduced frequency* $K$, is defined as

$$K = \frac{\omega C}{V_{ref}} \tag{1.2}$$

where $\omega$ is the angular frequency, $C$ the chord length and $V_{ref}$ the reference velocity. By rearranging Equation 1.2, we have

$$K = \frac{2\pi C/V_{ref}}{T} \propto \frac{\tau}{T} \tag{1.3}$$

in which the reduced frequency relates the time $\tau$ taken for a fluid particle to convect over the blade chord $C$ to the blade oscillation period $T$. This implies that the reduced

frequency is a measure of temporal scales. Also, the reduced frequency can be interpreted as a ratio of spatial length scales (Figure 1.5). Subsequently, the definition of reduced frequency can be expressed as

$$K = \frac{2\pi C}{V_{ref} T} \propto \frac{C}{\lambda} \tag{1.4}$$

where $\lambda$ is the convected wavelength induced by a sinusoidal oscillation at an angular frequency of $\omega = 2\pi/T$.

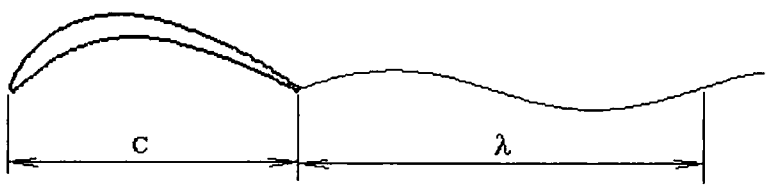


**Figure 1.5: An interpretation of reduced frequency**

The flow unsteadiness in turbomachines has a large span of reduced frequency values. If the reduced frequency is small (say $K < 0.1$), the wavelength of disturbance is very large compared to the reference length (blade chord). In other words the time scale of flow unsteadiness is small relative to the blade oscillating period, and the flow can be treated as quasi-steady. Whereas for a large value of reduced frequency, unsteady effects dominate. In unsteady flow predictions, the relevant length scales of interest are assessed by the reduced frequency, so that mesh adoption, discretisation and integration schemes can be appropriately arranged. The general experience is that flutter only occurs below a certain value of reduced frequency (simple aeroelastic design considerations being $K > 0.2$ for the first bending mode and $K > 0.6$ for a first torsion mode), which has been widely taken as a rule of thumb in the blade aeroelastic design.

An apparent feature of turbomachinery blades is that turbomachinery blades work in a row rather than an isolated environment (see Figure 1.6). Between neighbouring blades there exists aerodynamic coupling, which is accounted for by a parameter called the *inter-blade phase angle* (IBPA). The aerodynamic coupling through IBPA is the most prominent factor distinguishing the self-excited instability of blade flutter from its external counterpart — wing flutter. The pioneer work to introduce the concept of IBPA into turbomachinery aeroelasticity was done by Lane (1956). Provided that all

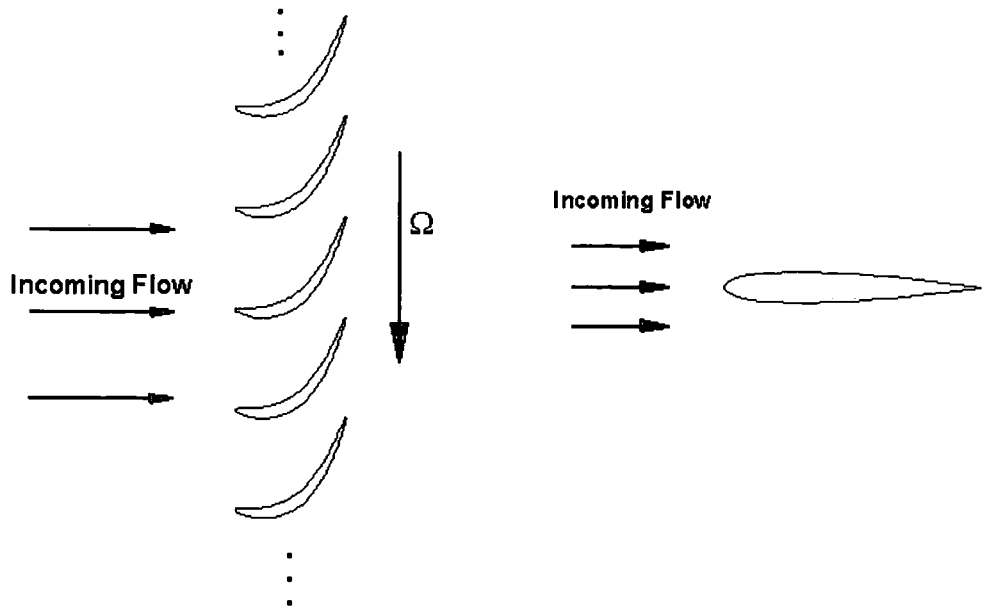


(a) Blades in a row (b) Isolated aircraft wing

**Figure 1.6: Blade row and isolated wing**

blades in a row are identical and equally spaced, and that structural linearity holds, each individual blade can be assumed to vibrate with the same amplitude and frequency but with a constant IBPA. This kind of cascade is the so-called "*tuned cascade*". In a tuned cascade, the time-dependent blade displacement can be expressed as:

$$D(m,t) = A_x \sin(\omega_0 t + m\sigma_0) \tag{1.5}$$

where $m = 0, 1, 2, ..., N_b - 1$ is the blade index in the row with $N_b$ blades, $A_x$ the amplitude of the vibration, $\omega_0$ the vibration angular frequency and $\sigma_0$ the IBPA of blade vibration. It has been proved that the IBPA of blade vibration can only take a series of discrete values, which satisfy full cycle periodicity, as expressed in Equation 1.6.

$$\sigma_0 = \frac{2\pi \cdot k}{N_b} \qquad (1 \leq k \leq N_b) \tag{1.6}$$

where $k$ is the number of *nodal diameters* (NDs) of blade vibration. The vibration of blades in a tuned row is such that it propagates circumferentially in a travelling wave and there are $k$ diameters along which the instantaneous displacement reaches zero. An example of nodal diameter pattern is shown in Figure 1.7. If the vibration propagates in the same direction of rotor rotation, it is defined as a *forward travelling wave mode.* Otherwise it is defined as a *backward travelling wave mode.*

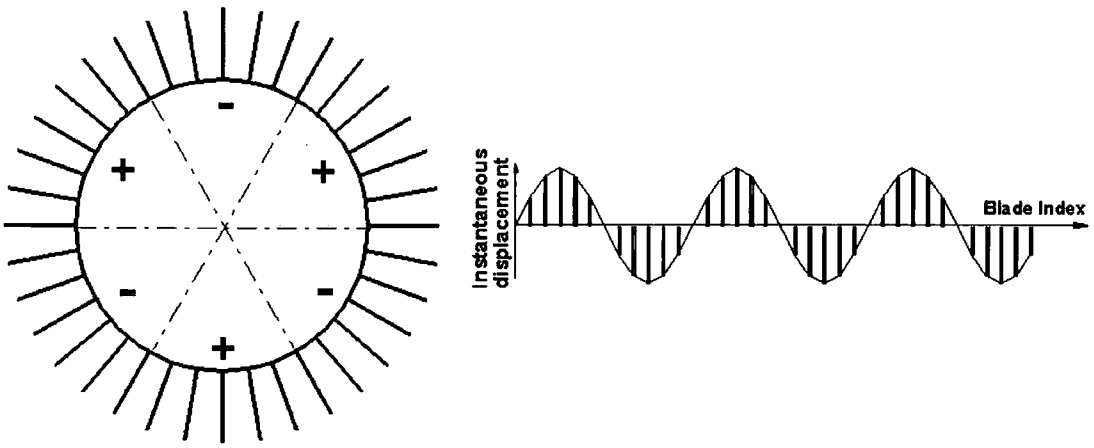


**Figure 1.7: Nodal diameter pattern (3 NDs)**

For the blade flutter analysis, it is the IBPA that can change aerodynamic damping from a positive value to a negative one at the same blade vibration frequency and mode shape. Hence, there exists the least stable IBPA, where the aerodynamic damping reaches its minimum.

## 1.3 Motivation and Objectives

In modern blade designs, with large amounts of twist and sweep and with very small inter-blade spacing, the turbomachinery flows are inherently three-dimensional. The oscillating blade flows are, if anything, more three-dimensional. However, as a matter of fact blade flutter predictions are mostly performed in a two-dimensional or quasi-three-dimensional fashion. This could be the most notable limitation in blade flutter predictions. In the last ten years or so, three-dimensional computational modelling tools for blade flutter predictions have begun to emerge, as will be reviewed later. Certainly, without validations against detailed three-dimensional experimental data, the designers' confidence in using these types of three-dimensional flutter tools would be very limited. Unfortunately, that is generally the case because most validations have been done only against two-dimensional experimental data or analytic/semi-analytic solutions due to lack of three-dimensional experimental data. It is therefore apparent that there is a demand for detailed three-dimensional flutter experimental data. To this end, several investigations (Bell and He, 2000; Queune and He, 2001; Yang and

He, 2004; Vogt and Fransson, 2004) have been carried out to improve understanding of three-dimensional oscillating flows and provide three-dimensional experimental data for the validation of advanced CFD tools. Despite these studies, it is still true that there are no published three-dimensional flutter cascade data on the turbine side. One of the present objectives is to study the oscillating cascade flow experimentally and produce a set of tuned cascade flutter data on the turbine side.

Currently, most computational models of vibrating blades assume an isolated blade row in an upstream/downstream truncated domain. Turbomachines, however, normally consist of multiple blade rows (stators and rotors). The existence of these adjacent blade rows leads to some potentially important intra-row interaction phenomena such as acoustic wave reflection, which an isolated blade row model is unable to capture. There are therefore two outstanding questions/issues: 1) Are the intra-row interaction effects significant in blade aeroelastic stability? 2) If important, how can they be predicted effectively? Until now, only a few studies (Buffum, 1995; Hall and Silkowski, 1997; Silkowski and Hall, 1998; Li and He, 2005a,b) have examined the intra-row interaction effects on the aeroelastic behaviour of turbomachines. Again, all these intra-row interaction studies have been performed on compressors and no work has yet been reported for turbines. The second objective of this study is, through using a multi-row CFD method, to investigate the influence of the upstream, fixed, nozzle blades on the self-excited aeroelastic behaviour of rotor blades in the last stage of an LP steam turbine.

LP steam turbine rotor blades are often unshrouded and the corresponding flow is characterised by a strong tip clearance jet. It has been well documented that the tip clearance flow is detrimental to turbomachine aero-thermal performance (Denton, 1993; Sjolander, 1997). Yet very little is known about the influence of the tip clearance flow on turbine blade flutter. The third objective is to experimentally and computationally examine the influence of tip clearance flow on turbine blade flutter.

As discussed earlier, the blade flutter is such that it may occur at a wide range of engine speeds. Current designs still strongly rely on passive measures to prevent flutter from occurring, normally at the penalty of aerodynamic performance. Among them, the part-span shroud is the most common measure taken. Whilst it is well known that

the introduction of part-span shrouds act to increase mechanical damping, no work has been done so far with regard to its effects on the blade flutter behaviours in the aerodynamic damping aspect. The final objective is to assess the influence of part-span shrouds on the aerodynamic characteristics of oscillating blades.

## 1.4 Overview of This Thesis

This thesis is aimed at detailed assessment of the three-dimensional nature of unsteady flows around oscillating blades in the LP turbines. For this purpose, a bespoke, linear, low speed, oscillating, turbine cascade and a realistic LP steam turbine rotor/stage are taken as the research vehicles. The study, documented herein, pursues a combined experimental and computational strategy.

In Chapter 2, the previous development in the turbomachinery aeroelasticity prediction and understanding is reviewed, with emphasis on progress relevant to this project, in order to highlight the present motivation. Chapter 3 covers the experimental techniques used in the measurements on the linear oscillating turbine cascade. Chapter 4 is devoted to the description of the CFD method employed in this investigation.

In Chapter 5, measurements and computations have been conducted to the linear cascade at its nominal setting in order to examine the three-dimensional response to the blade oscillation. Chapter 6 presents a computational investigation into the influence of the upstream stator on the rotor flutter stability in the realistic LP steam turbine stage. Chapter 7 deals with the influence of tip clearance flow on the oscillating flow in both the linear cascade and the realistic LP turbine configuration. Chapter 8 is concerned with the part-span shroud effects on the blade aeroelastic stability in the two research vehicles. Conclusions from the research are drawn in Chapter 9, along with some recommendations for future work being proposed.

# Chapter 2

# Review of the Literature

## 2.1 Experimental Investigations

Experimental flutter studies are conducted both for design purposes and to understand the underlying mechanisms of the self-excited aeroelastic problems. Specifically, the purposes of experimental studies directed at turbomachinery flutter generally lie in three aspects. The first is to generate a flutter boundary data bank which can be used to form empirical flutter design rules. The second is to provide validation data for advanced numerical methods. The third is to verify new designs by conducting tests on the prototypes. Based on different purposes, the experimental set-up and methodology are adopted accordingly.

### 2.1.1 Blade Oscillating Schemes

As described earlier, blade flutter is a self-excited phenomenon. Flutter conditions can be therefore achieved in their natural ways in experiments. These types of experiments correspond to *free flutter tests.* Alternatively, flutter conditions can be enforced in controlled ways and these are so-called *controlled flutter tests.*

#### 2.1.1.1 Free Flutter Tests

Free flutter tests are usually aimed to detect if flutter occurs at certain flow conditions, say the whole range of operational conditions of real machines. In the engine development chain of "design – build – test – deliver", full-scale prototype machines

are instrumented and tested to obtain design verification. This is the case as stated by Kielb (1999) that "although we have, and use, sophisticated design analysis tools, test validation of new engine designs will be required for many years to come". In these experiments, the emphasis is to identify the flutter stability margins and susceptible aerodynamic conditions rather than to obtain detailed unsteady aerodynamic response. It should be realised that these types of tests are inherently high in cost and complexity and mainly confined to big companies. In open literature, full-scale machine flutter tests are rarely reported.

Sanders et al. (2004) presented a free flutter study on a transonic low-aspect ratio fan blisk that experienced both subsonic/transonic and supersonic stall flutter. The incipient and deep flutter operating conditions were accomplished by slowly throttling the fan up each of the speedlines while maintaining the desired bypass ratio and monitoring the strain gages for any signs of non-synchronous activity indicative of flutter. Snyder and Commerford (1974), Hennings and Send (1998) and Urban et al. (2000) carried out free flutter tests in cascade rigs. In these investigations, blades were elastically suspended and flutter conditions were achieved by adjusting the stiffness of the blade mounting system and applying back pressure (loading). When applied to a linear cascade, the free flutter approach does, however, experience some difficulty in obtaining good periodicity, as observed by Snyder and Commerford (1974). In their work, a linear cascade of five elastically mounted fan blades was employed to examine the property of supersonic unstalled flutter. The results revealed nonuniform behaviour across the entire cascade. Indeed, the individual blades in this cascade vibrated at different amplitudes and at different values of IBPA, although a constant frequency was ensured. This observation was expected and attributed to the inherent finiteness of the linear cascade. Due to the proximity of the wind tunnel sidewalls, end blades sense localised unsteady pressure field rather differently from that sensed by the central blades and as a result vibrate at different amplitude and phase angle. In the discussion, Snyder and Commerford suggested that "The *effective finiteness* of the cascade could be greatly reduced if the cascade were forced to vibrate at the same (but adjustable) frequency, amplitude and IBPA."

Free flutter data can only be obtained at the least stable condition, i.e. the least

stable IBPA. That is to say, there will be no vibration induced unsteady pressure data (hence aerodynamic damping data) if the test system is not fluttering. Therefore, no conclusions can be made as to how sensitive the test system is if it is stable at the test conditions.

#### 2.1.1.2 Controlled Flutter Tests

In controlled flutter tests, blades are forced to vibrate in a desired mode (including mode shape and frequency). The vibration induced unsteady response (time-dependent pressure) is measured and the corresponding aerodynamic damping is thus obtained. It is worthy to point out that controlled flutter tests are the most used in acquiring experimental data to validate advanced numerical methods. Under the premise that flutter is largely of a linear phenomenon, tuned cascade data can be obtained by two schemes, i.e. the *travelling wave mode method* (Lane, 1956) and the *influence coefficient method* (Hanamura et al., 1980). It has been shown by Crawley (1984) that both the travelling wave mode and the influence coefficient method give the same aeroelastic formulation mathematically under the linear assumption. A numerical study by Gerolymos (1990) showed the influence coefficient method using seven blade passages yielded nearly the equivalent first harmonic pressure coefficients results as the travelling wave method for a compressor blade in a supersonic inviscid flow. Experimental validation studies of the influence coefficient method have also been performed and these works will be referred to in a later discussion.

**Travelling Wave Mode Method:** In travelling wave mode tests, all blades in the test cascade are driven to oscillate at the same mode shape and frequency but at a certain IBPA. These schemes are straightforward applications of the tuned cascade theory. The time-dependent pressure is measured only on the reference blade.

**Influence Coefficient Method:** In tests employing the influence coefficient method, only one blade is driven to oscillate and measurements are taken on all blades in the test cascade. The measured influence coefficients (unsteady pressure) on all blades are linearly superposed to reconstruct the tuned cascade data.

Obviously, it is cheaper and less complicated to design a facility with only one blade oscillating as in tests using the influence coefficient method. In terms of time-consumption in obtaining experimental data, these two methods have different disadvantages and strengths. If the aerodynamic damping at a certain IBPA is pursued, the influence coefficient method is more time-consuming because it needs to move the instrumented blade into all other non-instrumented blade positions in order to measure the influence coefficients on all blades. However, if the aerodynamic damping behaviours at a wide range of IBPA values are concerned, say in order to determine the least stable IBPA, the travelling wave mode method is more time-consuming because all the measurements must be repeated for every IBPA.

The employment of the influence coefficient method is restricted by its linear assumption, and the validity of linear assumption should be assured for cases concerned. Generally, linear assumption does not hold for conditions with strong separation flow and large shock wave excursion.

### 2.1.2 Experimental Facilities

Experimental studies directed at blade flutter range from measurements on a single blade up to prototype full-scale tests. Due to the extremely high costs, the full-scale machine tests are not suitable for detailed investigations of unsteady flow behaviours. The most used facilities are high speed rotating rigs and stationary cascades (annular and linear). The model rigs have been developed in order to overcome the difficulties due to accessibility problems in the real machine. Moreover, they make it easier to isolate and vary the major parameters of importance (Gallus, 1987). Low speed rotating rigs, although used for forced vibration research, are normally not used for flutter experiments because they offer no significant advantage over linear cascades (Fleeter and Jay, 1987).

#### 2.1.2.1 High Speed Rotating Rigs

High speed rotating rigs, which reproduce almost all important aerodynamic and mechanical environment of real machines, are the most realistic model vehicles for the

study of blade flutter. In order to determine the onset of instability, various efforts have been made to measure blade stress levels and mode shapes during blade flutter. Stargardter (1977) presented some measurements of fan blade deflections during stall flutter using optical techniques. In this work, the magnitude of blade vibration in both bending and torsion was determined. Due to the limited image recording speed, neither a phase angle nor nodal diameter pattern during flutter was resolved. Aiming at experimentally verifying the mode shape prediction of a bladed-disk, Mikolajczak et al. (1975) reported a holographic measurement of vibration pattern. High-speed rotating rigs have also been utilised for the measurement of unsteady oscillating blade flows. Frey and Fleeter (2001) investigated the unsteady aerodynamic response of a rotor blade row oscillating in torsion through implementation of the experimental influence coefficient technique. The measured unsteady pressure influence coefficient data decayed rapidly with increasing distance from the reference blade. Results also showed significant effects of oscillation amplitude and steady loading on the unsteady characteristics of oscillating blades. Sanders et al. (2004) recorded unsteady aerodynamic response at stalled flutter regimes at the 90% span section on a transonic low-aspect ratio fan blisk. In this work, a forward mounted 100 channel slip ring unit was employed to transfer data from the rotating instrumentation to the stationary reference frame and unsteady pressure measurements were referenced to the blade motion via signals of strain gages.

Experimental studies employing high speed rotating rigs are very costly and detailed and accurate measurements remain a considerable challenge. This is mainly reflected in several respects. Firstly, all data obtained from the rotating instrumentation must be transferred to the stationary reference frame and noise introduced in this process surely adds some uncertainty to the measurements. Secondly, costly, high-response, miniature instrumentation is often required in these types of experiments. Thirdly, much effort in calibration under operational conditions is needed to minimise the sensitivity of high-response transducers to changes in temperature as well as to acceleration affects of the blade, as demonstrated by Manwaring and Wisler (1993) and Manwaring et al. (1997). Fourthly, highly likely transducer signal failure, due to the severe centrifugal loads associated with high rotational speeds, presents an additional problem (Manwaring

et al., 1997; Sanders et al., 2004).

#### 2.1.2.2 Stationary Annular Cascades

As compared to rotating rigs, stationary annular cascades share the nature of automatical periodicity, the most important aspect in turbomachinery flow tests, but hold more advantages such as reduced cost and increased flexibility.

The inherent periodicity of annular cascades allows the flexibility to perform either free flutter tests or controlled flutter tests, for example Jutras et al. (1981) and Kobayashi (1989) respectively. Jutras et al. (1981) performed a comprehensive flutter test in a stationary annular cascade operating at subsonic/transonic conditions and intended to investigate negative incidence choke flutter and positive incidence stall flutter in mid-stage compressor bladings. In this investigation, excellent correlation was obtained between the annular cascade flutter and that of the modelled rotor in terms of Mach number and incidence angle. Kobayashi (1989) carried out a parametric investigation of the effects of shock waves on aeroelastic instability of an annular cascade in a transonic flow. Both turbine and compressor blades were employed for this research purpose. It was found that the aeroelastic stability of turbine and compressor was significantly affected by the excursion of shock waves, which oscillated chordwisely in a range of 6 percent chord length. The effects of shock wave movements were also identified to be associated with the reduced frequency and IBPA. For the compressor cascade oscillating at an IBPA of 90°, the unsteady force induced by the shock wave movement changed from being a stimulator to a damper when reduced frequency increased. While the shock movement effect was markedly controlled by the IBPA for the turbine cascade, where shock movement promoted blade vibration at an IBPA of 67° and damped blade vibration at an IBPA of $-67°$.

Fransson (1990) reported an influence coefficient technique based decomposition to explore the mechanism of the flutter susceptibility of the last stage of a steam turbine. In this study, the tuned cascade data were experimentally obtained using a travelling wave mode and decomposed into unsteady aerodynamic influence coefficients. This decomposition revealed that the instability of the cascade arose largely as a result of the unsteady aerodynamic coupling between the reference blade and its immediate

suction neighbour.

The application of the influence coefficient method (Hanamura et al., 1980) enables a much simplified experimental setup. The validity of the influence coefficient method has been experimentally investigated by Körbächer and Bölcs (1994) on compressor side and by Nowinski and Panovsky (2000) on turbine side. Körbächer and Bölcs (1994) presented an experimental investigation aiming to assess the correlation between the influence coefficient method and the travelling wave mode in a stationary annular cascade. The cascade consisted of 20 blades of a NACA-3506 airfoil profile. They concluded that the superposition principle used in an influence coefficient method was valid for cases with a low incidence angle where the supersonic and separation zones were small. The superposition principle was demonstrated to be inappropriate for the high incidence and high Mach number conditions tests where nonlinear behaviour became larger due to the existence of shocks and flow separation. Nowinski and Panovsky (2000) reported an experimental study combining a travelling wave test, an influence coefficient test and an alternating blade test. Nowinski and Panovsky, for the first time, validated the superposition principle used in the influence coefficient method for LP turbine blades vibrating in torsion. They also experimentally demonstrated the beneficial stabilizing effect of mistuning on flutter by vibrating only alternative blades in the cascades in a traveling wave pattern. In addition, mode shape was found to be the most important factor in determining the aeroelastic stability for the blades concerned and reduced frequency and steady loading were found to be less important.

Very often, reduced scale blades are adopted in annular cascade designs. This is mainly of an economic concern and becomes a disadvantage when compared with linear cascade tests where large scale blades can be used at equivalent costs. In order to limit the needed mass flow for achieving the required flow conditions whilst keeping the size of the test object large for easy instrumentation, Vogt and Fransson (2004) (also Vogt (2005)) employed an annular sector cascade, shown in Figure 2.1. Their study was aimed to assess effects of blade mode shape on the aeroelastic stability of a typical aero engine LP turbine blade row. This work, to the author's knowledge, is the only published three-dimensional flutter study on the annular cascade so far, although the tuned cascade data are only available at the middle span. The results indicated that


**Figure 2.1: Vogt and Fransson's annular sector cascade**

axial and edgewise modes featured little stabilizing effect whereas greater destabilizing contribution was observed for flex bending mode. It was also concluded that the effect of blade mode shape has shown a greater influence than the reduced frequency. On the same rig, Vogt and Fransson (2006) studied the effect of negative incidence on mode shape sensitivity of an oscillating LP turbine rotor blade row. The separation on the fore pressure surface associated with negative incidence operations was found to have a destabilising effect on bending modes of chordwise character whhereas an increase in stability could be noticed for bending modes of edgewise character. For torsion-dominated modes, the influence on blade flutter stability was close to neutral.

Another disadvantage associated with annular cascade facilities is that uniform inlet flow conditions are difficult to generate and usually require complex inlet geometries, as demonstrated by Bölcs (1983).

#### 2.1.2.3 Linear Cascades

Linear cascades can be seen as sectors of unwrapped annular cascades. Comparing to rotating rigs and annular cascades, linear cascades have less blades, say 5 to 11 in general, and this has at least two aspects of financial benefits. First, it would be less expensive to build these types of facilities. Second, using less blades means the enlarged scale can be employed in linear cascades without increasing the demand for mass flow

delivery, hence operational costs. Apart from the financial benefits, linear cascades possess several other advantages. First, the employment of large-scale prismatic blades allows detailed straightforward instrumentation and provides favourable conditions for flow visualisation. Second, the decreased complexity of three-dimensional steady flow features lends interpretation of experimental results comparative ease. Third, linear cascades offer much flexibility to vary flow speed, incidence angle, vibration mode shape and frequency for parametric studies. These are what make the linear cascade the most widely used experimental facility to study unsteady flow around vibrating turbomachinery blades.

It has been well recognised that good steady-state blade-to-blade periodicity is essential for all types of turbomachinery experimental studies. However, it is difficult to generate good steady-state blade-to-blade periodicity in linear cascades due to limited blade number. One possible solution is to use a fairly large number of blades in a linear cascade, but this is not typically practical (Fleeter and Jay, 1987). Very often, a pair of downstream "tailboards" are used, for example Carta and St. Hilaire (1978, 1980), Buffum and Fleeter (1990a, 1993, 1994), Buffum et al. (1998), Ott et al. (1998) and Lepicovsky et al. (2001). Carta and St. Hilaire (1978, 1980) conducted comprehensive parametric experiments to investigate the unsteady aerodynamics at subsonic conditions near stall in an oscillating linear cascade. The cascade consisted of 11 NACA-65 compressor blades, which were shaft-mounted and mechanically driven in pitching mode at a prescribed frequency. At the trailing edges of ceiling and floor end blocks, movable tailboards were employed to guide the exit flow to establish downstream periodicity. Within the range of parameters tested, the results showed that the IBPA was the most influential parameter affecting the aeroelastic stability of the cascade. Additionally, they observed that there was no evidence of stall occurrence when "stalled flutter" happened. This finding supported an earlier observation made by Mikolajczak et al. (1975) that separation was not a prerequisite of stall flutter. Lepicovsky et al. (2001) carried out a combined experimental and numerical study to address the flow uniformity and periodicity in the NASA transonic flutter cascade. Their results showed that the tailboard setting angle strongly affected the periodicity of the cascade and boundary layer bleed did not improve the cascade flow periodic-

ity. Besides, Lepicovsky et al. suggested that cascade sidewalls must be shaped like predicted mid-passage streamlines in order to minimise the endwall interference.

As reviewed earlier, linear cascades are not appropriate for free flutter tests (Snyder and Commerford, 1974) due to their inherent finiteness. Following the contribution of Snyder and Commerford (1974), tests in linear cascades have been most frequently conducted in controlled flutter fashions, for example Carta and St. Hilaire (1978, 1980), Hanamura et al. (1980), Rothrock et al. (1982), Carta (1983), Szechenyi (1987), Buffum and Fleeter (1990a, 1993, 1994), Buffum et al. (1998), He (1998), Ott et al. (1998) and Lepicovsky et al. (2001). Carta (1983) carried out a systematic test to examine the gapwise periodicity of the oscillating linear cascade earlier commissioned in Carta and St. Hilaire (1978, 1980). At two tested incidences (2° and 6°), the measured data satisfied the dynamic periodicity condition over most of the operating ranges and over most of the blade leading edge region. At a high incidence of 6°, pressure amplitude periodicity deteriorated towards the leading edge. However, this periodicity deterioration was observed to be local within 5 percent of the chord aft of the leading edge, where the highest unsteady pressure activity was recorded. A similar investigation was made into the steady and dynamic periodicity of a linear oscillating cascade by Buffum and Fleeter (1993). Their cascade of four biconvex airfoils was driven simultaneously in a harmonic torsion mode of vibration. Unsteady measurements were made at various values of IBPA and reduced frequency. It was found that good dynamic periodicity manifested for certain values of IBPA but poor for others. Based upon results of a linearized flat plate analysis, it was suggested that the pressure waves reflected from the wind tunnel sidewalls were responsible for the poor dynamic periodicity. However, one can argue that the poor dynamic periodicity experienced by Buffum and Fleeter (1993) might be due to extremely small blade number (only 4). This problem was very much relaxed in the test of Carta (1983), where 11 blades were used.

In an attempt to improve blade-to-blade periodicity in a later study of Buffum et al. (1998), an acoustic treatment, i.e. wall perforation and pressure wave absorbing, was introduced to the upper sidewall and the lower tailboard. However, the effectiveness of this treatment has not been well proven. A study by Ott et al. (1998) indicated that the porous walls created additional harmonic disturbances and had to be replaced by

solid ones.

The combination of the linear influence coefficient technique and the linear cascade proved to be very attractive owning to its simplicity and high cost effectiveness and has been widely employed to study the aerodynamic behaviour around oscillating blades. Among them, Hanamura et al. (1980), Szechenyi (1987), Buffum and Fleeter (1990b), Norryd and Bölcs (1997), He (1998), Ott et al. (1998) and Lepicovsky et al. (2002) can be cited. Hanamura et al. (1980) performed an experiment in a water channel using the influence coefficient technique and demonstrated its validity in incompressible flow. The validity of the influence coefficient method has been experimentally assessed in linear cascades for fan blades (Szechenyi, 1987) and biconvex airfoils (Buffum and Fleeter, 1990b). Szechenyi (1987) performed an experimental verification with a supersonic inlet flow where the summation of influence coefficients had a good comparison with data with two neighbouring blades oscillating. Szechenyi (1987) found the shock wave oscillation was a dominant contributor to the blade excitation in two-dimensional wind tunnel experiments in which a shock wave was attached to the leading edge of the blade. The results of Buffum and Fleeter (1990b) demonstrated that the unsteady aerodynamic influence coefficient data generally exhibited good correlation with the travelling wave mode data except cases in the vicinity of the acoustic resonance points. This method has, however, been shown to be adequately valid in experiments in a transonic fan cascade (Lepicovsky et al., 2002) and an LP turbine cascade (He, 1998) where flow separation was present. Norryd and Bölcs (1997) applied the influence coefficient technique to an experimental investigation concerning the influence of tip clearance on the steady and unsteady blade surface pressure response in a linear turbine cascade. The influence of a change in tip clearance on both the steady and unsteady blade surface pressure distribution is observed at mid-span. Unfortunately, the instrumentation was limited to the mid-span section which provided no direct evidence regarding the tip clearance effect.

It should be pointed out that the aforementioned experimental studies in linear cascades were all conducted at a two-dimensional section (midspan). Recently, several flutter tests (Bell and He, 2000; Queune and He, 2001; Yang and He, 2004) were performed in University of Durham to assess the three-dimensional nature of unsteady aerodynamic

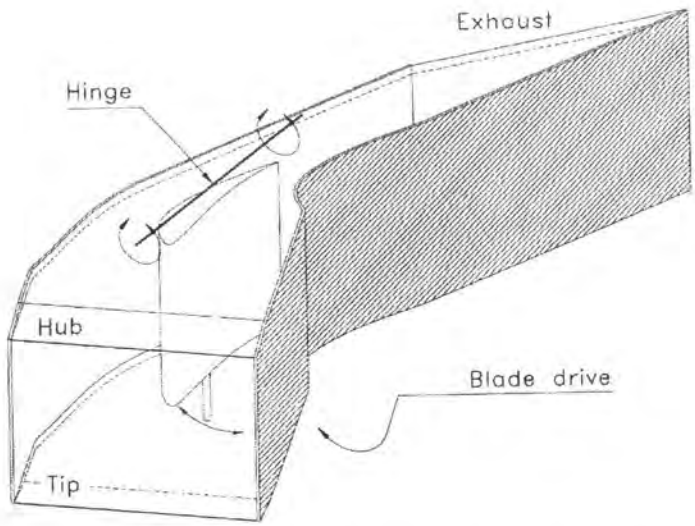


**Figure 2.2: Bell and He's single blade facility**

**Figure 2.3: Yang and He's compressor cascade**

response around oscillating turbomachinery blades. Bell and He (2000) presented, for the first time, three-dimensional test data for a single turbine blade, oscillating in a profiled channel, shown in Figure 2.2. The blade was externally driven in a sinusoidal pattern and a three-dimensional bending mode was achieved by hinging the blade at root and driving the tip section. The test data indicated a significant three-dimensional effect, whereby the amplitude of the unsteady pressure response at different spanwise locations is largely insensitive to the local bending amplitude. Their results, concerning

the influence of tip leakage, showed a consistent variation in the amplitude of the unsteady pressure response with changes in tip gap. Unfortunately, this study neglects the blade-to-blade interference, which is an important characteristic of turbomachinery blade flutter. A further experimental investigation on the same rig with massive part-span flow separation was carried out by Queune and He (2001) and they found that, in the separated flow region, the unsteady pressure had a destabilising effect on the blade aeroelasticity. Yang and He (2004) conducted a flutter experiment on a linear oscillating compressor cascade (Figure 2.3) with consideration of both three-dimensional effects and the blade-to-blade interference. The measured results demonstrated a strong three-dimensional behaviour of unsteady aerodynamic response to the blade oscillation in a three-dimensional bending mode. The significant influence of blade aerodynamic coupling was found to be largely from the directly adjacent blades.

The low-speed linear facilities have been widely used in the tubomachinery aerodynamic performance studies. Apart from shock waves and blade row rotating, low-speed linear facilities can be employed for wide range of parametric studies. In turbomachinery aeroelastic applications, there are several publications available in literature, such as He (1998), Bell and He (2000), Queune and He (2001) and Yang and He (2004). All these studies demonstrated high quality of test dada in terms of accuracy and repeatability.

## 2.2 Computational Methods

Turbomachine blade flutter analyses involve the prediction of unsteady aerodynamic response to the blade oscillation. Over the last two decades, unsteady aerodynamic models for use in turbomachinery aeroelastic applications have significantly progressed and a number of approaches emerged at different approximation levels of the unsteady flows. The most actively pursued methods can be classified into two categories, namely frequency domain methods and time domain methods.

### 2.2.1 Frequency Domain Methods

Time-linearisation technique was first applied to two dimensional, inviscid, unsteady potential flow equations (Verdon and Caspar, 1982, 1984; Whitehead, 1987; Hall and

Verdon, 1991). This technique enables the effect of blade steady loading upon the unsteady aerodynamic response to be included. However, these potential flow analyses do not have the capability to model unsteady flows containing strong shocks due to their inherent assumption of an isentropic and irrotational flow. Ni and Sisto (1976) was the first to perform the time-linearised Euler analysis to address the effects of strong shocks on the unsteady response. In this calculation, the pseudo-time time-marching technique, local time stepping and multiple grid acceleration were used. Hall and Crawley (1989) and Holmes and Chuang (1993) developed two-dimensional time-linearised Euler codes to analyse the aeroelastic instabilities of turbomachinery blade rows. In order to consider three-dimensional effects, Hall and Lorence (1993) presented a fully three-dimensional time-linearised Euler analysis for unsteady flows to predict flutter and forced response. In the studies of Hall and Lorence (1993) and Holmes and Chuang (1993), deforming computational grids, which had already been successfully used in nonlinear time-marching analyses, were adopted. By using deforming computational grids, there is no need to extrapolate the flow variables from the boundary of the grids to the instantaneous location of the blade surface. Later, the time-linearisation technique was extended to solve the three-dimensional time-linearised Reynolds-averaged Navier-Stokes equations (Holmes and Lorence, 1997). In this study, the two-equation $k-\omega$ turbulence model was linearised with a wall function adopted to avoid using very fine meshing in the near wall region. Sbardella and Imregun (2001) presented a three-dimensional finite volume scheme based on hybrid grids to solve the linearised, unsteady Favre-averaged Navier-Stokes equations. The results showed that the linerisation of the turbulence model plays an important role wherever the viscous effects are important.

In these time-linearised methods, basic assumption is made that the unsteady flow is composed of a perturbation to the steady flow. Furthermore, the perturbation is assumed to be very small so that nonlinear effects can be neglected. These assumptions allow any flow variable to be broken up into a steady part and an unsteady part. Then the governing equations can be time-linearised. The resulting linearised variable coefficient equations are time-independent and can be solved using conventional steady flow techniques. Typically, a time-linearised unsteady calculation is thought to be

equivalent to solving two 'steady' flow problems in a single-passage. In this way, it is of high computational efficiency. Actually, the time- linearised methodology has been widely used in industry because of its high efficiency. However, the validity of time linearised methods may break down under strong nonlinear conditions, where separated flow prevails or shock and boundary layer interaction is important.

Recently, the frequency domain approaches have made considerable progress by including some elements of the nonlinear effects. To relax the linear assumption about unsteadiness whilst to retain the high computational efficiency of the time-linearised method, He (1996) proposed a novel computational model — the nonlinear harmonic method. In this method, the flow is taken as an unsteady perturbation to a time-averaged flow rather than a steady flow used in time-linearised methods. Application of the nonlinear harmonic methodology (Ning and He, 1998; He and Ning, 1998) results in coupled equations for the time-averaged flow and the small unsteady perturbation. The nonlinear interaction between the time-average flow and the unsteady perturbation is included by a simultaneous pseudo-time integration scheme, leading to a strongly coupled solution. More recently, nonlinear harmonic method has been extended to calculating rotor-stator interactions (Chen et al., 2001) and analysis of rotor-rotor/stator-stator interferences (He et al., 2002). In a principally similar attempt, the harmonic balance technique was developed by Hall et al. (2002). Both the nonlinear harmonic and harmonic balance techniques now enable the inclusion of harmonic perturbations of orders higher than one. The results of Hall et al. (2002) showed that the inclusion of higher order harmonics can improve the prediction of nonlinearity. Nevertheless, these two methods do have their limitation due to the truncation of higher order harmonic components. When nonlinear effects are very strong, they can only qualitatively capture the nonlinear behaviour.

Until now, only a few studies have examined the intra-row interaction effects on the aeroelastic behaviour of turbomachines. Among them, Buffum (1995), Hall and Silkowski (1997) and Silkowski and Hall (1998) used a 'coupled model' to obtain the behaviour of the multistage machine from the individual cascades' reflection and transmission coefficients, which were predicted by a time-linearised Euler solver. Their results suggest that the aerodynamic damping of an isolated cascade of vibrating airfoils

can differ markedly from the aerodynamic damping when the cascade is surrounded by neighbouring blade-rows and that the intra-row spacing significantly affects the aerodynamic damping. Saiz et al. (2006) developed a three-dimensional time-linearised unsteady Navier-Stokes approach to predict the multistage aeroelastic effects for both flutter and forced response. For the tested cases, the results did not indicate strong multistage effects.

### 2.2.2 Time Domain Methods

The time domain methods, namely the nonlinear time-marching methods, provide more comprehensive physical modeling capabilities to simulate the unsteady flow phenomenon in turbomachines. As its name suggests, the time-marching method, is the most straightforward one, which time-marches the flow state from one instant to the next, finally to a converged state in which flow shows a 'steady-state' periodicity. It is generally valid and can be easily extended from the steady counterpart. The time-marching unsteady calculations of turbomachinery flows were initially confined to the simulation of blade row interactions (Erdos et al., 1977; Rai, 1987, 1989; Giles, 1990b). During the last two decades, the time domain schemes in turbomachinery aeroelastic applications have evolved from the early two-dimensional inviscid fashions (Fransson and Pandolfi, 1986; Gerolymos, 1988; He, 1990) to the fully three-dimensional viscous tools, for example Giles and Haimes (1993), He and Denton (1994), Isomura and Giles (1998), Ji and Liu (1999), Grüber and Carstens (2001), Silkowski et al. (2001) and Sanders et al. (2004).

The major advantage of the time domain method manifests itself in modelling nonlinearities. However, it has been recognised that running a time-domain method is very time consuming. The relatively high time consumption of these types of methods mainly results from two aspects. The first is of the difficulty in realising a solution in a single passage computational domain. Normally, a multiple-passage (M.P.)/whole-annulus domain is required to meet the circumferential periodicities of disturbances. The second is associated with the rigid definition requirement of consistent physical time step in unsteady flow calculations.

Obviously, if the computational domain can be confined to a *single-passage* (S.P.) domain, the time consumption would be reduced dramatically. To do so, phase-shifted periodicities are assumed. At present, there are three established techniques to deal with the phase-shifted periodic boundary conditions. The conventional way to implement phase shifted periodic boundary conditions is the *Direct Store* approach (Erdos et al., 1977), in which the flow variables on the periodic boundary are stored over a period of unsteadiness. The stored periodic boundary variables during the previous period are recalled to update the solutions in the present period. As its name implies, the application of Direct Store is straightforward, but suffers the requirement for large computer memory, especially when a three-dimensional computation domain and an explicit time-marching scheme are employed. The worst is its inability in practical terms when multiple disturbances of arbitrary frequencies are involved and the corresponding beating period is very long. To remove the large storage expense incurred by Direct Store, Giles (1988) proposed a novel method, termed the *Time Inclination*, in which the computation time plane is inclined along the blade pitchwise direction according to a given IBPA. Then the direct periodic boundary condition can be applied on the transformed computational plane. Relatively, this method has a faster convergence rate compared to Direct Store. However, its application range of IBPA (in form of the time-inclination angle) is restricted by the characteristics of the governing equations. Also, the Time Inclination method can only cope with a single disturbance/IBPA. The third option is the *Shape Correction* scheme proposed by He (1990). in which the time-wise variations of periodic boundary variables are approximated in the Fourier series. Since a few orders of Fourier coefficients are stored instead of a whole period history of flow variables, the computer storage expense would be greatly relieved. The Shape Correction method has been extended to deal with multiple perturbations (He, 1992). Since extra computational time is incurred in calculating the Fourier coefficients, the CPU time of a Shape Correction based single-passage solution is approximately equivalent to that of a multiple-passage calculation with 2-2.5 passages. Despite this, the time saving by employing a Shape Correction based single passage calculation is still very much encouraging when one notes that there are 60 or more blade passages in a typical LP turbine row.

The rigid time definition in unsteady calculations is such that the maximum possible time step is restricted by the minimum mesh spacing. As is well known, when the Navier-Stokes equations are used, the minimum spatial mesh spacing becomes very small to resolve thin viscous boundary layers and wakes. In this case, the allowable time step for traditional explicit methods become very small to satisfy uniform time step in the whole computational domain. To speed up time-marching in unsteady calculations, one possible way is to relax the time definition in the temporal integration. To this end, there emerged two important treatments. One is the time-consistent scheme proposed by He (1993) and the other is the dual-time stepping concept of Jameson (1991). Both methods are implemented in a multi-grid fashion. The simplest implementation of the *time-consistent multi-grid* is to use just two-level grids, for example He (1993) and Höhn and Heinig (2000) for two-dimensional applications and He and Denton (1994) for a three-dimensional case. He (2000) extended the time-consistent multi-grid to the general formulation in an application to investigate the effects of blade-row axial gap on turbine stage performances. The *dual-time multi-grid* has been applied to Euler solutions (Jameson, 1991) and Navier-Stokes calculations (Ji and Liu, 1999; Doi and Alonso, 2002). A comparison study of different acceleration techniques was conducted by Von Hoyningen-Huene and Jung (2000) in unsteady turbine stage flow calculations. The results showed that the time-consistent multi-grid method proved to model the time-resolved entropy distribution very accurately, but there were some discrepancies in modelling the time-dependent skin friction and the time-dependent pressure distribution on the stator and the rotor blades. Whilst calculations with the dual time stepping also exhibited some deviation in the skin friction prediction on the suction surface, the time-dependent pressure and entropy were modeled well.

In the aeroelastic problems, there has been some general consensus that viscous effects can be neglected except in stall and choke flutter problems (Bendiksen, 1990). A recent research by Grüber and Carstens (2001) found that viscous effects might cause a significant change in the aerodynamic damping. This behaviour was demonstrated by two cases in which an Euler calculation predicts a damped oscillation whereas a Navier-Stokes computation leads to an excited vibration. The underlying reason for these contrary results is that shock/boundary layer interactions, with accompanying

strong viscous effects, change the aerodynamic damping dramatically.

Li and He (2005a,b) investigated the intra-row effects on the aerodynamic damping of compressor rotors using a three-dimensional, time-marching, single-passage, Navier-Stokes solver. For a vibrating rotor embedded in a compressor stage (Li and He, 2005a), the predicted non-monotonic relationship between the rotor blade aerodynamic damping and gap distance suggests the existence of an optimum gap regarding rotor flutter stability. It has also been shown that the intra-row interaction effect on the rotor aerodynamic damping may be altered by changing the number of stator blade numbers. In a further study by Li and He (2005b) for a one and half stage transonic compressor, it was found that the intra-row gap spacing could have either stabilising or destabilising effects. The optimisation analysis revealed significant damping variation ($\sim$ 300%) within the chosen intra-row gap design space. The results also indicated that the rotor-stator gap had much more significant impacts on the rotor aerodynamic damping than the IGV-rotor gap effects.

The tip clearance flow modelling has been less developed and understood in the flutter predictions. Sanders et al. (2004) found that tip clearance had a marked impact on both the magnitude and phase angle of the predicted unsteady surface pressure distributions in the tip region of a transonic fan. Their results demonstrated that the unsteady aerodynamics in the region of the fan was influenced by tip clearance effects to a much larger extent than the time-average flow field. The results also revealed that accurate flutter predictions were obtained for supersonic operational conditions using a simple tip clearance model (periodic boundary conditions across the non-gridded region between the blade tip and the outer casing) and a scaled tip gap.

The foregoing time-domain turbomachinery flutter investigations all employed the *fluid/structure* (F/S) decoupled model based on the Energy Method. From a more general point of view, turbomachinery flutter is a fluid/structure coupled problem. Fluid/structure coupled methods have also been pursued in blade flutter predictions, for examples He (1994), Marshall and Giles (1997), Sayma et al. (1998), Carstens and Belz (2000), Vahdati et al. (2001) and Doi and Alonso (2002). The basic attempt of coupled methods is to treat the aeroelasticity problem in one continuous medium with an inner boundary between the blade surface and its surrounding flow. In a coupled

method, the nonlinear aerodynamic equations and the structure equations are simultaneously solved using a time-marching scheme with information being transferred between two sides at every time step. On the aerodynamic side, the information obtained is the blade spatial position and its vibrating velocities whilst on the structural side, the instantaneous aerodynamic forces and moments are input from the aerodynamic counterpart. This kind of calculation is normally carried out in a multiple-passage/whole annulus domain and disturbances of all IBPAs but the unstable one will die out during solution converging. Unfortunately, the numerical solution of fully fluid/structure coupled three-dimensional turbomachinery flutter predictions is a formidable task that typically requires weeks/months of intensive computing.

## 2.3 Closing Remarks

There is a high demand for three-dimensional flutter data, especially three-dimensional tuned cascade data, which can be directly used for the validation of advanced three-dimensional CFD methods. The published three-dimensional data are summarised in Table 2.1. Obviously, there is a justification for the present experiment proposal to produce a set of three-dimensional tuned cascade data on the turbine side. In addition, the low speed test environment offers several advantages: high quality data, large scale test objects (blades), low cost and so on. Table 2.2 is the summary of the computational methods currently under active development. In the present project, parametric studies involve a large amount of computation. Therefore, a single-passage, time-marching, Navier-Stokes method is adopted for its computational efficiency and nonlinearity modelling capability.

**Table 2.1: Summary on 3D Experimental Studies**

| Study | Features |
|---|---|
| Bell and He (2000) | 3D single blade data, turbine, low speed |
| Queune and He (2001) | 3D single blade, turbine, low speed, large separation |
| Yang and He (2004) | 3D tuned cascade data, compressor, low speed |
| Vogt and Fransson (2004) and Vogt (2005) | mid-span tuned cascade data, 3D influence coefficient data on neighbour blades, high speed |

Given that the remarkable effects of adjacent blade rows on the rotor aeroelastic sta-

**Table 2.2: Summary on Computational Methods**

| Methods | Features |
|---|---|
| Frequency Domain (S.P.) | fast, linear or partially nonlinear, parametric study |
| Time Domain (S.P.) | affordable time consumption, nonlinear, parametric study |
| Time Domain (M.P.) | time consuming, nonlinear modelling |
| Time Domain (F/S coupled) | extreme time consuming, highest fidelity |

bility have been identified in compressors (Buffum, 1995; Hall and Silkowski, 1997; Silkowski and Hall, 1998; Li and He, 2005a,b), it is natural to ask how the adjacent bade rows influence the rotor aeroelastic stability in turbines. This issue is also to be addressed in the thesis. In addition, tip clearance flow and part-span shrouds, two of the most prevalent features in LP turbines, are to be studied in terms of their influence on the blade aeroelastic characteristics.

# Chapter 3

# Experimental Methods

## 3.1 Description of Test Facility

The tests have been conducted in a low speed facility, shown in Figure 3.1, in the Thermodynamics and Fluid Mechanics Laboratories of the School of Engineering at the University of Durham. Main characteristics of this facility are listed as follows:

- Low speed, uniform, flow delivery to the working section is achieved;
- The working section consists of a seven-blade cascade with the middle blade being driven to oscillate at a harmonic rate;
- Large scale, prismatic blades are employed with detailed instrumentation;
- A three-dimensional bending mode is enforced by hinging the blade at the hub and driving at the tip;
- Realistic reduced frequencies are established at low frequencies of blade vibration and off-board pressure transducers are used;
- Unsteady pressure signal distortion along the tubing lengths is corrected by a tubing transfer function scheme;
- Measurements are made on the five middle blades and the tuned cascade flutter data are reconstructed using the influence coefficient technique;
- High quality flutter data are obtained in terms of accuracy and repeatability.

**Figure 3.1: Test facility**

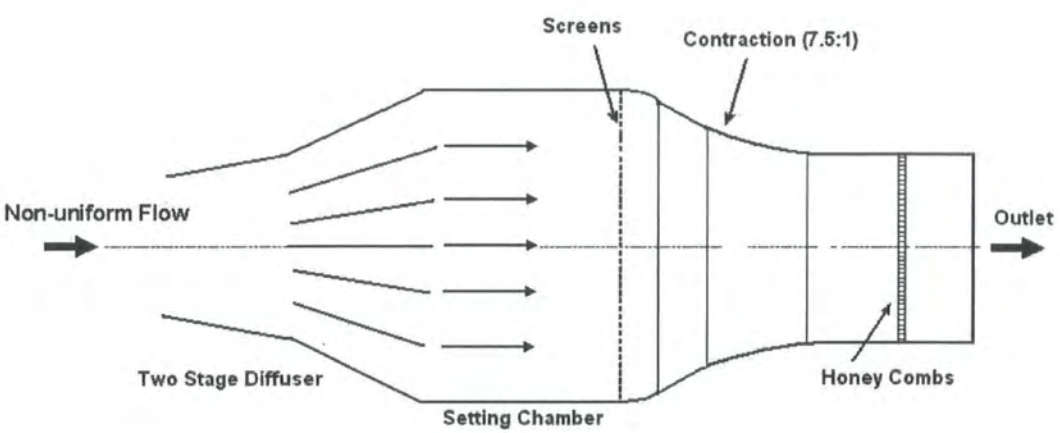


(a) Side view

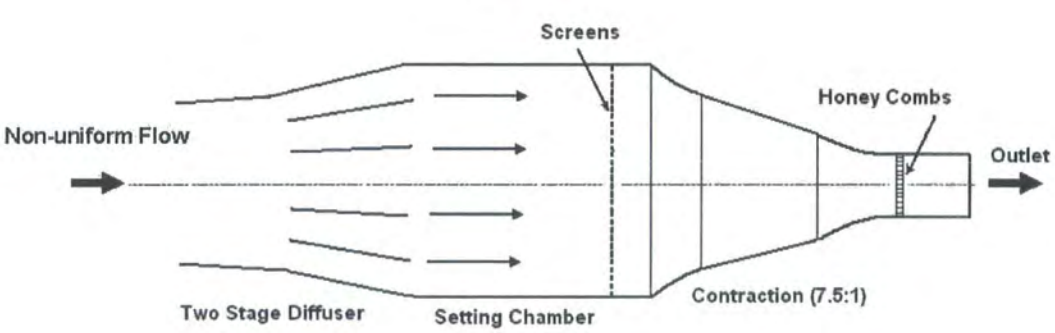


(b) Top view

**Figure 3.2: Schematic of the low speed wind tunnel**

### 3.1.1 Low Speed Wind Tunnel

A low speed wind tunnel, built during a previous compressor blade flutter research project (Yang, 2004), was adopted for the present experimental study. This wind tunnel, shown in Figure 3.2, is an open facility, which has a rectangular exhaust cross-section of $250mm \times 800mm$. In this rig, air flow is driven by a centrifugal fan (powered by an eleven *kilowatt* A.C. motor; speed: 0-1500$rpm$) through a two-stage, slatted diffuser and into a large settling chamber. The flow, under a propelling force generated by the high pressure in the settling chamber, accelerates through a shaped contraction and discharges into the working section. The quality of the flow discharge into the working section is largely dependent upon the contraction, specially its shape and the ratio of inlet and exit areas. The contraction shape follows an established design known as the Vitoshinskii nozzle (Gorlin and Slezinger, 1964). The contraction consists of four sections with flat and curve planes being alternatively applied to the horizontal and vertical sidewalls and a contraction ratio of 7.5:1 is achieved. To help establish uniform flow delivery to the working section, screens and honeycombs are deployed before and after the contraction, respectively. The wind tunnel is of a variable speed facility, with the mass flow being accurately controlled by a digital three phrase invertor.

### 3.1.2 Working Section

The working section, shown in Figure 3.3, is actually a self-contained linear turbine cascade. It consists of seven prismatic turbine blades, Perspex endwalls and a wooden frame. The blade profile is a bespoke, low speed, design which was developed within the framework of the present investigation. The top and bottom sidewalls of the wooden frame are profiled to simulate two blades adjacent to the seven middle blades in cascade; therefore eight blade passages are formed, with four passages on each side of the middle reference blade. Previous studies (for example He (1998) and Yang and He (2004)) showed a linear cascade of seven blades would not experience considerable sidewall interference if the influence coefficient method is employed. The endwalls are made of Perspex in an attempt to obtain good visual access to the working section. Bleed slots are located at one chord length upstream of blades to break down the boundary layer

development on the endwalls whereas no such effort is made to remove the boundary layer on the profiled top and bottom sidewalls. Two adjustable tailboards, acting as the extension of top and bottom sidewalls, are used to help establish blade-to-blade periodicity.

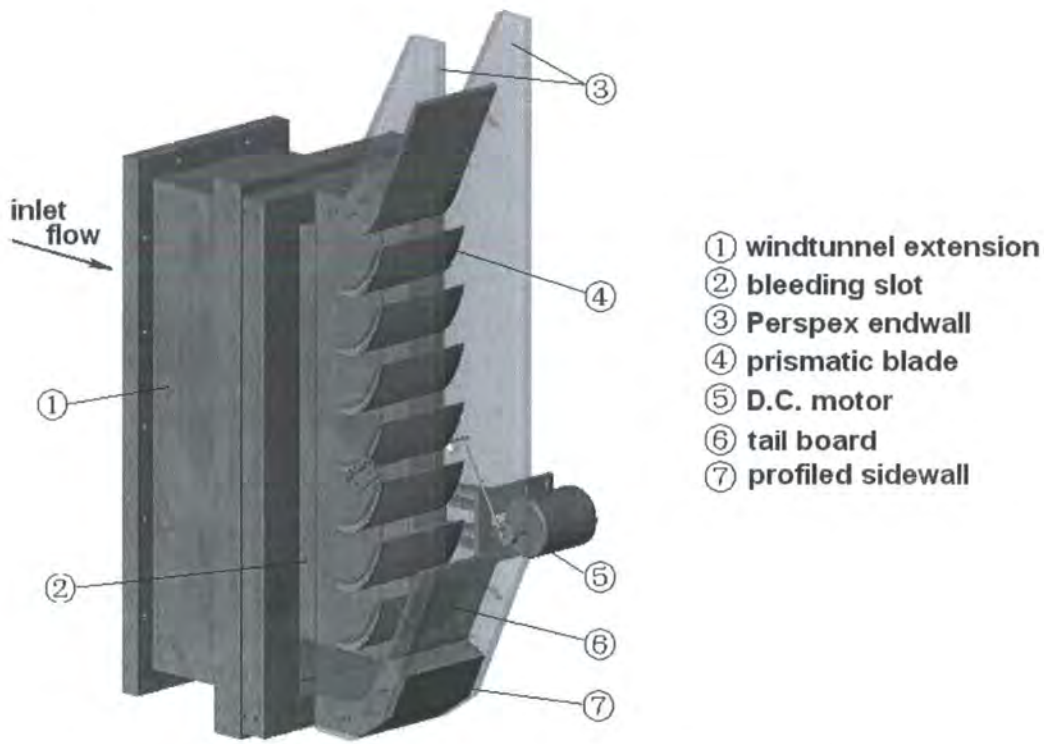


**Figure 3.3: The working section (generated by SolidWorks)**

### 3.1.3 Blade Choice/Design

Being that there was no specialised blade design tool available to this project, a 'Cut and Try' blade design procedure, shown in Figure 3.4, was adopted. In this design procedure, a blade profile, taken from a typical high speed blade, is manually redesigned (blade cut) in terms of thickness, deflection angle, etc and evaluated (CFD test) in terms of steady loading in order to obtain a good low speed design. The choice of the final design is based on visual inspection of the predicted steady flow loading. Figure 3.5 shows the final blade profile and nomenclature and a summary of the blade cascade properties is presented in Table 3.1. The coordinates of the blade profile are presented in the Appendix. For ease of instrumentation, a large scale (blade chord: 143 mm) is

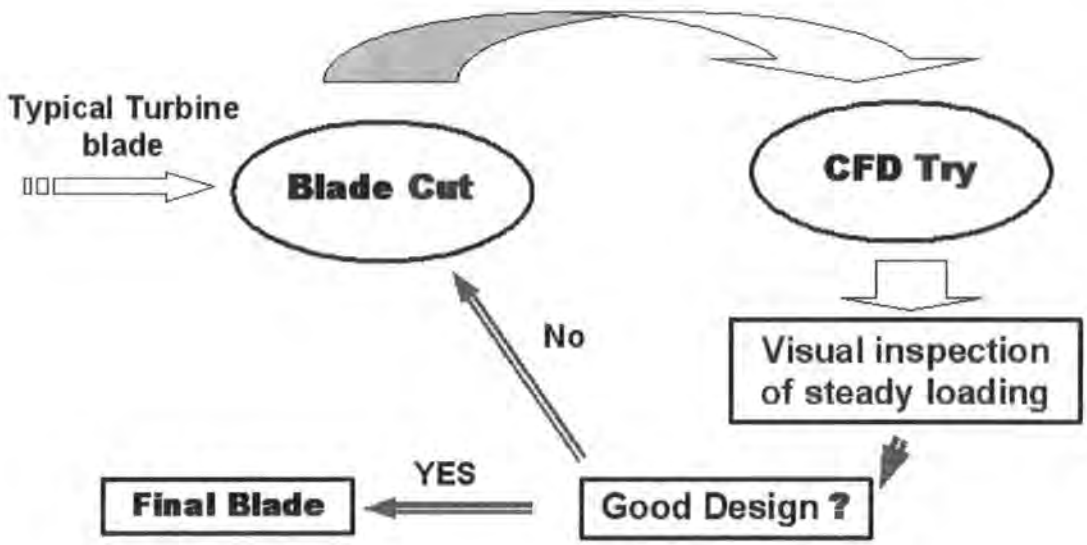


**Figure 3.4: 'Cut and Try' blade design procedure**

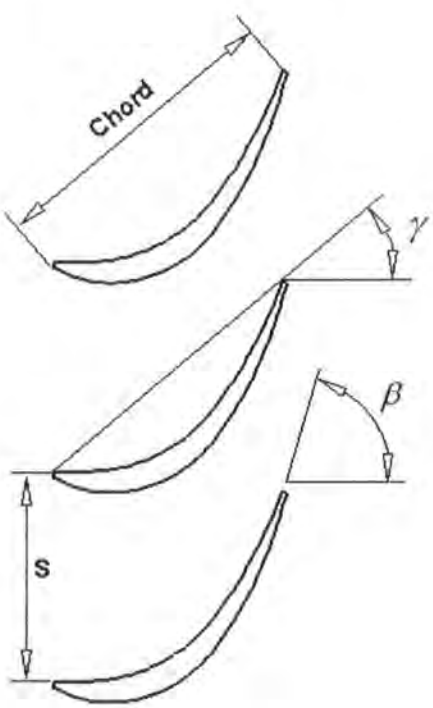


**Figure 3.5: Blade profile and nomenclature**

utilised. Due to the limit of facility size, the aspect ratio is chosen to be 1.259 although aspect ratios as large as 10 might be encountered in realistic low-pressure turbines. Despite the limited aspect ratio, it is believed that a significant three-dimensional

behaviour would be introduced by an appropriate application of the three-dimensional bending mode. And prismatic blades are employed in the present work to provide a largely two-dimensional steady base flow and this enables relatively easier identification of the unsteady effects purely associated with the three-dimensional mode of oscillation.

**Table 3.1: Cascade properties**

| | |
|---|---|
| Number of blades, $N_b$ | 7 |
| Chord length, $C$ | $0.143m$ |
| Aspect ratio, $h/C$ | 1.259 |
| Solidity, $C/s$ | 1.430 |
| Maximum thickness | $0.080C$ |
| Stagger angle, $\gamma$ | 40° |
| Blade inlet angle, $\alpha$ | 0.0° |
| Blade exit angle, $\beta$ | 70.0° |
| Leading edge radius | $1.596mm$ |
| Trailing edge radius | $1.000mm$ |

### 3.1.4 Blade Oscillating Drive

To achieve a three-dimensional bending/flapping condition, the reference (middle) blade is hinged at the hub and driven at the tip, as shown in Figure 3.6. This allows a linear variation in bending amplitude along the span, corresponding to the first bending mode. The direction of bending is set normal to the blade chord line, with the positive being from the pressure side to the suction side. A sinusoidal oscillation rate is enforced by using a single bar crank connection between a DC motor shaft and a rod protruding from the blade tip. In theory, the single bar crank connecting mechanism described does not produce a pure sinusoidal oscillation. To obtain a good approximation to a pure sinusoidal oscillation, two aspects should be taken into account. The first is to ensure the length of the crank arm being much (say twenty times) greater than the amplitude of blade bending. The second is to align the crank arm with the bending direction. As shown in Figure 3.7, a close approximation to a pure sinusoidal oscillation is achieved in the current setup. Since the hinge at the hub is mounted outside the working section, it should be noted that a small displacement is introduced to the hub of the oscillating blade. Indeed, an amplitude at the hub is a tenth of that at the tip (Table 3.2).

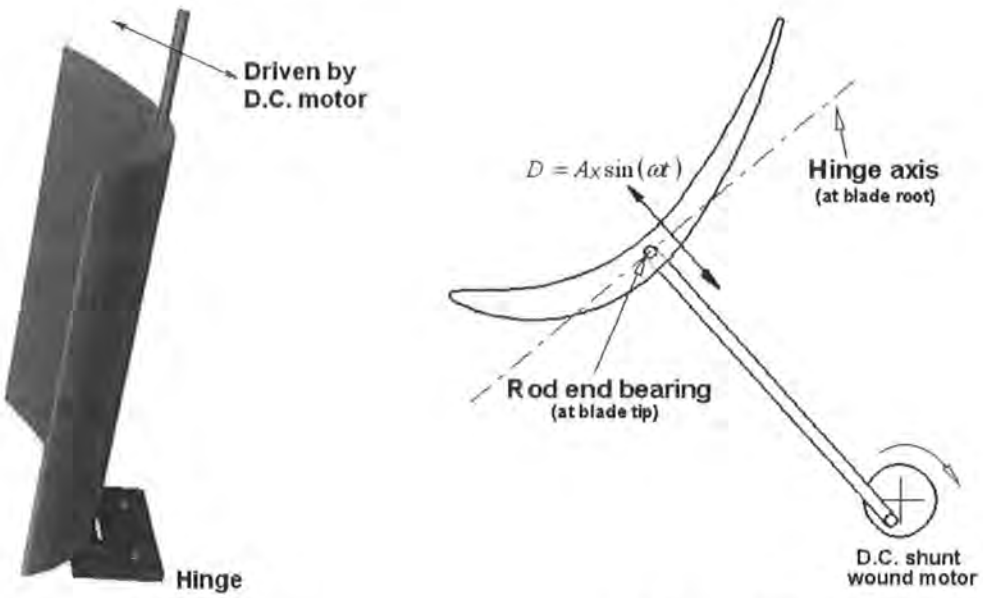


(a) 3D (b) Projected 2D

**Figure 3.6: The blade drive mechanism**

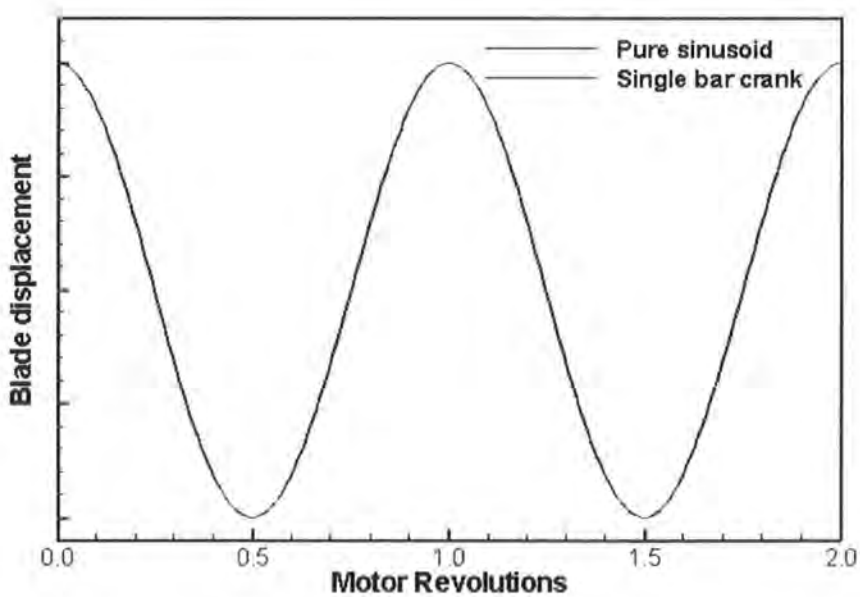


**Figure 3.7: Locus of blade displacement delivered by the single bar crank**

**Table 3.2: Bending mode shape**

| | |
|---|---|
| Bending mode direction | Normal to the absolute chord |
| Bending amplitude at tip, $A_{x,tip}$ | $3.0\%C$ |
| Bending amplitude at hub | $0.3\%C$ |

### 3.1.5 Blade Instrumentation

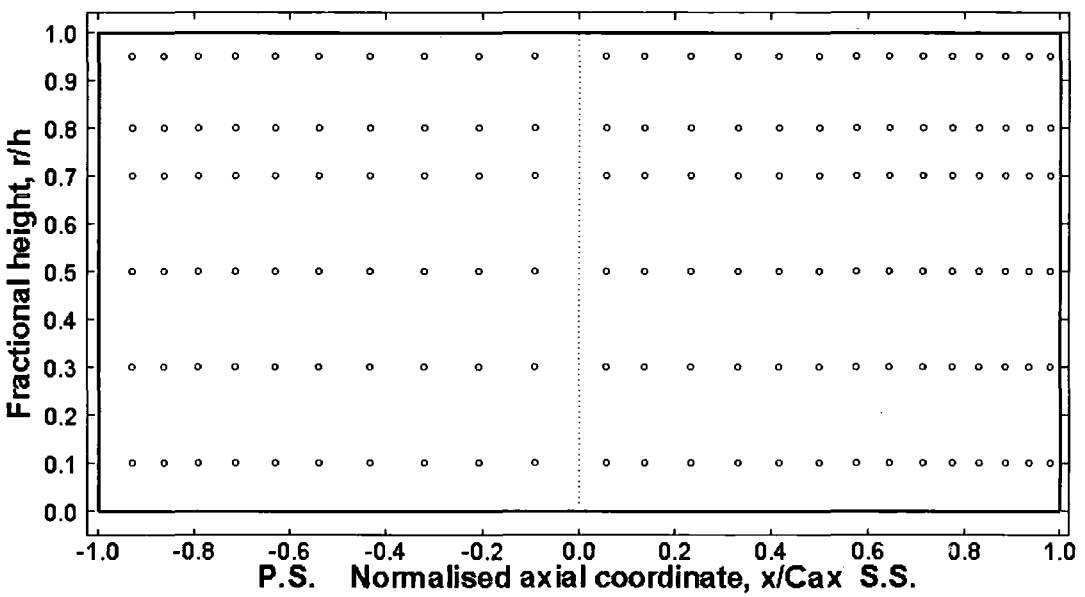


**Figure 3.8: Locations of blade surface pressure tappings**
(Tappings located at six spanwise sections:
10%, 30%, 50%, 70%, 80% and 95%Span)

The oscillating blade and one non-oscillating blade are extensively instrumented with 144 pressure tappings each. These pressure tappings are used for both steady and unsteady pressure measurements. The instrumented non-oscillating blade is interchangeable with all other stationary blades, thereby enabling both steady and unsteady pressure measurements at all blade positions in the cascade. The pressure tappings are located at six spanwise sections of 10%, 30%, 50%, 70%, 80% and 95% Span. At each spanwise section, there are 10 pressure tappings on the pressure surface and 14 on the suction surface. The positions of pressure tappings on each section are described in Figure 3.8 and Table 3.3. Six tappings (with one at each section) of the same chordwise position share one flush mounted brass tube (Figure 3.9), which is spanwisely laid along the blade and egressed through the blade root with a tail of $30mm$. Totally,

**Table 3.3: Axial location of tappings, $x/C_{ax}$**

| Pressure surface | | Suction Surface | |
|---|---|---|---|
| P1 | 0.0902 | S1 | 0.0547 |
| P2 | 0.2068 | S2 | 0.1379 |
| P3 | 0.3195 | S3 | 0.2337 |
| P4 | 0.4319 | S4 | 0.3318 |
| P5 | 0.5371 | S5 | 0.4180 |
| P6 | 0.6283 | S6 | 0.5010 |
| P7 | 0.7134 | S7 | 0.5748 |
| P8 | 0.7901 | S8 | 0.6449 |
| P9 | 0.8631 | S9 | 0.7135 |
| P10 | 0.9300 | S10 | 0.7745 |
| | | S11 | 0.8302 |
| | | S12 | 0.8869 |
| | | S13 | 0.9369 |
| | | S14 | 0.9801 |

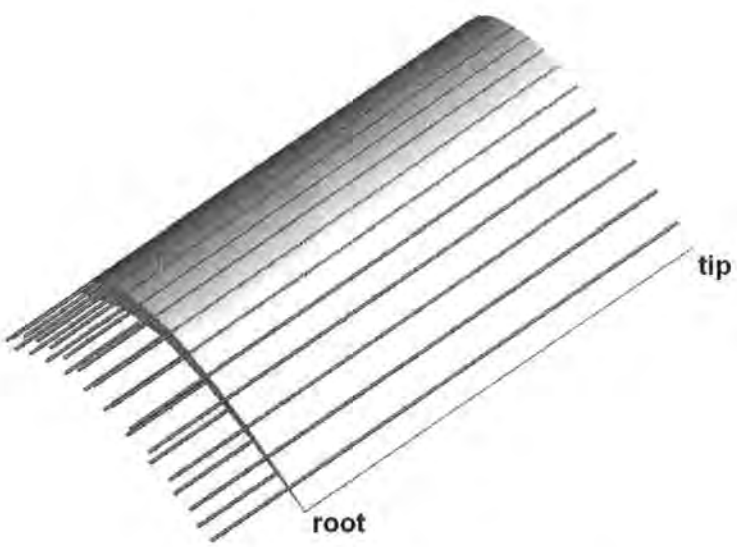


**Figure 3.9: Instrumented blade**

24 brass tubes are used. The brass tubes are sealed at the blade tip end and left open at the tail end for connection to a pressure measuring device. This arrangement only allows the pressure measurement to be taken at one spanwise section each time. Therefore, the pressure tappings at one section are left open in the tests and those at the others are blocked. The current practice is to employ a self-adhesive tape to cover the desired pressure tappings. This kind of self-adhesive tape is thin and would cause little disturbance to the flow.

### 3.1.6 Operational Conditions

The nominal operational conditions imposed in the test are listed in Table 3.4. The experimental measurements were carried out at a low flow speed with a Reynolds number of $2.2 \times 10^5$ applied throughout. Here, the definition of Reynolds number is based on the isentropic exit velocity:

$$V_{ref} = \sqrt{\frac{2(P_{01} - P_2)}{\rho}} \tag{3.1}$$

where $P_{01}$ is the inlet total pressure, $P_2$ the back pressure and $\rho$ the density of air.

**Table 3.4: Summary of operational conditions**

| Operational conditions | |
|---|---|
| Inlet flow angle, $\beta_1$ | 0.0° |
| Isentropic exit velocity, $V_{ref}$ | $22.0ms^{-1}$ |
| Reynolds number, $Re$ | $2.2 \times 10^5$ |
| Reduced frequencies, $K$ | 0.2, 0.4, 0.6 |
| Nominal vibration frequencies, $f$ | 5.2, 10.3, 15.5 $Hz$ |

(*Nominal vibration frequencies at ambient conditions of 1 atm. and 20 °C*)

In any controlled flutter test, the reduced frequency is the most important parameter. In this low speed test facility, realistic values of reduced frequency can be achieved at low frequencies of blade vibration. For example, a nominal frequency of $10.3Hz$ here is equivalent to a reduced frequency of 0.4, which is based on the blade chord and exit isentropic velocity.

## 3.2 Data Acquisition and Reduction

### 3.2.1 Data Acquisition

Blade flutter is a pressure driven phenomenon. Blade surface steady-state and time-dependent pressures, which define the blade steady loading and its aeroelastic stability respectively, have been extensively measured. Blade surface steady-state pressure measurements were obtained using an inclined manometer bank. The measured pressure was then reduced to normalised pressure coefficient with respect to the exit isentropic

dynamic head ($P_{01} - P_2$) as follows

$$C_p = \frac{P - P_2}{P_{01} - P_2} \tag{3.2}$$

As described earlier, realistic values of reduced frequency can be achieved at low frequencies of blade vibration and this makes it possible for the unsteady pressure signals to be recorded with off-board pressure transducers of relatively large sizes (much cheaper). This study employed five temperature compensated, signal conditioned, pressure transducers (type: Sensym 42C01D, $0 - 1psi$ range; sensitivity: $5volts/psi$) for the unsteady pressure measurements. The unsteady pressure measurements were performed on the middle five blades and this meant that a total of 150 sets of measurements were required to cover $144 \times 5$ pressure tappings in one test. Because one full test would usually span several days, a stable response of the data acquiring system was believed to be essential. Figure 3.10 shows two sets of calibration plots, which were obtained for the same pressure transducer on different days. Owing to temperature compensation and a regular voltage supply ($8.00 \pm 0.01volts$), the response of the pressure transducer revealed highly linear and constant behaviour over the pressure range concerned. Based on the highly linear behaviour of the pressure transducers, a two-point calibration procedure was performed before each test of unsteady pressure measurements. In this calibration procedure, the voltage response to an arbitrary non-zero pressure, which was simultaneously loaded on each each transducer and the manometer, was recorded for each transducer. This measurement as well as the voltage offset reading (at zero pressure load) enabled the linear response of each transducer to be accurately defined. This calibration procedure prevented the errors being introduced by not only the variation in the response of the pressure transducers but also the deviation in the behaviour of data logging card.

Figure 3.11 shows a schematic representation of the unsteady pressure acquisition system employed. The basic function of this system is to acquire synchonised unsteady pressure signals, following a procedure as follows:

1) the D.C. motor drives the reference blade to oscillate at a prescribed frequency, which is set by the speed control unit with the guidance of the digital tachometer's reading;

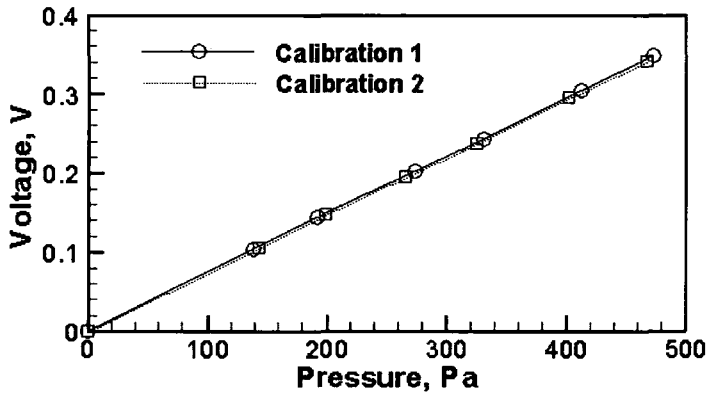


**Figure 3.10: Sample pressure transducer response**

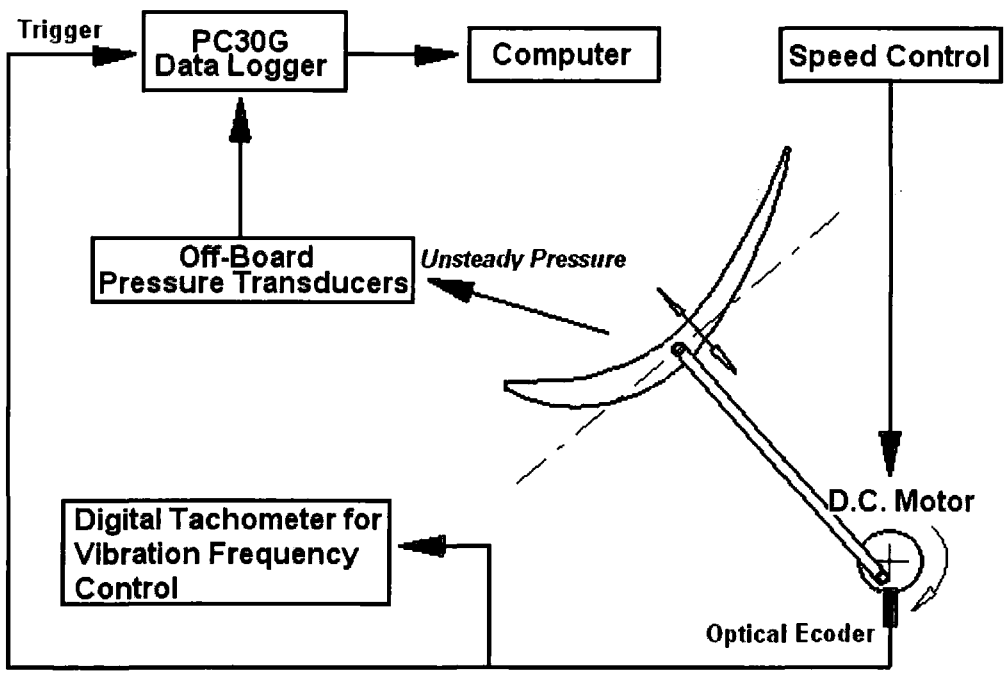


**Figure 3.11: Schematic of the unsteady pressure acquisition system**

2) the optical encoder delivers a one-per-rev pulse signal to the digital I/O port of an Amplicon PC30G data logging card;

3) the computer monitors the trigger pulse on the I/O port of the data logging card and launches the acquisition of unsteady pressure measurements at a fixed phase position of the blade oscillation.

The unsteady pressure signals, or rather voltages, from the five pressure transducers were discretised and logged on a PC using the PC30G card with analogue-to-digital (A/D) channels onboard. The A/D converter is of a 12-bit one and provides 4096 quantisation levels equally distributed over the input voltage range of 0-5$volts$. The maximum error introduced by the A/D conversion is of half a quantisation level, which is equivalent to an accuracy level of $\pm 0.8pa$ in this study.

**Table 3.5: Sampling rates**

| Reduced Frequency | 0.2 | 0.4 | 0.6 |
|---|---|---|---|
| Nominal frequency ($Hz$) | 5.2 | 10.3 | 15.5 |
| Sampling rate ($Hz$) | 1000 | 2000 | 3000 |
| Number of samples/period | 192 | 194 | 193 |

The PC30G data logging card was set to work at a sequential sampling mode with the time between sampling the consecutive A/D channels defined by the overall sampling rate, i.e. the sampling rate for an individual channel multiplied by the number of channels being sampled. This meant that the sampling of channel 1 was initiated by the trigger signal whilst the sampling of the other channels were initiated slightly later, with the sampling of channel 5 being triggered latest of all. At the sampling rates described in Table 3.5, the phase shift introduced by the sequential sampling procedure to the first pressure harmonic is within a range of 0° to 1.9°. These sampling rates allows a minimum 190 sampled points in a period of the first harmonic pressure. According to Shannon's Sampling Theorem (Lynn and Fuerst, 1989), these rates are sufficient to capture harmonic components up to the $95^{th}$ order. Although the high order harmonic components are beyond the present practical interest, the high sampling rates certainly enhance accuracy in the evaluation of Fourier coefficients of the low order harmonic components through increasing the number of sampled points in the period of blade oscillation. The unsteady pressure signals from each tapping were ensemble-averaged:

$$P(x,t) = \frac{1}{N}\sum_{n=1}^{N} P(x, t + (n-1)T) \tag{3.3}$$

where $N$ was the number of periods averaged and T the time period. It is found that the unsteady pressure signals ensemble-averaged over 150 periods give well defined periodic signals as indicated by Figure 3.12, which shows examples of raw and ensemble-averaged unsteady pressure signals. The process of ensemble-averaging acts to reduce

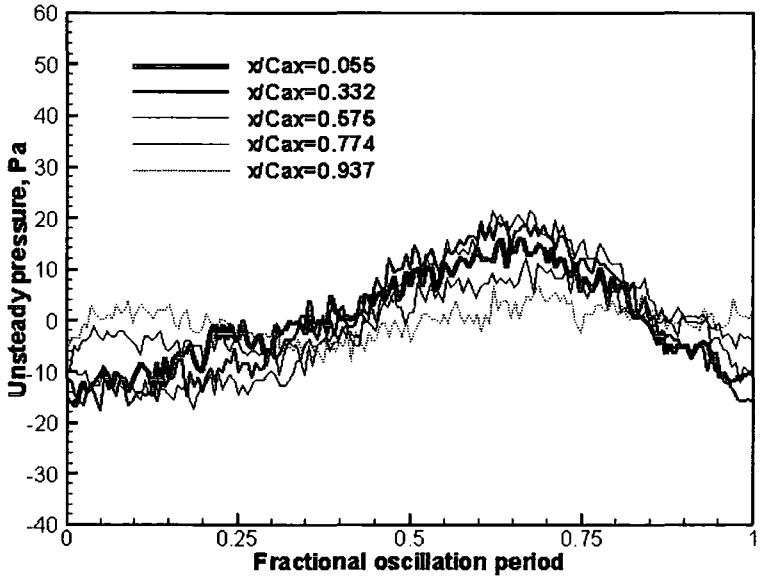


(a) Raw unsteady pressure signals

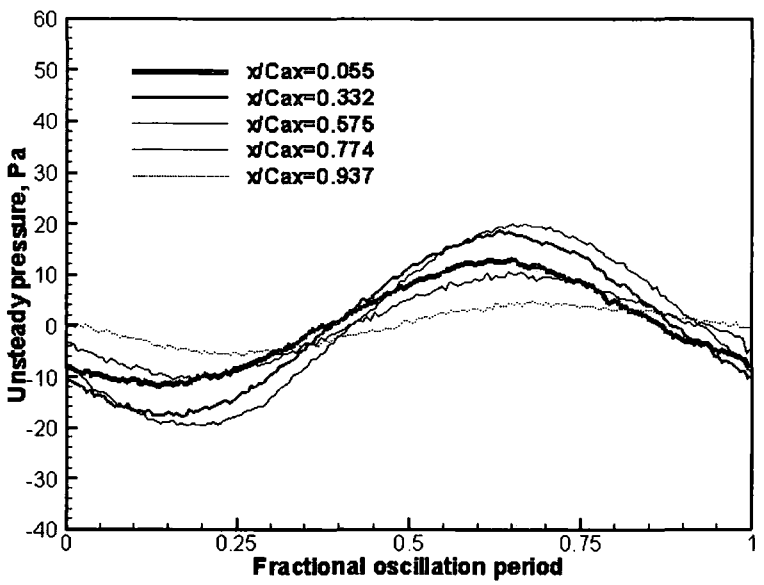


(b) Ensemble-averaged unsteady pressure signals over 150 periods

**Figure 3.12: Raw and ensemble-averaged unsteady pressure signals at 70% span on the suction surface of blade 0, $K$=0.4**

the contribution from random errors, such as turbulent fluctuations and electrical signal noise, and improve the signal to noise ratio.

The unsteady pressure response $P(t)$ to the blade harmonic oscillation can be decom-

posed into a time-averaged part $\bar{P}$ and a time-dependent perturbation $\tilde{P}(t)$:

$$P(t) = \bar{P} + \tilde{P}(t) \tag{3.4}$$

The time-dependent pressure perturbation $\tilde{P}(t)$ can be expressed as a Fourier series characterised by the frequency of blade oscillation:

$$\tilde{P}(t) = \sum_{n=1}^{\infty}(a_n \cos(n\omega t) + b_n \sin(n\omega t)) \tag{3.5}$$

where

$$a_n = \frac{2}{T}\int_0^T \tilde{P}(t)\cos(n\omega t)\,dt \quad (n = 1, 2, 3\cdots) \tag{3.6}$$

$$b_n = \frac{2}{T}\int_0^T \tilde{P}(t)\sin(n\omega t)\,dt \quad (n = 1, 2, 3\cdots) \tag{3.7}$$

The time-dependent pressure perturbation $\tilde{P}(t)$ can also be expressed as a summation of a series of harmonic components, with each harmonic defined by an amplitude $A_{p,n}$ and a phase angle $\phi_n$ with regard to the blade motion.

$$\tilde{P}(t) = \sum_{n=1}^{\infty} A_{p,n}\sin(n\omega t + \phi_n) \tag{3.8}$$

where $A_{p,n} = \sqrt{a_n^2 + b_n^2}$ and $\phi_n = \arctan(a_n/b_n)$. Equally, the complex form of the time-dependent pressure perturbation can be written as:

$$\tilde{P}(t) = \sum_{n=-\infty}^{\infty} \hat{A}_{p,n}e^{in\omega t} \tag{3.9}$$

where $i$ is the imaginary unit such that $i^2 = -1$; $\hat{A}_{p,n}$ is the complex amplitude of the $n^{th}$ order pressure harmonic and has an expression as:

$$\hat{A}_{p,n} = \frac{1}{2}(a_n - ib_n) \tag{3.10}$$

$$\hat{A}_{p,-n} = \frac{1}{2}(a_n + ib_n) \tag{3.11}$$

For ease of data correlation, the unsteady pressure amplitude was normalised with respect to the blade tip oscillation amplitude and the exit isentropic dynamic head such as to yield a pressure coefficient as given by Equation 3.12.

$$C_{p,n} = \frac{A_{p,n}}{(P_{01} - P_2)\cdot A_{x,tip}} \tag{3.12}$$

The complex form of the $n^{th}$ order unsteady pressure coefficient amplitude was then defined as:

$$\hat{C}_{p,n} = \frac{\hat{A}_{p,n}}{(P_{01} - P_2)\cdot A_{x,tip}} \tag{3.13}$$

### 3.2.2 Correction on Tubing Effects

It has been recognised that none-zero length of tubing connection between tappings and pressure transducers would introduce distortion to the unsteady pressure signals in terms of amplitude and phase angle. That is to say, the amplitude is either amplified by resonance effects or attenuated by viscous effects, whilst a phase lag is usually caused upon the phase angle during the pressure signals travelling through the tubing connection. To correct the unsteady pressure signal for attenuation and phase shift along the tubing lengths, a *tubing transfer function* (TTF) scheme, proposed by Irwin et al. (1979), was applied. The present application of the TTF method followed the procedures of Sims-Williams (2001) and Yang (2004).

Taking $\tilde{P}'(t)$ to be the time-dependent part of the real pressure signal at the tapping and $\tilde{P}''(t)$ that measured by the pressure transducer, their expression in a complex Fourier series can be rewritten as:

$$\tilde{P}'(t) = \sum_{n=-\infty}^{+\infty} \hat{A}'_{p,n} e^{in\omega t} \tag{3.14}$$

$$\tilde{P}''(t) = \sum_{n=-\infty}^{+\infty} \hat{A}''_{p,n} e^{in\omega t} \tag{3.15}$$

where $\hat{A}'_{p,n}$ and $\hat{A}''_{p,n}$ are the $n^{th}$ order complex Fourier coefficients. Then the tubing transfer function is defined by Equation 3.16.

$$TTF_n = \frac{\hat{A}''_{p,n}}{\hat{A}'_{p,n}} \tag{3.16}$$

To apply this method, the tubing transfer function $TTF_n$ was experimentally determined. A diagram of the apparatuses used in the measurement of $TTF_n$ of the tubing system is shown in Figure 3.13. In this setup, a swept sine wave is generated by a sweep function generator, amplified by the an audio amplifier and fed to a loudspeaker. The loudspeaker produces a pressure fluctuation in a small cavity. A reference pressure transducer is attached directly to the cavity and another test pressure transducer is connected to the cavity through a same tubing connection as used on the cascade rig. A series of measurements, covering the range of frequencies concerned, were performed through these two pressure transducers. For each case, $\tilde{P}'(t)$ on the reference pressure

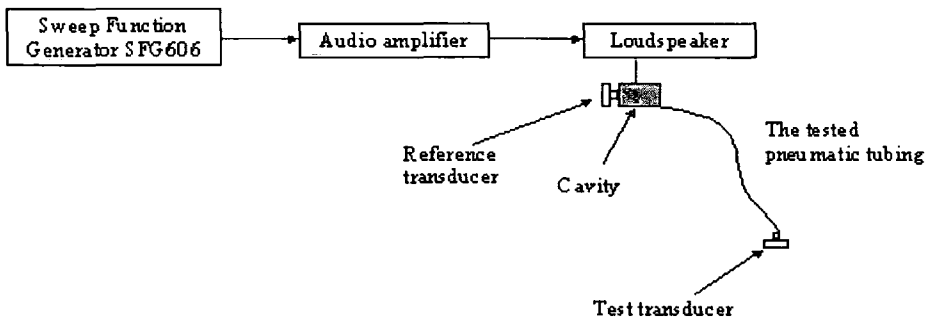


**Figure 3.13: Measurement of the tubing transfer function, Yang (2004)**

transducer and $\tilde{P}''(t)$ on the test pressure transducer were simultaneously recorded. The resulting Fourier coefficients $\hat{A}'_{p,n}$ and $\hat{A}''_{p,n}$ were then used to calculate the tubing transfer function $TTF_n$ according to its definition in Equation 3.16. In order to obtain a better approximation to the real tubing transfer function, M (greater than 20) sets of data were obtained for each case and averaged:

$$TTF_n = \frac{1}{M}\sum_{j=1}^{M}\left(\frac{\hat{A}''_{p,n}}{\hat{A}'_{p,n}}\right)_j \tag{3.17}$$

Once the tubing system transfer function $TTF_n$ was known by Equation 3.17, a correction was subsequently applied to the blade surface pressure measurement $\tilde{P}(x,t)$, as shown in Equation 3.18.

$$\tilde{P}(t) = \sum_{n=-\infty}^{+\infty}\frac{\hat{A}_{p,n}}{TTF_n}e^{in\omega t} \tag{3.18}$$

The application of the tubing transfer function enables a systematic correction on the tubing distortion and results in a more accurate representation of the blade surface unsteady pressure.

### 3.2.3 Influence Coefficient Method

In a finite cascade of $2N+1$ blades oscillating in a travelling wave mode with an IBPA $\sigma_0$, as shown in Figure 3.14 where $N$ equals to 3, the complex pressure coefficient $\hat{C}_{p,tw}$, acting on the reference blade 0, can be interpreted as:

$$\hat{C}_{p,tw} = \sum_{n=-N}^{+N}\hat{C}^{0,n}_{p,ic}e^{in\sigma_0} \tag{3.19}$$

where $\hat{C}_{p,ic}^{0,n}$ is the complex influence coefficient of the oscillating blade $n$, acting on the non-oscillating reference blade 0; the subscripts $tw$ and $ic$ donate the travelling wave mode and the influence coefficient method respectively. The sign convention for $\sigma_0$ (IBPA) is such that a negative $\sigma_0$ corresponds to a backward travelling wave mode, where blade +1 lags behind blade 0 in oscillation.

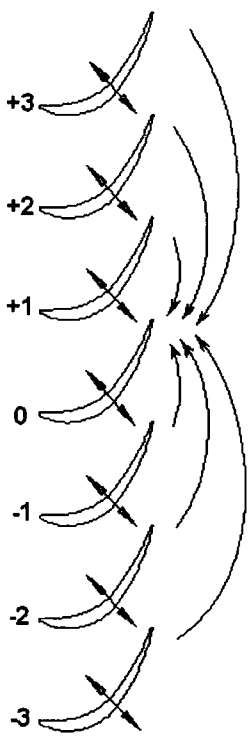


**Figure 3.14: Unsteady aerodynamic response in a travelling wave mode**

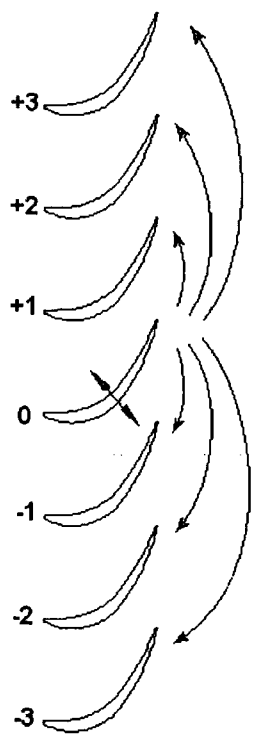


**Figure 3.15: Influence coefficients in a cascade with one oscillating blade**

In a cascade oscillating in a travelling wave mode, the pressure coefficient $\hat{C}_{p,tw}$ can be directly measured on the reference blade. However, Equation 3.19 offers an alternative approach to obtain $\hat{C}_{p,tw}$, i.e. oscillating one blade each time and measuring the influence coefficients $\hat{C}_{p,ic}^{0,n}$ on the reference blade. By assuming blade 0 has the same influence on blade blade $-n$ as blade $+n$ does on blade 0, the influence coefficient $\hat{C}_{p,ic}^{0,n}$ can be determined by only oscillating the reference blade 0 and measuring the influence coefficient $\hat{C}_{p,ic}^{n,0}$ on the reference blade itself and all stationary neighbours, as shown in Figure 3.15. Therefore, the time-dependent pressure coefficient $\hat{C}_{p,tw}$ can be expressed as

$$\hat{C}_{p,tw} = \sum_{n=-N}^{+N} \hat{C}_{p,ic}^{n,0} e^{-in\sigma_0} \tag{3.20}$$

The superposition using Equation 3.20 is the so-called influence coefficient technique. The aerodynamic influence $\hat{C}_{p,ic}^{0,0}$ induced by the oscillating blade on itself is independent of the IBPA and termed the *direct term*, whilst the other contributions $\hat{C}_{p,ic}^{-N,0}e^{iN\sigma_0}$, $\cdots$, $\hat{C}_{p,ic}^{-1,0}e^{i\sigma_0}$, $\hat{C}_{p,ic}^{1,0}e^{-i\sigma_0}$, $\cdots$, $\hat{C}_{p,ic}^{N,0}e^{-iN\sigma_0}$ are termed the *coupling terms*, which vary with respect to the IBPA.

For validity of the influence coefficient method in the linear cascade applications, two aspects are essential. One is quick pitchwise convergence of the unsteady aerodynamic response as the blade is away from the reference blade and the other is requiring linear aerodynamic response to the blade oscillation. Quick pitchwise convergence ensures that measurements of a limited number of neighbours blades are sufficient to obtain the tuned cascade data with good accuracy. A number of studies have addressed the coupling extent during their cascade flutter tests (Hanamura et al., 1980; Fransson, 1990; Buffum and Fleeter, 1990b; He, 1998; Nowinski and Panovsky, 2000; Yang, 2004). In general, the immediate neighbours (blades $\pm 1$) contribute the most share of the coupling content. In this study, it will be revealed that quick pitchwise convergence was attained and the tuned cascade data were then reconstructed only from measurements on the five middle blades. The linearity of aerodynamic response to the blade oscillation were examined through comparing two tests with different bending amplitudes and studying the relative amplitude of the second harmonic pressure with respect to the first, which will be presented in Chapter 5.

### 3.2.4 Aerodynamic Damping

Currently, the Energy Method is the most commonly used technique to evaluate the aeroelastic stability of blades. Simply speaking, the blade is unstable if the energy input from the surrounding flow is positive during one period of vibration. To use this method, the *aerodynamic damping coefficient*, which is a non-dimensional parameter to directly indicate the energy exchange between the oscillating blade and its surrounding flow, is evaluated.

Consider an arbitrary point on the blade surface, its displacement in the present sinu-

soidal vibration is given by

$$D(t) = A_x \sin(\omega_0 t) \tag{3.21}$$

and the vibration velocity by

$$V(t) = A_x \omega_0 \cos(\omega_0 t) \tag{3.22}$$

It is known that, only the first harmonic pressure does aerodynamic work ('Modal Work') on the sinusoidally oscillating blade. The aerodynamic work done per unit area to the blade is defined as

$$W_{period} = \pi A_x A_{p1} sin(\phi_1) \tag{3.23}$$

where $A_{p1}$ is the amplitude of the first harmonic pressure. Subsequently, the total work (WorkSum) to the blade can be obtained by $\sum W_{period} \Delta A$, where the summation is done over the whole blade surface. The local aerodynamic damping $\xi_l$ (at an arbitrary point) is expressed in Equation 3.24.

$$\xi_l = \frac{-W_{period}}{(P_{01} - P_2) \cdot A_{x,tip}^2} = \frac{-\pi A_x |C_{p1}| sin(\phi_1)}{A_{x,tip}} \tag{3.24}$$

where the minus sign means that a positive aerodynamic damping corresponds to a negative work done and indicates a stable condition. The aerodynamic damping at a certain spanwise section is then obtained through integrating the local aerodynamic damping over the blade chord on both pressure and suction surfaces as demonstrated in Equation 3.25.

$$\xi_{span} = \left(\frac{1}{C}\int_0^C \xi_l ds\right)_{pre} + \left(\frac{1}{C}\int_0^C \xi_l ds\right)_{suc} \tag{3.25}$$

Subsequently, the global aerodynamic damping $\xi$ is obtained through integrating the aerodynamic damping $\xi_{span}$ along the blade span as shown in Equation 3.26.

$$\xi = \frac{1}{h}\int_0^h \xi_{span} dz \tag{3.26}$$

## 3.3 Experimental Errors and Repeatability

The errors of unsteady pressure measurements are expected from two general categories, i.e. systematic errors and random errors. The former is associated with the

experimental model with the most significant contributions from the off-board measuring system, the linear superposition and the neglect of influence away from blade pair ±2. The correction of tubing distortion induced by the off-board measuring system has been presented in Section 3.2.2 and the other two errors, associated with the linear superposition and limited measured blades, will be discussed later.

Random errors arise from flow turbulence, electrical noise, data discretisation, inaccuracies in setting of operating conditions for each case, the accuracy of the pressure transducers, etc. Because the unsteady pressure response is fairly small, the unsteady pressure data usually have a high noise ratio. This results in the measurements taking on values within certain confidence intervals. Therefore, it is important to show the extent of the possible errors of the measurements especially when comparing experiments with numerical predictions. Despite the ensemble-averaging process employed, the overall random errors introduced by the complex procedures for unsteady pressure measurements need to be addressed further. To this end, a series of tests were performed to evaluate the experimental errors and repeatability. In these tests, five tappings were chosen from the 70% span of the oscillating blade to provide a representative range of unsteady pressure response, as indicated in Table 3.6. For each tapping, 40 sets of measurements were obtained, through the experimental procedure described in Section 3.2, at a reduced frequency of 0.4. The results are presented in Figure 3.16 in terms of the deviation from the mean in measured value of amplitude $|C_{p1}|$ and phase angle $\phi_1$. The measurements all fell within a range of ±0.08 for the non-dimensional amplitude of the first harmonic pressure and ±5° for the phase angle. The corresponding overall *standard deviation* (SD) was below 0.029 in $|C_{p1}|$ and 1.95° in $\phi_1$, indicating an excellent level of repeatability.

**Table 3.6: Overall standard deviation in the measurement of $|C_{p1}|$ and $\phi_1$**

| | Sample 1 | Sample 2 | Sample 3 | Sample 4 | sample 5 |
|---|---|---|---|---|---|
| Tapping No. | P2 | P8 | S2 | S6 | S11 |
| $\|C_{p1}\|$ | 0.93 | 0.63 | 1.33 | 1.96 | 0.64 |
| $SD_{amplitude}$ | 0.023 | 0.017 | 0.018 | 0.014 | 0.029 |
| $SD_{phase}$ | 1.26° | 1.11° | 1.12° | 0.74° | 1.95° |

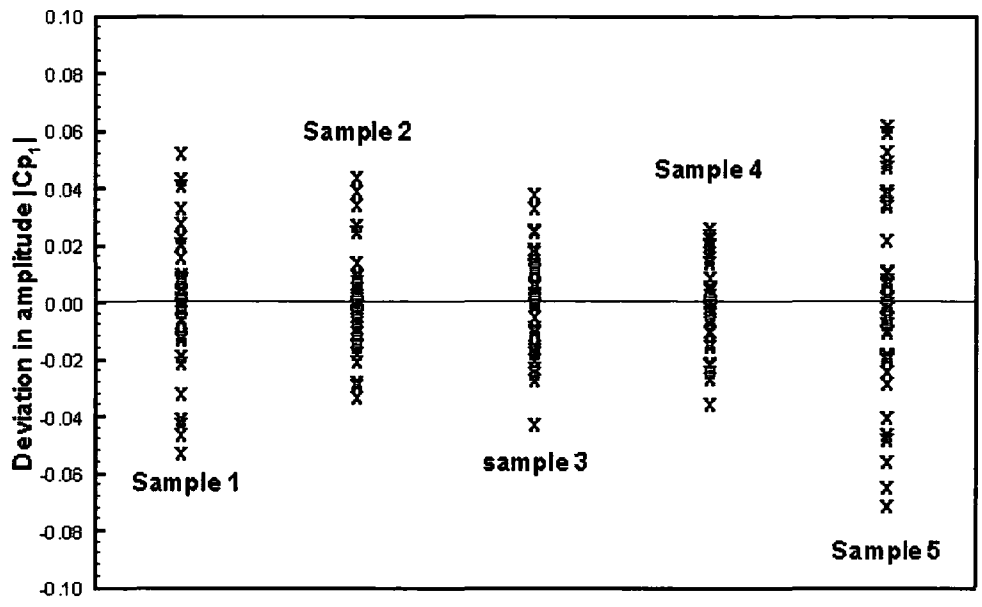


(a) Deviation in measurement of amplitude

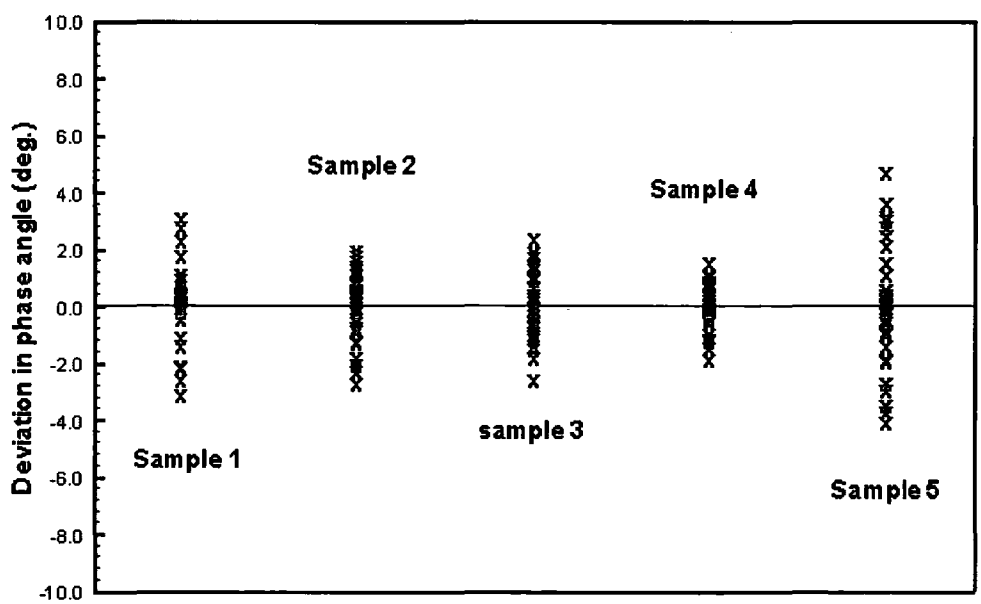


(b) Deviation in measurement of phase angle

**Figure 3.16: Repeatability and errors in the measurement of amplitude and phase angle of the first harmonic pressure response**

# Chapter 4

# Computational Methods

The computational results presented hereafter were obtained from an extended version of a three-dimensional, single-passage, time-marching Navier-Stokes method, under continuous development (He and Denton, 1994; He, 2000; Li and He, 2005a).

## 4.1 Basic Flow Model

For convenience of simulating flows in turbomachines, the cylindrical ($x$,$\theta$,$r$ — axial, circumferential and radial) coordinates are chosen; an absolute frame of reference is adopted to avoid the Coriolis terms associated with the rotor's rotation. Consider a control volume/cell $\delta V$ with a close surface $\delta A$, which moves with velocities $u_{mg}$, $v_{mg}$ and $w_{mg}$; let $p$, $\rho$, $u_x$, $u_\theta$, $u_r$, $e$ denote the primitive variables, i.e. the pressure, density, total energy and velocity components respectively; the three-dimensional unsteady *Reynolds averaged Navier-Stokes* (RANS) equations, which represent the conservation of mass, momentum and energy, are given in an integral form as following:

$$\begin{aligned}\frac{\partial}{\partial t}\iiint_{\delta V} U dV + \oiint_{\delta A} \left((F - Uu_{mg})\, n_x + (G - Uv_{mg})\, n_\theta + (H - Uw_{mg})\, n_r\right) \cdot d\vec{A} \\ = \iiint_{\delta V} S dV + \oiint_{\delta A} \left(V_x n_x + V_\theta n_\theta + V_r n_r\right) \cdot d\vec{A}\end{aligned} \tag{4.1}$$

where on the left hand side of equation, $U$ is the vector of conservative flow variables, and $F$, $G$ and $H$ the inviscid flux vectors; the terms $Uu_{mg}$, $Uv_{mg}$ and $Uw_{mg}$ derive from the contribution of moving grid due to the blade vibration and rotation; $\vec{n} = (n_x, n_\theta, n_r)$ is a unit vector in the outgoing normal direction of the cell surface. On the right hand side, $S$ is the inviscid source term to account for the centrifugal effect and $V_x, V_\theta, V_r$

the full viscous terms:

$$U = \begin{pmatrix} \rho \\ \rho u_x \\ r\rho u_\theta \\ \rho u_r \\ \rho e \end{pmatrix}; \qquad F = \begin{pmatrix} \rho u_x \\ \rho u_x u_x + P \\ r\rho u_\theta u_x \\ \rho u_r u_x \\ (\rho e + P)u_x \end{pmatrix}; \qquad G = \begin{pmatrix} \rho u_\theta \\ \rho u_x u_\theta \\ r(\rho u_\theta u_\theta + P) \\ \rho u_r u_\theta \\ (\rho e + P)u_\theta \end{pmatrix}$$

$$H = \begin{pmatrix} \rho u_r \\ \rho u_x u_r \\ r\rho u_\theta u_r \\ \rho u_r u_r + P \\ (\rho e + P)u_r \end{pmatrix}; \quad S = \begin{pmatrix} 0 \\ 0 \\ 0 \\ \rho {u_\theta}^2/r \\ 0 \end{pmatrix}; \quad V_x = \begin{pmatrix} 0 \\ \tau_{xx} \\ r\tau_{\theta x} \\ \tau_{rx} \\ u_x\tau_{xx} + u_\theta\tau_{\theta x} + u_r\tau_{rx} - q_x \end{pmatrix}$$

$$V_\theta = \begin{pmatrix} 0 \\ \tau_{x\theta} \\ r\tau_{\theta\theta} \\ \tau_{r\theta} \\ u_x\tau_{x\theta} + u_\theta\tau_{\theta\theta} + u_r\tau_{r\theta} - q_\theta \end{pmatrix}; \qquad V_r = \begin{pmatrix} 0 \\ \tau_{xr} \\ r\tau_{\theta r} \\ \tau_{rr} \\ u_x\tau_{xr} + u_\theta\tau_{\theta r} + u_r\tau_{rr} - q_r \end{pmatrix}$$

With Stokes hypothesis, the viscous stresses are:

$$\begin{aligned}
\tau_{xx} &= \mu\left(\frac{4}{3}\frac{\partial u_x}{\partial x} - \frac{2}{3}\left(\frac{1}{r}\frac{\partial r u_r}{\partial r} + \frac{1}{r}\frac{\partial u_\theta}{\partial \theta}\right)\right) \\
\tau_{\theta\theta} &= \mu\left(\frac{4}{3}\left(\frac{1}{2}\frac{\partial u_\theta}{\partial \theta}\right) - \frac{2}{3}\left(\frac{\partial u_r}{\partial r} + \frac{\partial u_x}{\partial x}\right)\right) \\
\tau_{rr} &= \mu\left(\frac{4}{3}\frac{\partial u_r}{\partial r} - \frac{2}{3}\left(\frac{1}{r}\frac{\partial u_\theta}{\partial \theta}\frac{\partial u_x}{\partial x} + \frac{u_r}{r}\right)\right) \\
\tau_{x\theta} &= \tau_{\theta x} = \mu\left(\frac{\partial u_\theta}{\partial x} + \frac{1}{r}\frac{\partial u_x}{\partial \theta}\right) \\
\tau_{xr} &= \tau_{rx} = \mu\left(\frac{\partial u_r}{\partial x} + \frac{\partial u_x}{\partial r}\right) \\
\tau_{\theta r} &= \tau_{r\theta} = \mu\left(\frac{1}{r}\frac{\partial u_r}{\partial \theta} + r\frac{\partial}{\partial r}\left(\frac{u_\theta}{r}\right)\right)
\end{aligned}$$

And the heat fluxes, which arise from the temperature gradients, are obtained from the Fourier's heat conduction law:

$$q_x = -k\frac{\partial T}{\partial x}; \qquad q_\theta = -k\frac{\partial T}{r\partial \theta}; \qquad q_r = -k\frac{\partial T}{\partial r}$$

where $k$ is molecular thermal conductivity. For laminar flows, the viscosity and thermal conductivity can be obtained by the Sutherland's Law, and the system equations are closed by the equation of state:

$$P = (\gamma - 1)\rho\left(e - \frac{1}{2}\left(u_x^2 + u_\theta^2 + u_r^2\right)\right) \tag{4.2}$$

For turbulent flows, the eddy-viscosity hypothesis is used to account for the effect of turbulence. The molecular viscosity $\mu$ and the molecular thermal conductivity $k$ are then replaced with

$$\mu = \mu_l + \mu_t \tag{4.3}$$

$$k = c_p\left(\frac{\mu_l}{\mathrm{Pr}_l} + \frac{\mu_t}{\mathrm{Pr}_t}\right) \tag{4.4}$$

where, subscripts $l$ and $t$ denote laminar and turbulent states respectively. The Prandtl number is obtained by its definition, a ratio of momentum diffusivity to thermal conductivity $\mathrm{Pr}_l = \frac{\mu_l c_p}{k_l}$. At moderate temperatures, the Prandtl number for gases can be estimated also from an empirical relation of $\mathrm{Pr}_l = \frac{4\gamma}{7.08\gamma - 8.0}$. Similar to the definition of the laminar Prandtl number, the turbulent Prandtl number is defined basing on the eddy viscosity and eddy conductivity as $\mathrm{Pr}_t = \frac{\mu_t c_p}{k_t}$. For most applications, the turbulent Prandtl number can be assumed to be a constant and for applications involving air, a turbulent Prandtl number of 0.86-0.9 is typically used. The turbulent viscosity (eddy viscosity) $\mu_t$ is computed using the *mixing-length* model of Baldwin-Lomax (1978). This model is a two-layer model. For the inner region,

$$\mu_t = \rho l^2 |\vec{\nabla} \times \vec{u}| \tag{4.5}$$

with $l$ is the mixing length. The mixing length commonly uses an expression in the Van Driest damping function

$$l = K(1 - e^{-(y^+/A^+)})y \tag{4.6}$$

where $K = 0.41$ is the Von Karman constant; the parameter $A^+$ is suggested to be 26.0 for zero-pressure gradient flow. The nondimensional space coordinate $y^+$ is defined as usual by

$$y^+ = \frac{y}{\nu}\sqrt{\frac{\tau_w}{\rho}} \tag{4.7}$$

where $\tau_w$ is the wall shear stress and y denotes the distance to the wall. The outer layer turbulent viscosity is defined by

$$\mu_t = 0.0168\beta\rho I_0 y_{\max}\Gamma_{\max} \tag{4.8}$$

The intermittency function $I_0$ is expressed by

$$I_0 = \left(1 + 5.5(0.3y/y_{\max})^6\right)^{-1} \tag{4.9}$$

The function $\Gamma$ is defined by

$$\Gamma = y\left(1 - e^{-(y^+/A^+)}\right)|\vec{\nabla} \times \vec{u}| \tag{4.10}$$

and $y_{\max}$ is the $y$ location where $\Gamma$ reaches its maximum $\Gamma_{\max}$. The constant $\beta$ is generally taken a value of 1.6.

## 4.2 Spatial Discretisation and Temporal Integration

The governing equations are discretised in space using the cell-centered finite volume scheme and the space-discretized equations are time-marched using the explicit four-step Runge-Kutta approach.

$$U^{n+1/4} = U^n \frac{\Delta V^n}{\Delta V^{n+1/4}} - \frac{1}{4}\frac{\Delta t}{\Delta V^{n+1/4}}(R_i^n + R_v^n - D^n) \tag{4.11}$$

$$U^{n+1/3} = U^n \frac{\Delta V^n}{\Delta V^{n+1/3}} - \frac{1}{3}\frac{\Delta t}{\Delta V^{n+1/3}}(R_i^{n+1/4} + R_v^n - D^n) \tag{4.12}$$

$$U^{n+1/2} = U^n \frac{\Delta V^n}{\Delta V^{n+1/2}} - \frac{1}{2}\frac{\Delta t}{\Delta V^{n+1/2}}(R_i^{n+1/3} + R_v^n - D^n) \tag{4.13}$$

$$U^{n+1} = U^n \frac{\Delta V^n}{\Delta V^{n+1}} - \frac{\Delta t}{\Delta V^{n+1}}(R_i^{n+1/2} + R_v^n - D^n) \tag{4.14}$$

where $R_i$ is the net inviscid fluxes and $R_v$ the net viscous fluxes through cell surfaces.

$$R_i = \sum((F - Uu_{mg})\Delta A_x + (G - Uv_{mg})\Delta A_\theta + (H - Uw_{mg})\Delta A_r) + S\Delta V \tag{4.15}$$

$$R_v = \sum(V_x A_x + V_\theta A_\theta + V_r A_r) \tag{4.16}$$

To damp numerical oscillations, the artificial dissipation term $D = \sum d$ is introduced, where the summation is taken over the finite volume boundary. The construction of $d$ follows the method of Jameson et al. (1981), i.e. a blend second-order and fourth-order adaptive smoothing is utilized. In detail, at the surface between cell $(i, j, k)$ and cell $(i + 1, j, k)$ we have

$$d_{i+\frac{1}{2},j,k} = \varepsilon^{(2)}_{i+\frac{1}{2},j,k}\Delta_{i+\frac{1}{2},j,k} - \epsilon^{(4)}_{i+\frac{1}{2},j,k}(\Delta_{i+\frac{3}{2},j,k} - 2\Delta_{i+\frac{1}{2},j,k} + \Delta_{i-\frac{1}{2},j,k}) \tag{4.17}$$

where

$$\Delta_{i+\frac{1}{2},j,k} = Q_{i+\frac{1}{2},j,k}(U_{i+1,j,k} - U_{i,j,k}) \tag{4.18}$$

and $Q_{i+\frac{1}{2},j,k}$ is an approximation of spectral radii of the local convective flux Jacobian matrices,

$$Q_{i+\frac{1}{2},j,k} = \frac{1}{2}\left(\frac{\Delta V_{i+1,j,k}}{\Delta t^*_{i+1,j,k}} + \frac{\Delta V_{i,j,k}}{\Delta t^*_{i,j,k}}\right) \tag{4.19}$$

with $\Delta t^*$ being the local time step at $CFL$ taking 1. The coefficients $\varepsilon^{(2)}$ and $\varepsilon^{(4)}$ are defined as

$$\varepsilon^{(2)}_{i+\frac{1}{2},j,k} = \min(\frac{1}{2}, c_2 \upsilon_{i+\frac{1}{2},j,k}) \tag{4.20}$$

$$\varepsilon^{(4)}_{i+\frac{1}{2},j,k} = \max(0, c_4 - c\upsilon_{i+\frac{1}{2},j,k}) \tag{4.21}$$

where

$$\upsilon_{i+\frac{1}{2},j,k} = \max(\upsilon_{i-1,j,k}, \upsilon_{i,j,k}, \upsilon_{i+1,j,k}, \upsilon_{i+1,j,k}) \tag{4.22}$$

with the pressure as a sensor

$$\upsilon_{i,j,k} = |\frac{P_{i+1,j,k} - 2P_{i,j,k} + P_{i-1,j,k}}{P_{i+1,j,k} + 2P_{i,j,k} + P_{i-1,j,k}}| \tag{4.23}$$

The artificial dissipation $D$ is of first order in the neighborhood of shock to suppress oscillations and third order in the smooth field to prevent odd-even decoupling. Typically, the second order smoothing factor $c_2$ is taking $1/2$, the fourth order smoothing factor $c_4$ $1/64$ and the blending factor $c$ 1.0.

It has been recognised that the physically consistent time definition in unsteady problems causes the speed bottleneck of a time-marching procedure. To speed up time-marching in unsteady calculations, the time-consistent multi-grid method, developed previously by He (1993, 2000), is adopted in the present study (The dual-time stepping technique (Jameson, 1991) is also available in the code but tends to be less efficient). In the time-consistent multi-grid method, a uniform global time-step length $\Delta t$ is usually chosen to be about 10-30 times the time-step $\Delta t'$ determined by the numerical stability requirement:

$$\Delta t' = FT \cdot \frac{\Delta s}{a_0} \tag{4.24}$$

where $\Delta s$ is the minimum mesh spacing, $a_0$ the absolute speed of sound based on inlet stagnation parameters and $FT$ the time-step multiplying factor. For stability $FT$ should be approximately less than $2.5/(1+M_{max})$, where $M_{max}$ is the maximum relative Mach number expected in the computational domain. To use the time-consistent multi-grid technique, the computational domain is divided into small coarse mesh blocks with more or less equal spatial sizes, which are dependent on the values of $\Delta t/\Delta t'$ and $\Delta s$. The simplest implementation of the time-consistent multi-grid technique is to use just two-level grids as in He (1993). To improve accuracy, several levels intermediate grids

between the basic fine grid and the coarse grid are generally applied. Therefore, the general time-consistent multi-grid formulation for the temporal change of flow variables on the fine mesh is

$$\delta U_f = \Delta t_f \frac{R_f}{\Delta V_f} + \sum_{i=1}^{i=M} \Delta t_i \frac{R_i}{\Delta V_i} + \Delta t_c \frac{R_c}{\Delta V_c} \tag{4.25}$$

where the subscripts $f$, $i$ and $c$ denote the fine mesh, the $i^{th}$ intermediate mesh (of M levels) and the coarse mesh respectively. $\Delta t_f$ and $\Delta t_i$ are the allowable time-step lengths on the fine mesh and the $i^{th}$ intermediate mesh respectively. For unsteady calculations, the uniform time-step length $\Delta t$ is maintained throughout the computational domain by selecting the coarse block stepsize $\Delta t_c$ to satisfy:

$$\Delta t_c = \Delta t - \Delta t_f - \sum_{i=1}^{i=M} \Delta t_i \tag{4.26}$$

## 4.3 Boundary Conditions

A numerical solution of the fluid governing equations can not be obtained without boundary conditions being specified. For general turbomachinery application, there are three types of boundaries, i.e. periodic boundary, inlet/outlet boundary, solid wall boundary. If a multiple-row configuration is considered, intra-row interface is another boundary.

### • Periodic Boundaries

In a steady flow study, a single-passage computational domain (Figure 4.1) is typically employed with repeating boundary conditions applicable to the periodic boundary. For the unsteady flow problems such as flutter, multiple passages are generally required to enable the application of direct repeating periodic boundary conditions. The number of passages for a 15 bladed-row, for example, are shown in Table 4.1. Unsteady time-marching computations of a complete annulus are extremely time consuming, especially when one notes that there are typically 60 or more blades in a row of the LP turbines. The condition of computing load gets even worse when multiple-row computations are required. Apparently, if the unsteady computation can be confined in a single-passage

domain, the intensive time consumption of time-marching solutions will be drastically relieved. In this study, a single-passage method based on the shape-correction technique (He, 1990, 1992) is employed. The implementation of the shape-correction technique is described as follows.

**Table 4.1: Relation between Nodal Diameters, IBPAs and Passages**

| Nodal Diameters | | IBPA (deg) | | Number of Passages |
|---|---|---|---|---|
| Plus | Minus | Forward | Backward | (min. required) |
| 0 | -0(15) | 0 | -0 | 1 |
| 1 | -1(14) | 24.0 | -24.0 | 15 |
| 2 | -2(13) | 48.0 | -48.0 | 15 |
| 3 | -3(12) | 72.0 | -72.0 | 5 |
| 4 | -4(11) | 96.0 | -96.0 | 15 |
| 5 | -5(10) | 120.0 | -120.0 | 3 |
| 6 | -6(9) | 144.0 | -144.0 | 5 |
| 7 | -7(8) | 168.0 | -168.0 | 15 |

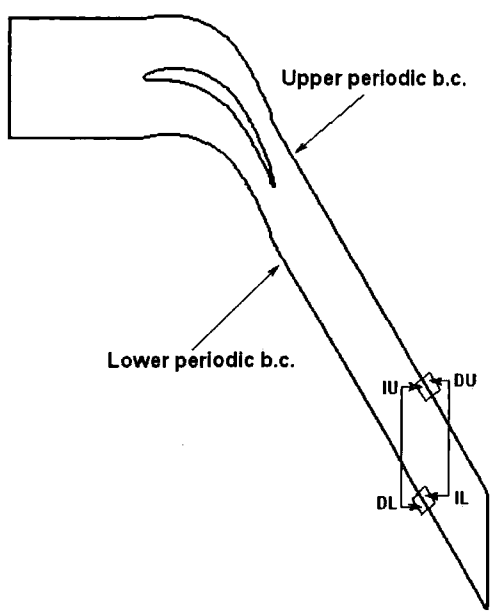


**Figure 4.1: Single passage domain**

Assume the unsteady sources that we deal with hear are periodic, temporally and spatially (in circumferential direction). Based on the assumption of the temporal periodicity, any flow variables $U$ can be decomposed into a time-averaged part $\bar{U}$ and a number of unsteady disturbances $u_i$ identifiable by their temporal periodicities. Each

disturbance can be approximated by a set of Fourier series in time.

$$U(x,\theta,r,t) = \bar{U}(x,\theta,r) + \sum_{i=1}^{N_{pt}} u_i(x,\theta,r,t) \tag{4.27}$$

$$u_i(x,\theta,r,t) = \sum_{n=1}^{N_{fou}} \left(A_{n,i}\sin(n\omega_i t) + B_{n,i}\cos(n\omega_i t)\right) \tag{4.28}$$

where $N_{pt}$ is the number of disturbances; $\omega_i$ is the fundamental frequency of the $i^{th}$ unsteady disturbance; $A_{n,i}$ and $B_{n,i}$ are the corresponding Fourier coefficients; $N_{fou}$ is the order of the Fourier series; $x, \theta$ and $r$ are axial, circumferential and radial coordinates respectively and $t$ the physical time.

In addition, based on the circumferential periodicity assumption, the unsteady disturbances satisfy the phase-shifted periodic condition as defined in Equation 4.29.

$$u_i(x,\theta+G,r,t) = \sum_{n=1}^{N_{fou}} \left(A_{n,i}\sin(n(\omega_i t+\sigma_i)) + B_{n,i}\cos(n(\omega_i t+\sigma_i))\right) \tag{4.29}$$

where $G$ is the circumferential angular spacing between two neighbouring blades in a row and $\sigma_i$ the IBPA of the $i^{th}$ disturbance. Equations 4.28 and 4.29 are the principal formulations of the shape-correction technique, applied to a single-passage domain for a single-row configuration shown in Figure 4.1 (multiple-row cases will be discussed later, Figure 4.2).

During the computation, the Fourier coefficients, which are used to approximate the flow variables (Equation 4.28), are stored and updated at the periodic boundary inner cells (IL and IU). To apply periodic boundary conditions, flow variables at the dummy cells (DL and DU) adjacent to the periodic boundary inner cells need to be determined at every time step. According to Equation 4.29, the flow variables at dummy cells DL and DU are obtained from the stored Fourier coefficients at inner cells IU and IL respectively.

A particular issue that arise here is how to update the Fourier coefficients at the periodic boundary inner cells for multiple disturbances. As described by He (1992), acceleration of updating of the Fourier coefficients can be achieved by two measures. One is the partial-substitution technique, which enable us to update the Fourier coefficients once

in one period of its corresponding disturbance rather than one beating period. That is, the Fourier coefficients are evaluated through the following formulas:

$$A_{ni} = \frac{\omega_i}{\pi} \sum_{1}^{N_{p,i}} (U - R_i) \sin(n\omega_i t)\, \Delta t \tag{4.30}$$

$$B_{ni} = \frac{\omega_i}{\pi} \sum_{1}^{N_{p,i}} (U - R_i) \cos(n\omega_i t)\, \Delta t \tag{4.31}$$

where $R_i = \sum_{j \neq 1}^{N_{pt}} \sum_{n=1}^{N_{fou}} (A_{n,j} \sin(n\omega_j t) + B_{n,j} \cos(n\omega_j t))$ is the contribution of all disturbances except that from the $i^{th}$ perturbation and $N_{p,i}$ the number of time steps in one period of the $i^{th}$ disturbance. The other measure is to carry out several timewise integrations of Fourier coefficients starting at different moments in one period of the corresponding disturbance.

It is worthy to note that this single-passage method is an inherently nonlinear method because the cross-coupling (nonlinear effects) among the time-averaged flow and various unsteady disturbances are automatically accounted for by the formulation and implementation described above (Equations 4.30 and 4.31).

### • Bladerow Interface

Since one of the present objectives is to investigate the influence of an upstream stator on the rotor flutter stability, a multiple-row, single-passage, domain is needed (the passage with bold boundaries in Figure 4.2, other passages are only involved in the solution reconstruction). The implementation of the shape-correction on the periodic boundaries of each blade row is the same as described for the single-row configuration. The bladerow interface treatment using the shape-correction method is presented in this section.

At the bladerow interface, the meshes on both sides are patched with each other. For ease of implementation of the shape-correction technique at the bladerow interface, buffer cells of a whole-annulus plane are introduced to the blade rows on both sides. The information exchange between stator and rotor in steady flow calculations is achieved by using the 'mixing plane' treatment proposed by Denton (1983), which conserves

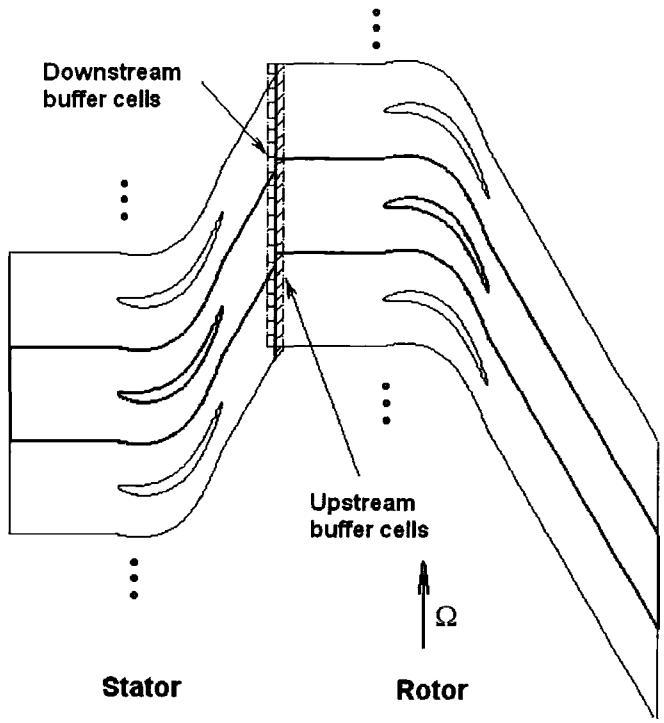


**Figure 4.2: Bladerow interface treatment**

mass, energy and momentum cross the bladerow interface. The present mixing-plane treatment follows the non-reflective procedure by Saxer and Giles (1993). For unsteady flow calculations, flow variables of buffer cells adjacent to the single-passage domain are updated from those of interior cells in a one-sided manner. The expression of the flow variables of these buffer cells can be written in a Fourier series as:

$$U(\theta, r, t) = \bar{U}(\theta, r) + \sum_{i=1}^{N_{pt}} u_i(\theta, r, t) \tag{4.32}$$

$$u_i(\theta, r, t) = \sum_{n=1}^{N_{fou}} \left(A_{n,i} \sin\left(n\omega_i t\right) + B_{n,i} \cos\left(n\omega_i t\right)\right) \tag{4.33}$$

The instantaneous flow variables of the buffer cells over the whole annulus can be reconstructed from the single-passage solution according to the circumferential periodicities of all disturbances.

$$U(\theta + jG, r, t) = \bar{U}(\theta, r) + \sum_{i=1}^{N_{pt}} u_i(\theta + jG, r, t) \tag{4.34}$$

$$u_i(\theta + jG, r, t) = \sum_{n=1}^{N_{fou}} \left(A_{n,i} \sin\left(n\left(\omega_i t + (j-1)\sigma_i\right)\right) + B_{n,i} \cos\left(n\left(\omega_i t + (j-1)\sigma_i\right)\right)\right) \tag{4.35}$$

For any real cell on one side of the interface, its corresponding position on the whole buffer annulus on the other side of the interface can be found. Then a direct second-order interpolation and correction method (He, 1997) enables local information to be transferred instantaneously across the bladerow interface. This bladerow interface treatment has been applied for a three bladerow configuration by Li and He (2005b).

For an LP stator/rotor configuration with the rotor in vibration, there are two unsteady sources. On the rotor side, disturbances are those generated by the stator wake and the rotor blade vibration. On the stator side, unsteadiness corresponding to the upstream running potential wave from the rotor and that of the vibration with a Doppler frequency shift have to be included. The phenomenon of Doppler frequency shift can be expressed as:

$$\omega_0' = \omega_0 + k\Omega \tag{4.36}$$

where $\omega_0'$ is the vibration angular frequency sensed by the stator, $\omega_0$ is the vibration angular frequency viewed in the rotor frame, $k$ is the number of nodal diameters and $\Omega$ is the rotor rotational angular speed.

### • Inlet/Exit Boundaries

The inlet and outlet boundaries are known as the far-field boundaries, and the general requirement for far-field boundary conditions is that there should not be nonphysical reflections back into the neighbourhood of the blades. The straightforward treatment is to employ infinitely long ducts of a constant cross-section at upstream and downstream of the blades to let outgoing flow disturbances damp out. This would incur a large amount of computational time, which is undesirable. In this investigation, a shortened computational domain is used and a local one-dimensional non-reflective boundary procedure proposed by Giles (1990a) is adopted to prevent artificial reflections of outgoing waves at inlet or/and exit. To be compatible with the flow propagation properties, the stagnation parameters and flow angles are specified at the inlet, with the pitchwise mean static pressure at the outlet.

## • Solid Wall Boundaries

At solid walls, the mesh grid points on solid wall surfaces are moving to comply with the blade rotation and/or oscillation. The analytic solid wall boundary condition is that there is no relative flow normal to the wall. Computationally, this is implemented by setting to zero the convective fluxes across the finite volume faces on the solid walls; while for the energy equation, work terms done by pressure due to surface movements are retained. Such treatments only involve restriction of the velocity normal to the solid wall surface. As for the velocity tangential to the solid wall surface, a non-slip condition is usually imposed in viscous analyses. Here, the tangential velocity at a wall surface is allowed to slip, but restricted by the wall shear stress. The wall shear stress is determined from an approximation of the logarithmic-law (Denton, 1992):

$$\frac{\tau_w}{0.5\rho_w u_w^2} = -0.001767 + \frac{0.03177}{\ln(Re_w)} + \frac{0.25614}{(\ln(Re_w))^2} \tag{4.37}$$

where $u_w$ and $\rho_w$ are velocity and density at the first grid point (normal distance $\triangle n$) away from the solid surfaces and $Re_w = \rho_w u_w \triangle n/\mu$. Comparing to the non-slip condition, this slip wall condition allows coarser meshes in the near wall region.

# Chapter 5

# Experimental and Computational Study of Turbine Cascade at Nominal Condition

The linear turbine cascade flow is extensively studied in this project using both experimental and computational tools the nominal setting and variable settings with a tip clearance or part-span shrouds. The nominal setting is such that there are no major three-dimensional flow sources more than the endwall effects in the steady base flow. The results presented here are obtained at the nominal setting, whilst those under influence of tip clearances and part-span shrouds are discussed in Chapter 7 and Chapter 8 respectively.

In this chapter, the experimental measurements are presented and discussed first, with an attempt to identify the unsteady flow characteristics associated with three-dimensional blade vibration. Computational studies are then applied to the linear turbine flow covering all tested cases. These computational studies also serve a purpose to validate the present numerical method.

## 5.1 Experimental Results

### 5.1.1 Steady Flow Measurements

The steady flow results are discussed first with the main steady flow features to be identified. Also, the blade-blade periodicity is to be addressed. Since the major unsteady pressure response happens on the central three blades, which will be verified later, the steady flow results are, therefore, presented only on the central three blades.

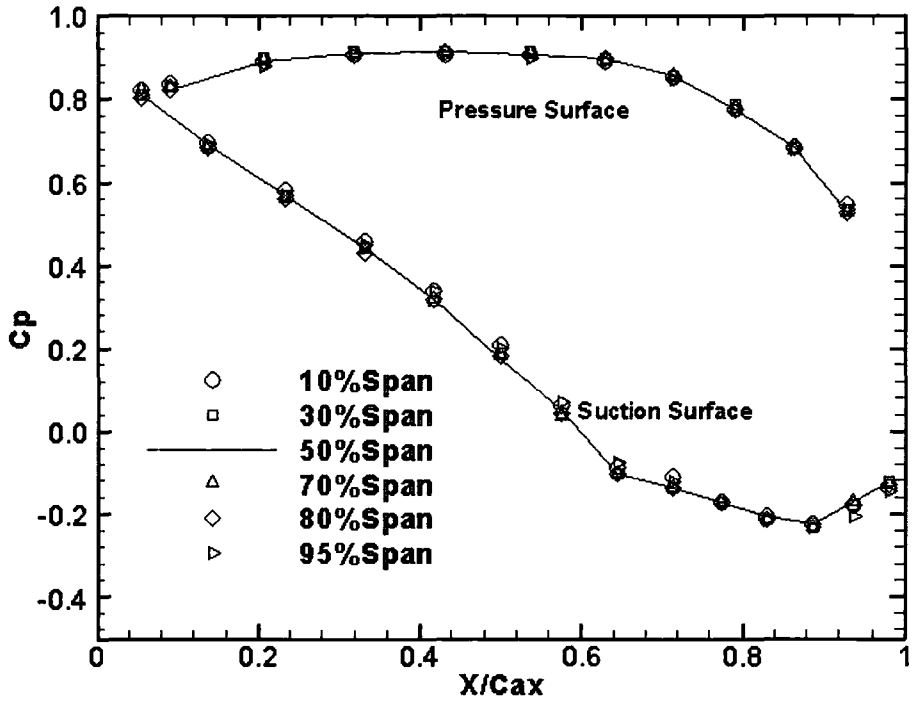


**Figure 5.1: Steady flow blade surface pressure distributions at different spanwise sections on Blade -1**

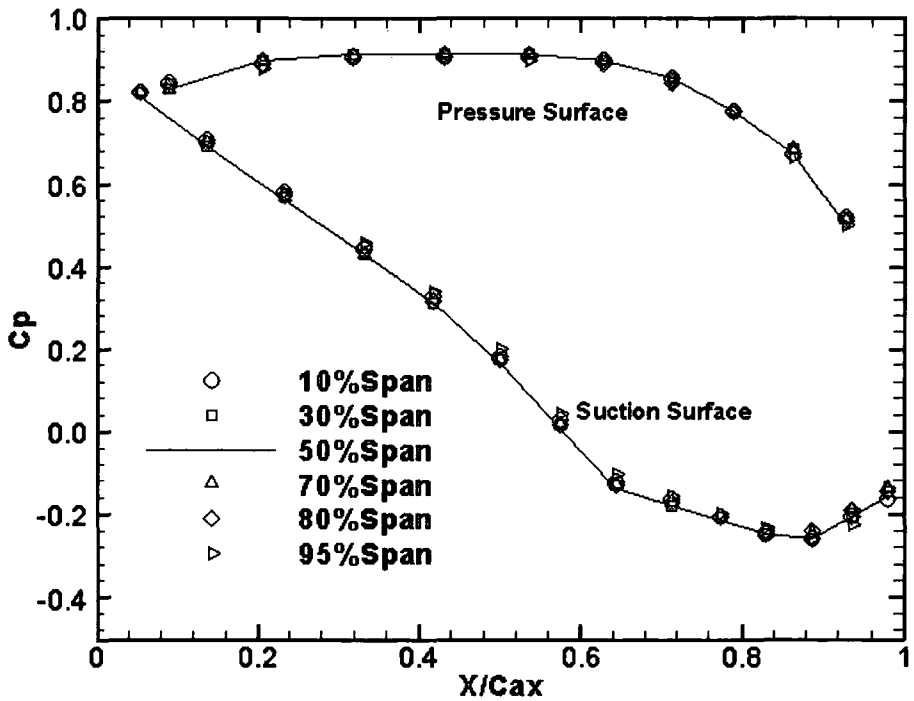


**Figure 5.2: Steady flow blade surface pressure distributions at different spanwise sections on Blade 0**

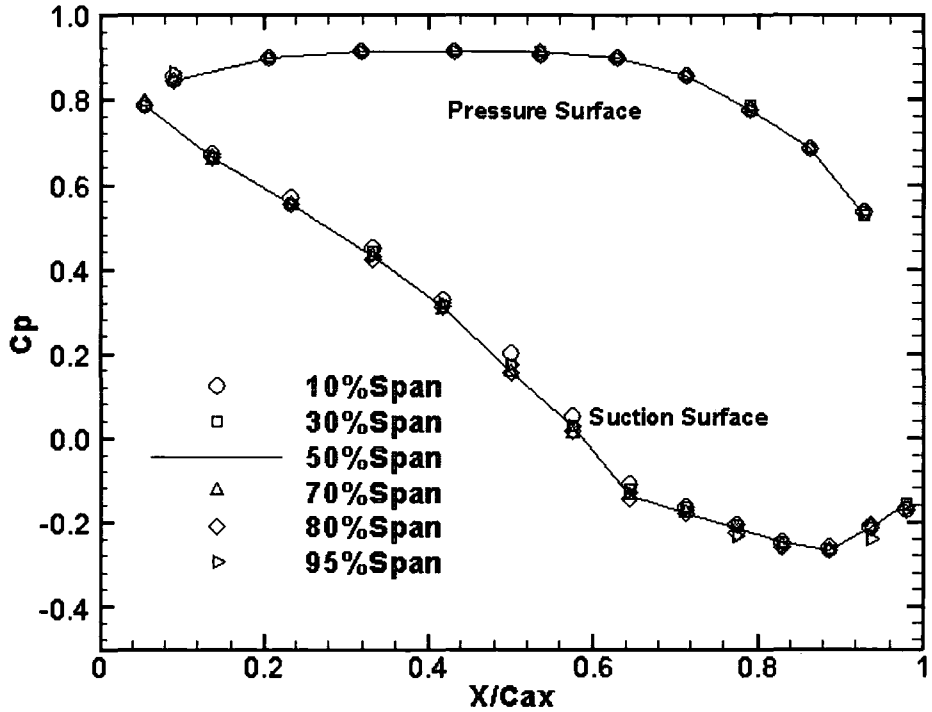


**Figure 5.3: Steady flow blade surface pressure distributions at different spanwise sections on Blade 1**

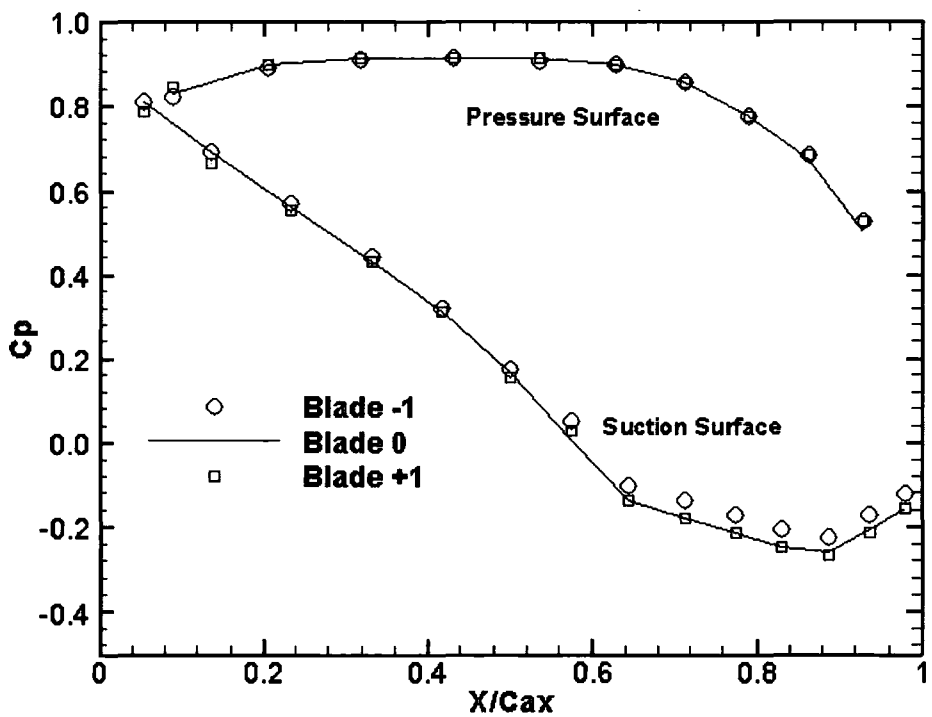


**Figure 5.4: Comparison of blade surface pressure distributions at mid-span**

Shown in Figures 5.1 to 5.3 are the steady flow blade surface pressure distributions for the three middle blades at the flow conditions described in Table 3.4 (page 42). The steady flow blade surface pressure measurements were obtained at six spanwise sections from 10% to 95% span. For each blade, the blade surface pressure distributions are almost identical for different spanwise sections, although slight deviations in pressure distribution are observed towards blade ends over the suction surface. These deviations are believed to be associated with the endwall effects with slight unloading present on the suction surface. These slight endwall effects are attributable to the favorable pressure gradient present in the cascade and the relatively small blade deflection angle. Overall, the results indicate that the steady flow blade surface pressure response is predominantly two-dimensional.

Figure 5.4 shows the comparison of the steady flow blade surface pressure distributions at the mid-span section on the three central blades. Because of the predominant two-dimensional feature of the steady flow, this comparison at the mid-span section is sufficient to verify the blade-blade periodicity in the cascade. The plot demonstrates an excellent comparison on the pressure surface, whilst a good comparison is achieved on the suction surface despite some deviation present on the rear half chord of blade -1. Good blade-blade periodicity achieved in the cascade steady flow surely forms a good basis for the unsteady flows presented hereafter.

## 5.1.2 Unsteady Flow Measurements

### 5.1.2.1 Evaluation of Pitchwise Convergence and Linearity of Unsteady Response

Pitchwise finiteness is an inherent nature of linear cascades. Therefore, the basic requirement of a linear cascade experiment when using the influence coefficient method is that the unsteady pressure response is to attenuate quickly away from the oscillating blade in the pitchwise direction. This pitchwise convergence in the present linear cascade is to be evaluated herein.

Figure 5.5 shows the amplitude of the first harmonic pressure coefficient at the mid-span section on the five middle blades with blade 0 oscillating at a reduced frequency of 0.4. Clearly, the unsteady aerodynamic response converges quickly away from the

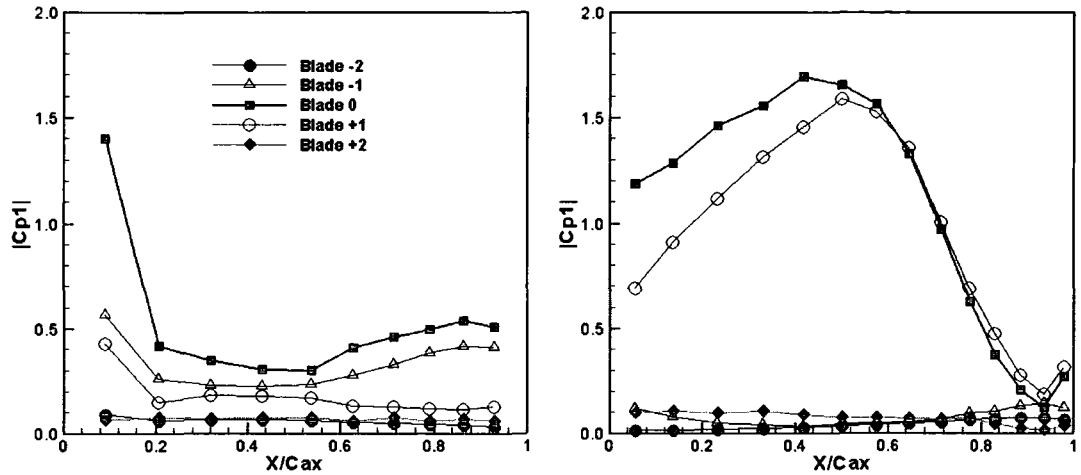


(a) Pressure Surface (b) Suction Surface

**Figure 5.5: Experimental test for pitchwise convergence — unsteady pressure response on the five central blades due to the oscillation of blade 0 ($K$=0.4)**

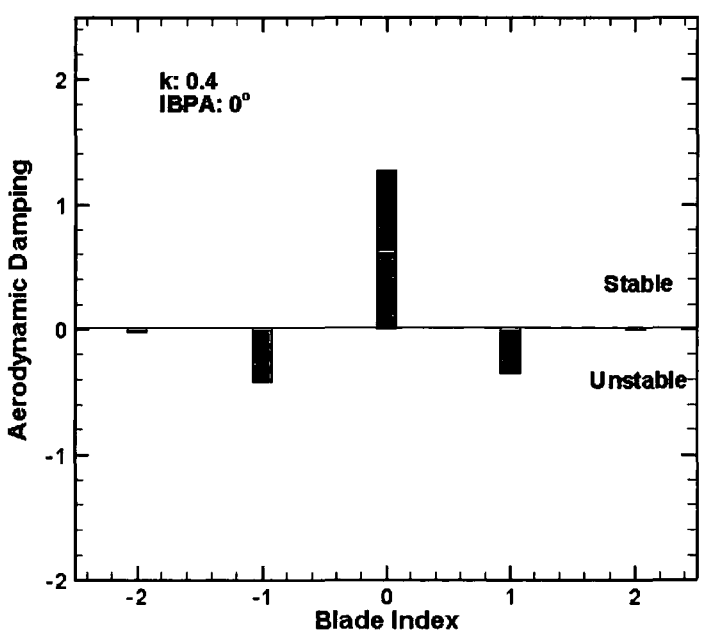


**Figure 5.6: Experimental test for pitchwise convergence — aerodynamic damping contribution from the five central blades, ($K$=0.4, $\sigma_0$=0°)**

reference oscillating blade. On the suction surface, the amplitude of the first harmonic pressure on the blade +1 (the immediate suction surface neighbour viewed by the reference blade) shows the same order of magnitude as the reference blade, whilst blades $-1$ and $\pm 2$ have an order of magnitude lower than the reference blade. On the pressure surface, the main unsteady pressure response happens on blades 0 and $\pm 1$, and blades $\pm 2$ sense much smaller unsteady disturbance. Figure 5.6 shows the global aerodynamic damping contributions from the middle five blades to the tuned cascade at a reduced frequency of 0.4 and an IBPA of 0°. The oscillating blade exerts the stabilising contribution (direct term). At this IBPA, the coupling terms do have the destabilising contributions. For different values of IBPA, the direct term would remain unchanged whereas coupling terms vary as indicated by Equation 3.20. From Figure 5.6, it is found that aerodynamic coupling effects are mainly from the immediate neighbours (blade $\pm 1$) whilst the contributions from blade $\pm 2$ are of negligible magnitudes[1].

The linearity assumption is the fundamental premise of the application of the influence coefficient method. Moreover, it is of general interest in the unsteady aerodynamic modelling of oscillating blade flows. Two sets of measurements of unsteady pressure response at different oscillating amplitudes were performed, in order to evaluate the linearity assumption of the superposition employed to reconstruct the tuned cascade data. The values of two bending oscillation amplitudes at the blade tip were arbitrarily

[1]In the controlled flutter tests, the aerodynamic damping is generally utilised to indicate the blade aeroelastic stability. However, the aerodynamic damping can be expressed as a otherwise widely used parameter, termed the *logarithmic-decrement* (Log-Dec), which is a ratio of the aerodynamic work to the blade strain energy as defined by

$$Log\text{-}Dec = -\frac{WorkSum}{StrainEnergy} = \frac{-WorkSum}{m \cdot \omega^2 \cdot D^2} \tag{5.1}$$

The aerodynamic damping of Equation 3.26 can be rewritten as

$$\xi = \frac{-WorkSum}{0.5\rho V_{ref}^2 \cdot D^2 \cdot h} \tag{5.2}$$

where $m$ is the blade mass and $\rho$ the air/gas density. Based on the Equation 1.1, the blade mass can be expressed as

$$m = C_{mass} \cdot \rho\pi(C/2)^2 \cdot h \tag{5.3}$$

Then we have

$$Log\text{-}Dec = \xi \cdot \frac{V_{ref}^2}{0.5 C_{mass}\pi C^2 \omega^2} \tag{5.4}$$

By assuming $C_{mass} = 200$ (a typical value of turbomachinery blades (He, 1994)), an aerodynamic damping value of 1 presented in Figure 5.6 is equivalent to a Log-Dec value of 0.015.

chosen to be 3% and 5% chord. The different bending amplitudes were achieved by changing the eccentric centre on the shaft of the D.C. motor to fix the crank arm bar (refer to Figure 3.6 on page 39). Figure 5.7 compares the amplitudes and phase angles of the first harmonic pressure coefficients on the reference blade at the two oscillating amplitudes. The results presented in this figure shows a predominantly linear behaviour of the unsteady pressure response with very good agreement in the first harmonic pressure coefficients in terms of both amplitude and phase angle between the two different oscillating amplitudes.

Another measure of linearity of the oscillating blade flows is the relative amplitude of the second harmonic pressure response. Figures 5.8 to 5.10 present the amplitudes of the second harmonic pressure coefficients relative to the first harmonic on the reference blade for three reduced frequencies (0.2, 0.4 and 0.6). At most locations on the suction surface, the amplitudes of the second harmonic pressure reveal to be an order of magnitude lower than those of the first, which indicates a predominant linear behaviour of the unsteady pressure response throughout the range of reduced frequencies investigated. On the suction surface, high relative amplitudes of the second harmonic pressure aft of $80\%C_{ax}$ at the 10% span section, to less extent at the 30% span section, are evident, whilst on other spanwise sections, which have much higher bending amplitudes, do not reveal similar behaviour. Considering this, the high relative second harmonic pressure response at spanwise sections located near the hub is believed to be most likely arising from a leakage flow through the imperfect hub sealing as well as the relative low pressure response (locally near the hub), rather than indicating a nonlinear unsteady aerodynamic response to the blade oscillation. In addition, low signal-to-noise ratio is expected towards the trailing edge on the suction surface where the amplitude of unsteady pressure is small. On the pressure surface, the relative amplitudes of the second harmonic pressure are relatively bigger, which certainly is attributable to the smaller amplitude of the unsteady pressure response and accordingly the lower signal-to-noise ratio. This is especially the case at the reduced frequency of 0.2. Overall, the unsteady pressure response to the blade oscillation is largely linear on both surfaces.

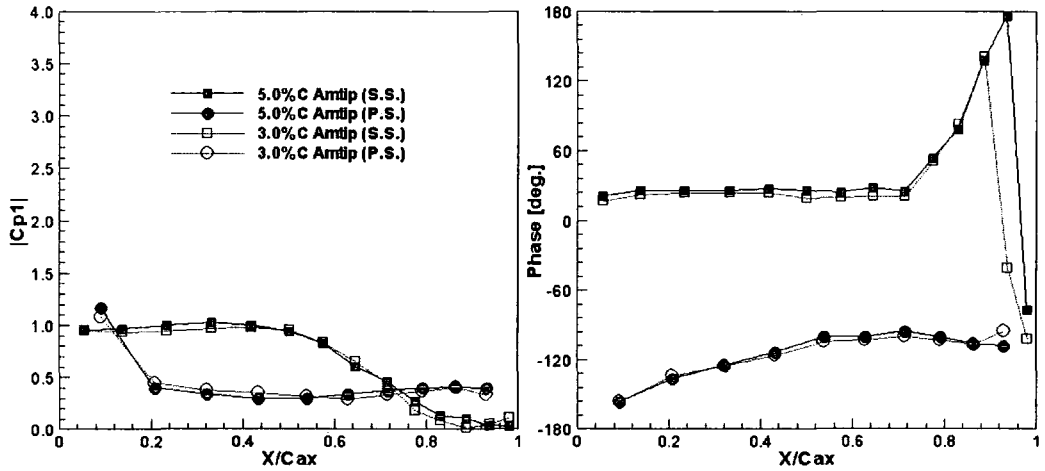


(a) 10% Span

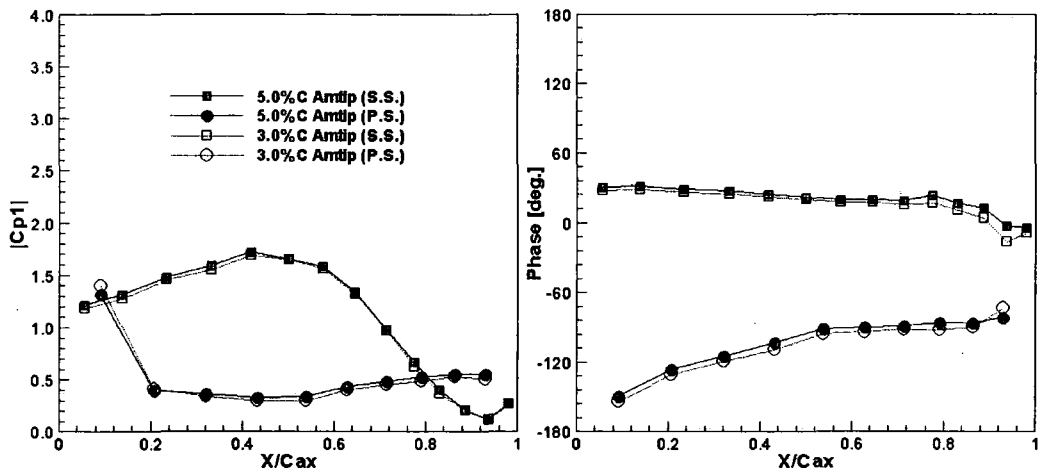


(b) 50% Span

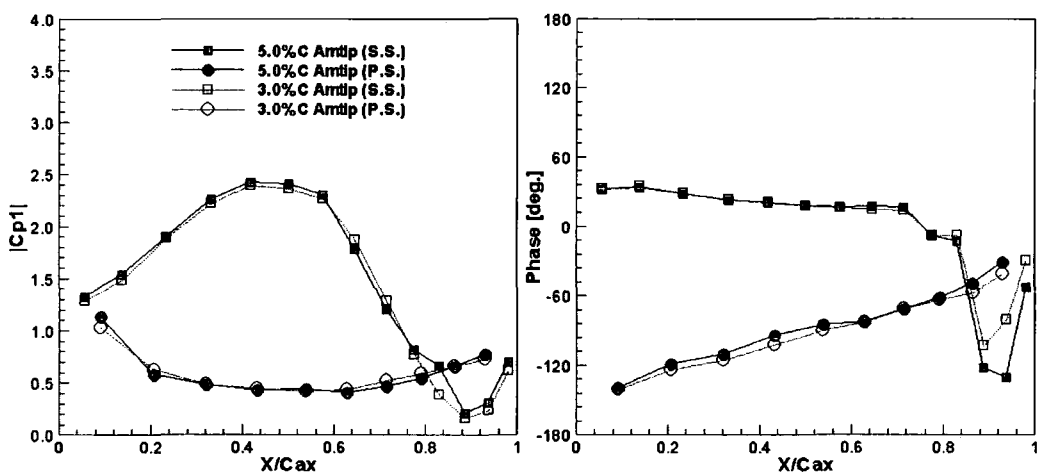


(c) 95% Span

**Figure 5.7: Experimental test for linearity — first harmonic pressure coefficient on the reference blade at two different oscillating amplitudes, ($K$=0.4)**

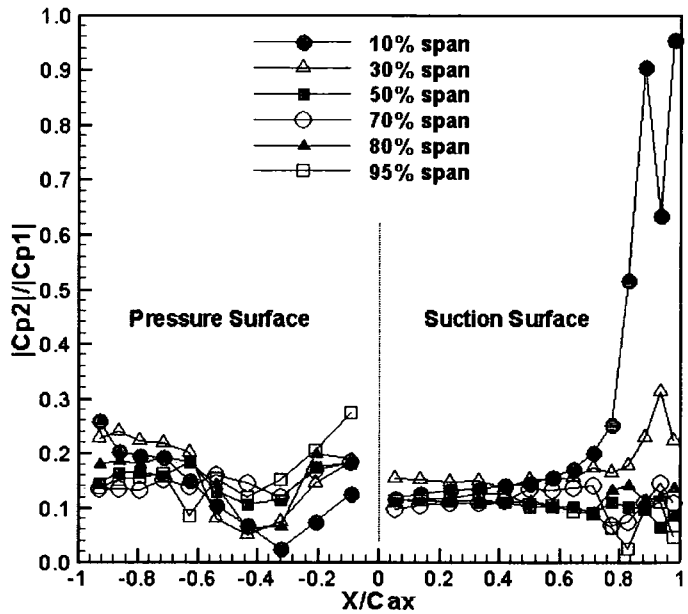


**Figure 5.8: Experimental test for linearity — relative amplitude of the second harmonic pressure coefficient on the reference blade, ($K$=0.2)**

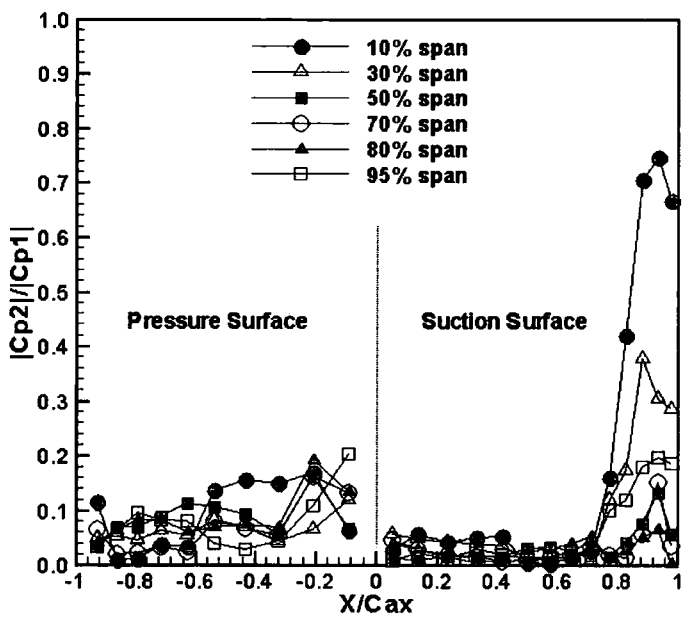


**Figure 5.9: Experimental test for linearity — relative amplitude of the second harmonic pressure coefficient on the reference blade, ($K$=0.4)**

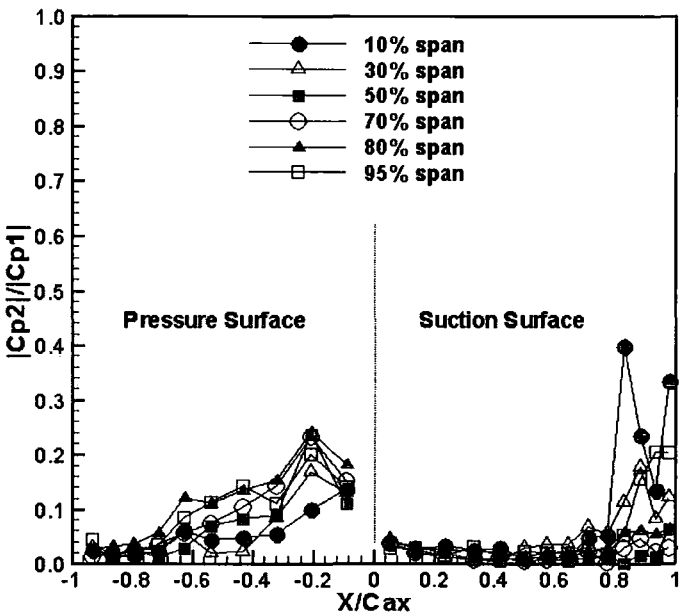


**Figure 5.10: Experimental test for linearity — relative amplitude of the second harmonic pressure coefficient on the reference blade, ($K$=0.6)**

#### 5.1.2.2 Tuned First Harmonic Pressure

The following results were obtained with the middle blade tip being oscillated at an amplitude of 3% chord. The unsteady influence coefficients were measured on the five central blades and the tuned cascade unsteady data were constructed by utilising a superposition based on the influence coefficient method. Then, unsteady flow characteristics associated with the tuned cascade are going to be identified and presented. Upon inspection of the first harmonic pressure measurements, very similar trends in the unsteady pressure response to the blade oscillation were observed throughout the reduced frequencies tested ($K$: 0.2, 0.4, 0.6). Therefore, only the results for the reduced frequency of 0.4 are to be presented in this section. Still, the unsteady measurements for reduced frequencies 0.2 and 0.6 will be presented together with the computational results in the next section.

The amplitudes and phase angles of the first harmonic pressure, presented in Figure 5.11 and 5.12, are for the tuned cascade at an IBPA of $-60°$ and a medium reduced frequency of 0.4. This particular IBPA is chosen, because it has been identified to be

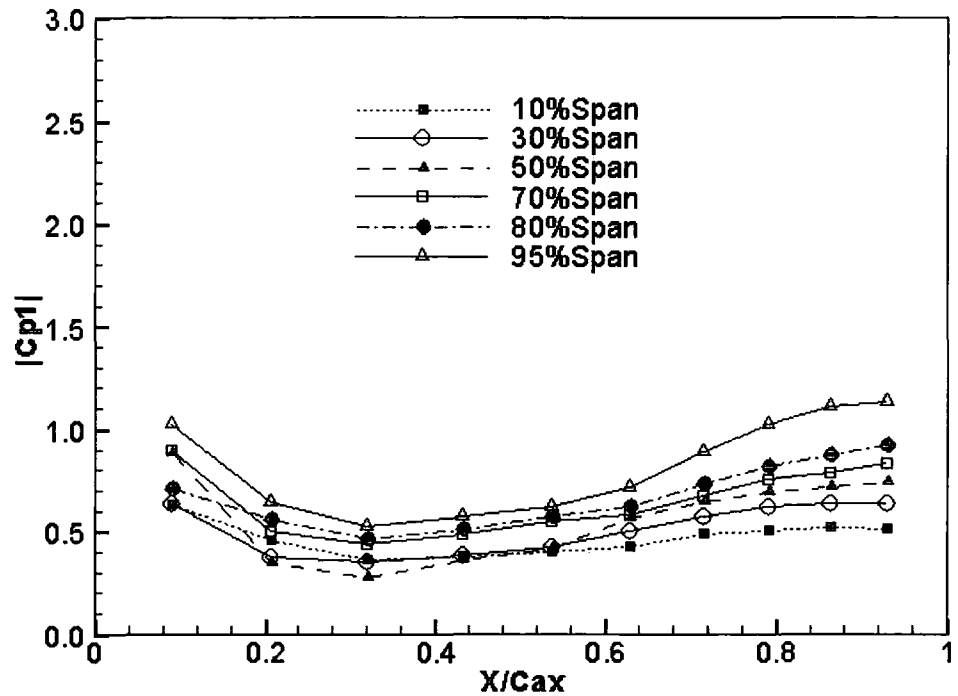


(a) Pressure surface response

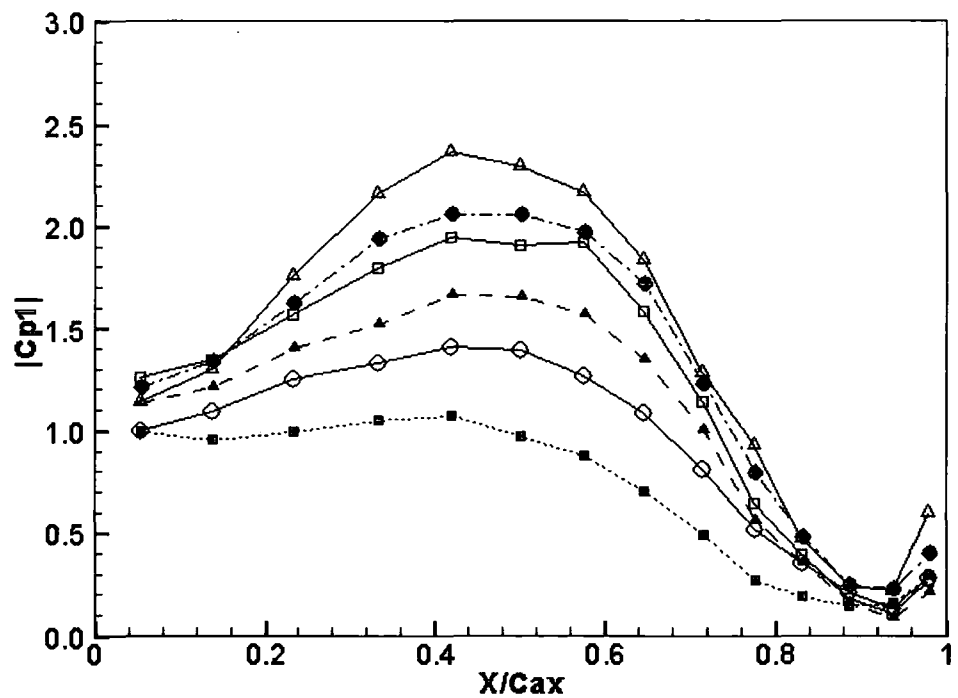


(b) Suction surface response

**Figure 5.11: Amplitude of the first harmonic pressure response ($K$=0.4, $\sigma_0$=−60°)**

the least stable IBPA at the reduced frequency of 0.4. The effects of IBPA on the blade stability will be presented in Figure 5.13.

Figure 5.11b shows the amplitudes of the first harmonic pressures on the suction surface. Along the blade span, the amplitude of the first harmonic pressure consistently increases upwards from the hub except for the area towards the leading edge. However, the increase in the amplitude of the first harmonic pressure is not proportional to the increase in the local blade vibration amplitude along the span. In fact, the amplitude of the first harmonic pressure at 95% span is only about 2.5 times that at 10% span, whilst the local vibration amplitude at 95% span appears to be 5 times that at 10% span. This non-proportional unsteady response to the local vibration amplitude, at different blade spanwise sections, certainly indicates that the unsteady flow response is of a strong three-dimensional nature. On the pressure surface, displayed in Figure 5.11a, a consistent increase in the amplitude along the span height is noticed for a range from $55\%C_{ax}$ to the trailing edge. Towards the leading edge, the change of the first harmonic pressure amplitude is not in a clear trend along the span on both surfaces. The unsteady response is highly sensitive to the local incidence and the experimental errors are expected to be relatively high in this region. Overall, the presence of unsteady pressure peak around mid-chord of the suction surface and towards the trailing edge of the pressure surface suggests that the unsteady response is largely driven by the passage area change during flutter.

In Figure 5.12b, the phase angle distributions of the first harmonic pressure along the chord are plotted at 6 spanwise sections on the suction surface. Apart from the 95% span section, the phase angle shows a consistent shift along the chord from 10% to 80% span section. The phases become more diverse near the trailing edge, particularly at 10% and 95% span, which may suggest some three-dimensional endwall effects. Also, the influence of the imperfection of endwall sealing should be recognised. The phase angles on the pressure surface (Figure 5.12a) are on the whole insensitive to the local span height.

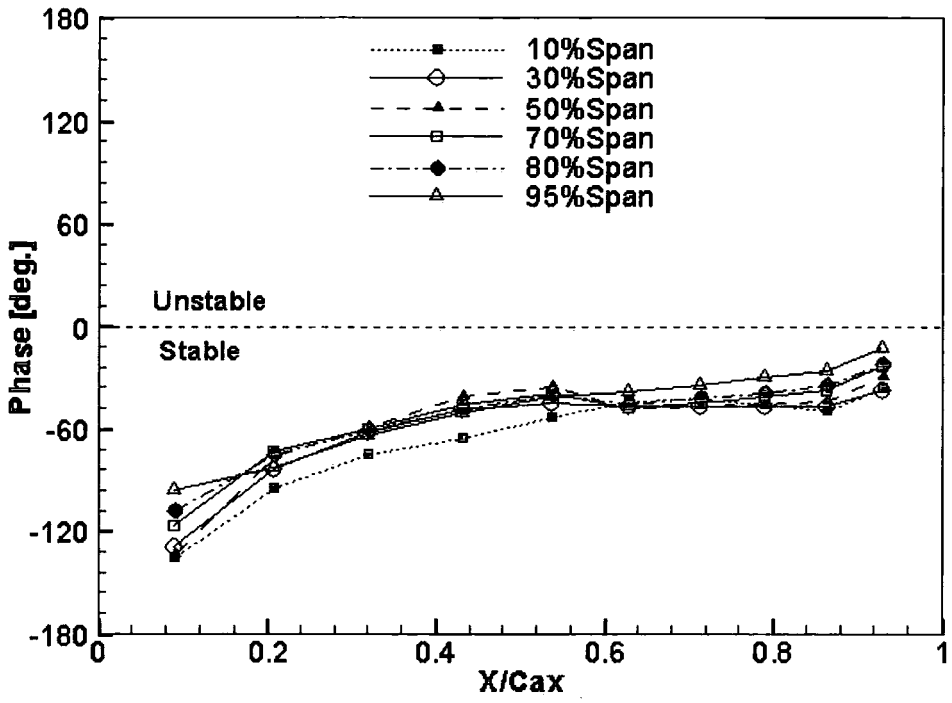


(a) Pressure surface response

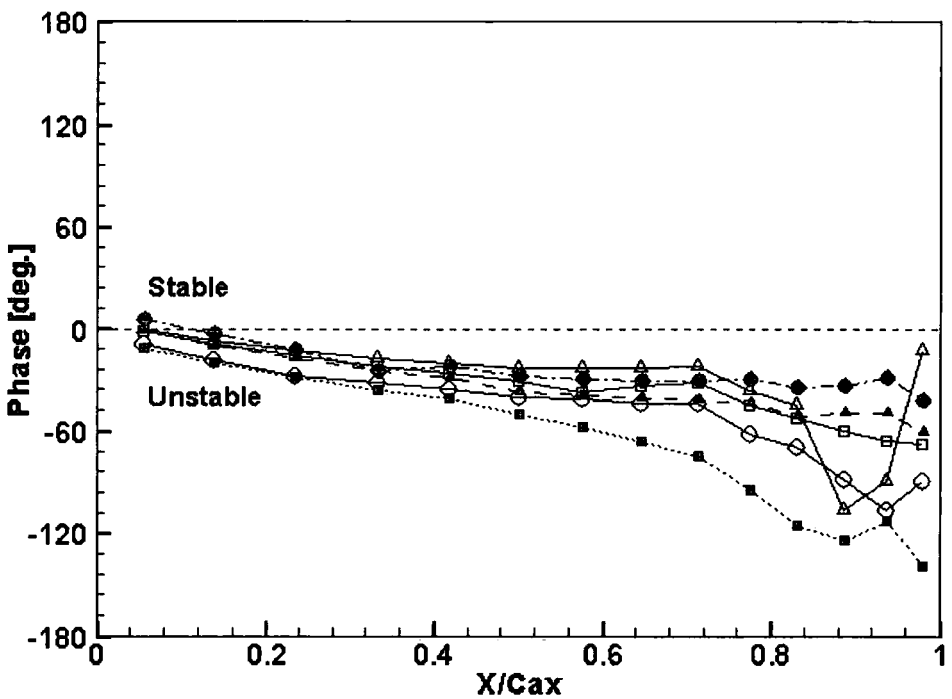


(b) Suction surface response

**Figure 5.12: Phase of the first harmonic pressure response ($K$=0.4, $\sigma_0$=−60°)**

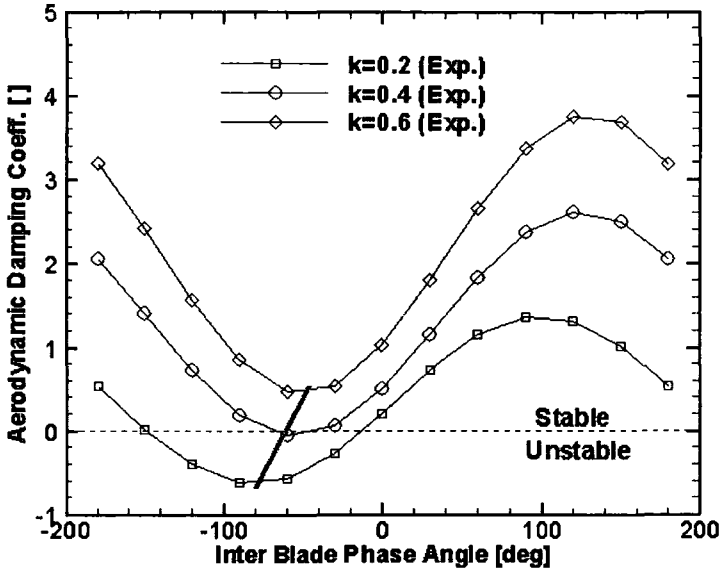


**Figure 5.13: Global aerodynamic damping at three reduced frequencies**

#### 5.1.2.3 Aerodynamic Damping

Figure 5.13 shows the global aerodynamic damping for three reduced frequencies tested. The global aerodynamic damping, which gives a direct indication of aeroelastic stability, is an overall assessment of the unsteady aerodynamic response to the blade oscillation. It allows easy comparison of the influence of reduced frequency on the unsteady pressure response and direct examination of the variation of aeroelastic stability with regard to the IBPA for each reduced frequency.

Apparently, the variation of the global aerodynamic damping with regard to the IBPA reveals an S-curve shape as expected of a summation of sinusoidal functions for each reduced frequency. The vertical position of the damping S-curve depends on the value of reduced frequency. Generally, it shifts consistently upward as well as rightward as reduced frequency increases. That is to say, the increased reduced frequency generally leads to increased aerodynamic damping. This observation is surely consistent with an industrial design practice (a rule of thumb) regarding the reduced frequency that blade flutter only occurs below a certain value of reduced frequency. For a reduced frequency 0.2, the present cascade is unstable based on the aerodynamic damping for a range of IBPAs from $-150°$ to $-10°$. As the reduced frequency increases to 0.4, the cascade is

unstable at a small range of IBPA values around $-60°$, whereas the cascade is stable at the whole range of IBPA for a reduced frequency of 0.6.

The damping S-curve is the direct reflection of the aerodynamic coupling between blades. The consequence of the aerodynamic coupling is such that blade flutter only picks up the least stable IBPA, which has the lowest aerodynamic damping. Upon examining the least stable IBPA for different reduced frequencies, it shows a consistent shift as indicated by the bold line in the plot. Indeed, the least stable IBPA is identified to be around $-80°$, $-60°$ and $-45°$ for the reduced frequencies of 0.2, 0.4 and 0.6 respectively. The least stable IBPA ($-60°$) at the reduced frequency of 0.4 was therefore chosen for the inspection of the unsteady three-dimensional behaviour (as previously presented).

## 5.2 Computational Study

In this section, the computational solutions for the linear turbine cascade at the nominal condition are presented, of which the experimental measurements have been described previously. The results were obtained from the unsteady, three-dimensional, single-passage, time-marching, Navier-Stokes flow solver, which was described in Chapter 4. The computational mesh, shown is Figure 5.14, is of a single-H type. To examine the mesh dependency, three meshes (Table 5.1) were employed. For the computation of each unsteady test case, the reduced frequency was matched and the experimental Reynolds number of $2.2 \times 10^5$ retained. The blade oscillating amplitude was, however, reset to 1% chord for a better solution convergence. It is well known that the density based compressible flow solver is unsuitable to calculate flows of very low Mach number. The flow velocity was therefore elevated to avoid the difficulty. The exit Mach number, prescribed in the calculations, was around 0.3, at which the flow compressibility influence was still negligible.

**Table 5.1: Mesh dependency study**

| Mesh name | Mesh density(axial,circumferential,radial) |
|---|---|
| Mesh 1 | $107 \times 31 \times 41$ |
| Mesh 2 | $107 \times 41 \times 51$ |
| Mesh 3 | $128 \times 51 \times 51$ |

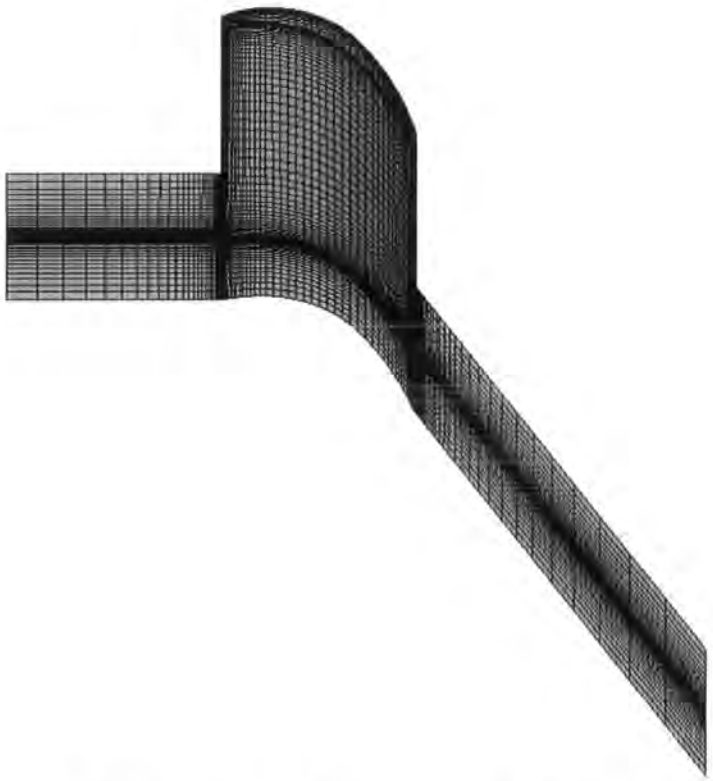

Figure 5.14: 3D Computational Mesh

### 5.2.1 Steady Flow Computations

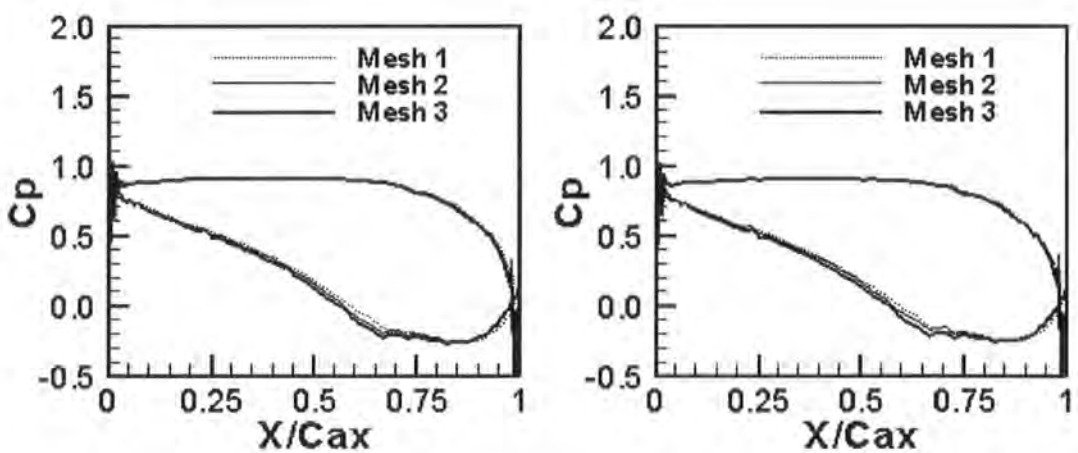


(a) 50% span

(b) 95% span

**Figure 5.15: Mesh dependency study: steady blade surface pressure predictions**

Figure 5.15 shows the predicted steady surface pressure distributions at two representative sections of 50% and 95% span for three meshes listed in Table 5.1. The steady

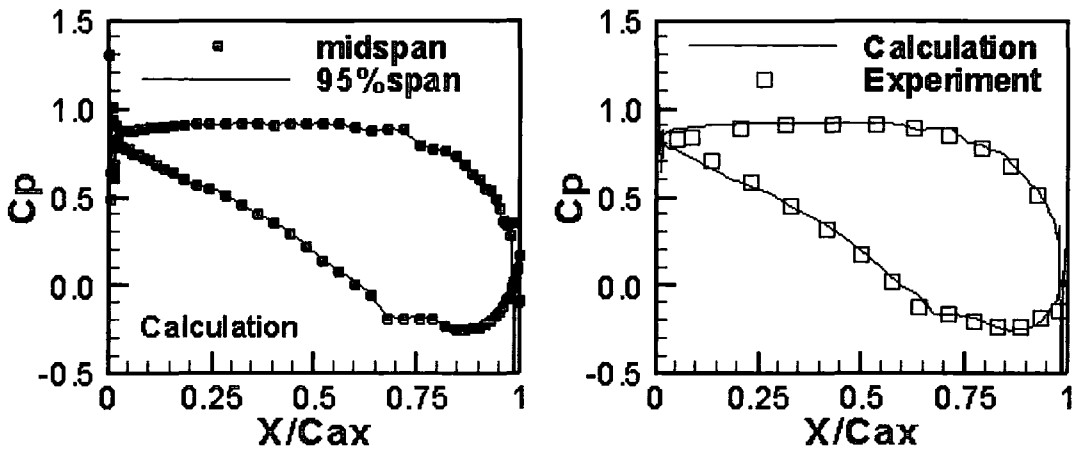


(a) Predicted steady pressures at two spanwise sections

(b) Steady pressures at midspan

**Figure 5.16: Predicted and measured steady blade surface pressure distributions (Mesh 2)**

surface pressure distribution curves lie well in line with one another and show minor differences around $60\%C_{ax}$ on the suction surface. This suggests small dependency of the steady loading prediction on the mesh density. Shown in Figure 5.16 are the predicted (using Mesh 2) and measured steady flow blade surface pressure coefficient distributions. Since the predicted steady pressure distributions are almost identical at all sections, only the steady pressure distributions at two spanwise sections of 50% and 95% span are presented in Figure 5.16a. The predicted steady pressure clearly demonstrates a predominantly two-dimensional flow. Because almost identical steady loading predictions were obtained for these three meshes, it is justifiable to only compare the steady prediction from one mesh with the measured data. In Figure 5.16b, good agreement with the experimental measurements is evident for the prediction over the whole chord at the midspan. Also, because both the experiment and computation show the steady flow is of a two-dimensional behaviour, the comparison between the measurement and the prediction is made only at the midspan section.

### 5.2.2 Unsteady Flow Predictions

A series of unsteady flow computations was carried out at several values of IBPA for three tested reduced frequencies. In these computational studies, three meshes with different densities listed in Table 5.1 are applied. The considered IBPAs cover

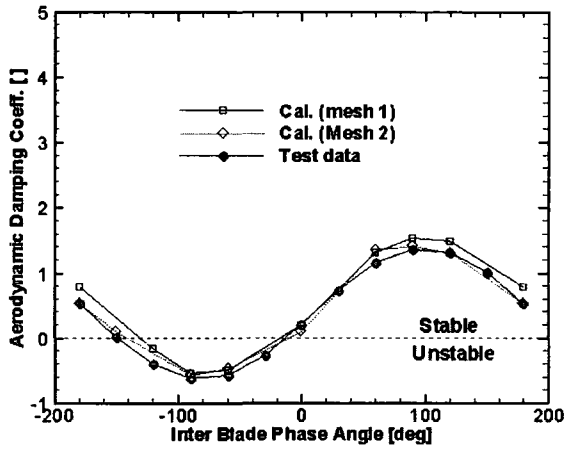


(a) Reduced frequency $K = 0.2$

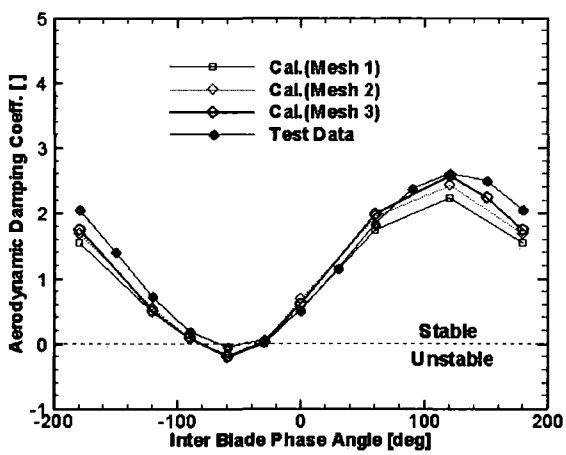


(b) Reduced frequency $K = 0.4$

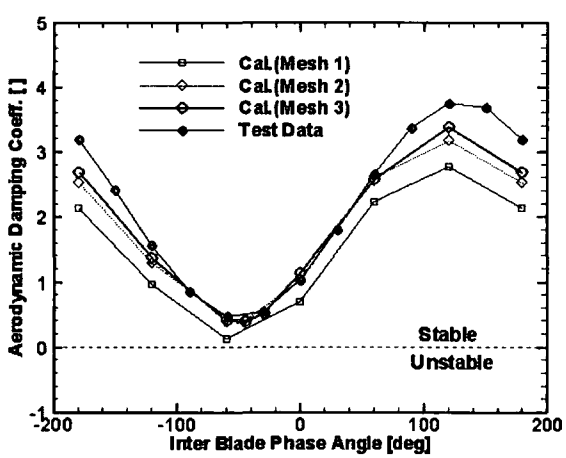


(c) Reduced frequency $K = 0.6$

**Figure 5.17: Aerodynamic damping prediction at nominal conditions, $\xi$**

the whole range of possible values from $-180°$ to $180°$ but with an interval of $30°$. The massive results generated by the series of unsteady computations mean that it is easier to compare the global parameter, namely the global aerodynamic damping, for each case. Also, it is the global aerodynamic damping that ultimately determines the aeroelastic stability of blades. From the engineering application point of view, the most important requirement for computations is the accuracy and consistency with which the aerodynamic damping is predicted. Figure 5.17 shows the predicted global aerodynamic damping together with the experimental data for reduced frequencies of 0.2, 0.4 and 0.6. The computational solutions were obtained through a single-passage Navier-Stokes solver with blades oscillating in a travelling wave mode. The experimental data were acquired in a linear cascade using the influence coefficient technique and reported in Section 5.1. For reduced frequency 0.2, results for Mesh 1 and Mesh 2 are presented in Figure 5.17a. It is evident that damping predictions from both meshes give excellent qualitative and quantitative agreement with the experimental results. For reduced frequencies 0.4 and 0.6, although all predictions from three meshes achieve good approximation of measured damping, predicted damping from Mesh 3, with the highest mesh density, exhibits the best correlation with the experimental data. By examining the present mesh strategy, two general observations can be made. First, the unsteady solution shows higher dependency on the mesh used than the steady solution. Second, the high reduced frequency case has higher dependency on mesh than the low reduced frequency case. As indicated by the definition of reduced frequency in Equations 1.3 and 1.4, the reduced frequency is a measure of temporal and spatial scales of the disturbance induced by the blade vibration. Therefore, the higher the reduced frequency is, the smaller mesh length and time-step length should be used in order to achieve the same level of accuracy. Overall, Mesh 2 is the best compromise between prediction accuracy and computing cost. The results presented in the rest of this chapter were obtained on Mesh 2.

To scrutinise in more detail the prediction capability of the present CFD scheme, the predicted first harmonic pressures are presented and compared with the measured data in Figures 5.18 to 5.29. For each reduced frequency, the first harmonic pressure predictions at the least and most stable IBPAs are provided, with two figures for each

IBPA. The first shows a comparison of predicted and measured amplitudes of the first harmonic pressure and the second the corresponding phase angles.

At the reduced frequency of 0.2, the predicted amplitude of the first harmonic pressure for the least and the most stable IBPAs, shown in Figures 5.18 and 5.20 respectively, exhibits excellent agreement with the experimental data at all spanwise sections over both the pressure surface and suction surface. The predicted phase angle of the first harmonic pressure response, shown in Figure 5.21, also reveals excellent agreement with the experimental measurements at all sections on both the pressure surface and the suction surface for the most stable IBPA (90°). For the least stable IBPA (−90°), shown in Figure 5.19, the predicted phase angle of the first harmonic pressure demonstrates excellent agreement with the experimental data on the suction surface. Whilst excellent agreement between the predicted and measured phase angle of the first harmonic pressure is evident up to $60\%C_{ax}$ on the pressure surface, there is discernible deterioration in the quantitative agreement between the predicted and measured phase angle towards the trailing edge.

At the reduced frequency of 0.4, the predicted amplitude of the first harmonic pressure shows excellent correlation to the experimental measurements at most spanwise sections on both pressure surface and suction surface for the least and the most stable IBPAs (see Figures 5.22 and 5.24). Discrepancy between the predicted and measured amplitude of the first harmonic pressure is observed at sections near the cascade endwalls. Displayed in Figures 5.23 and 5.25, excellent correlation of the predicted phase angle of the first harmonic pressure to the test data is evident for the least and the most stable IBPAs over most locations on both pressure surface and suction surface except area towards the trailing edge.

At the reduced frequency of 0.6, good agreement between the predicted and measured amplitude of the first harmonic pressure is observed over most locations on the blade surface for the least stable IBPA (−45°), shown in Figure 5.26, whilst disparity is getting bigger towards the leading and trailing edges. For the phase angle of the first harmonic pressure at the least stable IBPA, there is good agreement between the predicted and measured data at all spanwise sections over the pressure surface and most the suction surface up to $75\%C_{ax}$. Aft of $75\%C_{ax}$ and towards the trailing edge,

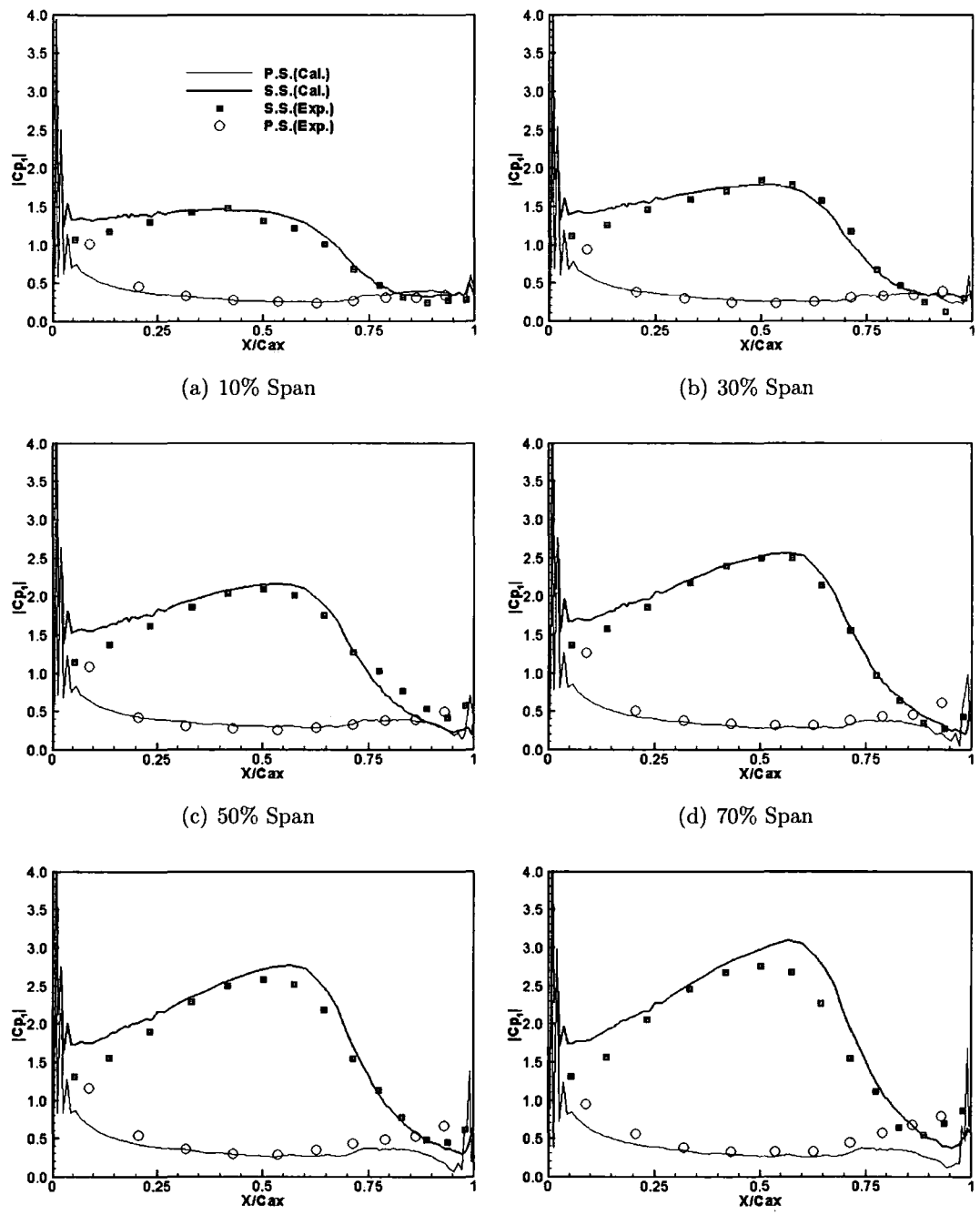


(a) 10% Span

(b) 30% Span

(c) 50% Span

(d) 70% Span

(e) 80% Span

(f) 95% Span

**Figure 5.18: Predicted and measured amplitude of the first harmonic pressure (Mesh 2, $K$=0.2, $\sigma_0$=−90°)**

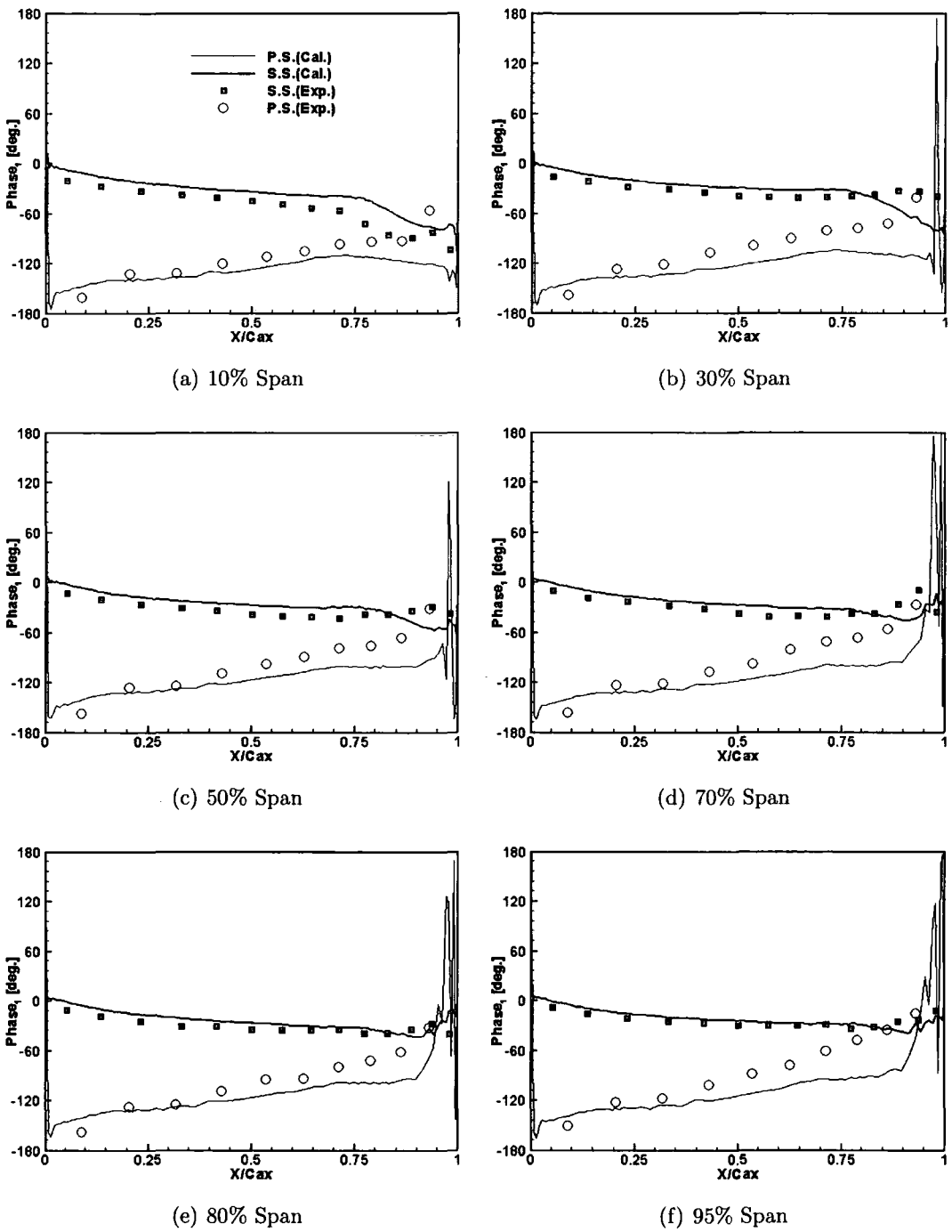


(a) 10% Span

(b) 30% Span

(c) 50% Span

(d) 70% Span

(e) 80% Span

(f) 95% Span

**Figure 5.19: Predicted and measured phase angle of the first harmonic pressure (Mesh 2, $K$=0.2, $\sigma_0$=−90°)**

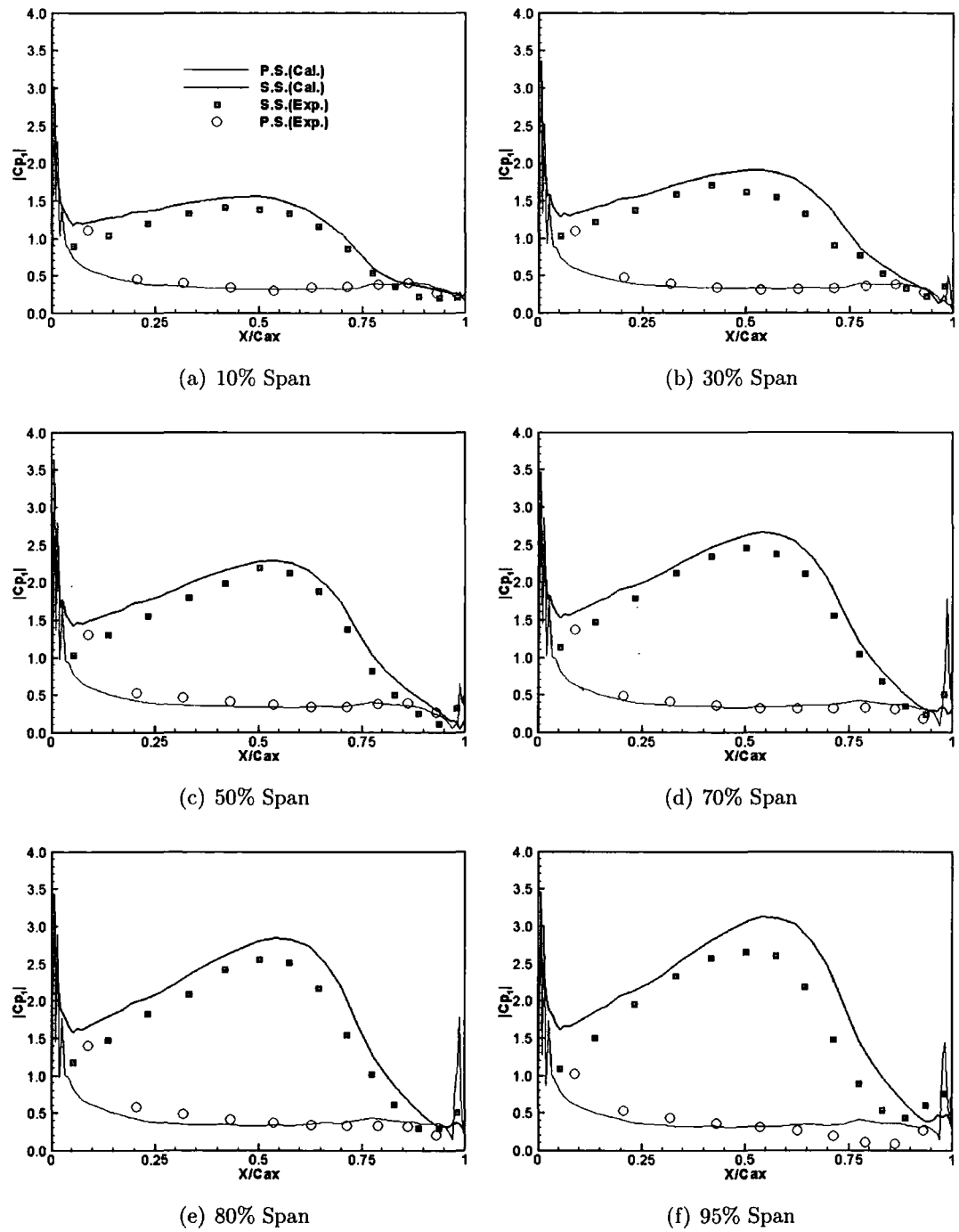


(a) 10% Span

(b) 30% Span

(c) 50% Span

(d) 70% Span

(e) 80% Span

(f) 95% Span

**Figure 5.20: Predicted and measured amplitude of the first harmonic pressure (Mesh 2, $K$=0.2, $\sigma_0$=90°)**

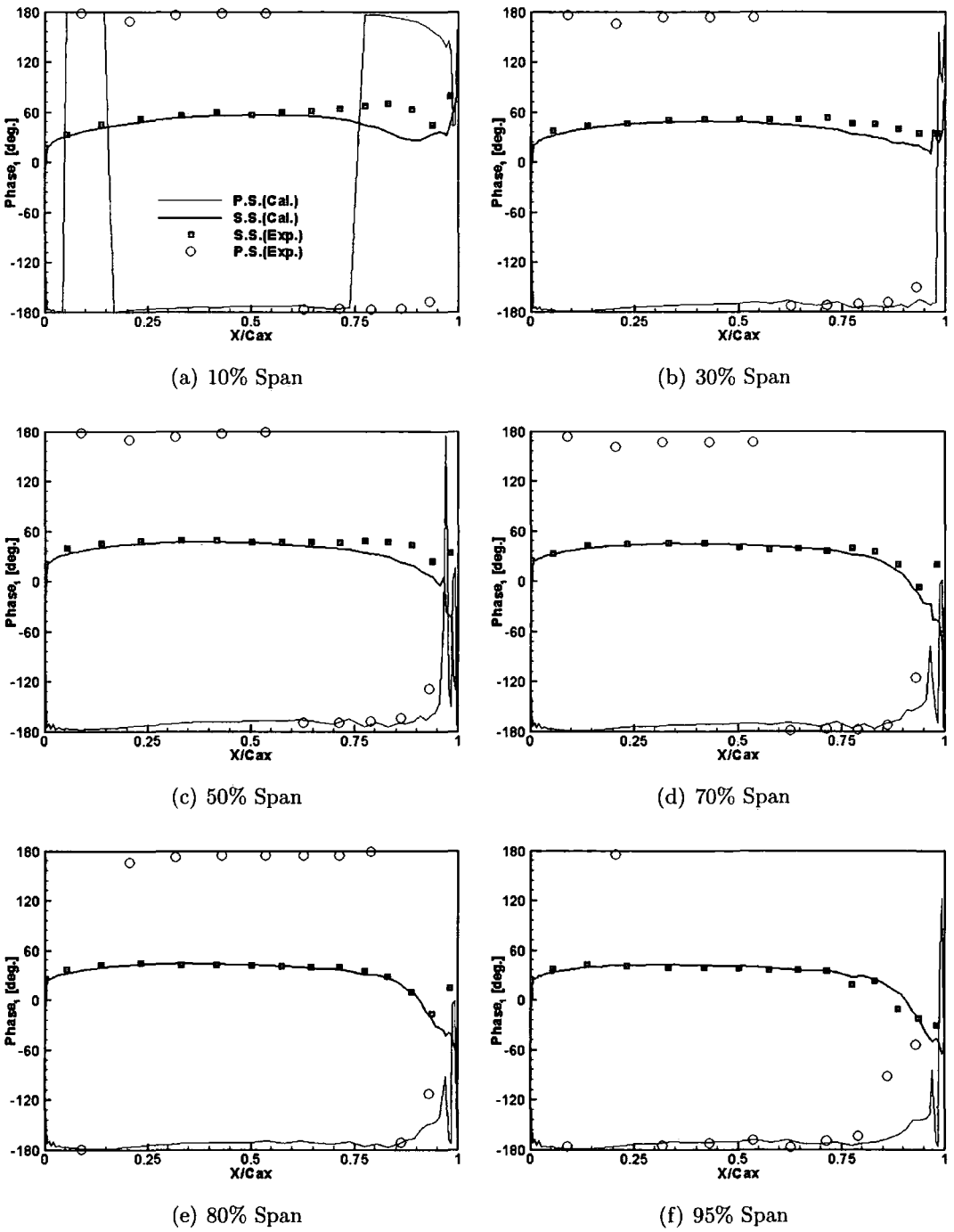


(a) 10% Span

(b) 30% Span

(c) 50% Span

(d) 70% Span

(e) 80% Span

(f) 95% Span

**Figure 5.21: Predicted and measured phase angle of the first harmonic pressure (Mesh 2, $K$=0.2, $\sigma_0$=90°)**

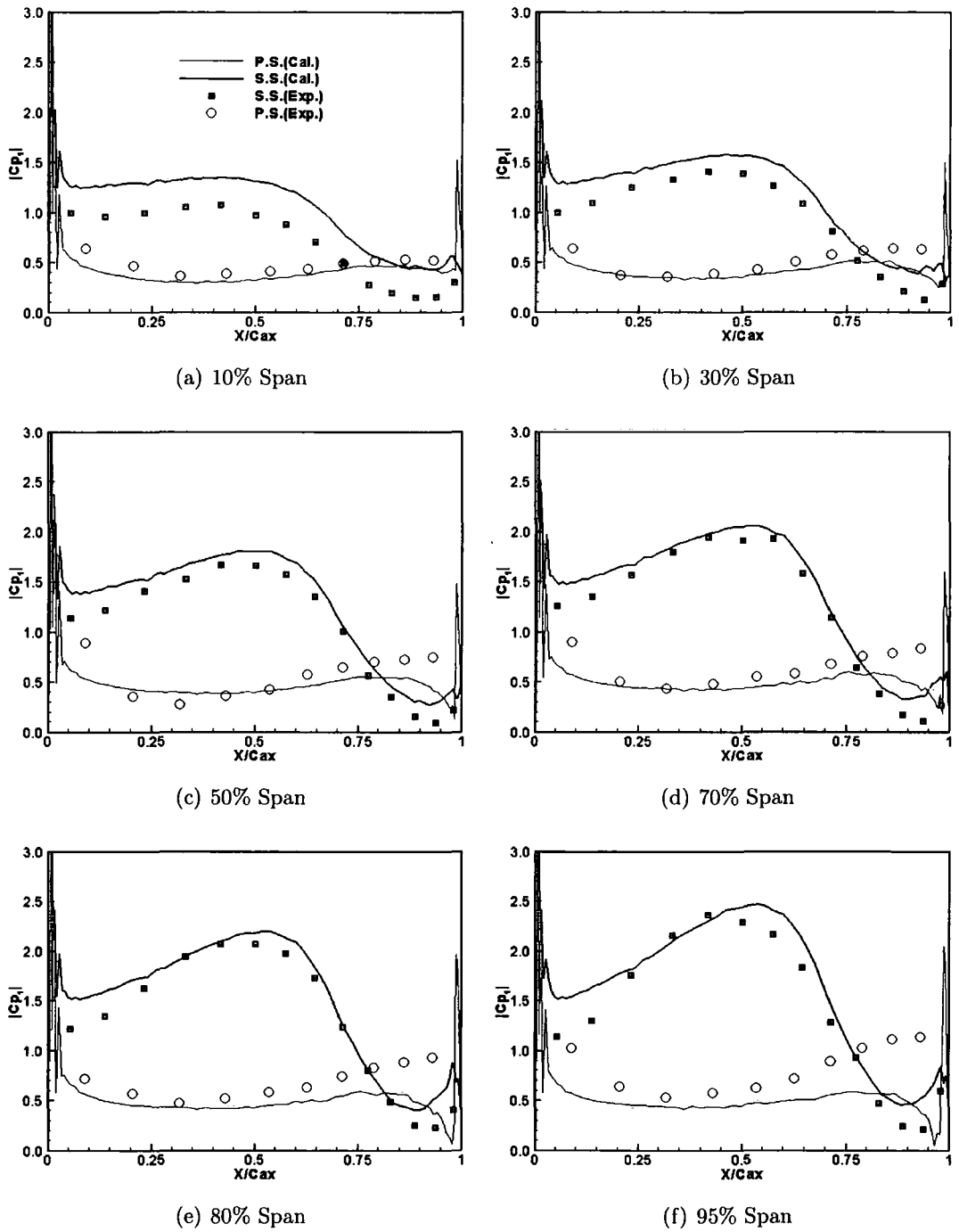


(a) 10% Span

(b) 30% Span

(c) 50% Span

(d) 70% Span

(e) 80% Span

(f) 95% Span

**Figure 5.22: Predicted and measured amplitude of the first harmonic pressure (Mesh 2, $K$=0.4, $\sigma_0$=−60°)**

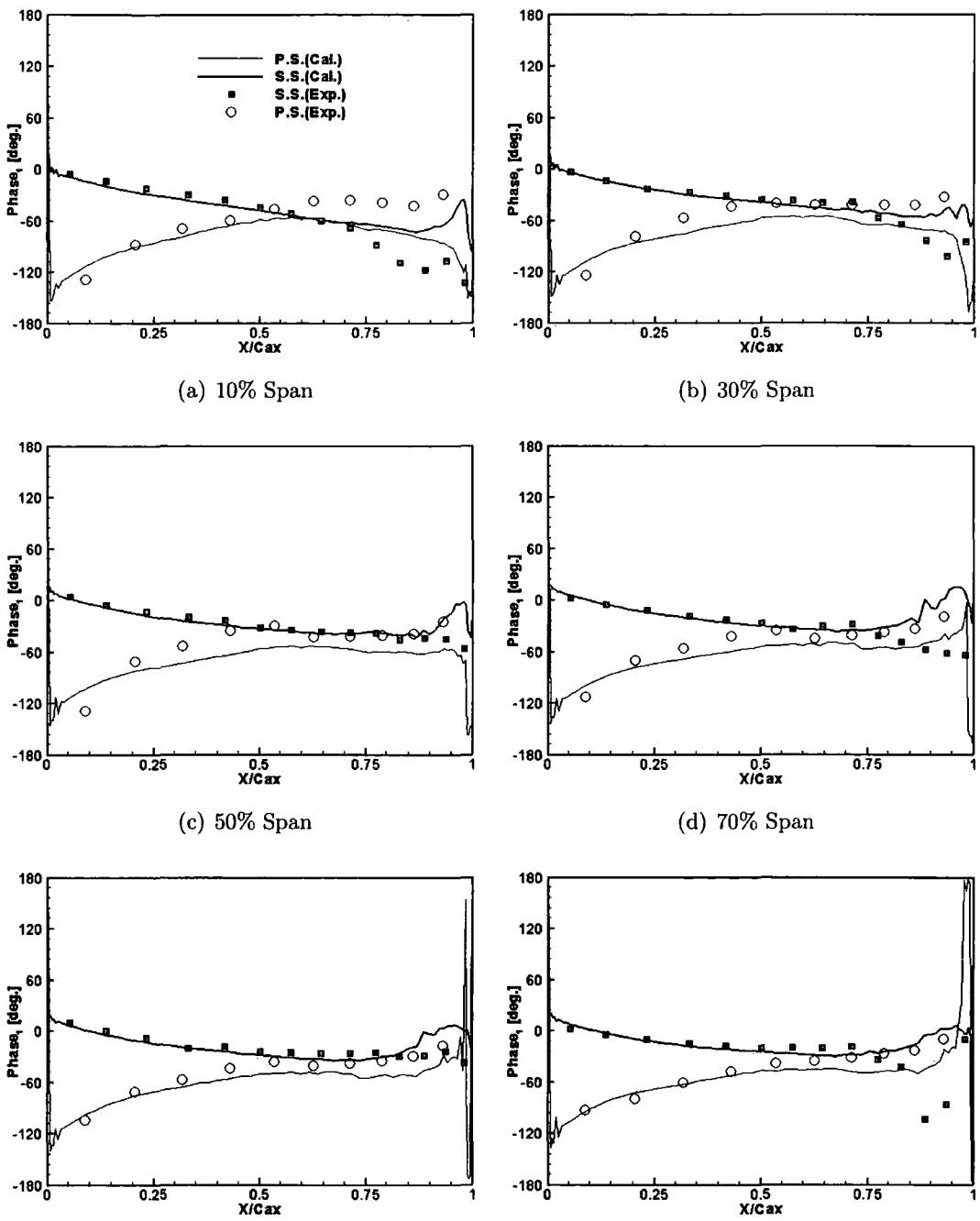


(a) 10% Span

(b) 30% Span

(c) 50% Span

(d) 70% Span

(e) 80% Span

(f) 95% Span

**Figure 5.23: Predicted and measured phase angle of the first harmonic pressure (Mesh 2, $K$=0.4, $\sigma_0$=−60°)**

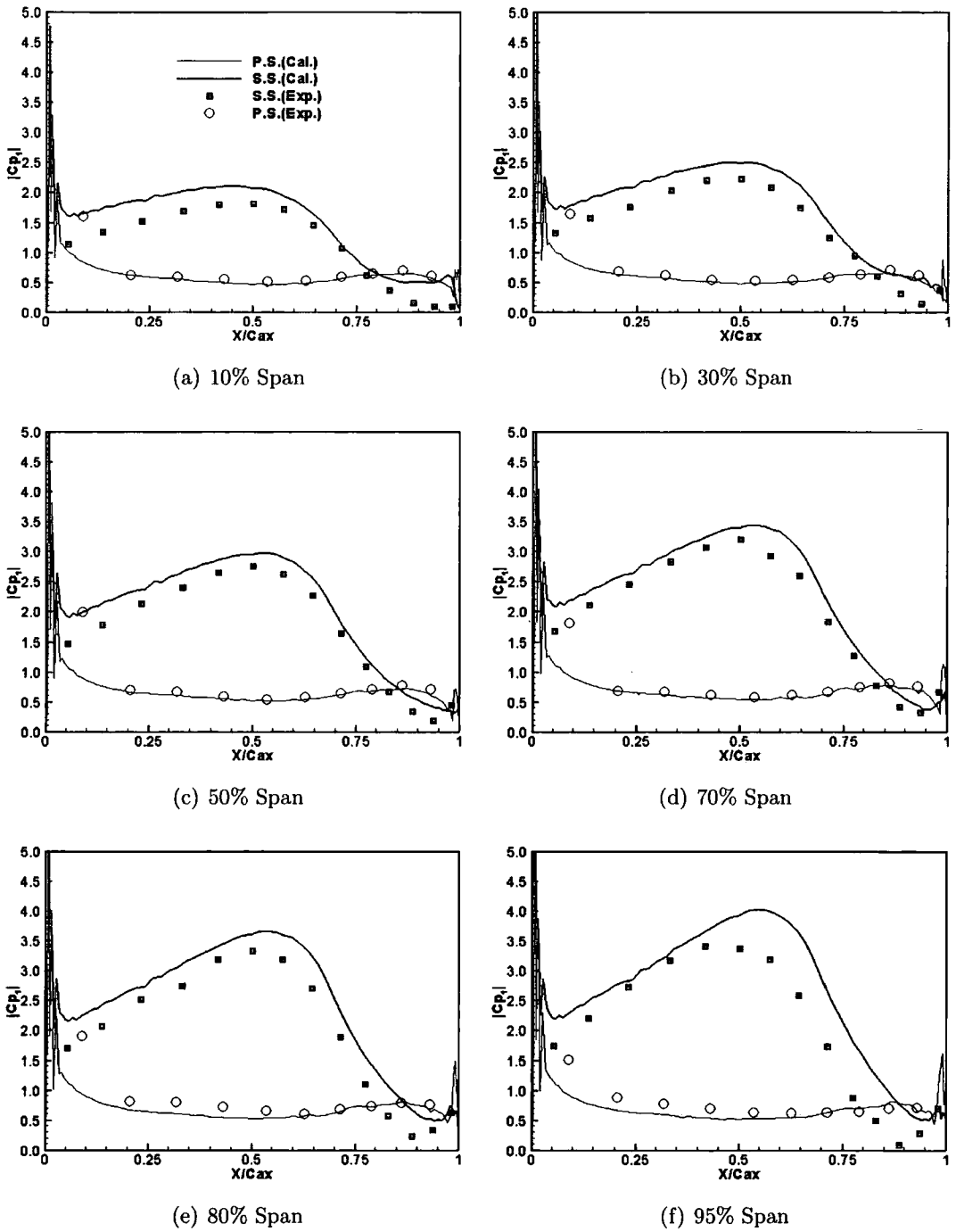


(a) 10% Span

(b) 30% Span

(c) 50% Span

(d) 70% Span

(e) 80% Span

(f) 95% Span

**Figure 5.24: Predicted and measured amplitude of the first harmonic pressure (Mesh 2, $K$=0.4, $\sigma_0$=120°)**

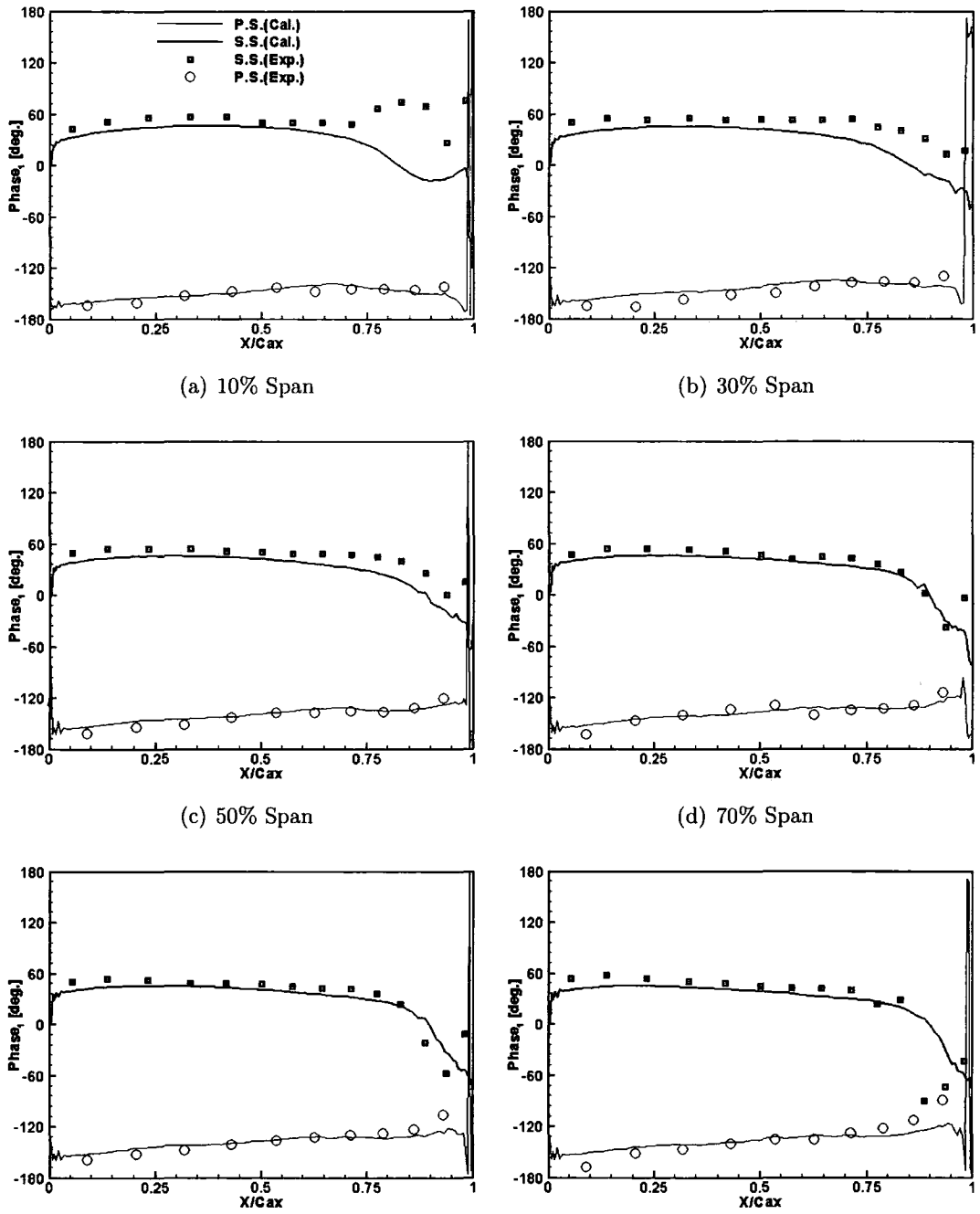


(a) 10% Span

(b) 30% Span

(c) 50% Span

(d) 70% Span

(e) 80% Span

(f) 95% Span

**Figure 5.25: Predicted and measured phase angle of the first harmonic pressure (Mesh 2, $K$=0.4, $\sigma_0$=120°)**

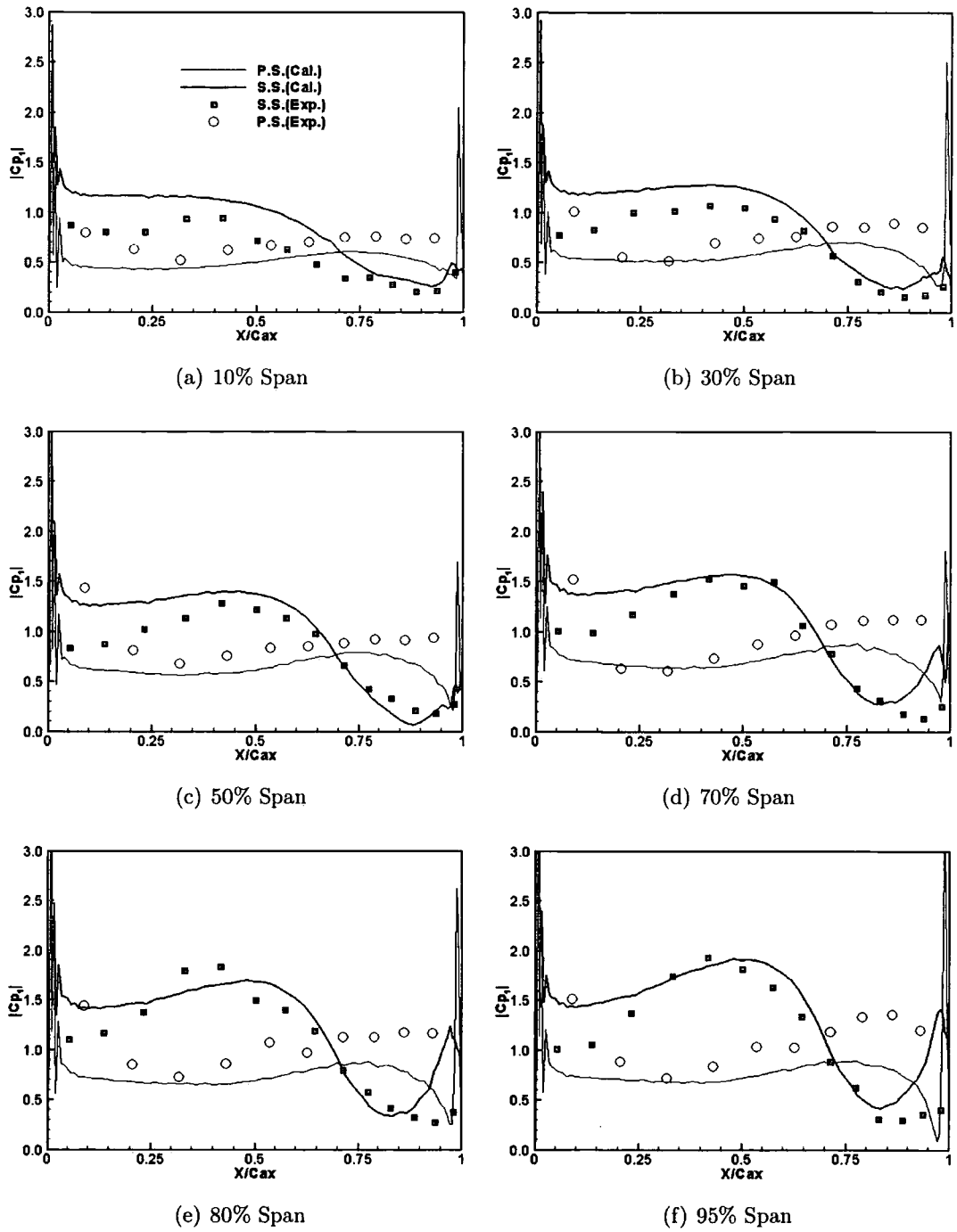


(a) 10% Span

(b) 30% Span

(c) 50% Span

(d) 70% Span

(e) 80% Span

(f) 95% Span

**Figure 5.26: Predicted and measured amplitude of the first harmonic pressure (Mesh 2, $K$=0.6, $\sigma_0$=−45°)**

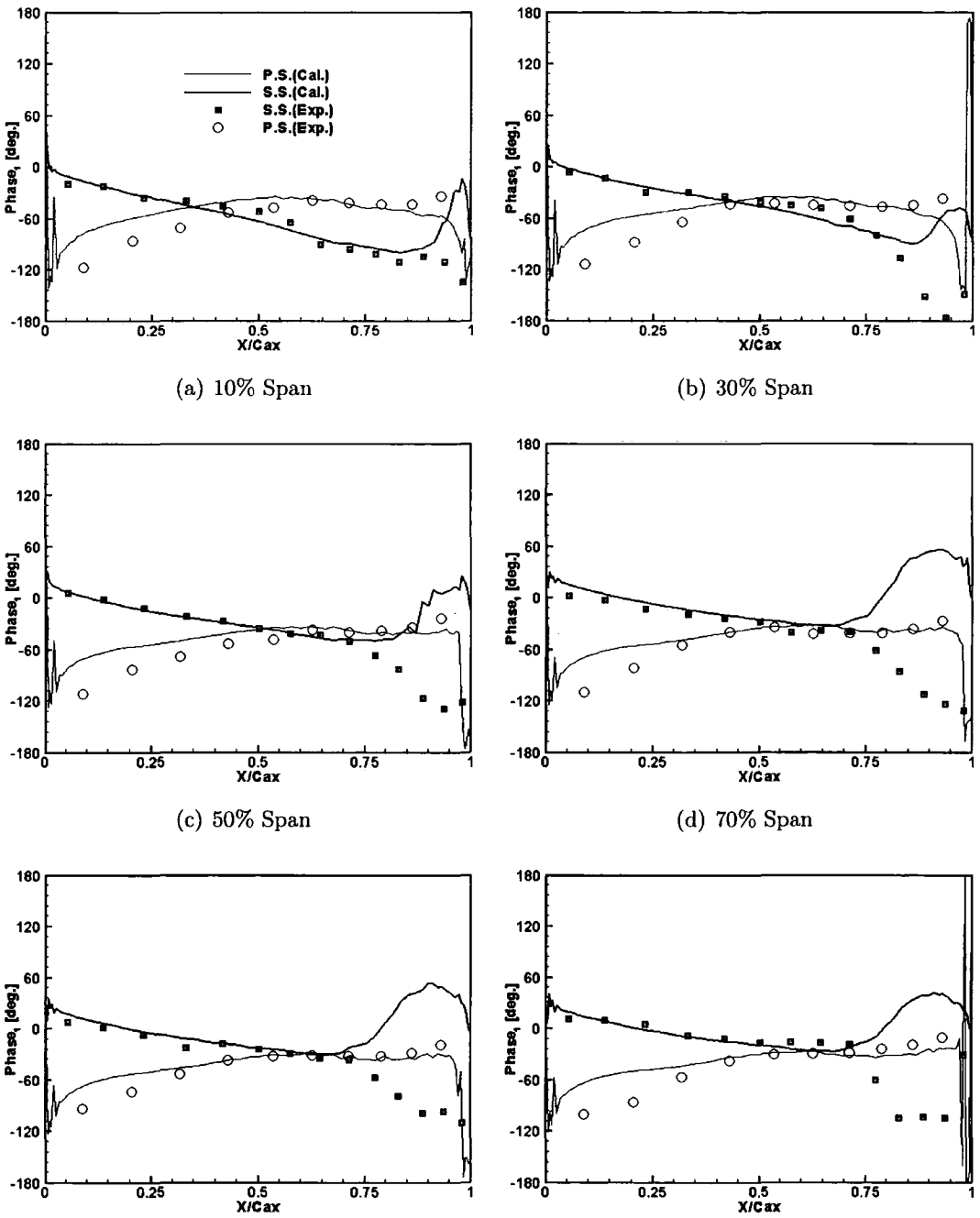


(a) 10% Span

(b) 30% Span

(c) 50% Span

(d) 70% Span

(e) 80% Span

(f) 95% Span

**Figure 5.27: Predicted and measured phase angle of the first harmonic pressure (Mesh 2, $K$=0.6, $\sigma_0$=−45°)**

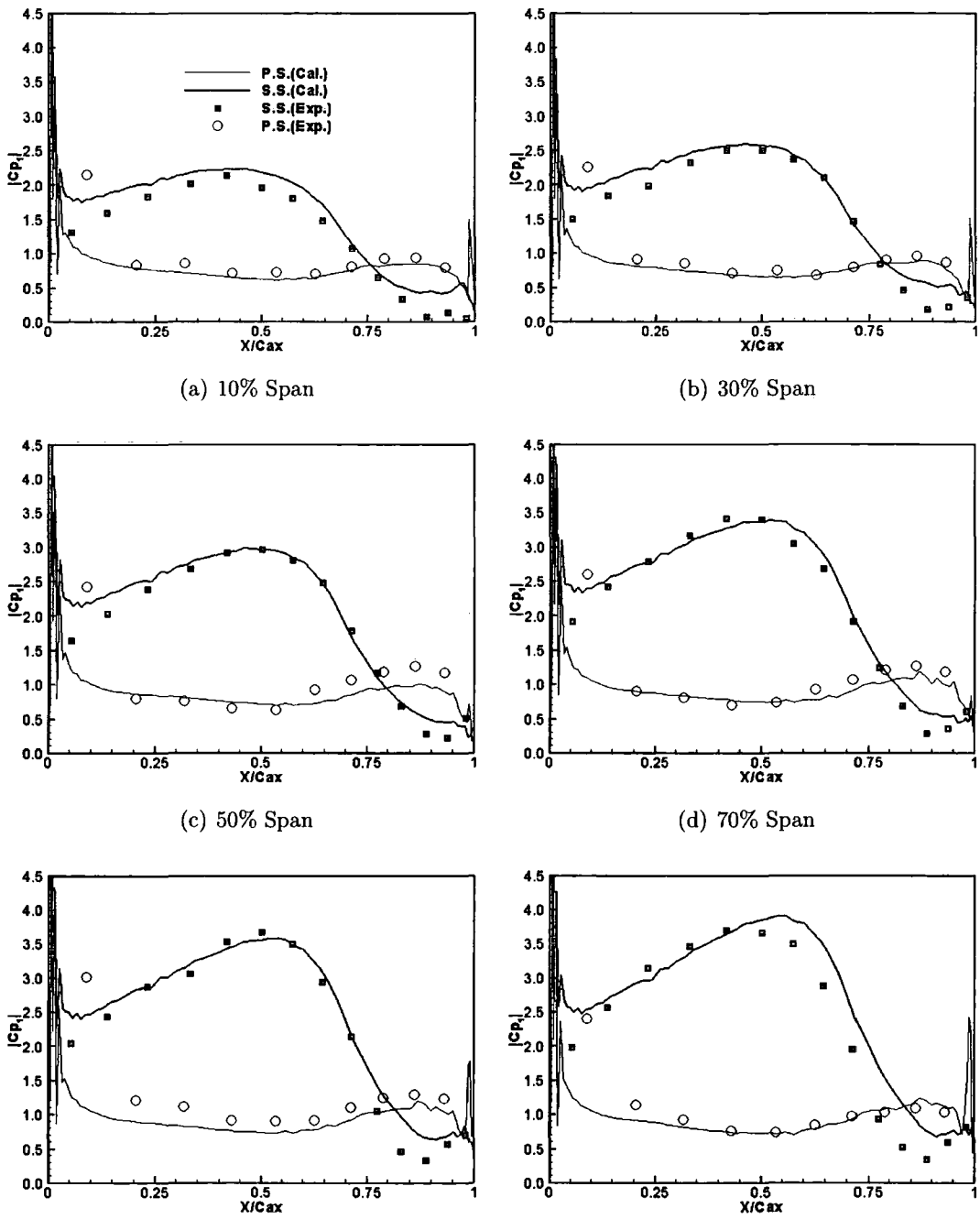


(a) 10% Span

(b) 30% Span

(c) 50% Span

(d) 70% Span

(e) 80% Span

(f) 95% Span

**Figure 5.28: Predicted and measured amplitude of the first harmonic pressure (Mesh 2, $K$=0.6, $\sigma_0$=120°)**

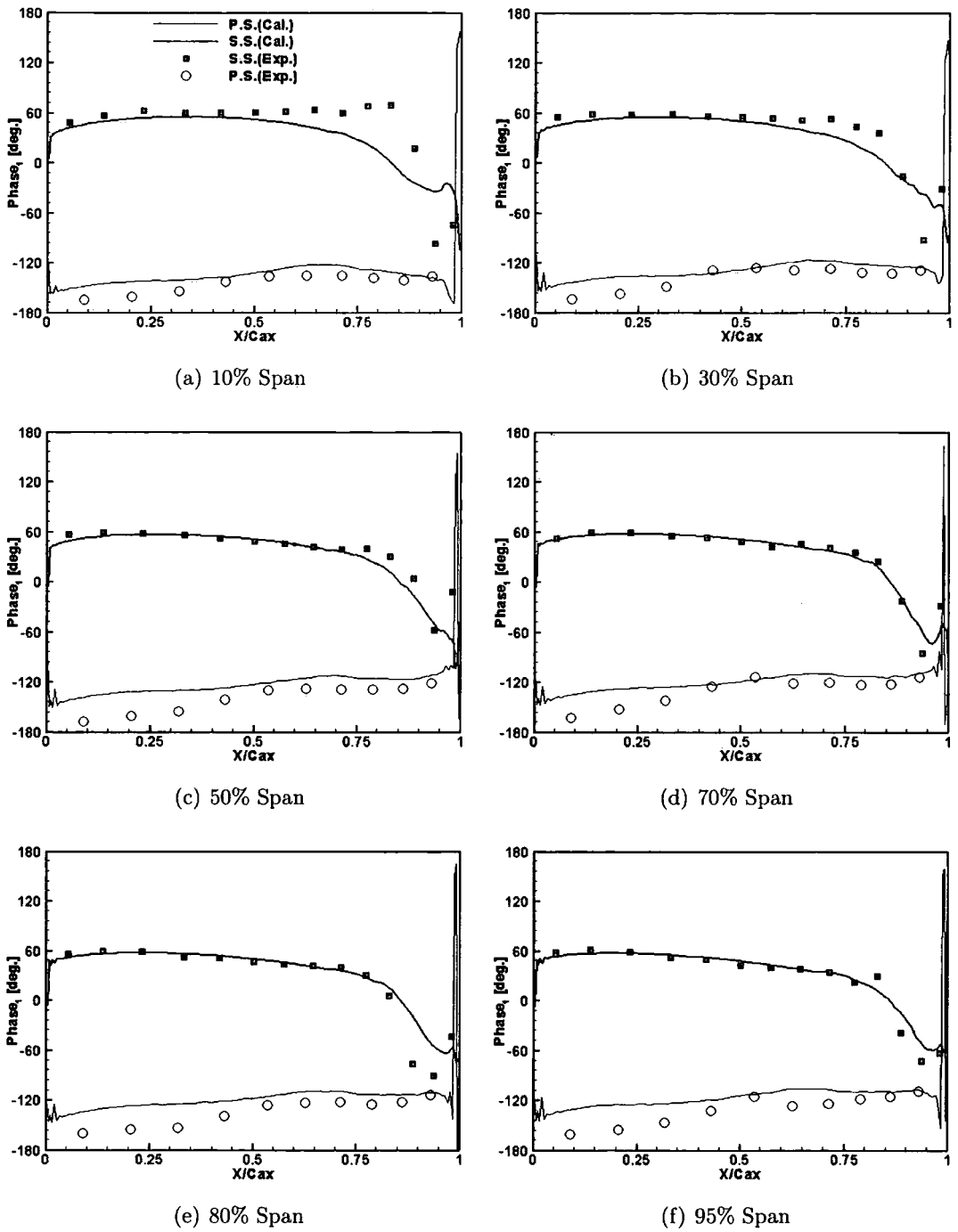


(a) 10% Span

(b) 30% Span

(c) 50% Span

(d) 70% Span

(e) 80% Span

(f) 95% Span

**Figure 5.29: Predicted and measured phase angle of the first harmonic pressure (Mesh 2, $K$=0.6, $\sigma_0$=120°)**

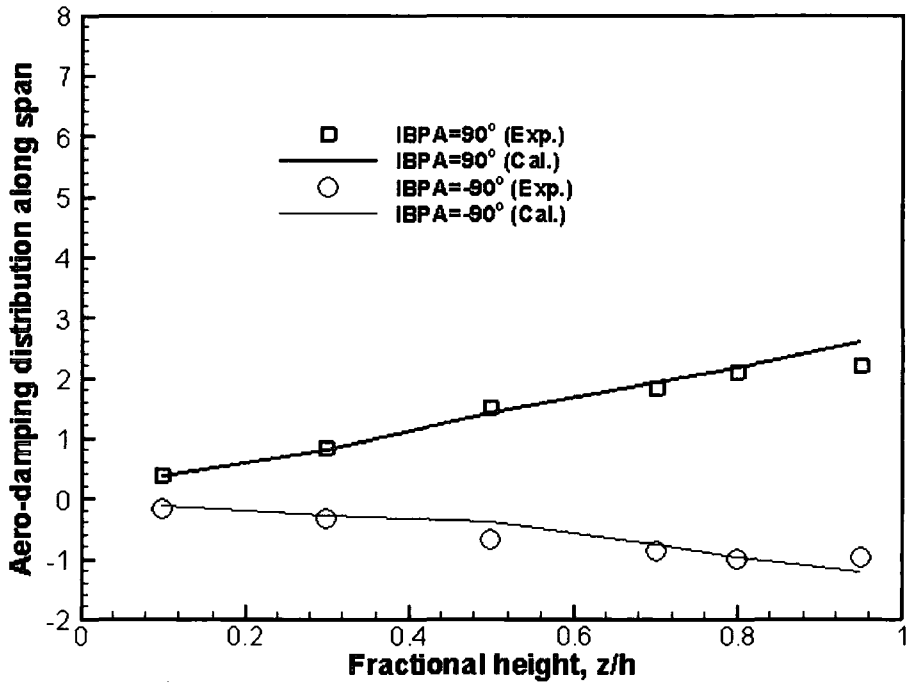


**Figure 5.30: Aerodynamic damping variation along blade span, $\xi_{span}$, $K$=0.2**

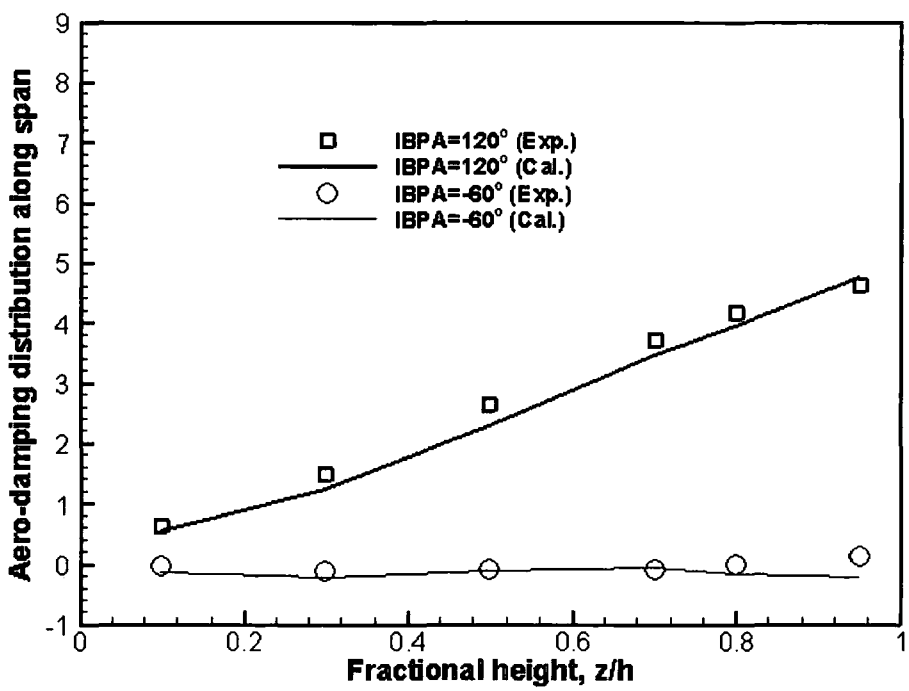


**Figure 5.31: Aerodynamic damping variation along blade span, $\xi_{span}$, $K$=0.4**

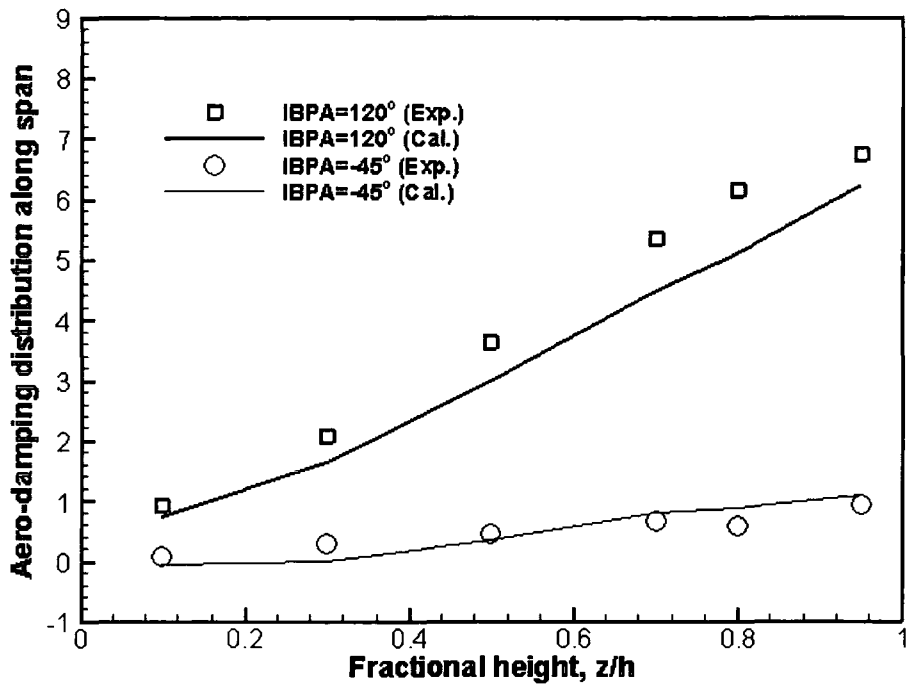


**Figure 5.32: Aerodynamic damping variation along blade span, $\xi_{span}$, $K$=0.6**

a marked deterioration in both the quantitative and qualitative level of agreement between the predicted and measured phase angle is observed on the suction surface for the least stable IBPA. For the most stable IBPA (120°), excellent correlation of the predictions to the test data was achieved at all sections on both the pressure surface and the suction surface in terms of both the amplitude and the phase angle of the first harmonic pressure, as shown in Figures 5.28 and 5.29. Although for the global damping prediction, shown in Figure 5.13, the biggest discrepancy between the predicted and measured values is observed at the most stable IBPA ($\sigma_0$=120°) of a reduced frequency of 0.6, the first harmonic pressure prediction at this case, shown in Figures 5.28 and 5.29, exhibits the same level of accuracy as others.

The predicted and measured variation in local aerodynamic damping along the blade span are presented in Figures 5.30 to 5.32 at the least and the most stable IBPAs for each reduced frequency. The local aerodynamic damping $\xi_{span}$ gives an aggregate indication of the quality of the amplitude and phase angle of the first harmonic pressure prediction at different spanwise sections. Clearly, these plots show excellent local aerodynamic damping predictions throughout all three reduced frequencies tested.

By comparison, a higher level of disparity between the predicted and measured first harmonic pressure is observed in areas towards the leading/trailing edges or near the wind tunnel endwalls. Not surprisingly, these areas coincide with those which have high experimental as well as computational modelling errors as discussed in Sections 3.3 and 5.1. Towards the leading edge, the unsteady response is highly sensitive to the incidence whilst error in the incidence setting can not be completely avoided. Towards the trailing edge, low signal-to-noise ratio is expected due to the low pressure activity. For the area near the cascade hub endwall, imperfect sealing does contribute some experimental errors. On the computational side, the disparity between the predicted and measured data towards the leading edge is partially attributable to the inaccurate geometry representation of the blade leading edge, since discrete points/grids are used in computation. The disparity towards the trailing edge on the suctions surface, where the flow is subject to high diffusion, relative high errors are expected in both experimental and computational results. In blade aeroelastic applications, it is typically not affordable to use meshes as fine as in turbomachinery performance predictions. This also affects the approximation level of a computational solution.

Overall, the predicted results presented above are characterised by good to excellent qualitative and quantitative agreement with the test data at different IBPAs throughout the reduced frequencies concerned in terms of amplitude of the first harmonic pressure, phase angle and both local and global aerodynamic damping. The computational solutions, with a high level of correlation with test data, corroborate the experimental findings on the one hand and act to validate the present flow solver on the other hand.

## 5.3 Summary

An experimental and computational study, concerning the aerodynamic response of a linear turbine cascade oscillating in a three-dimensional bending mode, is presented and discussed. The measurements were made at six spanwise sections covering 10% to 95% blade span. The steady pressure coefficient distributions reveal a predominant two-dimensional steady flow established in the cascade. Whilst the unsteady pressure



measurements demonstrate a strong three-dimensional behaviour of unsteady pressure response to the 3D blade oscillation.

The computational solutions presented were obtained from a three-dimensional, single-passage, time-marching, unsteady, Navier-Stokes flow solver. Good to excellent qualitative and quantitative agreement with the experimental data is achieved, which provides mutual validation between the experimental measurements and computational predictions.

To the author's knowledge, these are the first published three-dimensional CFD results of the kind which are supported by detailed three-dimensional cascade flutter experimental data for turbine blading.

# Chapter 6

# Influence of Upstream Stator on Rotor Flutter Stability

Conventional blade flutter predictions are normally based on an isolated blade row model, yet little is known about the influence of adjacent blade rows. In this chapter, an investigation is presented into the influence of the upstream stator row on the aeroelastic stability of rotor blades in the last stage of an LP steam turbine. It opens with a general description of the influence of the upstream stator on the rotor aeroelastic stability, followed by the numerical modelling aspects. The results are presented finally.

## 6.1 Description of Intra-Row Interaction

Conventionally, the intra-row interaction refers to the wake/blade row interaction and potential interaction, both of which are due to the relative motion of stator and rotor rows. Here, in particular, the intra-row interaction involves a different aspect: an acoustic wave (pressure wave) propagation phenomenon in a stator/rotor stage environment. The wave is originated by blade vibration. Once the rotor blades are excited mechanically or aerodynamically, the rotor blade vibration will give rise to unsteady flow disturbance, which will radiate away from the rotor in flow characteristics. These characteristics correspond to two pressure waves, one vorticity wave and one entropy wave. If the flow is subsonic, one pressure wave is running upstream and the other travelling downstream. The entropy and vorticity waves are always convected downstream by the local flow. The corresponding axial wave numbers (Smith, 1972) are:

$$\begin{aligned}\alpha_{1,2} &= \frac{\bar{u}_x(\omega_0 + \beta\bar{u}_\theta) \pm c\sqrt{(\omega_0 + \beta\bar{u}_\theta)^2 - (a^2 - \bar{u}_x^2)\beta^2}}{a^2 - \bar{u}_x^2} \\ \alpha_{3,4} &= \frac{\beta\bar{u}_\theta + \omega_0}{\bar{u}_x}\end{aligned} \tag{6.1}$$

where, $\beta = \sigma_0/(r \cdot G)$ is the circumferential wave number, $\bar{u}_x$ and $\bar{u}_\theta$ are the averaged flow velocities in axial and circumferential directions respectively, and $a$ is the speed of sound. In an isolated row model, the unsteady flow waves are often allowed to be resolved in a long domain or pass through the inlet/outlet boundary of a truncated domain transparently by adopting non-reflective far-field boundary conditions. In practice, due to the existence of the neighbouring blade rows, the wave propagations will be disturbed. What we are interested in particularly here is the upstream-running pressure wave, which will go through the stator-rotor intra row zone (with a gap distance of $\Delta X$), impinge on stator blades, be reflected back and result in additional unsteady loading on the rotor blades. As discussed above, the flow disturbance induced by the rotor vibration is periodic in time and can be expressed by a set of Fourier series, i.e. the fundamental harmonic plus higher harmonics. Furthermore, for a blade undergoing a harmonic structural vibration, only the fundamental harmonic component of unsteady pressure disturbance contributes to the aerodynamic damping (worksum). The fundamental harmonic of the unsteady pressure originated from the rotor vibration is in the form:

$$P_{orig}(t) = A_p \cdot \sin(\omega_0 t + \phi) \tag{6.2}$$

where $A_p$ is the original pressure disturbance amplitude and $\phi$ is the phase between the pressure disturbance and the vibration of the reference rotor blade. Then, the reflected pressure disturbance experienced by the rotor blade will have a form of

$$\begin{aligned}P_{refl} &= \alpha \cdot P_{orig}(t + \Delta T) \\ &= \alpha \cdot A_p \cdot \sin(\omega_0 t + \phi + \Delta\phi)\end{aligned} \tag{6.3}$$

where $\alpha$ is the reflection coefficient, and $\Delta\phi$ is the phase difference between the original disturbance and the reflected disturbance, which accounts for the time difference $\Delta T$ for the pressure wave to travel from the rotor to the stator and then back to the rotor.

$$\Delta\phi = \frac{\Delta T}{T} \cdot 2\pi \tag{6.4}$$

where $T$ is the vibration period. Roughly, the time $\Delta T$ may be approximated by

$$\Delta T = \frac{\Delta X}{a - \bar{u}_x} + \frac{\Delta X}{a + \bar{u}_x} \approx \frac{2\Delta X}{a} \tag{6.5}$$

Let the speed of sound be the reference velocity and rewrite the expression of the reduced frequency as

$$K = \frac{\omega_0 C}{a} \tag{6.6}$$

The rotor vibration period can be expressed as

$$T = \frac{2\pi C}{K \cdot a} \tag{6.7}$$

and we have

$$\Delta\phi = \frac{\Delta T}{T} \cdot 2\pi = 2K \cdot (\frac{\Delta X}{C}) \tag{6.8}$$

Then the work sum, an aeroelastic stability related parameter, can be evaluated

$$\begin{aligned} WorkSum &= W_{orig} + W_{refl} \\ &= W \cdot \sin(\phi) + W \cdot \alpha \cdot \sin(\phi + \Delta\phi) \end{aligned} \tag{6.9}$$

From Equation 6.9, the following observations can be made:

1. Depending on the reflection magnitude and phasing, the reflected pressure disturbance might contribute more to the total worksum than the original pressure disturbance. That means that the aeroelastic stability of the rotor in a stage can be completely different from that of an isolated rotor.

2. The contribution from reflected pressure disturbance can be positive or negative depending on the intra-row gap distance as well as the frequency. In other words, the presence of the stator can have stabilising or destabilising effects on the rotor at different intra-row gaps.

3. The work sum contributed by the reflected pressure disturbance has a sinusoidal trend as the intra-row gap changes. This non-monotonic variation suggests a possible optimum gap distances regarding the self-excited aeroelastic stability of the rotor.

## 6.2 Aerodynamic Work Calculation in Multiple-Disturbance Environment

In a flutter prediction under the influence of neighbouring blade rows, multiple disturbances are introduced into the unsteady flow. Although all disturbances contribute to the unsteady lift, on average, only the disturbance at the fundamental vibration frequency does aerodynamic work on the sinusoidally vibrating blades. There are two schemes to evaluate the aerodynamic work, hence the aerodynamic damping, in a time-marching flow solver. One is utilising the original pressure and vibration history to compute the aerodynamic work in one beating period $T_b$, which is the minimal common multiple of all disturbance periods.

$$W = \frac{1}{N_0} \int_{T_b} P \cdot V_{blade} dt \tag{6.10}$$

where $N_0$ is the number of periods of the disturbance at the vibration frequency in one beating period $T_b$. The other is decomposing the original pressure (Figure 6.1) and using its component $P_0$ at the fundamental vibration frequency to calculate the aerodynamic work in one vibration period $T_0$.

$$W = \int_{T_0} P_0 \cdot V_{blade} dt \tag{6.11}$$

The former one is straightforward and can be easily implemented. However, in an engineering application with arbitrary blade vibration frequencies, a time-dependent computation might take a long time to reach a beating period. So, the latter procedure is pursued. In this procedure, the Fourier transform plays a key role again. The time-dependent pressure $P(t)$ can be expressed as a time-averaged part $\bar{P}$ and a summation of a number ($N_{pt}$) of time-dependent perturbations, whilst each perturbation $P_i$ can be expressed as a set of Fourier series in time:

$$\begin{aligned} P(t) &= \bar{P} + \sum_{i=1}^{N_{pt}} P_i(t) \\ &= \bar{P} + \sum_{i=1}^{N_{pt}} \sum_{n=1}^{N_{fou}} (A_{n,i} \sin(n\omega_i t) + B_{n,i} \cos(n\omega_i t)) \end{aligned} \tag{6.12}$$

where $A_n$ and $B_n$ are the Fourier coefficients and $N_{fou}$ the order of the Fourier series. From the time-marching solver, we store the converged blade surface pressure history

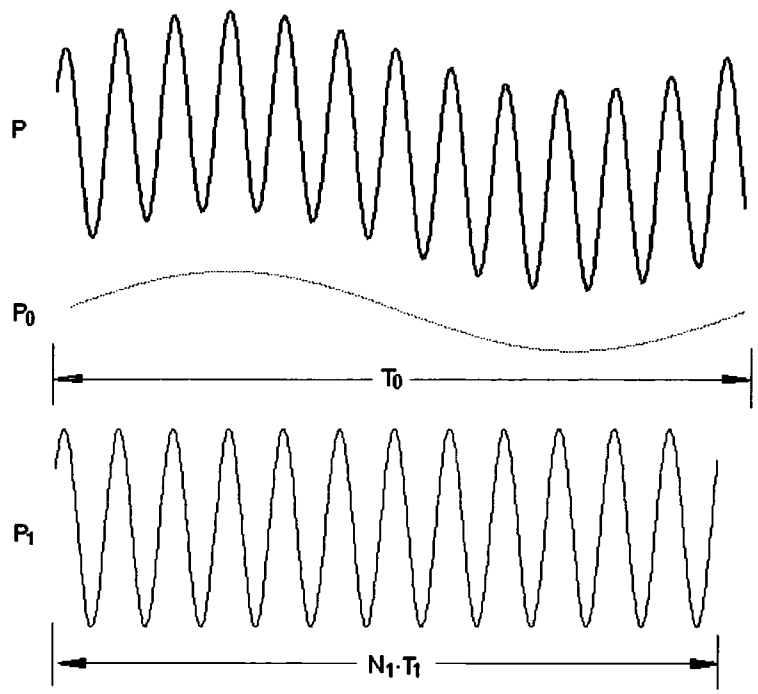


**Figure 6.1: Pressure signal decomposition**

for one stored period $T_{store}$ (the longest period of all disturbances). The remaining concern is how to integrate the Fourier coefficients using the data of a stored period rather than a beating period. Here, we adopt the partial-substitution technique, which has been successfully implemented in the present single-passage flow solver (see Chapter 4).

$$A_{ni} = \frac{\omega_i}{N_i \pi} \int_{N_i T_i} (P - R_i) \sin(n\omega_i t)\, dt \tag{6.13}$$

$$B_{ni} = \frac{\omega_i}{N_i \pi} \int_{N_i T_i} (P - R_i) \cos(n\omega_i t)\, dt \tag{6.14}$$

where $R_i = \sum_{j \neq 1}^{N_{pt}} \sum_{n=1}^{N_{fou}} [A_{n,j} \sin(n\omega_j t) + B_{n,j} \cos(n\omega_j t)]$ is the contribution of all perturbations except that from the $i^{th}$ and $N_i$ is the integer number of periods of the $i^{th}$ pressure perturbation in a stored period. From any initial values of Fourier coefficients, $A_n$ and $B_n$ can be updated once through an integration using Equations 6.13 and 6.14. Converged values of $A_n$ and $B_n$ are obtained by repeating this integration procedure a certain number times. Once the pressure component of the fundamental vibration frequency is obtained, the aerodynamic work can be evaluated by following

a routine integration (Equation 6.11). This damping calculation is entirely a post-processing procedure and does not represent a significant overhead in terms of CPU time.

## 6.3 Results and Discussion

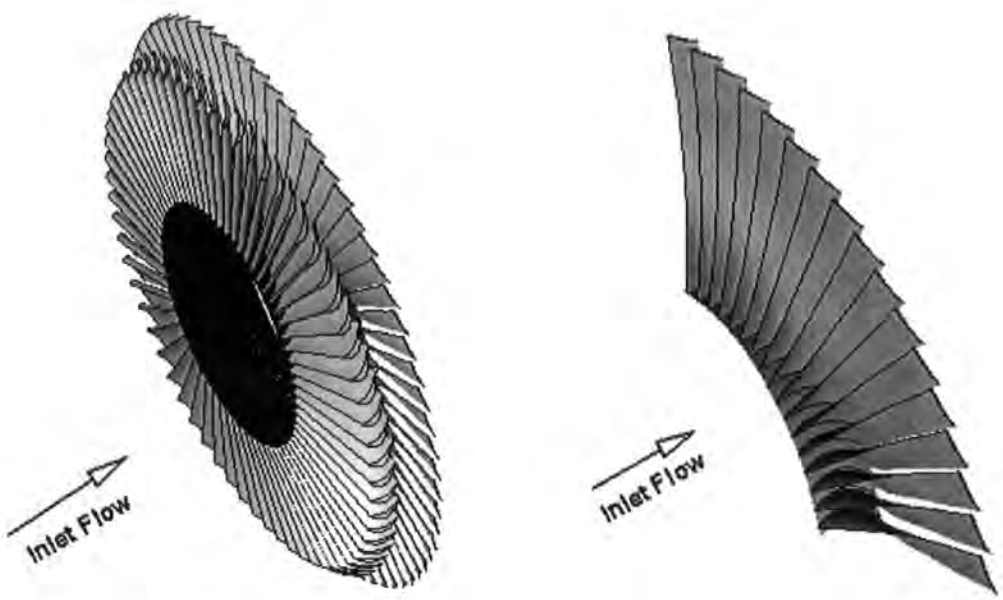


(a) Stage (b) A close-up view of rotor

**Figure 6.2: Model LP stage**

A hypothetical last stage of an LP steam turbine is used for the present work. The stage consists of 66 stator blades and 68 rotor blades. The rotor has a slender tip section and is fitted with a tip shroud (Figure 6.2, the tip shroud is not included). This LP stage has a realistic geometry and the boundary conditions are configured for realistic operating conditions in an LP steam turbine. The one dimensional exit velocity at rotor trailing edge is in the region of 200 m/s and the relative exit Mach number at the tip is around 1.5. For the rotor flutter analysis the first flap mode is considered, because this mode has frequencies in the critical range of reduced frequency.

The vibrating mode shape and frequency for the rotor blades are obtained from a standard FE analysis. For convenience, the mode shape is approximated as a solid body vibration with three components (i.e. torsion, axial flap and tangential flap), which are specified along the blade span. Although not presented here, it should be mentioned that the steady base flow predictions compare favourably with those obtained from ALSTOM Powers in-house CFD codes. In this section, results are first presented for a parametric investigation on a two dimensional geometry, extracted at the tip of the three dimensional configuration. The results for the complete three dimensional stage configuration are then presented.

### 6.3.1 Two-Dimensional Case

As previously discussed, the influence of the upstream stator is closely related to the intra-row gap distance. In this section, the intra-row gap effects are examined systematically, using a contrived two-dimensional computational domain. This was composed of the tip section of the stator and rotor blade, located on a constant radius and in a stream tube with constant thickness. Due to the different radius of the stator and rotor tip sections in the three-dimensional model, the stator blade was re-staggered in the two-dimensional model, to produce appropriate flow conditions at inlet to the rotor (incidence and Mach number).

Although it is much less expensive to perform parametric investigations using a two-dimensional model, the main reason to adopt this simplified model is that it is not possible to vary the intra-row spacing in the three-dimensional case without completely changing the steady flow aerodynamics. This is because of the high flare angle on the outer casing, shown in Figure 6.7, which is characteristic of an LP steam turbine cylinder. A computational mesh for the simplified two-dimensional model is shown in Figure 6.3, at an intra-row gap of 0.4 rotor chord lengths. In this mesh, $125 \times 31$ grid points are used for the rotor domain and $108 \times 31$ for the stator. As the intra-row gap increases, more axial mesh nodes were inserted in the stator domain, such that the spatial mesh density remains unchanged.

Computations were performed for both forward and backward travelling waves at four

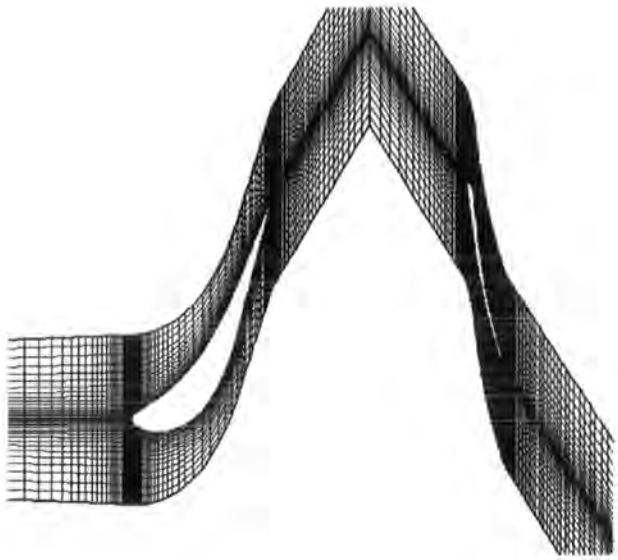

**Figure 6.3: Stator-rotor computational mesh (2D tip section)**

**Table 6.1: Natural frequency & mode-shape (2D tip section)**

| ND | Frequency (cycles/rev) | Amplitudes (torsion/components of flap) | | Phase angles (difference between torsion & flap) | |
|---|---|---|---|---|---|
| | | $A_{xx}/(A_{xto} \times C)$ | $A_{xx}/A_{x\theta}$ | $\phi_x - \phi_{to}$ (degrees) | $\phi_x - \phi_\theta$ (degrees) |
| 5 | 2.440 | 1.996 | 14.289 | 97.13 | -103.631 |
| 8 | 2.465 | 1.229 | 36.735 | 95.82 | -98.056 |
| 11 | 2.580 | 0.861 | 28.966 | 95.57 | 89.871 |
| 20 | 4.860 | 0.373 | 27.264 | 97.01 | 97.727 |

*(Frequency, amplitude and phase angle for backward travelling waves)*
*(Forward travelling waves can be obtained by changing the sign on all phase angles, including IBPA)*

different NDs in the first flap mode. The frequency and mode-shape for the backward travelling wave in each nodal diameter pattern is provided in Table 6.1. As shown in this table, the component of tangential flap in this highly staggered tip section is very small at all NDs. It is interesting, however, that the amplitude of torsion in this so-called "first flap" mode is of comparable magnitude to the amplitude of axial flap (see the ratio $A_{xx}/(A_{xto} \times C)$ in Table 6.1). In fact, as the ND increases, the amplitude of torsion increases, such that it becomes the most dominant component of

vibration above 8 NDs. It is also important to note that the phase angle between the torsional and axial flap components of vibration is non-zero, and approximately 95° for all backward travelling waves, and −95° for the forward travelling counterparts. These trends in the torsional component of vibration, relative to the axial flap, are associated with the tip shroud. The mode is essentially an axial flap, however, as the blades flap, torsion is introduced at an appropriate phase and amplitude to enable the tip shroud to remain interlocking. In further contrast to the vibration of free standing turbine blades in first flap, the presence of the tip shroud causes the frequency of the natural modes of vibration to increase with the ND, because of the trends in mode shape with the ND already described. This is reflected by the increase in natural frequency with the ND shown in Table 6.1.

#### 6.3.1.1 Validation of the Single Passage Solver

It is impossible to fully validate the present solver directly against experimental data, due to the absence of published unsteady loading measurements on oscillating blades embedded in a multi-row configuration. In order to verify the validity of the solver, an appropriate combination of component validation and code-to-code comparisons has therefore been performed. The capability of the multi-row, multi-passage, baseline solver to predict the aerodynamic response to blade-row interaction and blade oscillation has been verified against experimental data in He (2000). Furthermore, the single-passage methodology has been validated in an isolated row against a semi-analytical solution of Namba (He and Denton, 1994) and the linear turbine cascade data previously presented in Chapter 5. Here, a comparison is made between a single-passage and multiple-passage solution. This comparative study is expected to serve a validation purpose for the multi-row single-passage method. Figure 6.4 shows the normalised spectra of the unsteady rotor axial forces for the 20 ND backward travelling wave mode at an intra-row gap of 40 % chord. This mode is chosen simply because it has a higher vibration frequency and requires less computational time. Compared to the multiple-passage solution, the single-passage method under-predicts the aerodynamic damping by 2.4% (Figure 6.4 indicates 4.3% difference for the vibration induced force component). This discrepancy in the damping calculation is considered acceptable,

and demonstrates that the present Shape-Correction based, single-passage, method is capable of dealing with multiple disturbances in a stage configuration. A speed-up of 13 times is also achieved by the single-passage solution over the multiple-passage solution (33 passages for the stator and 34 passages for the rotor). If the whole annulus domain were used for the multiple-passage solution, the speed-up delivered by the single passage method would be doubled to a factor of 25.

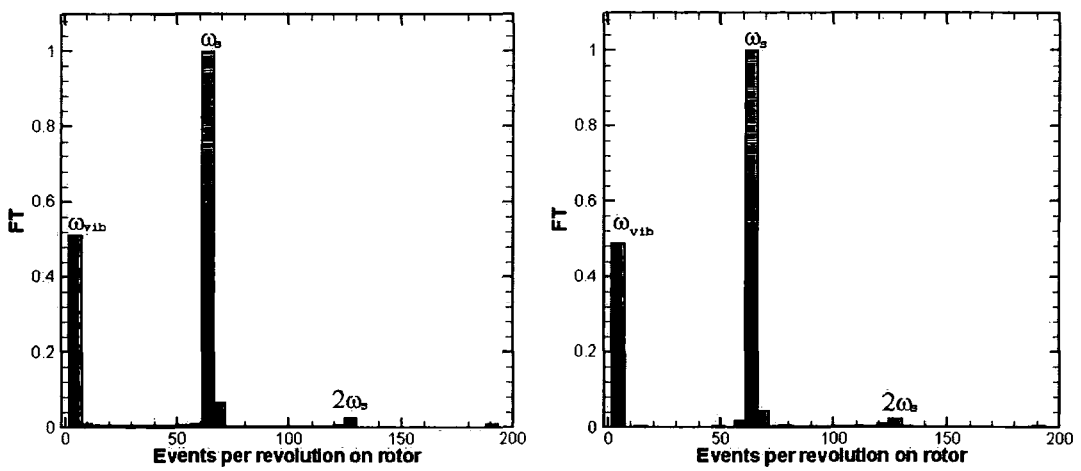


(a) Multiple-passage

(b) Single-passage

**Figure 6.4: Spectra of unsteady axial forces on the rotor**
($\omega_{vib}$–vibration frequency, $\omega_s$–stator blade passing frequency)

Furthermore, by examining the spectra of unsteady rotor axial forces, two points are demonstrated. First, the unsteadiness is dominated by its fundamental harmonic. Second, the nonlinear interaction between the fundamental disturbances is negligible in the present case. These indicate that a set of Fourier series with an order of as low as one should be sufficient.

#### 6.3.1.2 Overview of 2D Predictions

The results of the 2D predictions are shown in Figures 6.5 and 6.6, and summarised in Tables 6.2 and 6.3. Before the influence of the intra-row gap effect is considered, there are some general trends in the results that are worthy of comment and explanation. Firstly, all predictions for forward travelling waves indicate a stable aeroelastic condition, whereas for backward travelling waves an unstable condition is predicted (in the

absence of material damping). These contrasting results are associated with the change in phase angle between torsion and axial flap in the forward travelling wave compared to the backward counterpart. In the forward travelling wave, the phase difference between torsions and axial flap is around $-95°$, whereas for the backward travelling wave it is $+95°$. On consideration, these observations suggest that it is the cross coupling of the unsteady flow induced by one component of vibration doing work to the other component of vibration, or vice-versa, by virtue of the phase difference between each component of vibration.

It is also interesting to note from Tables 6.2 and 6.3, that the absolute magnitude of log-dec (isolated row prediction) tends to increase with nodal diameter up to at least the 11 nodal diameter pattern. This is associated with the increasing magnitude of the torsional component of vibration through these cases (Table 6.1). At 20 nodal diameters, the absolute magnitude of log-dec then falls for both forward and backward travelling waves. There are two reasons for this. First, the frequency of this nodal diameter is considerably higher than the others (Table 6.1), so the strain energy in the vibration is much higher and therefore the log-dec is reduced. Second, the increased frequency results in an increase in reduced frequency, which tends to have a stabilising effect.

#### 6.3.1.3 Intra-Row Gap Effects (2D)

To study the gap effects, for each nodal diameter, the stage predictions are presented over a range of intra-row gaps (from 0.40 to 1.41 rotor chord lengths) and then compared with the isolated rotor prediction. The variation of intra-row gap considered here represents a practical range for the stator-rotor gap in the last stage of an LP steam turbine. Figure 6.5 shows the predicted log-dec of both the stage and the isolated rotor for forward travelling wave modes (all being stable with positive log-dec). Table 6.2 shows a summary of the results for these forward travelling waves. These results confirm those observations from Equation 6.9. The reason for the lack of sinusoid variations for 5, 8 and 11 ND modes might be that their wavelength is much longer than the range in intra-row gap considered here, i.e. one rotor chord. On the other hand, the wavelength for the 20 ND mode is relatively short and the log-dec variation

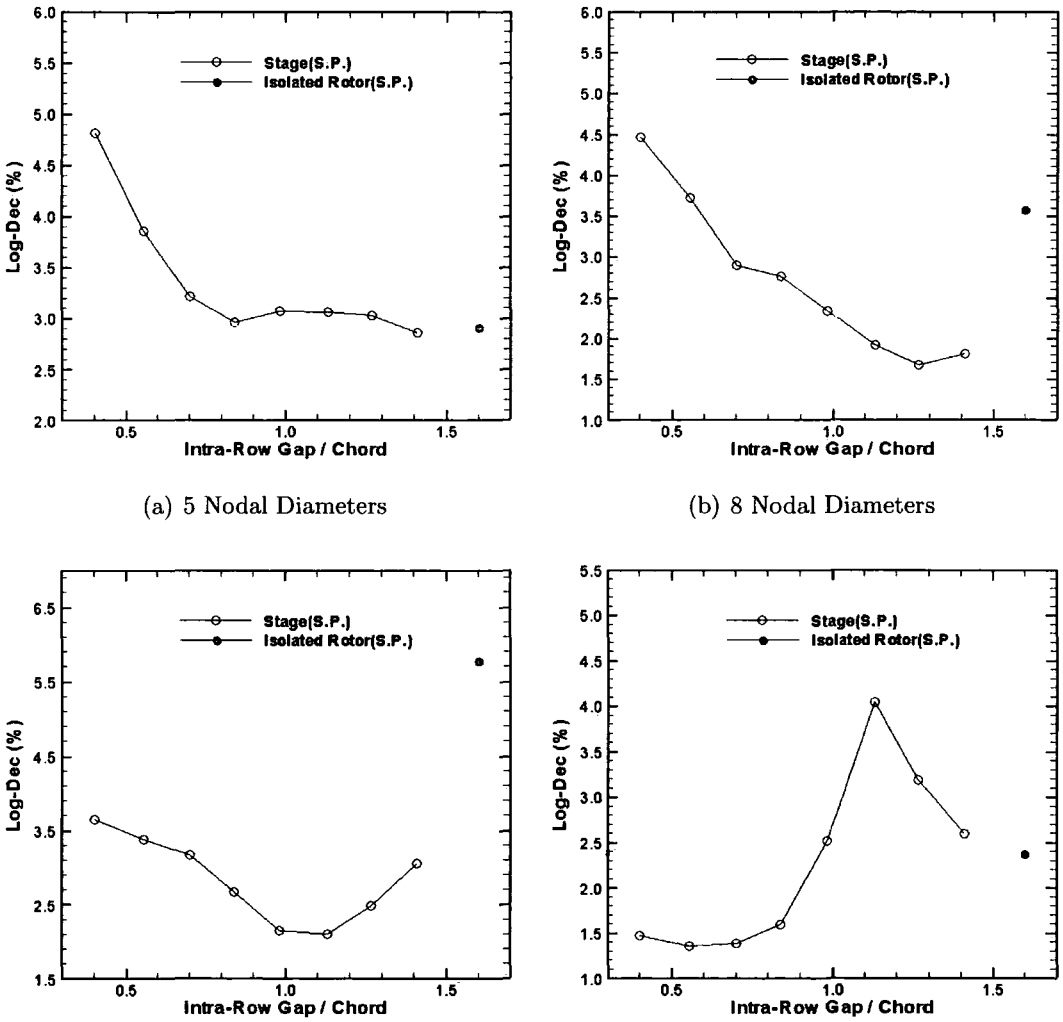


(a) 5 Nodal Diameters

(b) 8 Nodal Diameters

(c) 11 Nodal Diameters

(d) 20 Nodal Diameters

**Figure 6.5: Forward travelling wave modes**

**Table 6.2: Summary for the forward travelling wave modes**

| ND | Isolated row prediction Log-dec($10^{-2}$) | Stage prediction (Log-dec) | | |
|---|---|---|---|---|
| | | Max.($10^{-2}$) | Min.($10^{-2}$) | Variation range /Isolated row |
| 5 | 2.907 | 4.814 | 2.861 | 67.18% |
| 8 | 3.571 | 4.463 | 1.807 | 74.38% |
| 11 | 5.778 | 3.648 | 2.140 | 26.10% |
| 20 | 2.379 | 4.044 | 1.361 | 112.78% |

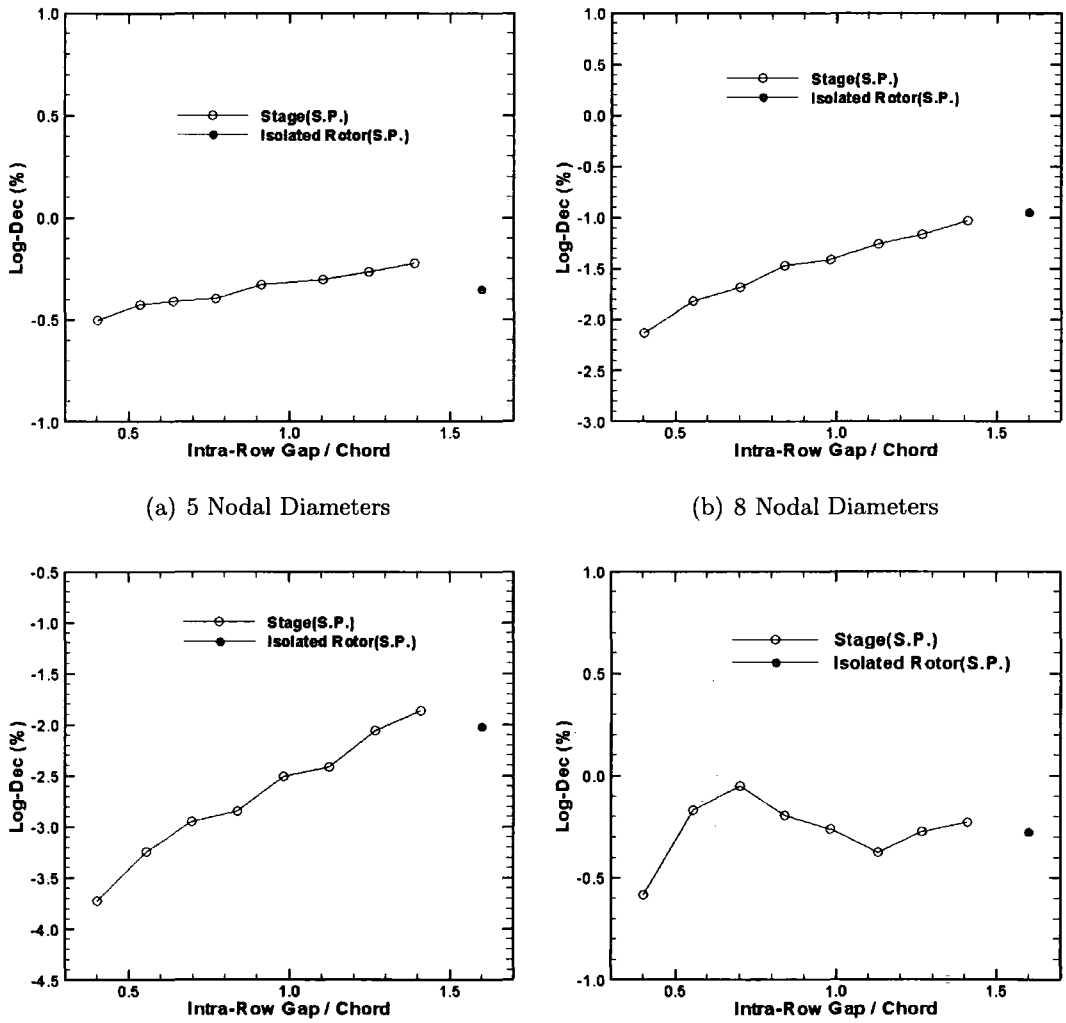


(a) 5 Nodal Diameters

(b) 8 Nodal Diameters

(c) 11 Nodal Diameters

(d) 20 Nodal Diameters

**Figure 6.6: Backward travelling wave modes**

**Table 6.3: Summary for the backward travelling wave modes**

| ND | Isolated row prediction Log-dec($10^{-2}$) | Stage prediction (Log-dec) | | |
|---|---|---|---|---|
| | | Max.($10^{-2}$) | Min.($10^{-2}$) | Variation range /Isolated row |
| 5 | -0.351 | -0.222 | -0.505 | 80.63% |
| 8 | -0.946 | -1.029 | -2.129 | 116.28% |
| 11 | -2.021 | -1.868 | -3.725 | 91.89% |
| 20 | -0.273 | -0.192 | -0.586 | 144.32% |

shows a variation more like to a sinusoidal curve.

Figure 6.6 presents the results for the backward travelling wave modes and Table 6.3 is the corresponding summary (all unstable). For the 5 ND backward travelling wave mode, the absolute log-dec variation over the concerned gap range is relatively small compared to its forward travelling counterpart. This does not mean that the influence of upstream fixed blades is small for the 5 ND backward travelling wave mode. The absolute variation is more associated with the original disturbance amplitude, while the relative change just reflects the influence of upstream fixed blades. From Table 6.3, it is shown that the relative change for the 5 ND backward travelling wave mode is still very big. From an engineering point of view, only the least stable mode is of interest in the aeroelastic analysis. Here the 11 ND backward travelling wave mode is the least stable one and both the absolute and relative changes due to the gap distance variation are very considerable. Note that the presence of upstream fixed blades can significantly change the aerodynamic damping of the least stable mode in both an absolute and relative sense.

For the 20 ND backward travelling wave mode, the influence of the upstream stator blades diminishes exponentially as the intra-row gap increases, while its forward travelling wave counterpart does not. This may be because the acoustic pressure waves tend to be cut-on for the forward mode and cut-off for the backward one. Actually, all forward travelling wave modes are cut-on and all backward travelling wave modes are cut-off in the present study (the cut-off waves have complex axial wave numbers, which are obtained by Equation 6.1, while the real axial wave numbers correspond to the cut-on waves). Cut-on waves will propagate un-attenuated, while the cut-off waves' amplitude will decay exponentially as a function the propagation distance and the wavelength. Even for cut-off modes, this attenuation effect will not obviously show up if the concerned gap variation is much shorter than the wavelength. This is the case for the 5, 8 and 11 ND backward travelling wave modes. Overall, the change of aerodynamic damping value by more 100% with the intra-row gap is of considerable engineering significance.

### 6.3.2 Three-Dimensional Stage

Given the significant dependence of flutter stability on the intra-row gap in the two-dimensional configuration, it is naturally of interest to see if one can identify a similar influence in a realistic 3D configuration. The full three-dimensional stage was therefore analysed, using the computational mesh shown in Figure 6.7. In this case, $117 \times 41 \times 51$ mesh nodes are used for the stator domain and $125 \times 41 \times 51$ nodes for the rotor. In order to identify the influence of the intra-row gap for this 3D configuration, baseline computations were obtained for the rotor in isolation, for comparison of aeroelastic stability, i.e. log-dec.

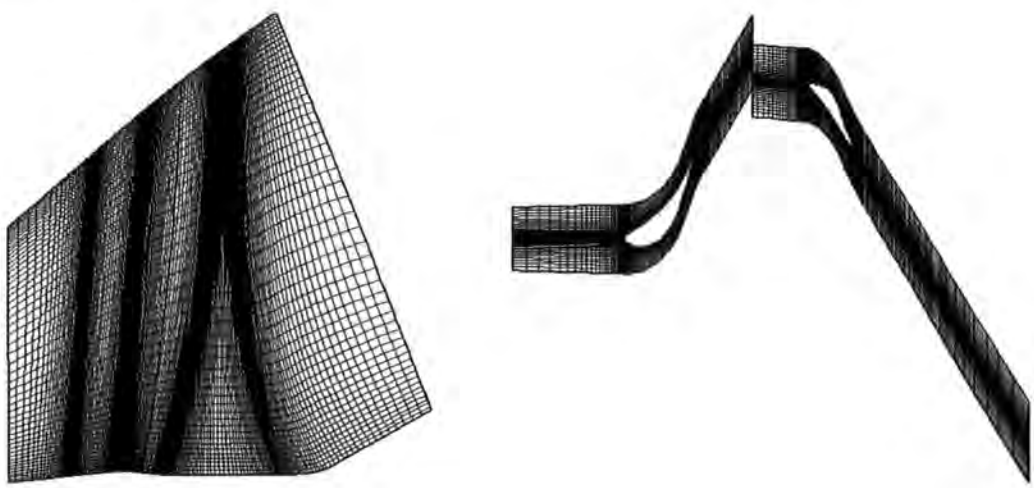

(a) Meridional View at Mid-Passage (b) Blade-Blade View at Mid-Span

**Figure 6.7: Computational mesh for the 3D LP steam turbine stage**

The computations were first performed on the isolated rotor in order to identify the most unstable aeroelastic condition, which was found to be the backward travelling wave at 11 NDs. This mode was therefore selected for additional modelling in the complete stator-rotor coupled stage configuration. Table 6.4 shows the predicted stability in this mode of vibration, in terms of Log-Dec, for both the stage and isolated rotor computations. The results show that the acoustic reflection from the upstream stator blade row leads to a 35% change in the Log-Dec, which is clearly significant.

In contrast to the 2D predictions of the backward travelling wave at 11 ND (Figure 6.6c), where the rotor is predicted to be less stable in the stage configuration, in the 3D case, the presence of the stator blade row makes the rotor considerably more stable.

**Table 6.4: 3D Predictions of Log-Dec ($\xi$)**

| Isolated Rotor Prediction ($\xi_0$) | Stage Prediction ($\xi_1$) | Relative difference ($\frac{\xi_1 - \xi_0}{\lvert\xi_0\rvert}$) |
|---|---|---|
| -1.265% | -0.819% | +35.3% |

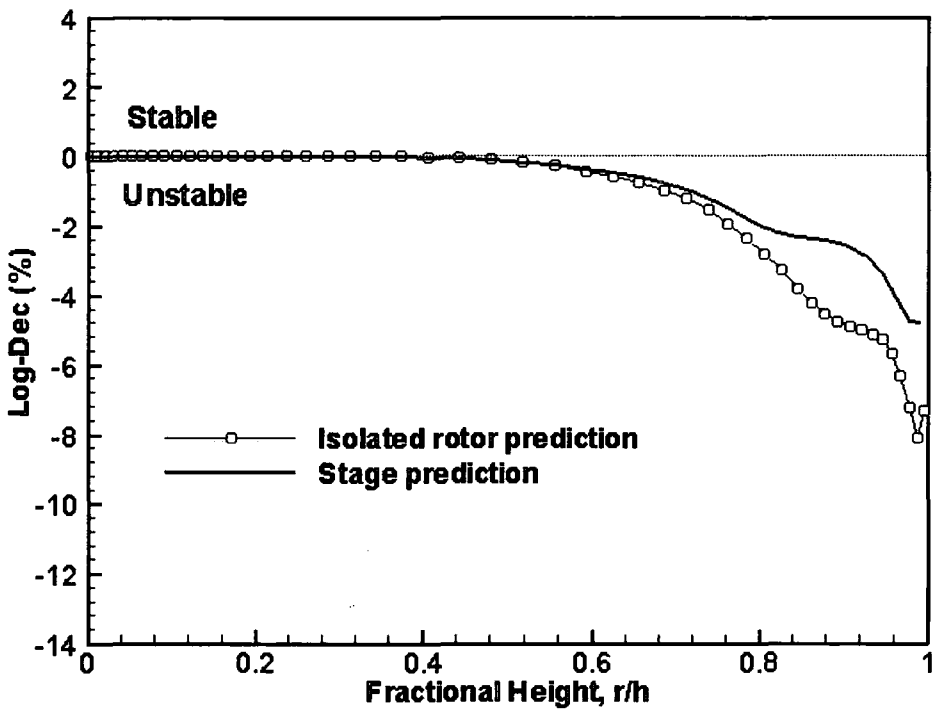


**Figure 6.8: Predicted spanwise variation in local Loc-Dec for staged rotor and isolated rotor, 11 ND backward travelling wave mode**

These opposing trends from the 2D and 3D predictions, therefore suggest that the pressure wave propagation is of a strong three-dimensional nature.

## 6.4 Summary

In this chapter, a multi-row, single-passage, Navier-Stokes, flow solver has been validated and applied to rotor blade flutter analysis in an LP steam turbine stage. The parametric study of the influence of intra-row interaction on the rotor aeroelastic stability in the modified two-dimensional tip section reveals up to 144% damping variation with respect to the intr-row gap change from 0.4 to 1.4 rotor chord length. The 3D stage prediction shows a more stable condition by 35.3% in terms of Log-Dec than the isolated rotor analysis.

# Chapter 7

# Influence of Tip Clearance on Oscillating Blade Flow

Due to mechanical constraint, there is always a gap between the outer casing and rotating blades. The tip clearance flow is, therefore, one of the most prevalent phenomena in unshrouded axial turbomachines. The driving mechanism behind the tip clearance flow is believed to be the pressure difference between the pressure and suction sides of the blade tip. The tip clearance flow is characterised by a strong jet discharging into the main passage flow and usually rolls up a streamwise vortex. The detrimental nature of the tip clearance flow on the turbomachinery aerothermal performance has been documented extensively (Denton, 1993; Sjolander, 1997). In aeroelastic applications, however, very limited understanding of the influence of tip clearance on blade flutter has been obtained so far.

## 7.1 Experimental Investigation

### 7.1.1 Experimental Setup

A series of experiments were conducted at three different settings of tip clearance ($1.25\%C$, $2.5\%C$ and $5\%C$) in the linear turbine cascade described in Chapter 3. Figure 7.1 shows a schematic of the blade tip clearance setting. For all tip clearance settings, the distance between hub and tip endwalls is held constant. On the hub endwall, slots are located to allow the blades to be translated through the hub endwall, in order to vary the tip clearance. With the translation of the oscillating blade, the hinge is

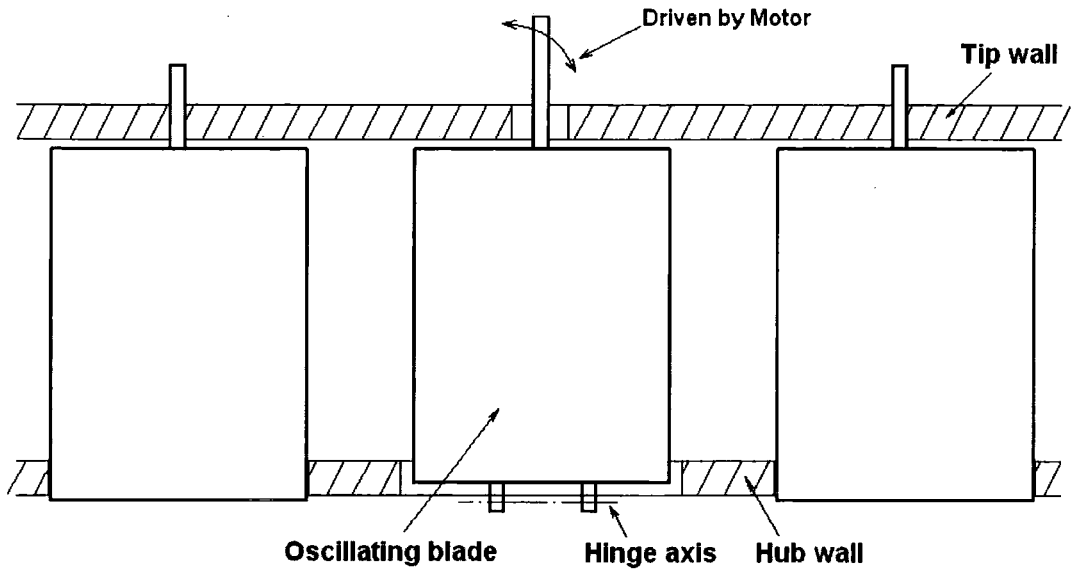


**Figure 7.1: Schematic of the blade tip clearance setting**

shifted away from the hub endwall by the same amount of distance. Therefore, the bending amplitude along the oscillating blade is unchanged. In this kind of tip clearance arrangement, it should be observed that the exact blade height is different from one setting of tip clearance to another. At this point, it is also worthy of mention that the tip clearance is arranged to all blades rather than only the oscillating blade in the cascade. Because the same instrumented blades are employed for the measurements at different tip clearance settings, the exact fractional height of measuring sections are also different from one setting to another. For example, the 95% span for zero tip clearance corresponds to 94.95%, 94.90% and 94.79% span for 1.25%$C$, 2.5%$C$ and 5%$C$ tip clearance respectively. To avoid confusion, the measuring sections will be referred to only by its fractional height at zero tip clearance.

### 7.1.2 Steady Flow

The steady flow measurements were aimed at providing a general aerodynamic background for the unsteady flow measurements and identifying the relevant natures of the steady tip clearance flow which may affect the blade aeroelastic behaviour.

It has been revealed that the steady flow through the linear cascade is largely of two-

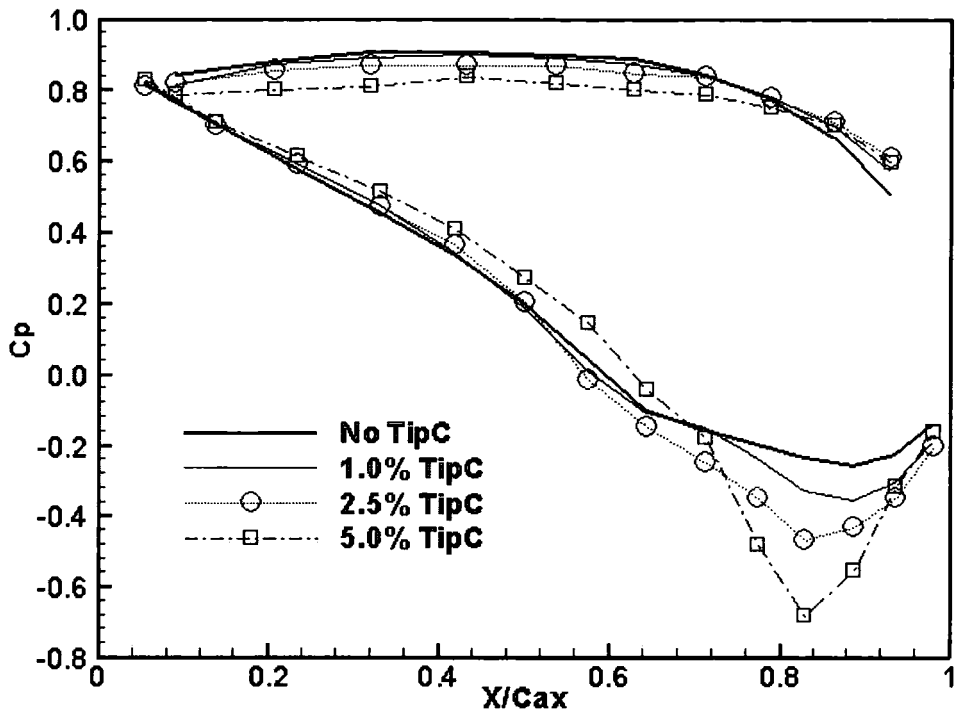


**Figure 7.2: Steady pressure distribution with different tip clearances at 95% span**

dimensional nature if there is no tip clearance (Figures 5.1 to 5.3). That is to say, the tip clearance is the only major source of three-dimensional flow which affects the steady blade pressure distribution. With the pressure tappings located close to the tip at a section of 95% span, the change of steady blade pressure induced by the tip clearance flow can be readily identified, locally in the blade tip region. Figure 7.2 shows the variation of measured steady blade pressure at 95% span section of the middle blade, with zero, 1.25%$C$, 2.5%$C$ and 5%$C$ tip clearances. When tip clearance is present, an unloading in the fore chord part of the suction surface and a reloading towards the rear are clearly observed at 95% span. On the pressure surface, the unloading manifests itself in lower pressure coefficient and reloading higher pressure coefficient, whilst on the suction surface, the trend for pressure coefficient change for unloading and reloading is reversed. When the size of tip clearance is increased, the strengths of unloading and reloading are accordingly increased. The marked, but consistent, change in the blade steady loading with regard to the tip clearance provides a sound environment to examine the influence of the tip clearance flow on the unsteady aerodynamic response of

the oscillating cascade. As will be seen later, the local loading redistribution associated with the tip clearance vortex in the steady flow will have a significant bearing in the local unsteady flow and aeroelastic stability.

### 7.1.3 Unsteady Results

Unsteady measurements directed at examining the influence of the tip clearance flow on the blade aeroelastic behaviour were performed at a reduced frequency of 0.4. At this reduced frequency, the most unstable IBPA has been identified to be around $-60°$. The influence of the tip clearance flow on the blade aeroelastic stability at this particular IBPA is assessed and presented, although the unsteady results at any value of IBPA for the tuned cascade can be obtained from one set of influence coefficient measurements. This is because blade flutter only occurs at the most unstable IBPA.

#### 7.1.3.1 Unsteady Pressure

Figure 7.3 shows the amplitude of the first harmonic pressure at 95% span for an IBPA of $-60°$ at the reduced frequency 0.4, and Figure 7.4 the corresponding phase angle. Differences in the amplitude of the first harmonic pressure are evident at 95% span on both suction and pressure surfaces for different tip settings. Comparing to the zero tip clearance case, decreased unsteady pressure amplitude in the fore chord region (up to $45\%C_{ax}$) is observed for three tip clearance settings, followed by a region of largely increased unsteady pressure amplitude ($45\%C_{ax}$-$98\%C_{ax}$), although slightly decreased pressure amplitude appears around $75\%C_{ax}$ for the tip clearance setting of $1.25\%C$. The decrease in unsteady pressure amplitude in the fore chord region is believed to be associated with the steady unloading on the suction surface, whilst the activity after $45\%C_{ax}$ can be attributed to the steady reloading induced by the tip clearance vortex. The rather erratic changes in amplitude of the tip clearance of $5\%C$ highly reflect a flow separation, on which a further observation from the phase angle will be made (Figure 7.4b). On pressure surface, shown in Figure 7.3a, the amplitude of the first harmonic pressure decreases as the tip clearance increases for the region from $65\%C_{ax}$ to the trailing edge. This region corresponds to the steady reloading towards the trailing edge on the pressure surface. On the fore chord ($15\%C_{ax}$-$65\%C_{ax}$), where a

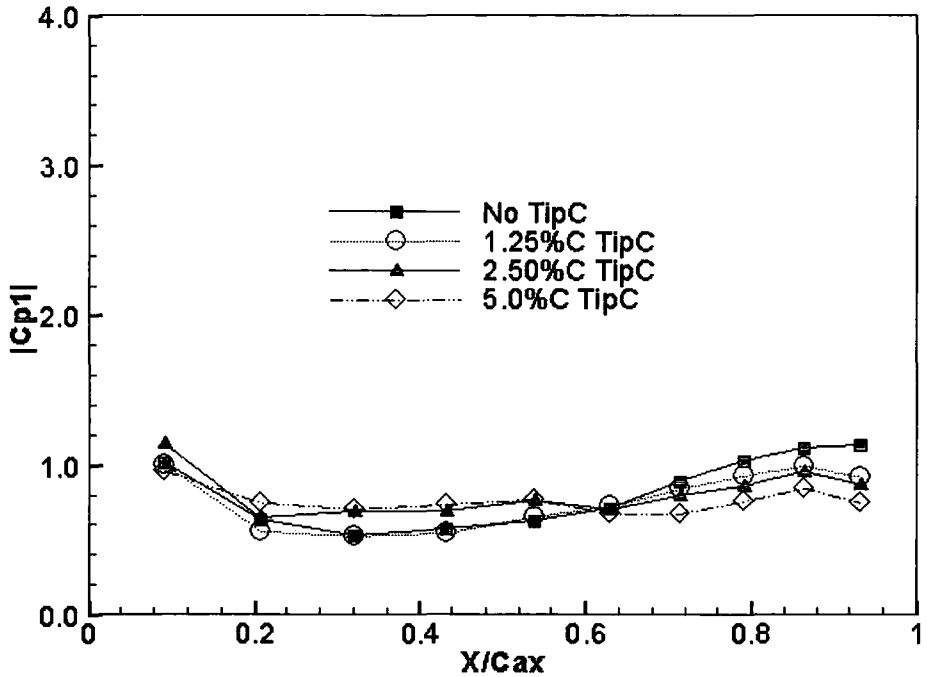


(a) Pressure surface

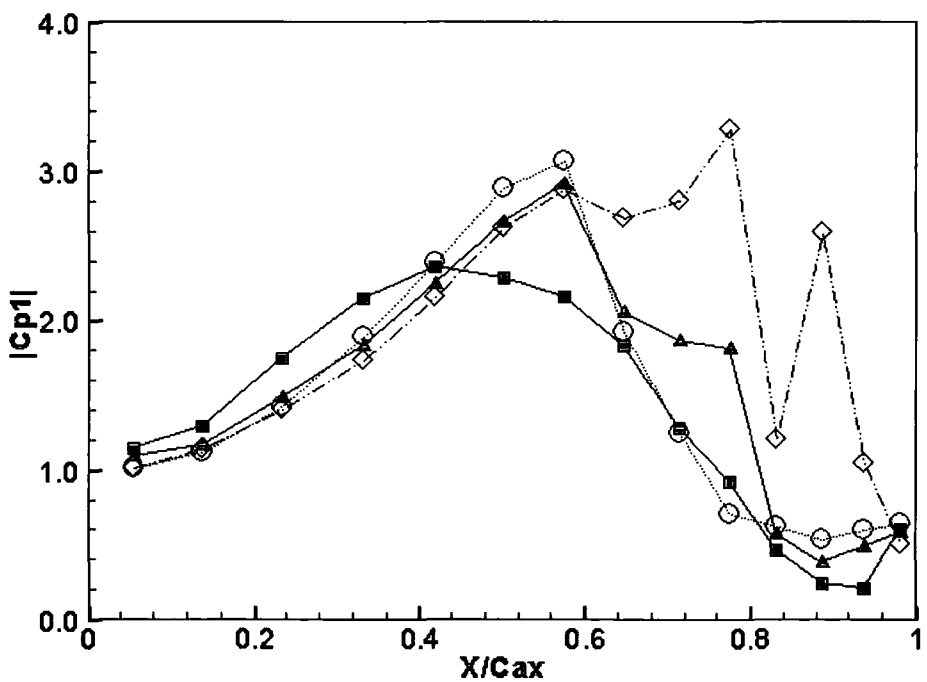


(b) Suction surface

**Figure 7.3: Amplitude of first harmonic pressure at 95% span ($K$=0.4, $\sigma_0$=−60°)**

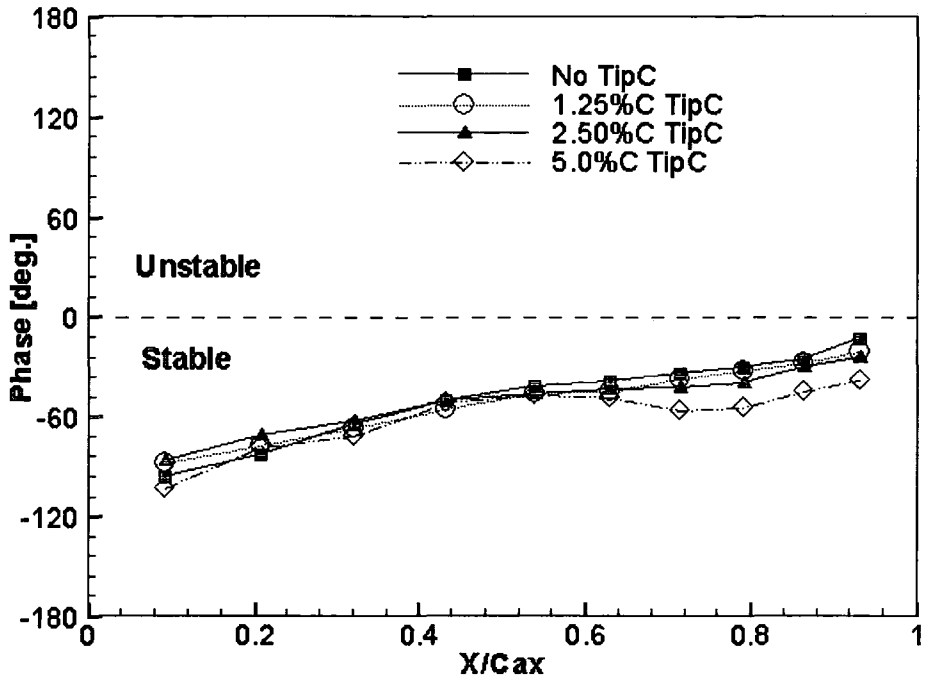


(a) Pressure surface

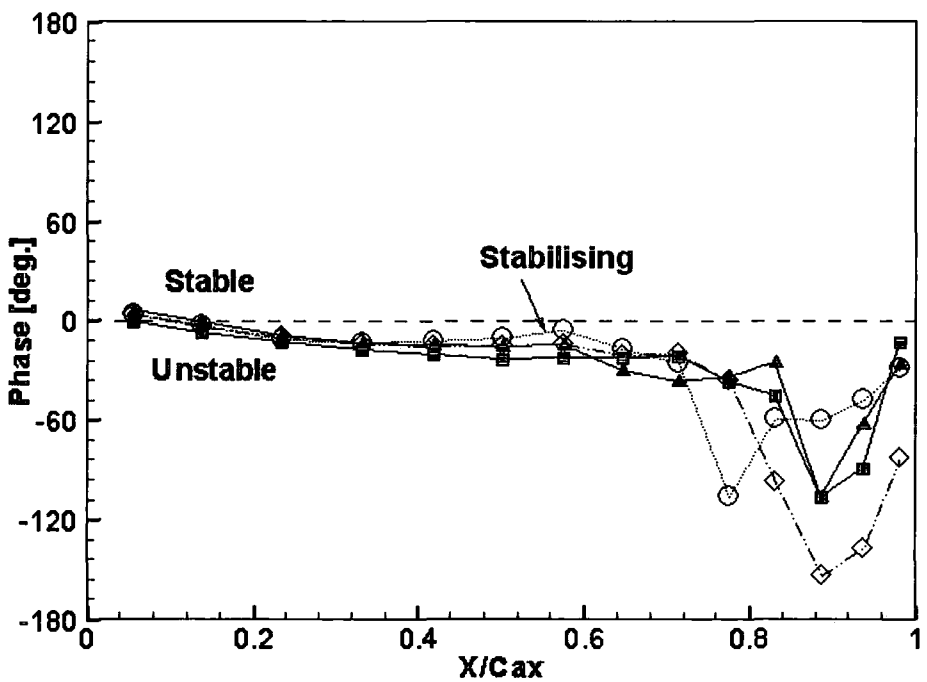


(b) Suction surface

**Figure 7.4: Phase angle of first harmonic pressure at 95% span ($K$=0.4, $\sigma_0$=−60°)**

steady unloading appears, a bigger amplitude is observed for the tip clearance settings of 2.5%$C$ and 5%$C$, while the amplitude of the tip clearance of 1.25%$C$ hardly differs from that of the zero tip clearance.

The phase angle distributions of the first harmonic pressure at 95% span on the suction surface for four tip clearance settings is provided in Figure 7.4b. The phase angles are almost identical for all four tip clearance settings upstream of 40%$C_{ax}$. Around mid-chord, the phase angle shifts towards 0° for three non-zero tip clearance settings comparing to the nominal setting although this shift is not proportional to the size of the tip clearance. Indeed, the tip clearance setting of 1.25%$C$ has the biggest phase angle shift in this region. For the region towards the trailing edge, the biggest phase angle change for the tip clearance setting of 5%$C$ indicates the biggest separation event happening among these four settings. On pressure surface (Figure 7.4a), the unsteady response shows increased phase lag when the tip clearance increases for the rear half chord. On the fore half chord, decreased phase lag is seen for tip clearances of 1.25%$C$ and 2.5%$C$, whilst not much difference can be told for the tip clearance of 5%$C$. Relatively, the unsteady pressure response induced by the tip clearance flow is concentrated on the suction surface.

#### 7.1.3.2 Aerodynamic Damping

Figure 7.5 presents the local aerodynamic damping distribution at the reduced frequency 0.4 and the IBPA of $-60°$ for four tip clearance settings. The main regions of activity associated with the tip clearance flow are located above 50% span, most especially in the outer 20% span.

On the suction surface, two distinctive events are apparent. First, a negative damping alleviation is observed around the middle chord towards the blade tip for a small tip clearance of 1.25%$C$ (Event 'A' as indicated in Figure 7.5b). Secondly, an event developing in the flow diffusion stage is noticed. For a small tip clearance of 1.25%$C$ (Figure 7.5b), this event can be noticed at 80%$C_{ax}$ towards the blade tip, though still in its inception. As the tip clearance is increased, this event develops. For the tip clearance setting of 5%$C$, it represents the dominant influence of the tip clearance (Event 'B' indicated by Figure 7.5d). The integrated aerodynamic damping at 95%

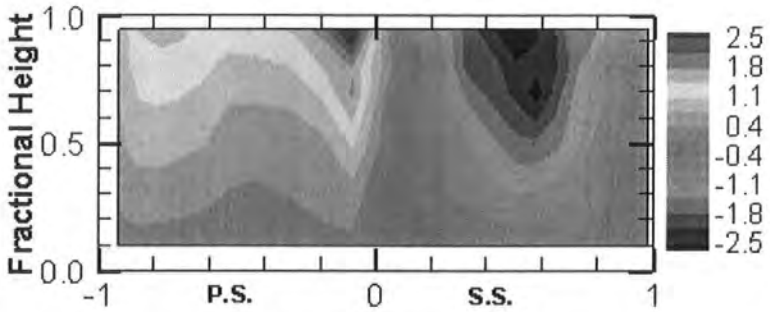


(a) No tip-clearance

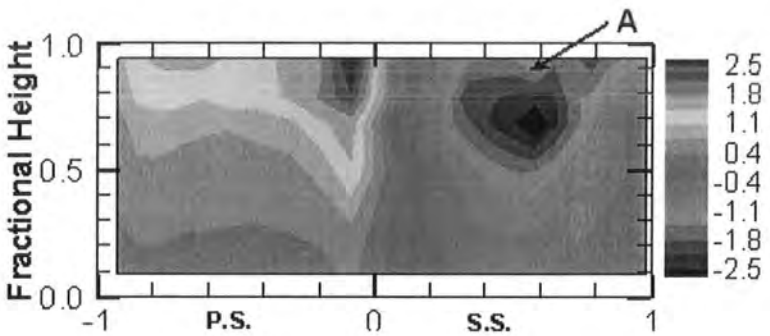


(b) 1.25%$C$ tip-clearance

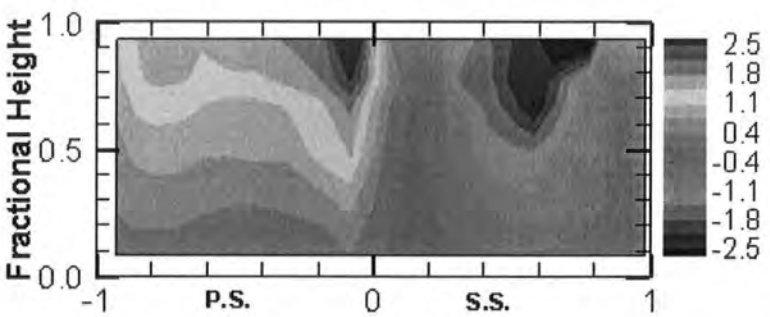


(c) 2.5%$C$ tip-clearance

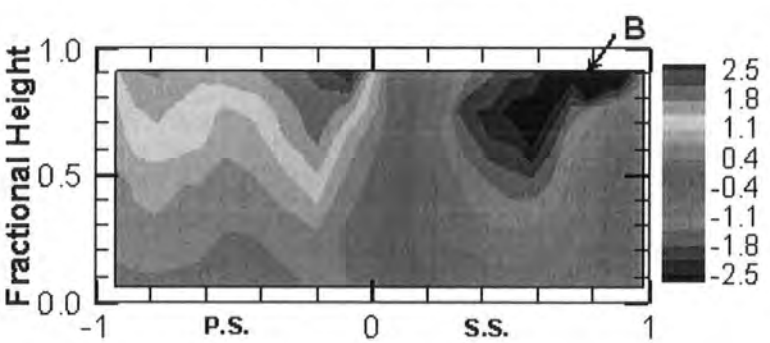


(d) 5.0%$C$ tip-clearance

**Figure 7.5: Local aerodynamic damping coefficient ($K$=0.4, $\sigma_0$=−60°)**

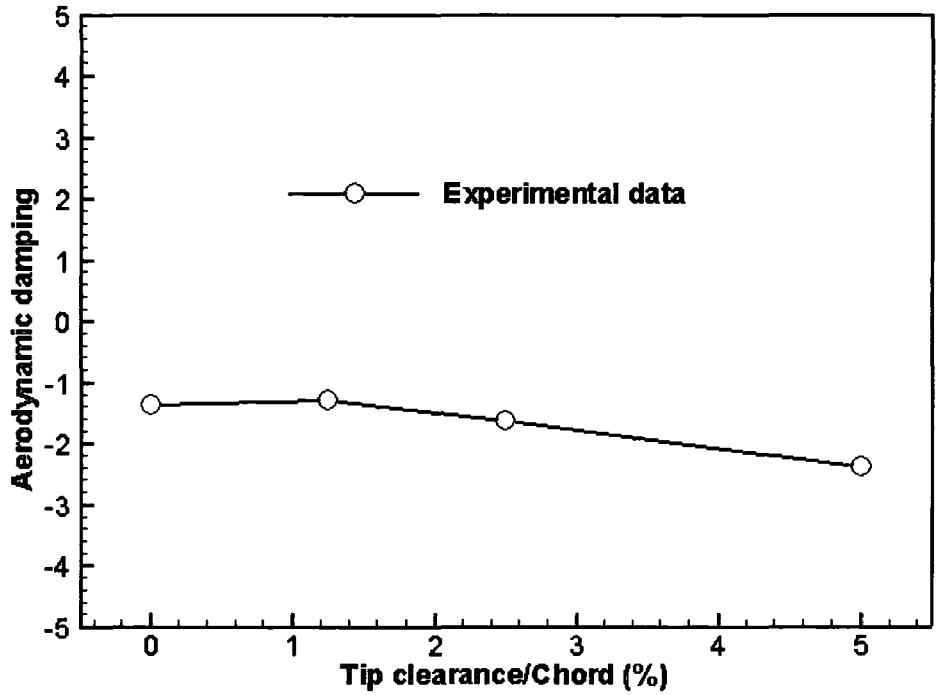


Figure 7.6: Measured aerodynamic damping coefficient at 95% span on the suction surface ($K$=0.4, $\sigma_0$=−60°)

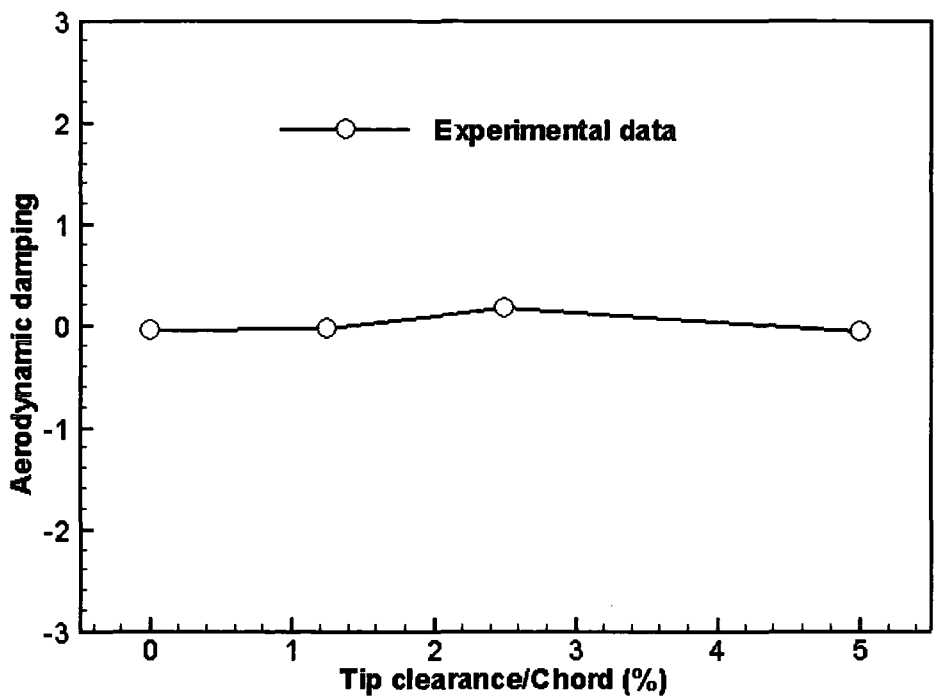


Figure 7.7: Variation of measured global aerodynamic damping coefficient with tip clearance ($K$=0.4, $\sigma_0$=−60°)

span of suction surface is displayed in the Figure 7.6, which gives an indication of the overall influence of these two events.

Figure 7.7 shows the variation of measured global aerodynamic damping with respect to the size of tip clearance at the reduced frequency 0.4 and an IBPA of $-60°$. For the small tip clearance ($1.25\%C$), an overall stabilising effect is found, though it is small. This stabilising effect is mainly due to the alleviation on the negative damping around mid-chord towards the tip on the suction surface (Figure 7.5b). For the medium tip clearance ($2.5\%C$), much positive damping is induced on the pressure surface tip region, which makes the global damping of this setting to stand out from the others. For the large tip clearance ($5\%C$), a significant amount of negative damping (Figure 7.5d) is generated in the flow diffusion region towards the trailing edge on the suction surface. However, this effect is offset by the increased positive damping on the pressure surface, and only a minor change in the global aerodynamic damping can be observed when compared to the zero tip clearance setting.

Overall, the global aerodynamic damping seems to be largely unaffected by the tip clearance in the present cases tested. Given the significant influence on the amplitude of the first harmonic pressure towards the tip on the suction surface, as shown in Figure 7.3b, one can however argue that the relatively small influence of tip clearance on the aerodynamic damping is due to the tested mode shape — straight flapping, which results in the phase angle of the first harmonic pressure response being around $0°$.

## 7.2 Computational Study

The computational method described in Chapter 3, combined with a simple tip clearance modelling, is utilised to investigate the tip clearance flow. Generally, an extra mesh block is needed at the blade tip gap to simulate the tip clearance flow. To avoid the complexity of employing a multi-block mesh solver, the blade tip is rounded and the gap is filled with by a simple H-type mesh, similar to that by Dawes (1987). Previous applications of this technique in steady flow (Dawes, 1987; Storer and Cumpsty, 1991; Van Zante et al., 2000; Walker et al., 2005) have shown that the strength of tip clearance flow can be adequately captured by this tip mesh treatment, although

it is recognised that detailed resolution of the tip clearance flow structure may not be possible. Here, this technique is used in simulating the unsteady aerodynamic response of the oscillating blades with considerable tip clearance flow.

### 7.2.1 Case One: Linear Turbine Cascade

The mesh used in the calculations of the linear turbine cascade flow with a tip clearance is shown in Figure 7.8. The overall mesh dimensions are $107 \times 41 \times 51$ (axial $\times$ pitchwise $\times$ spanwise) nodes, with 3, 6, and 11 cells used in the spanwise direction to resolve the tip clearance for the $1.25\%C$, $2.5\%C$ and $5.0\%C$ tip clearances, respectively. At this point, it should also be recognised that the blade profile used for the purposes of this investigation has a narrow cross-section and the spanwise extent of blade tip rounding is confined to 3 mesh cells. Over the blade tip, repeating flow conditions are enforced to communicate the pressure and suction sides. At the computational domain inlet, the same conditions as the nominal case are prescribed, namely uniform inlet flow. At the exit, a back pressure, equivalent to an exit isentropic Mach number of 0.3, is given. To include the viscous effects, a Reynolds number of $2.2 \times 10^5$, in the experimental test, is applied.

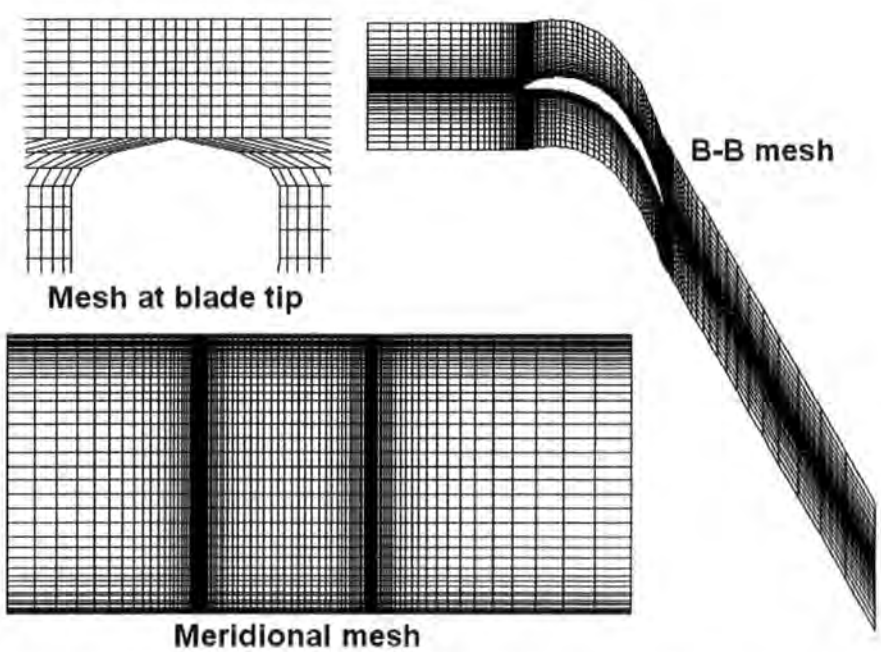


**Figure 7.8: Computational mesh for tip clearance flow calculations**

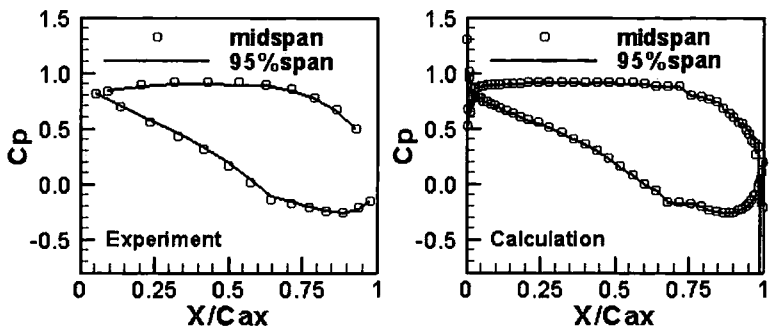


(a) No tip-clearance

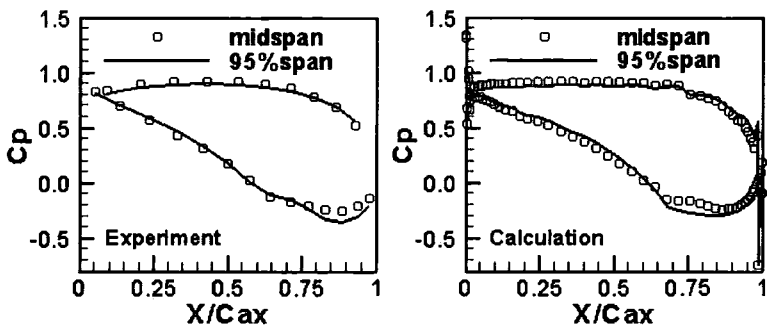


(b) 1.25%$C$ tip-clearance

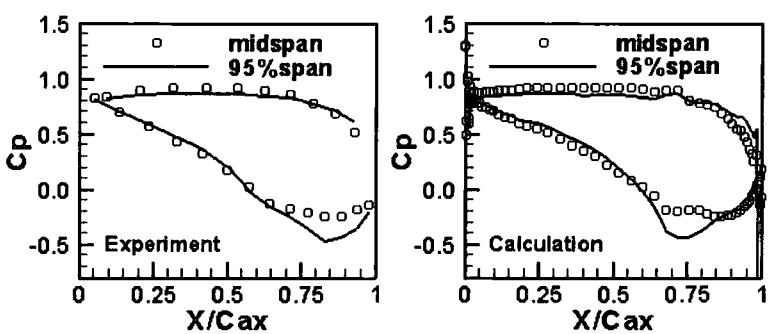


(c) 2.5%$C$ tip-clearance

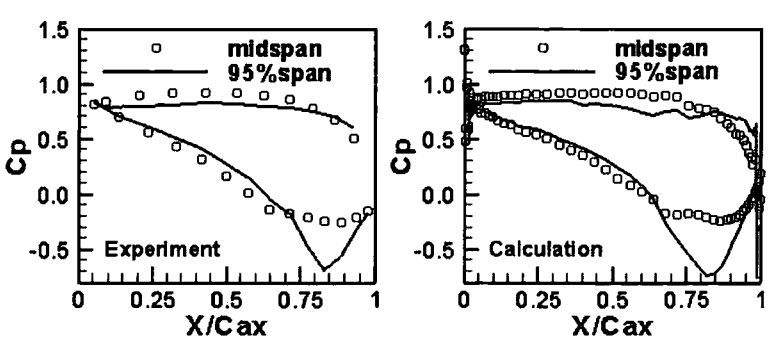


(d) 5.0%$C$ tip-clearance

**Figure 7.9: Blade surface steady pressure distribution (left: Experimental data; right: Calculation)**

Figure 7.9 shows the steady flow pressure at midspan and 95% span sections of the middle blade, with tip clearances of zero, 1.25%$C$, 2.5%$C$ and 5%$C$. For each tip clearance setting, the left-hand plot presents the experimental data and the right-hand the CFD results. At zero tip clearance, shown in Figure 7.9a, the two-dimensional steady flow nature is well predicted by the calculation. When a tip clearance is present, an unloading on the fore chord of the suction surface and reloading towards the trailing edge on both the pressure and suction surface are clearly observed at 95% span. Generally speaking, these regions of unloading and reloading are well predicted by the CFD calculations (Figure 7.9b-7.9d), demonstrating that the simple tip clearance model is able to capture the main features of steady tip clearance flow.

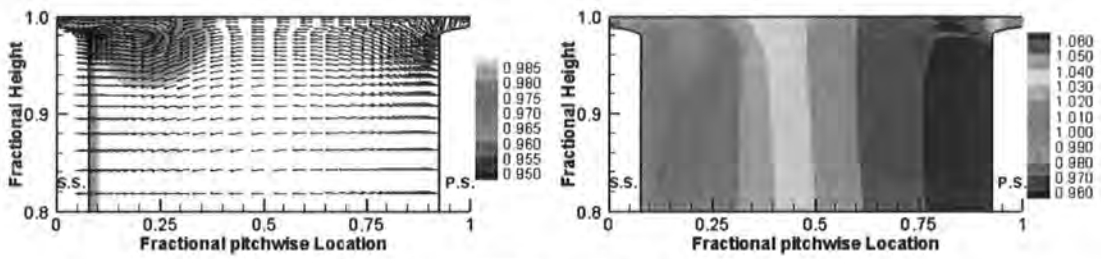


(a) 1.25%$C$ tip-clearance

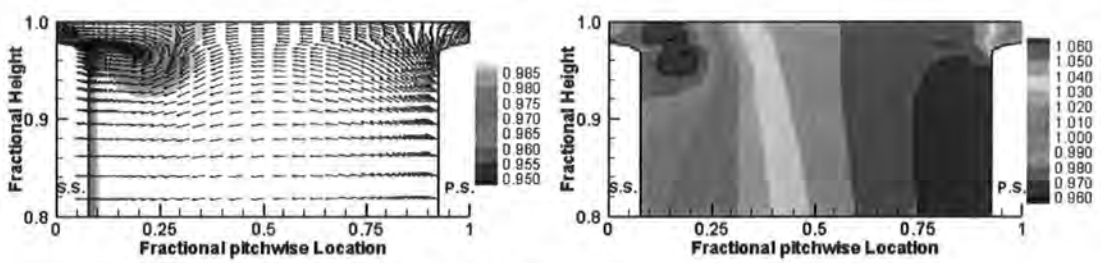


(b) 2.5%$C$ tip-clearance

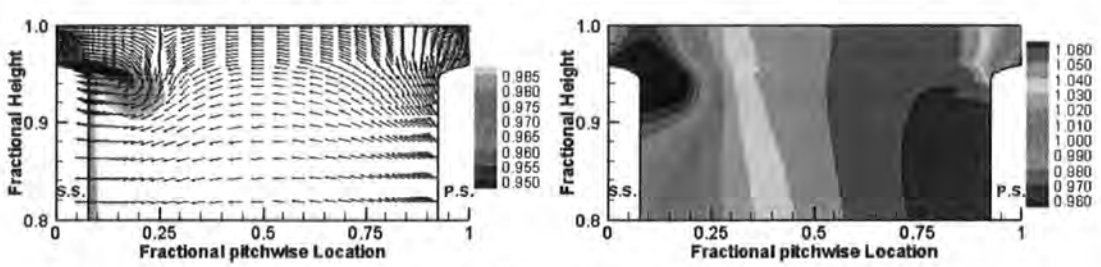


(c) 5.0%$C$ tip-clearance

**Figure 7.10: Entropy $[exp(-\Delta S/R)]$ contours with secondary velocity vectors (left) and static pressure contours (right) at 80%$C_{ax}$**

The clear low pressure peak around 80%$C_{ax}$ on the suction surface, shown in Figure 7.9, indicates a strong influence of the local tip clearance flow structure. To help

understanding of this flow behaviour CFD results are presented in Figure 7.10, in the form of contour plots (entropy and static pressure) and secondary velocity vectors at $80\%C_{ax}$. The high loss core [low value of the entropy parameter, $exp(-\Delta S/R)$] is seen to coincide with the centre of the tip clearance vortex. Notable flow turning over the tip can be observed with associated low static pressures locally. This tip vortex related turning and an associated low pressure region are most evident at the largest clearance gap (Figure 7.10c), although interestingly the pitchwise extent of the vortex at this condition is the smallest compared to those at smaller tip gaps. The pressure contours also illustrate the radial extension of the steady reloading, which is directly associated with the behaviours of tip clearance vortex. The largest reloading (reduction of pressure on the suction surface) certainly results from the strongest flow rolling-up (Figure 7.10c), which occurs at the largest tip clearance.

Figure 7.11 compares the predicted first harmonic pressure with the measured data with the left plot being the amplitude and the right the phase angle for each tip clearance setting. For the small tip clearance of $1.25\%C$ (Figure 7.11a), the amplitude of the first harmonic pressure is excellently predicted, whereas the phase angle shift (refer to Event 'A' in Figure 7.5b) around mid-chord on the suction surface is not captured. From $70\%C_{ax}$ farther downstream on the suction surface, where the flow is in its diffusion stage, the phase prediction tends to deteriorate. For the tip clearance of $2.5\%C$ and $5.0\%C$, the amplitude is excellently predicted up to $55\%C_{ax}$ on the suction surface and the amplitude peak is over-predicted, whilst on the pressure surface, the amplitude is well predicted. When the flow is separating ($75\%$-$90\%C_{ax}$) on the suction surface, the phase angle is not well predicted. On the pressure surface, the phase prediction deteriorates towards the blade trailing edge for all three tip clearance settings.

Figure 7.12 shows the integrated aerodynamic damping at 95% span on the suction surface, where Events 'A' and 'B' described in Section 7.1.3.2 are located. This figure demonstrates good qualitative and quantitative agreement between the CFD prediction and the measured aerodynamic damping, although CFD slightly over-predicts the blade aeroelastic instability at all tip clearance settings. Figure 7.13 presents the variation of the global aerodynamic damping with respect to the size of tip clearance. For all tip clearance settings, the overall aeroelastic instability is over-predicted. At the

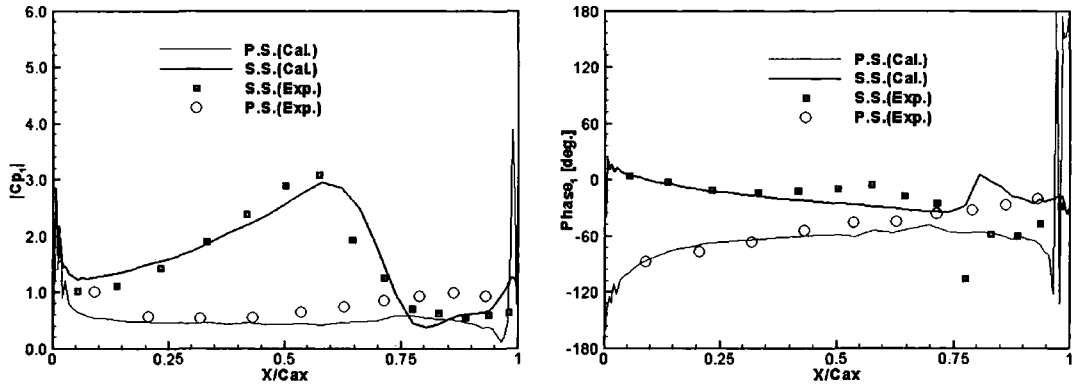


(a) 1.25%$C$ tip-clearance

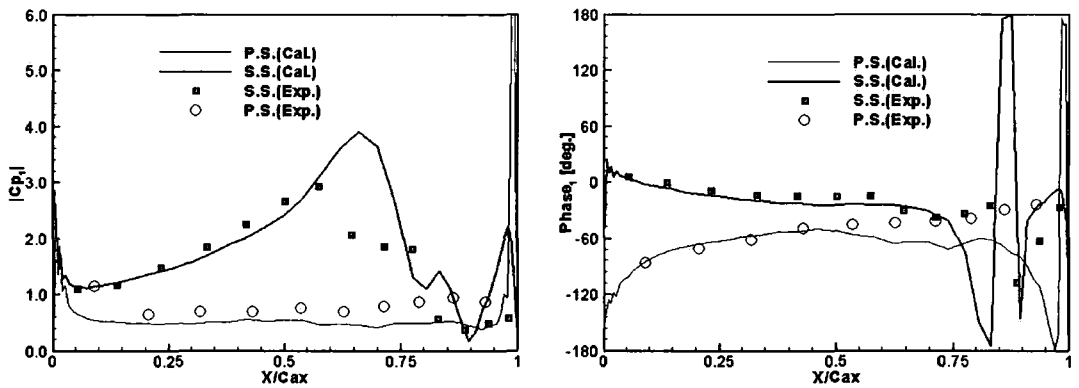


(b) 2.5%$C$ tip-clearance

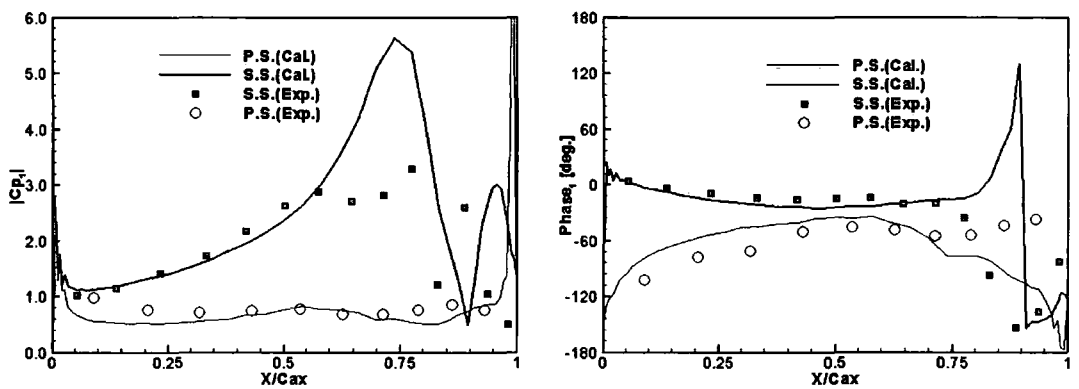


(c) 5.0%$C$ tip-clearance

**Figure 7.11: Predicted and measured amplitude (left) and phase angle (right) of first harmonic pressure at 95% span section**

medium tip clearance (2.5%$C$), the stabilising effect is not captured. Indeed, small destabilising influence is predicted for this tip clearance setting, since the positive damping contribution from the pressure surface is under-predicted. For the largest

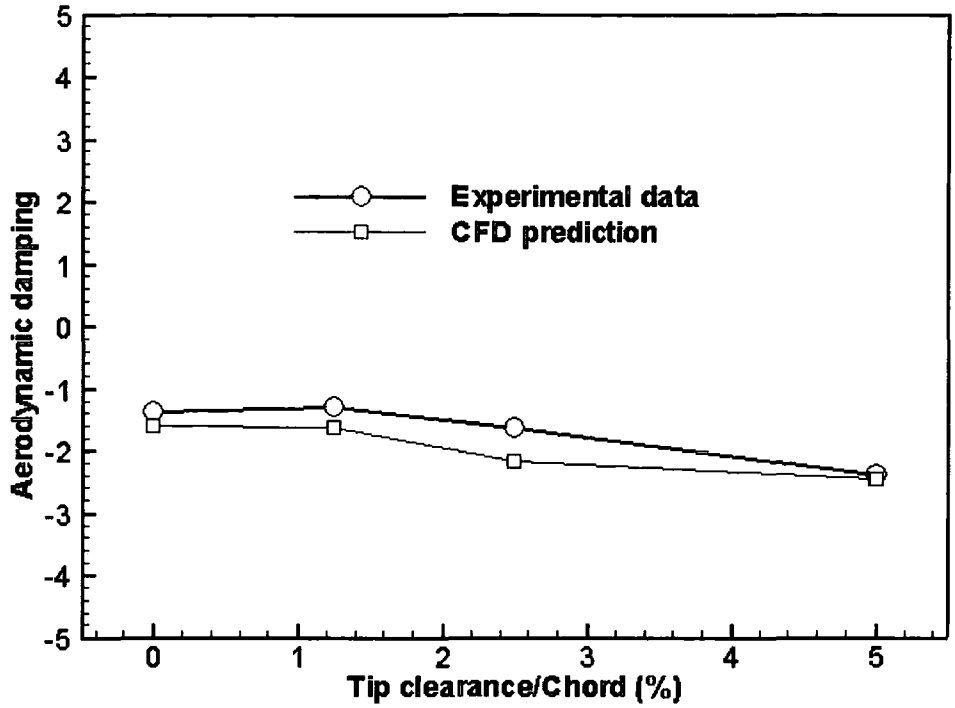


Figure 7.12: Aerodynamic damping at 95% span on the suction surface

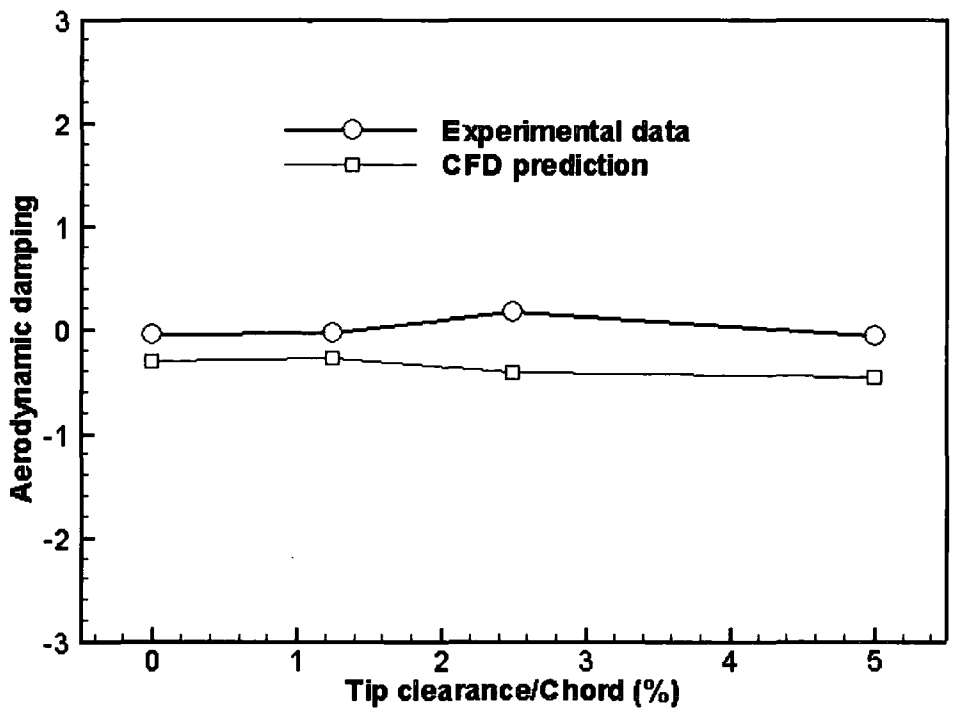


Figure 7.13: Variation of global aerodynamic damping with tip clearance

tip clearance (5.0%$C$), the slight destabilising observed in experiment is predicted. Overall, the predicted variation of the aerodynamic damping with respect to the size of tip clearance is in a small range, which is consistent with the experimental observation.

### 7.2.2 Case Two: LP Turbine Rotor

Realistic LP steam turbine rotors are normally characterised by high aspect ratio. The associated high vibration amplitude towards the tip of high aspect ratio blades means a significant contribution towards the aerodynamic damping from the blade tip region, as observed in Figure 6.8 (page 118). Therefore, it is of great interest to assess how much influence the tip clearance flow will have on the blade aeroelastic stability of the realistic LP turbine rotors. To this end, the rotor previously studied is adopted with a tip clearance. A hypothetical tip clearance is chosen to be 5% tip chord (equally 0.8% blade height), a typical value expected in realistic machines. The results obtained thereby are to be compared with the prediction of the nominal setting presented in Section 6.3.2.

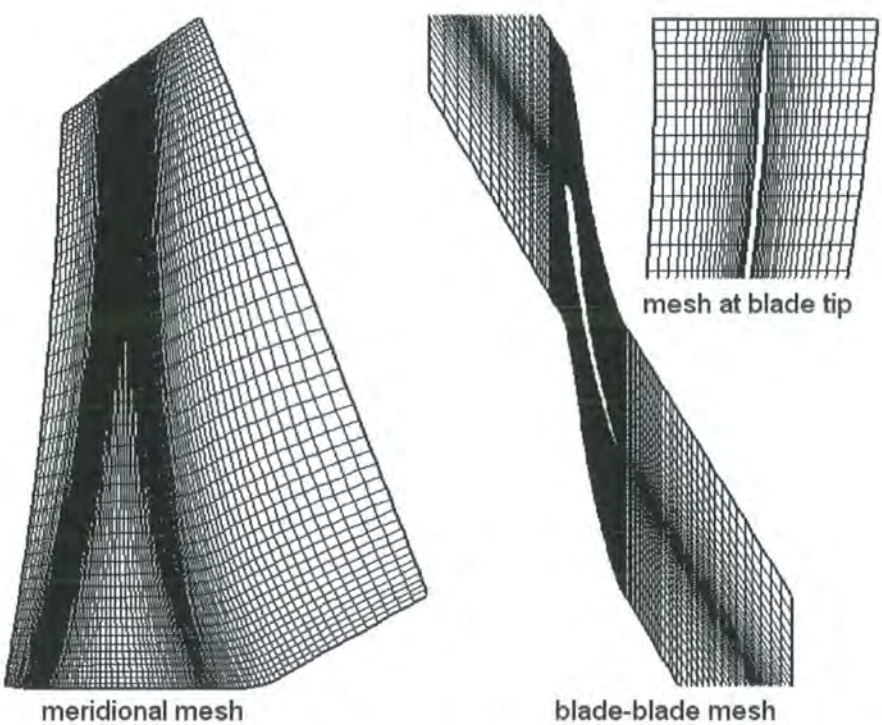


**Figure 7.14: Computational mesh for model LP rotor with a tip clearance**

The mesh used for the purpose of the present investigation is shown in Figure 7.14 including 125 nodes distributed in the streamwise direction, 41 nodes in the pitchwise direction and 51 nodes in the radial direction. The tip clearance is resolved using one cell in the radial direction. Other treatments of tip clearance are the same as stated in Section 7.2.1. The other boundary conditions and the mode shape have nothing different from those used in the nominal case.

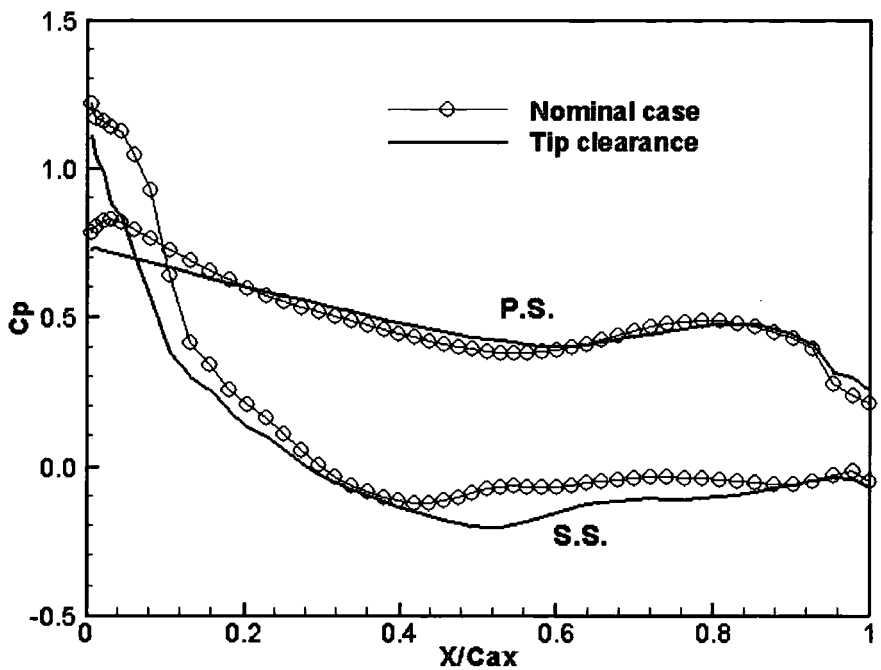


**Figure 7.15: Steady flow blade surface pressure coefficient distribution at 98% span**

**Table 7.1: Predicted Log-Dec ($\xi$) of LP Rotor with and without tip clearance**

| Nominal case ($\xi_0$) | With tip clearance ($\xi_1$) | Relative difference ($\frac{\xi_1 - \xi_0}{\lvert\xi_0\rvert}$) |
|---|---|---|
| -1.265% | -1.444% | -14.2% |

Figure 7.15 shows the steady flow blade surface loading at 98% span. On the pressure surface, unloading up to 20%$C_{ax}$ is observed when there is tip clearance, whilst reloading is evident over most of chord on the suction surface. Although the adverse pressure gradient becomes bigger from mid-chord further downstream on the suction surface when the tip clearance is present, it seems not to worsen the associated flow separation, as demonstrated by Figure 7.16 which plots the steady flow entropy contours at 98% span. However, this does not mean less loss when there is tip clearance

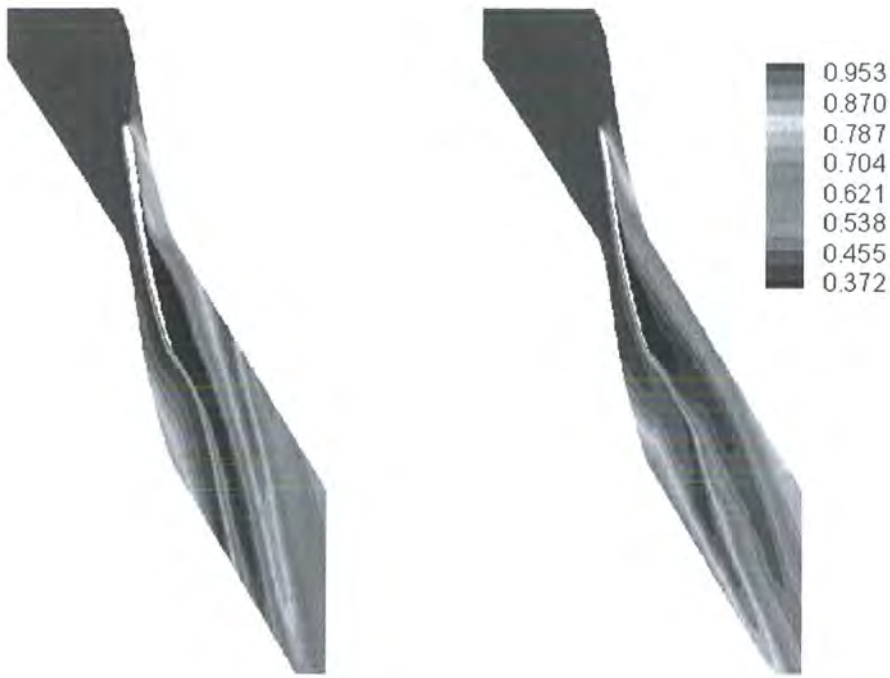


(a) Nominal rotor (b) Rotor with tip clearance

**Figure 7.16: Steady flow entropy $[exp(-\Delta S/R)]$ contours at 98% span**

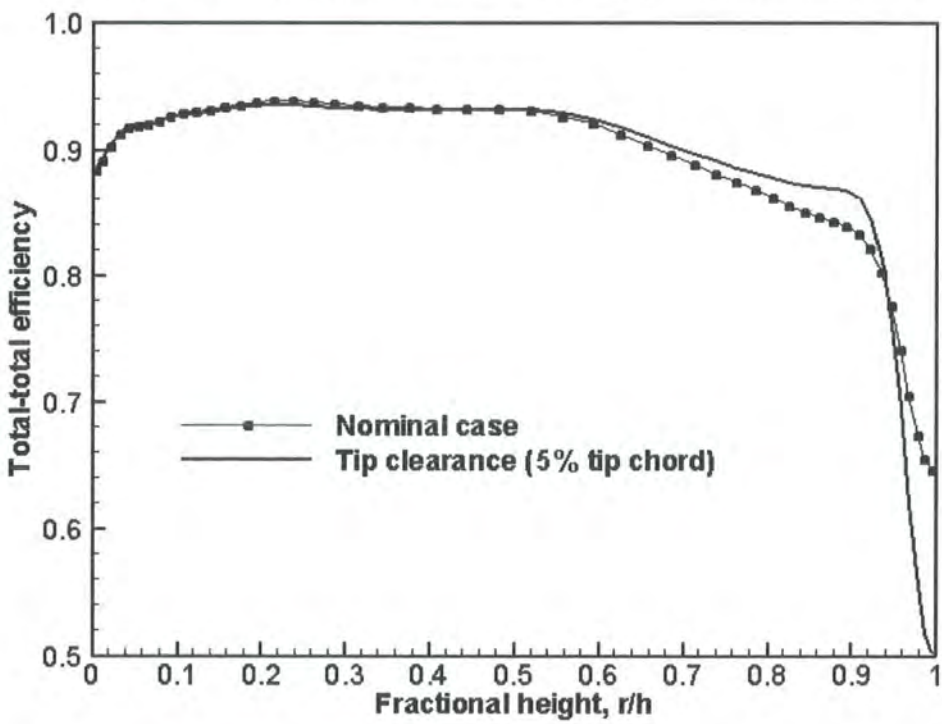


**Figure 7.17: Predicted spanwise variation in local total-to-total efficiency with and without tip clearance for the LP rotor**

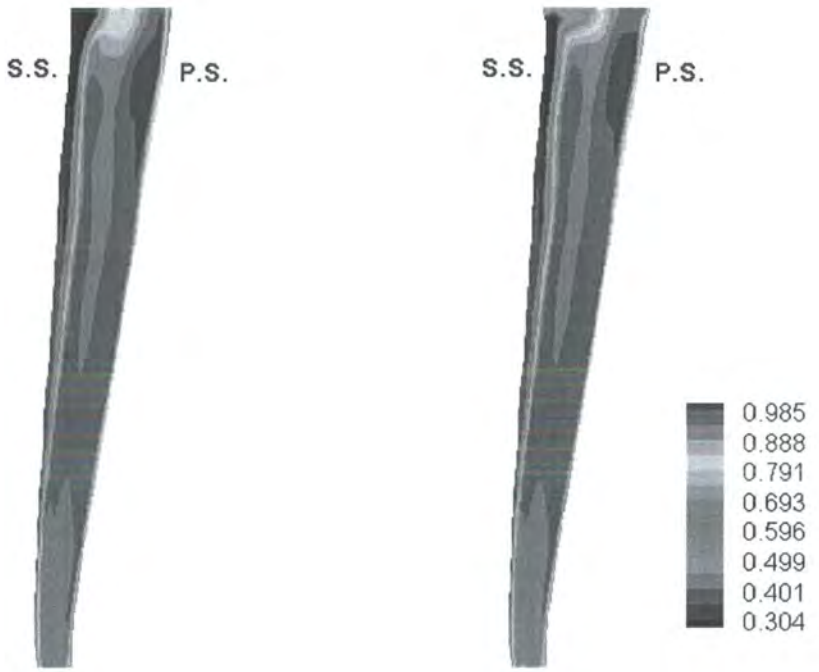


(a) Nominal rotor (b) Rotor with tip clearance

**Figure 7.18: Steady flow entropy $[exp(-\Delta S/R)]$ contours at 80%$C_{ax}$**

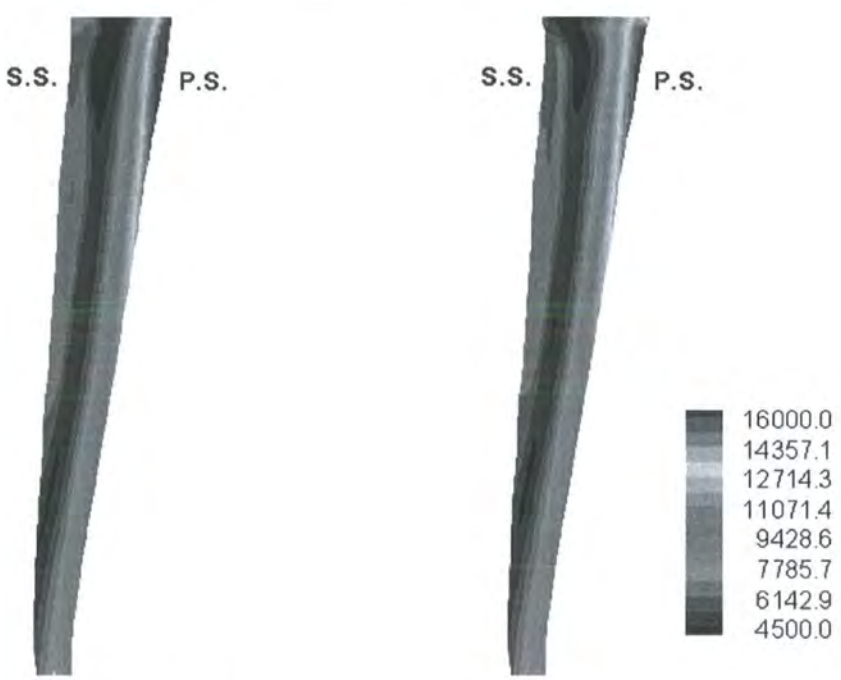


(a) Nominal rotor (b) Rotor with tip clearance

**Figure 7.19: Steady flow pressure contours at 80%$C_{ax}$**

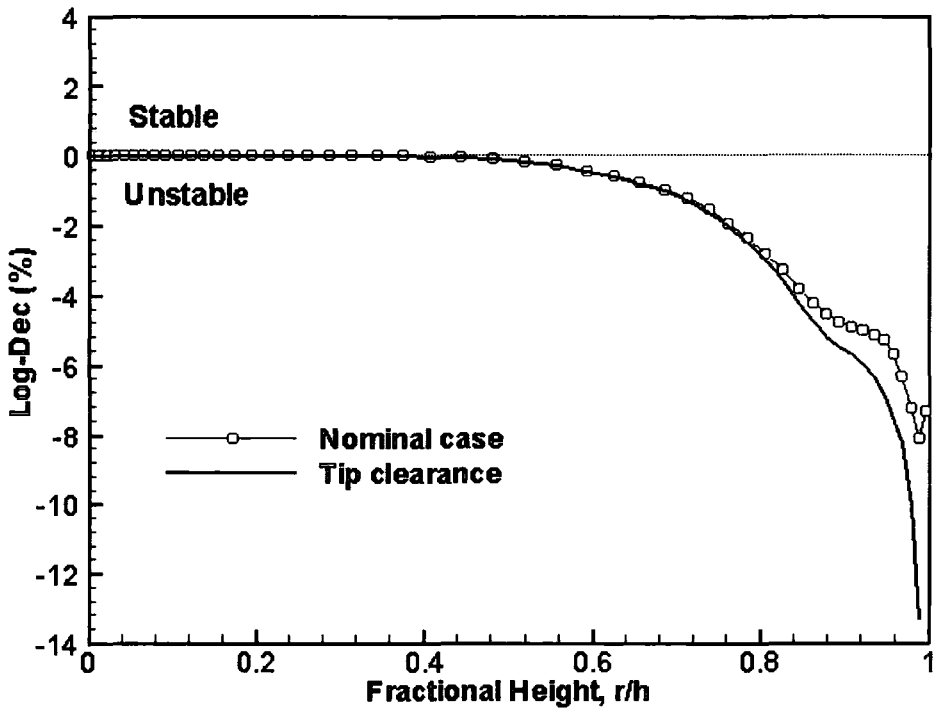


**Figure 7.20: Predicted spanwise variation in local Loc-Dec with and without tip clearance for the LP rotor, 11 NDs backward travelling wave mode**

flow. Figure 7.17 shows the spanwise variation of the local total-total efficiency for conditions with and without tip clearance. From 94% span outwards, there is more loss associated with tip clearance flow, whilst efficiency gain is observed over 55%-94% span when tip clearance flow is present. The overall total-total efficiency is 89.54 and 89.20 for the nominal case and the tip clearance case respectively.

When the rotor is tip shrouded (nominal case), the low energy flow, driven by the secondary flow, is accumulated towards the outer casing near the suction surface (Figure 7.18a). Whilst the tip clearance flow is present, the high energy flow from the pressure side drives the low energy flow, which is evident near the suction surface for the nominal case, to spread more widely (Figure 7.18b). Figure 7.19 presents the steady flow pressure contours in an axial plane at $80\%C_{ax}$. The bearing of tip clearance flow on the blade loading is evident in this figure. As discussed before, the blade loading change associated with the tip clearance flow is to affect the blade aerodynamic damping.

Figure 7.20 shows the variation of predicted Log-Dec along the blade height for the rotor with and without tip clearance. The strong destabilising effect of the tip clearance

is evident from 80% span outwards. Overall, the aggregate influence of tip clearance accounts for 14.2% Log-Dec/damping change, which is again considerable (Table 7.1).

Tip clearance flow concerned here is a phenomenon associated with the un-shrouded turbomachinery blades. It should be pointed out that the LP rotor presently studied has a tip shroud design. The tip clearance is artificially added in. Although tip-shrouded, this LP rotor still has a considerable vibratory amplitude towards the tip in the mode shape. Therefore, the observation obtained to this LP rotor with a tip clearance should be representative in terms of the influence of tip clearance in realistic LP steam turbine rotor blading.

## 7.3 Quasi-Steady Analysis

A simple analysis is presented here to help understand the apparent stabilising behaviour observed on the suction surface at a small tip clearance in the experiment (Event 'A' as shown in Figure 7.5b). Consider a turbine blade passage oscillating in a flapping mode (positive downward) with an IBPA as shown in Figure 7.21. The lower blade is the reference blade on which the aerodynamic work done by the fluid to the blade in one vibration period is given by:

$$W = \pi A_x A_f \sin(\phi_{fx}) \tag{7.1}$$

Where, $A_f$ is the amplitude of the unsteady force $F$ on the reference blade in the vibration direction, and $\phi_{fx}$ the phase lead of the force to the vibration motion, i.e.

$$F = A_f \sin(\omega_0 t + \phi_{fx}) \tag{7.2}$$

If varying quasi-steadily, the blade loading $F$ is inversely proportional to blade solidity. $F$ is expected to be proportional to the blade-to-blade spacing:

$$F \propto (A_x \sin(\omega_0 t) - A_x \sin(\omega_0 t + \sigma_0)) \tag{7.3}$$

At the zero frequency limit, we have:

$$F \propto -A_x \sin(\sigma_0) \tag{7.4}$$

This shows that quasi-steady unsteady loading induced by the flapping vibratory motion should be in phase with the IBPA ($\sigma_0$), but with a negative sign. Consequently we

have the maximum work done to blade (i.e. maximum magnitude of negative damping) when the IBPA is $-90°$. Note that for a turbine this corresponds to a backward travelling wave. The same argument applies to a compressor for which the most unstable mode corresponds to a forward travelling wave at an IBPA of 90°.

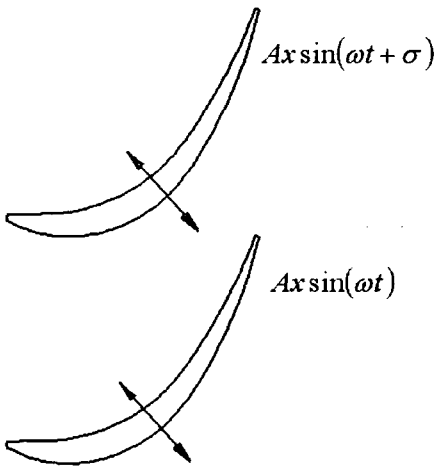


**Figure 7.21: Oscillating turbine passage**

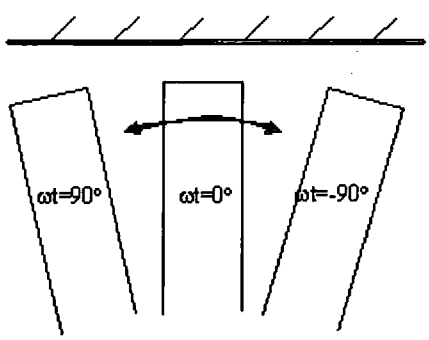


**Figure 7.22: Blade tip at the minimum, mean and maximum displacements (axial view)**

This quasi-steady argument on a 2D blade-to-blade section can now be used to as a basis to explain the stabilising behaviour of a small tip clearance (Figure 7.5b). A sketch of a tip gap (viewed from the axial direction) is given in Figure 7.22 for the three positions during a vibration period.

The 2D quasi-steady analysis presented above leads to the observation that for the most unstable IBPA ($-90°$), the maximum unsteady blade force would occur at the mean position ($\omega_0 t = 0°$). However, this phasing for the maximum blade force would

be affected by the tip-clearance. The steady results (Figure 7.9) clearly show that the suction loading near the tip varies directly with the clearance gap. It follows that during one vibration cycle, the maximum loading should occur at the phase angle with a maximum tip gap. Clearly we can see from Figure 7.22, the mean displacement position ($\omega_0 t = 0°$) corresponds to the minimum tip gap. Hence the maximum loading due to the tip-clearance is not in phase with that due to the blade-to-blade vibratory displacement at the most unstable IBPA. This phase offset should explain why it is possible to have a stabilising effect with a tip-clearance. The reason for the most pronounced effect at a small tip clearance may simply be because the relative tip gap variation during one vibration cycle is proportionally larger when the mean tip clearance is small.

At a large tip clearance, the tip vortex is already well developed (highly concentrated), as indicated in Figure 7.10c. Now an increase in the blade-to-blade spacing would no longer lead to any further strengthening of the tip vortex (and the local flow turning and its associated low pressure). Hence the maximum local low pressure peak at $80\%C_{ax}$ on the suction surface happens at ($\omega_0 t = 0°$), leading to a local destabilising region, i.e. Event 'B' (Figure 7.5d).

## 7.4 Summary

An experimental and computational investigation into the influence of the tip clearance flow on the flutter characteristics in a turbine cascade has been conducted. In a linear turbine cascade, extensive steady and unsteady measurements of blade surface pressure are first provided and discussed for a tip clearance range up to 5% chord. The steady flow results indicate a significant role played by the tip leakage vortex with notable unloading and reloading obvious at 95% span section through all tip clearance settings. For a small tip clearance ($1.25\%C$), the tip gap variation during blade oscillation provides a stabilising contribution around the mid chord on the suction surface near the tip. However, for large tip clearances ($2.5\%C$ and $5\%C$), this stabilising contribution is largely offset by a destabilising contribution measured around $80\%C_{ax}$, which is associated with a well developed tip clearance vortex. The global aerodynamic damping

is observed to be largely unaffected for the tested cases.

Predicted amplitude and phase angle of the first harmonic pressure with a simple tip clearance modelling exhibits a good level of correlation to the test data. CFD also predicts a minor aerodynamic damping change with respect to the tip clearance, which is consistent to the measurement. This simple tip clearance modelling is then applied to the LP rotor with a hypothetical tip clearance of 5% tip chord, which reveals a destabilising effect by 14.2% damping difference.

# Chapter 8

# Influence of Part-span Shrouds on Blade Aeroelastic Characteristics

LP steam turbine rotors are vulnerable to flutter occurrence. To prevent flutter occurring, passive measures are often introduced at the final blade design stage. Of them, using part-span shrouds ("dampers", "snubbers") is one typical option. Basically, part-span shrouds are integral protuberances on individual blades. When the machine is running at speed, part-span shrouds will interlock with each other to form a continuous ring in a rotor assembly. Subsequently, mechanical coupling of part-span shrouds is achieved and the mechanical damping present at the interfaces of part-span shrouds would help reduce excessive vibrations of aerodynamic origins. The presence of part-span shrouds would introduce blockage to the passage flow and result in extra aerodynamic loss (Roberts, 1999). It is not clear, however, how part-span shrouds would affect the blade aerodynamic damping and its modelling, as current unsteady CFD solvers have not included modelling the shrouds in blade flutter predictions.

In this chapter, a first-of-the-kind investigation, concerning the influence of part-span shrouds on the aerodynamic response of oscillating turbine blades, is documented. A linear cascade, which has been experimentally and computationally studied in Chapter 5 at its nominal conditions, is equipped with part-span shrouds at 75% span and extensively measured. A simple numerical modelling is developed and applied to the part-span shrouded linear turbine cascade. The comparison is made with the experimental test data to assess the capability of this simplified modelling and good agreement achieved. Then, this part-span shroud modelling is applied to an LP steam

turbine rotor and results presented and discussed.

## 8.1 Part-Span Shrouded Linear Cascade

### 8.1.1 Experimental Setup

After testing the oscillating linear turbine cascade at the nominal condition (Chapter 5), the cascade has been modified to include 75% span shrouds in blade passages. The shrouds are chosen to be flat plates for simplicity of application. A thickness of 3mm, equivalent to 1.67% blade height, is applied to the shrouds. The shrouded linear cascade is shown in Figure 8.1 and the specification of the part-span shrouds is summarised in Table 8.1. To accommodate the movement of middle oscillating blade, small gaps (2mm) are allowed in the immediate neighbouring passages of the middle blade. To block the radial leakage flow through the gap, a thin sliding card is designed at the gap location.

**Figure 8.1: Part-span shrouded linear cascade (endwall on the blade tip side is removed for clarity)**

**Table 8.1: Part-span shroud specification**

| | |
|---|---|
| Thickness | $3mm$ |
| Length in axial direction | $60mm$ |
| Spanwise location | 75% span |
| Axial location | 18%-78%$C_{ax}$ |

### 8.1.2 Numerical Modelling of Part-Span Shrouds

The unsteady RANS code is used with modified boundary conditions to accommodate the shroud surfaces. Figure 8.2 shows the mesh used for the study of the influence of part-span shrouds. This consists of $132 \times 41 \times 51$ mesh density, i.e. 132 nodes in the axial direction, 41 nodes in the pitchwise direction and 51 nodes in the spanwise direction. Mesh clustering is applied towards the shroud location in the spanwise direction and finer mesh towards the shroud leading and trailing edges is also applied. To eliminate the dependency of the results on the mesh, the same mesh density is utilised for both calculations of the nominal case and the part-span shrouds. During blade oscillation, the shrouds are assumed to stretch in a plane of constant span height. In other words, the radial movement of the shrouds is neglected.

### 8.1.3 Results and Discussion

The part-span shroud plates are thin and do not induce noticeable steady loading change on the blade surface. The results presented here are, therefore, confined to the

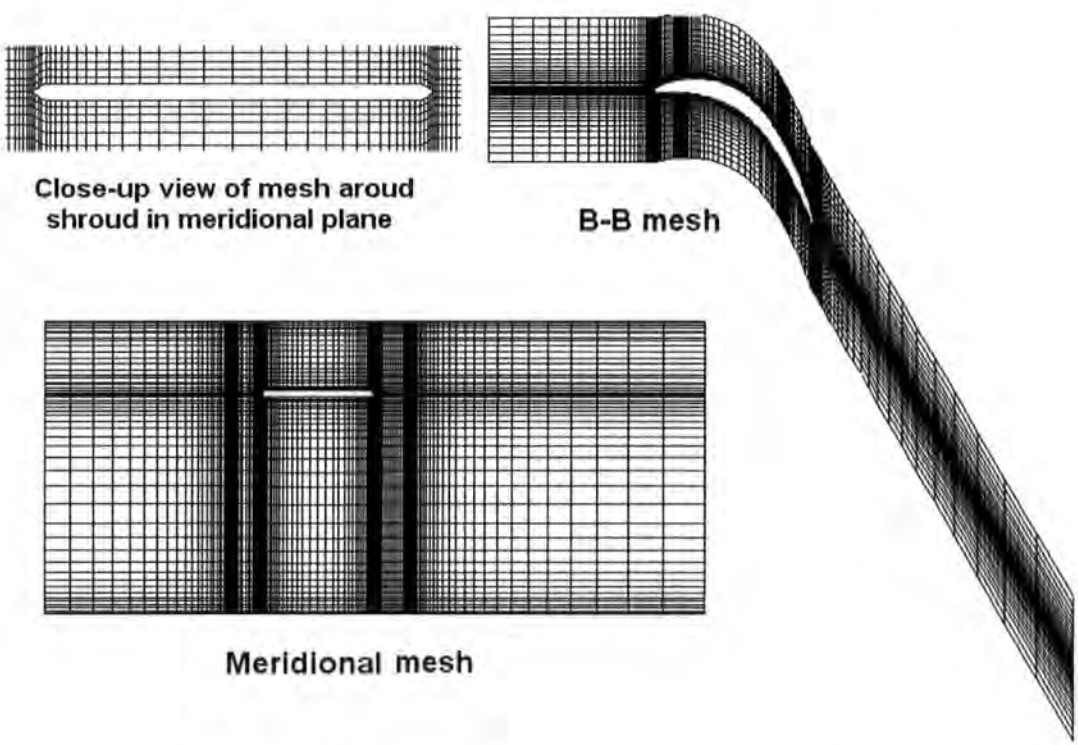


**Figure 8.2: Mesh used for part-span shroud calculation**

unsteady flow.

Figure 8.3 shows the amplitude of the first harmonic pressure at 50%, 70%, 80% and 95% span sections for settings with and without part-span shrouds. For each section, the left plot presents the measured data and the right the predicted results. Equally, Figure 8.4 shows the phase angle of the first harmonic pressure at 50%, 70%, 80% and 95% span sections for settings with and without part-span shrouds. Upon inspection of the set of the first harmonic pressure, it is found that the influence of part-span shrouds manifests itself mainly in the amplitude change of the first harmonic pressure on the suction surface, namely that the existence of part-span shrouds results in reduced amplitude for sections below 75% span and increased amplitude for sections above 75% span. Regardless the spanwise location, the phase angle of the unsteady pressure is largely unaffected. The computational results for settings with and without part-span shrouds reveal the same trends as measurements. For convenience of comparison between the predicted and measured results, Figure 8.5 plots the predicted first harmonic pressure together with the experimental measurements. This figure indicates the influence of the part-span shrouds, viz. the trends in the amplitude change of the first harmonic pressure due to the existence of part-span shrouds, being well predicted.

The opposite trends in the amplitude change of the first harmonic pressure for spanwise sections below and above 75% span, where the part-span shrouds are located, surely reflect the three-dimensional behaviour of the unsteady pressure propagation. Recall the finding in Chapter 5 that the amplitude of the first harmonic pressure is non-proportional to the local vibration amplitude along the blade span. The background mechanism of this phenomenon is that the radial redistribution of the unsteady pressure results in the unsteady loading being alleviated towards the tip and reinforced towards the hub. In the present case, the existence of part-span shrouds breaks down the radial propagation of unsteady pressure. Consequently, the amplitude of the first harmonic pressure with part-span shrouds is larger than that of the nominal case for sections above 75% span, whereas the trend in the amplitude change is reversed for sections below 75% span.

The ultimate reflection of the influence of the part-span shrouds on the blade aeroelastic stability is through the corresponding change in a global parameter, i.e. the overall

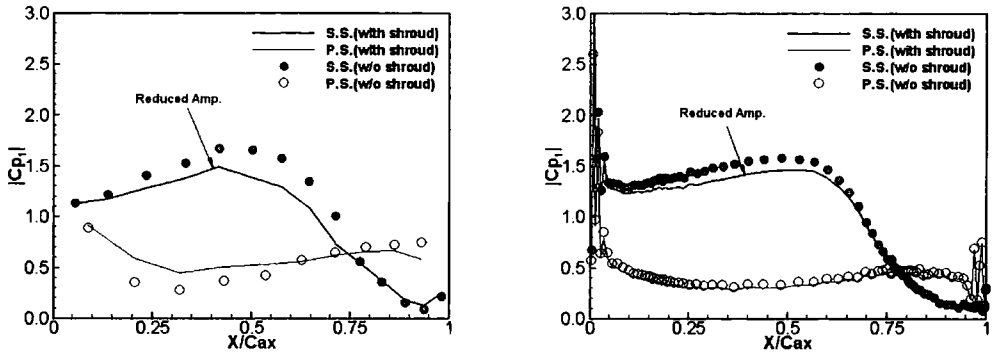


(a) 50% Span

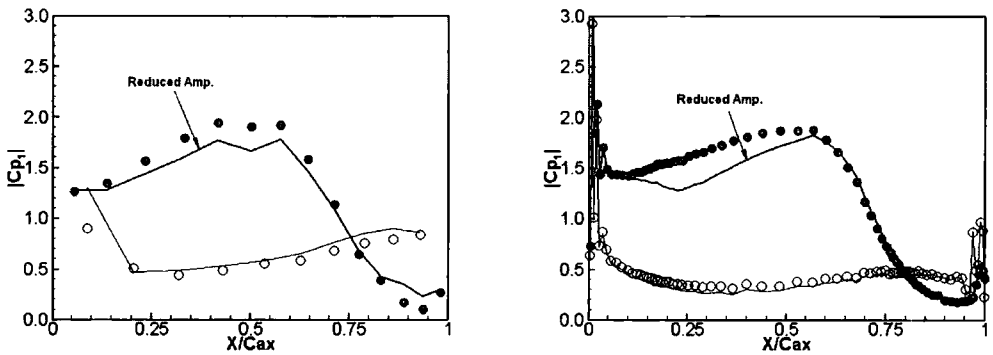


(b) 70% Span

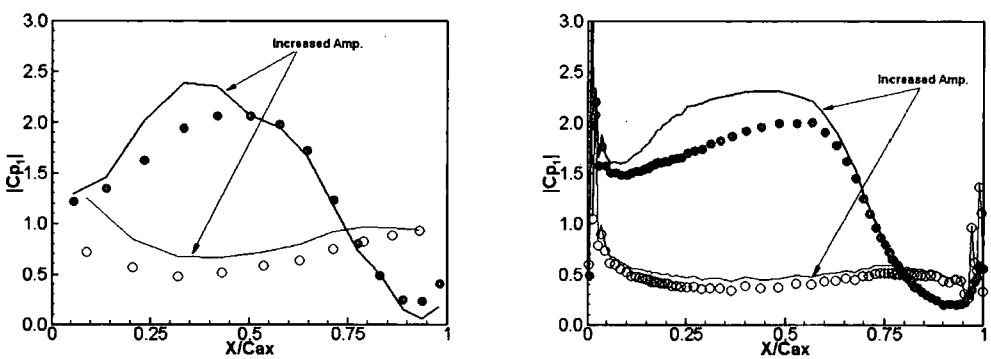


(c) 80% Span

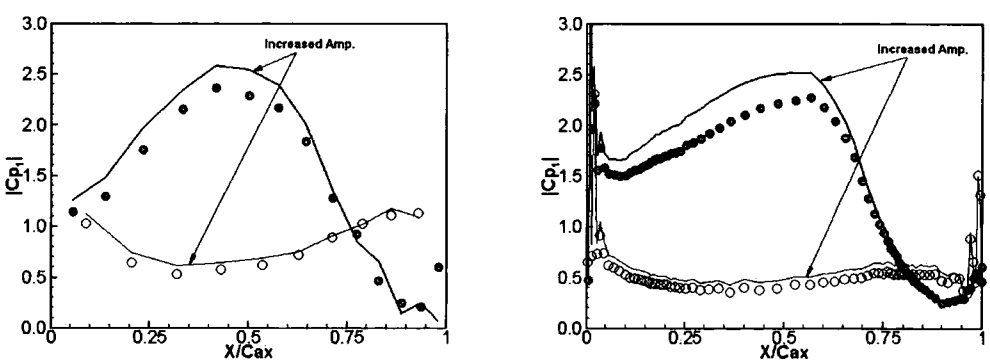


(d) 95% Span

**Figure 8.3: Effects of part-span shrouds on amplitude of the unsteady pressure response, left: experiment, right: calculation ($K$=0.4, $\sigma_0$=−60°)**

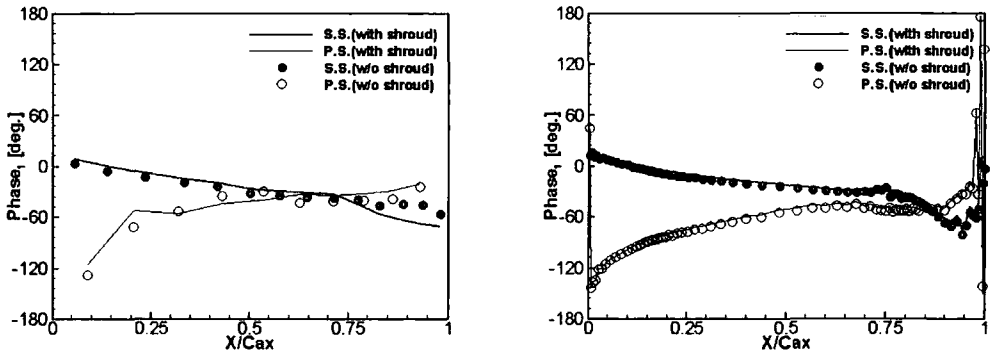


(a) 50% Span

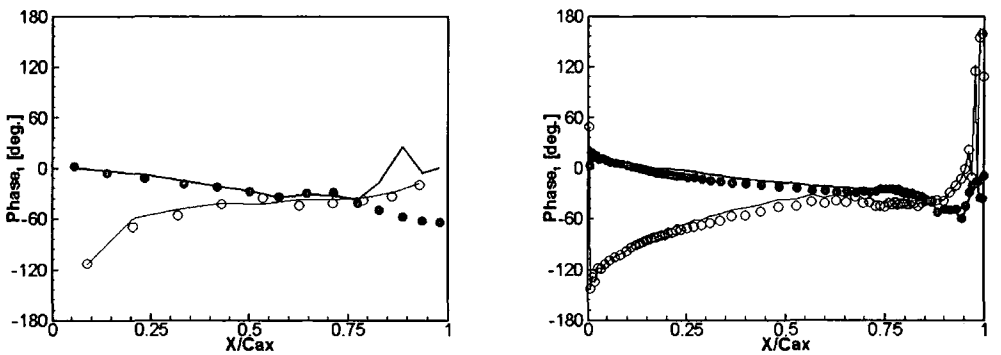


(b) 70% Span

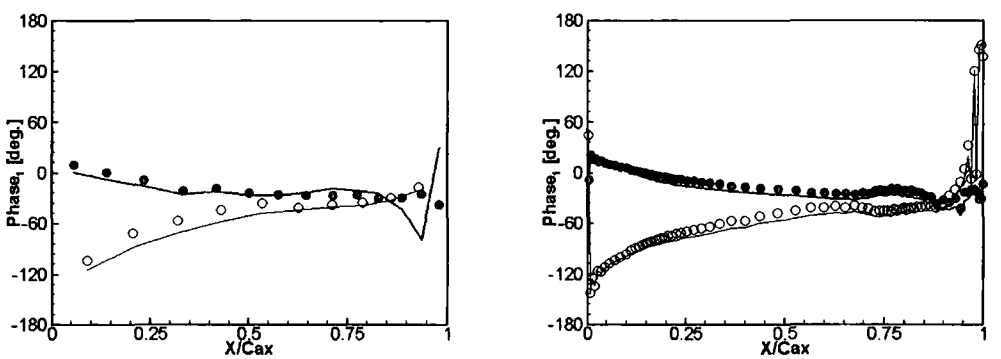


(c) 80% Span

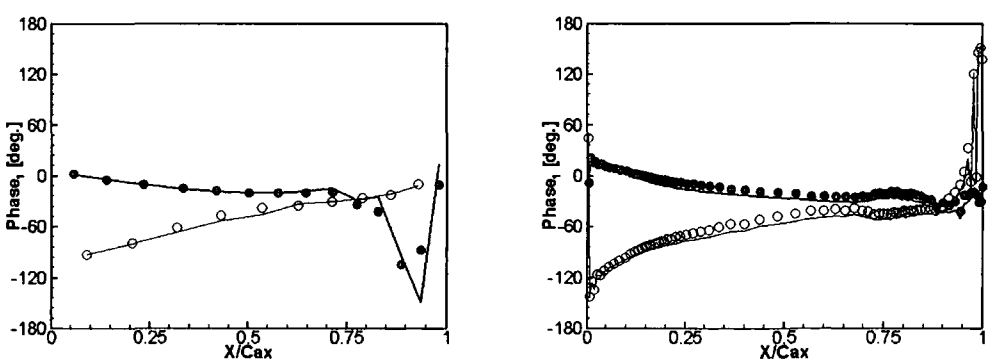


(d) 95% Span

**Figure 8.4: Effects of part-span shrouds on phase angle of the unsteady pressure response, left: experiment, right: calculation ($K$=0.4, $\sigma_0$=−60°)**

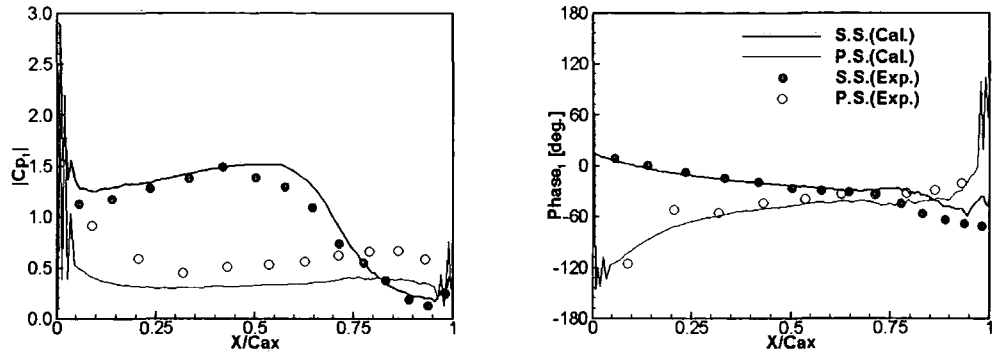


(a) 50% Span

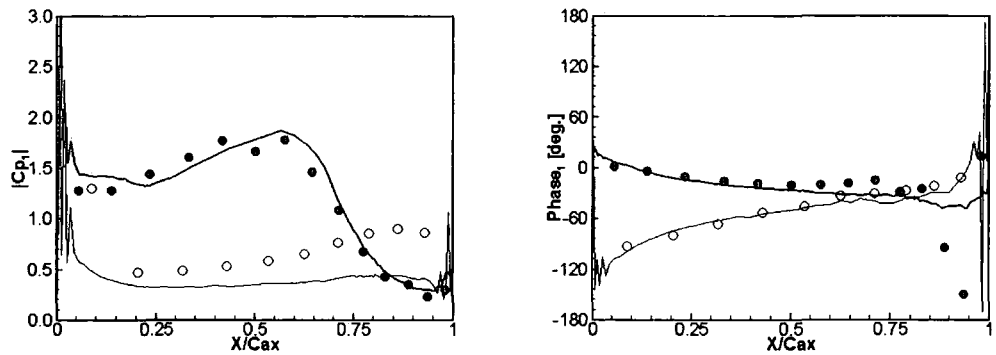


(b) 70% Span

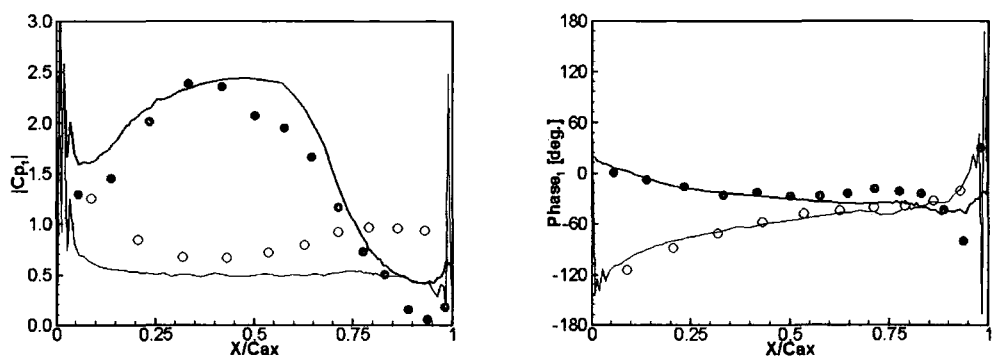


(c) 80% Span

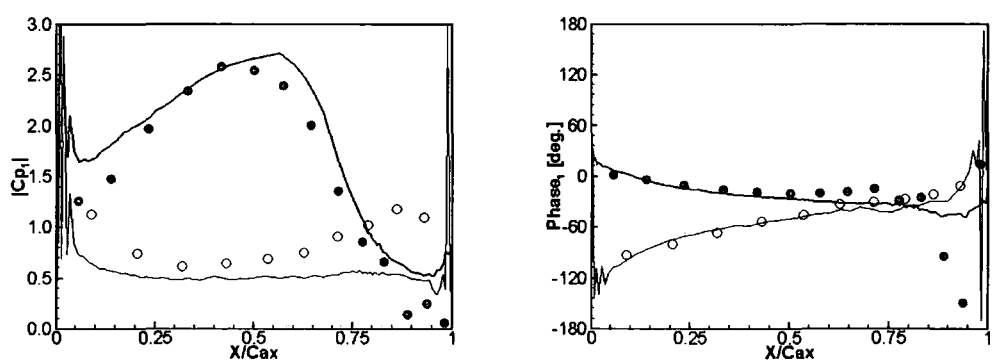


(d) 90% Span

**Figure 8.5: Comparison between experiment and calculation (with part-span shrouds, $K$=0.4, $\sigma_0$=−60°)**

**Table 8.2: Global aerodynamic damping coefficients for settings with and without part-span shrouds ($K$=0.4, $\sigma_0$=−60°)**

| | Aero-damping (Exp.) | Aero-damping (Cal.) |
|---|---|---|
| Nominal condition | -0.049 | -0.106 |
| Part-span shrouded | 0.156 | -0.073 |

aerodynamic damping. Table 8.2 shows the measured and predicted overall aerodynamic damping of the linear turbine cascade for settings with and without part-span shrouds. The measurements show that the existence of the part-span shrouds has a stabilising effect, although it is small. On the computational side, the part-span shrouds do not indicate much influence on the blade aeroelastic stability. Overall, both measurements and predictions reveals that the part-span shrouds exhibit a minor influence on the blade aeroelastic stability in the linear cascade.

## 8.2 Part-Span Shrouded LP Turbine Rotor

The present modelling of part-span shrouds is then applied to the LP steam turbine rotor configuration. The flutter prediction of this LP rotor at the nominal setting has been reported in Chapter 6. Here, hypothetical part-span shrouds are introduced to this rotor. In general, the introduction of part-span shrouds would stiffen the blades and alter natural modes of vibration. It is realised that the change of mode shape due to the part-span shrouds would result in different unsteady aerodynamic response, hence different aerodynamic damping. This study is, however, aimed at examining how the existence of part-span shrouds would influence the unsteady perturbation propagation and how the resulting damping would change. With this in mind, the mode shape of the rotor blades is assumed to be unaffected. The shrouds are approximated by flat plates with thickness of 1% blade height. The part-span shrouds are assumed to be located at 75% blade span and between 20%-80%$C_{ax}$ location. The mesh used here is shown in Figure 8.6 with 135, 41 and 53 cells in the axial, circumferential and radial direction respectively. Computational solutions for the 11 NDs backward travelling wave mode, which has been identified as the most unstable mode, are to be presented with and without part-span shrouds.

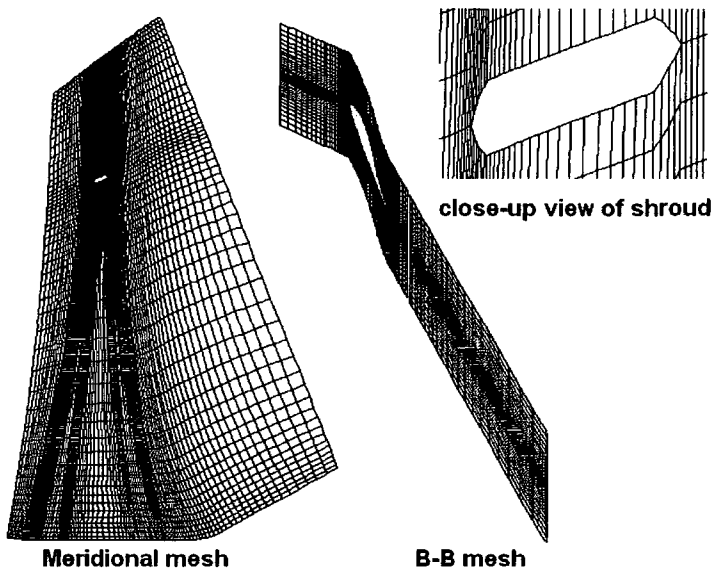


Figure 8.6: Computational mesh for model LP rotor with part-span shrouds

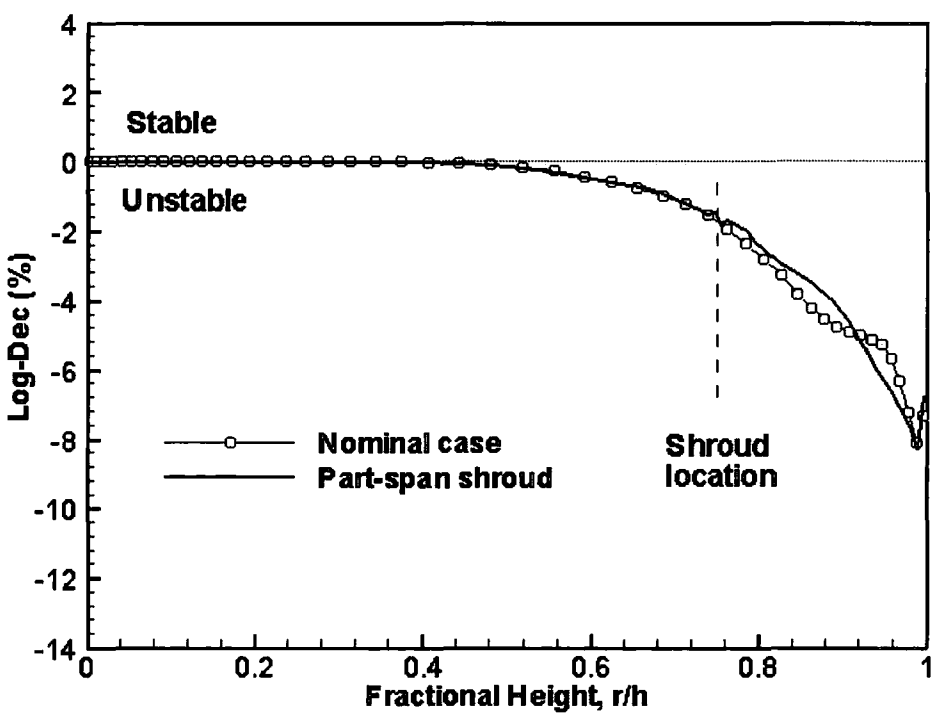


Figure 8.7: Predicted spanwise variation in local log-dec with and without with part-span shrouds for the LP rotor (shrouds located at 75% span)

Figure 8.7 shows the spanwise variation in the local log-dec predictios with and without part-span shrouds for the LP rotor. The plot reveals that the local log-dec is largely unaffected by the existence of part-span shrouds. Indeed, the part-span shrouds stabilise the rotor blades by 3.2% relative increase in aerodynamic damping, shown in Table 8.3.

**Table 8.3: Predicted Log-Dec ($\xi$) of the model LP rotor with and without part-span shrouds**

| Nominal case ($\xi_0$) | With part-span shrouds ($\xi_1$) | Relative difference ($\frac{\xi_1 - \xi_0}{\lvert\xi_0\rvert}$) |
|---|---|---|
| -1.265% | -1.224% | +3.2% |

Figure 8.8 shows the amplitude and the phase angle of the first harmonic pressure response at 70% span section and Figure 8.9 at 80% span section. It can be found that the existence of part-span shrouds induces notable variation in the first harmonic pressure response at span sections close to the part-span location, 75% span. Nevertheless, the part-span shrouds seem to only exert a local influence on the unsteady aerodynamic response to the blade vibration.

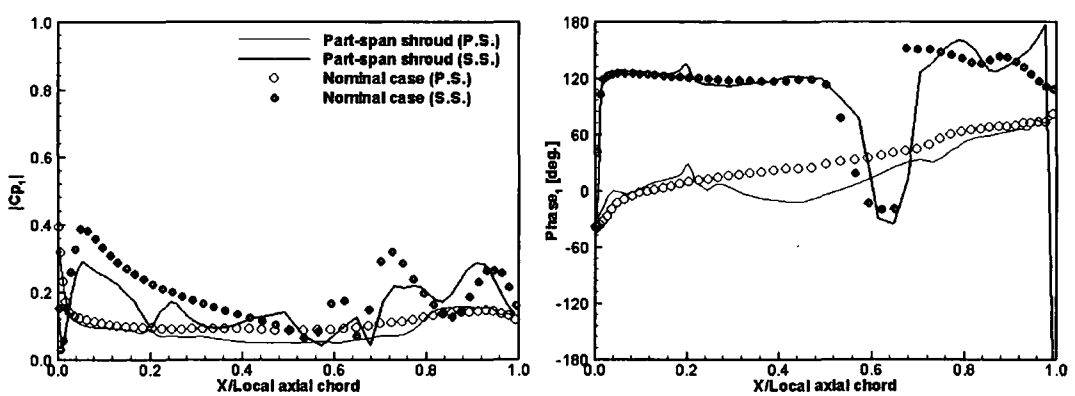


**Figure 8.8: Predicted first harmonic pressure at 70% span**

Local maximum damping change is observed around 85% span in Figure 8.7 where part-span shrouds are located at 75% span. To examine the influence of part-span shrouds at different spanwise locations, a further study of the LP rotor is then carried out with part-span shrouds located at 85% span. The result (Figure 8.10) also demonstrates a small overall Log-Dec difference (2.1% relative damping increase) comparing to the nominal case.

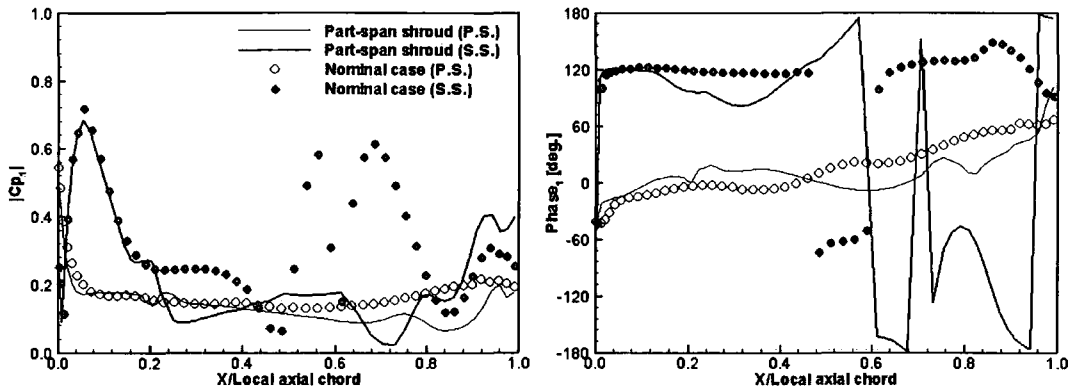


**Figure 8.9: Predicted first harmonic pressure at 80% span**

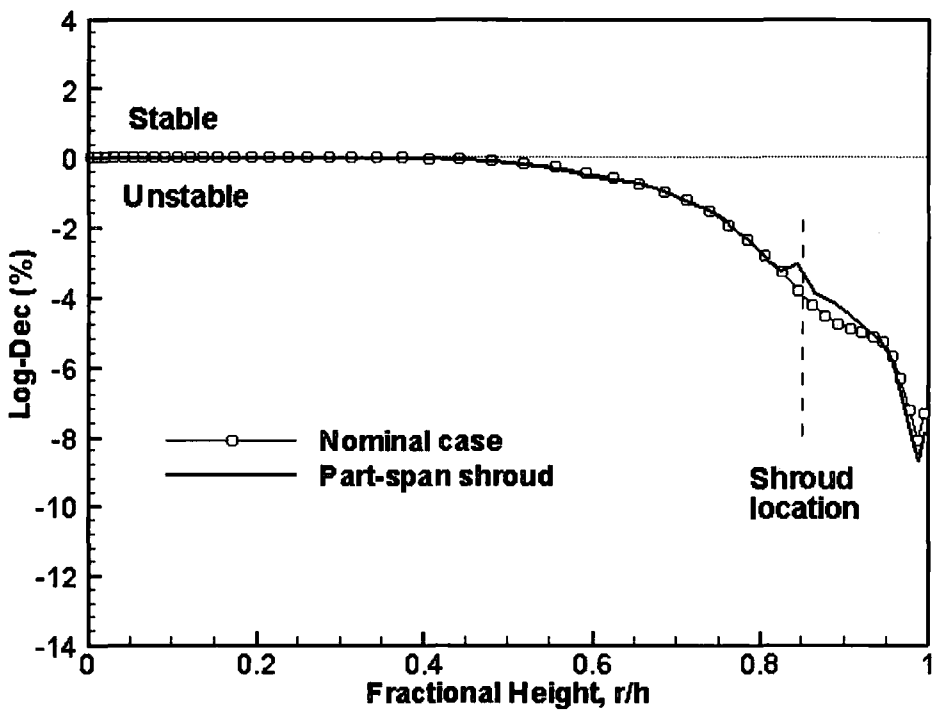


**Figure 8.10: Predicted spanwise variation in local log-dec with and without with part-span shrouds for the LP rotor (shrouds located at 85% span)**

## 8.3 Summary

An experimental and computational study has been performed to investigate the influence of part-span shrouds on the blade aeroelastic property in a linear oscillating turbine cascade. Both measurements and computations demonstrate a small influence of the part-span shrouds on the blade aeroelastic stability. A computational prediction of the LP steam turbine rotor using the present simple shroud model also reveals a

very small influence exerted by the part-span shrouds at 75% span and 85% span.

Given the small overall influence exerted by the part-span shrouds on the aerodynamic damping, it suggests that the part-span shroud modelling can be neglected at the current level of blade flutter prediction accuracy.

# Chapter 9

# Conclusions and Recommendations for Future Work

## 9.1 Conclusions

A detailed experimental and computational investigation into the behaviour of unsteady flow around oscillating blades in LP turbines has been performed with emphasis on the influence of adjacent rows, tip clearance and part-span shrouds.

A bespoke, linear, low speed, oscillating, test cascade is commissioned as the experimental vehicle, which consists of seven, large scale, prismatic blades with the middle blade being driven to oscillate in a three-dimensional bending mode. Detailed three-dimensional steady flow and unsteady flow measurements were carried out with the blades being extensively instrumented with pressure tappings at six sections from 10% to 95% span. With assistance of the tail-boards, excellent steady flow blade-to-blade periodicity was achieved in the cascade. Measurements of the unsteady pressure response were obtained through off-board pressure transducers with correction through the tubing transfer function to minimise the tubing distortion. An evaluation of the experimental repeatability and errors demonstrates that the unsteady measurements represent a good level of repeatability and accuracy. The measured unsteady pressure data were superposed to reconstruct the tuned cascade data by utilizing the influence coefficient method. The validity of the influence coefficient method has been confirmed by the pitchwise convergence of influence coefficients on those blades away from the central oscillating blade, and by the linearity of the unsteady pressure responses at

different oscillation amplitudes.

An advanced, single-passage, three-dimensional, time-marching, Navier-Stokes flow solver has been employed for the computational investigation. Computations have been first applied to the oscillating linear cascade flow at different experimental settings and later to the realistic LP steam turbine configurations.

### 9.1.1 Unsteady Flow around Oscillating Linear Turbine Blades

A first-of-its-kind set of three-dimensional unsteady measurements documented in Chapter 5 were obtained on the linear turbine cascade at its nominal setting. The test data demonstrates a strong three-dimensional behaviour of the unsteady flow induced by the blade vibration. The radial redistribution of unsteady response is evident. This is especially reflected by that the amplitude distribution of the first harmonic pressure at various spanwise sections is not proportional to the local vibration amplitude. The three-dimensional feature of the oscillating blade flow demonstrates the necessity for fully three-dimensional methods in the blade aeroelastic stability predictions. The big variation of the global aerodynamic damping with respect to the IBPA confirms that the adjacent blades exert significant influence on the blade aeroelastic stability.

The nominal oscillating cascade flow has been computationally studied. With adequate mesh resolution, excellent correlations with the experimental data are achieved over the whole range of IBPA at different reduced frequencies tested. This may well be the first time that a three-dimensional CFD solver for flutter predictions has been validated against detailed three-dimensional test data. The comparison clearly demonstrates the ability of the present CFD solver.

Regarding the influence of tip clearance in the linear cascade, a study was conducted with a tip clearance up to 5% chord using experimental and CFD tools. Both experimental and CFD results for steady flow indicates a significant role played by the tip leakage vortex. For a small tip clearance (1.25%C), a slight stabilising is observed at mid-chord towards the tip on the suction surface. However, for large tip clearances (2.5%C and 5%C), this stabilising contribution is largely offset by a destabilising contribution measured around 80%$C_{ax}$, which is associated with a well developed tip

clearance vortex. Overall, the blade aeroelastic stability is observed to be largely unaffected by the tip clearances tested.

With part-span shrouds at 75% span, increased amplitude of the first harmonic pressure on the suction surface is observed in measured results for those sections above 75% span when comparing to the nominal setting, whilst for the sections below 75% span, the converse is observed to be true. This opposite trends in unsteady pressure variation above and below the part-span shrouds are well predicted by CFD. The opposite trends for sections below and above 75% span are believed contributable to that the existence of part-span shrouds breaks down the radial redistribution, which is observed at the nominal setting. Although notable variation in the amplitude of first harmonic pressure response is observed at blade spanwise sections near the part-span shroud location on the suction surface, the influence of part-span shrouds on the global aerodynamic damping seems to be at a minor level.

The extensive steady flow and unsteady pressure measurements presented in this thesis provide the first three-dimensional test data of the kind, which can be exploited to serve the validation in the further development of advanced CFD flutter analysis techniques.

### 9.1.2 Prediction of the Realistic LP Steam Turbine Rotor

A computational investigation is presented in Chapter 6, which concerns the influence of upstream stator blades on the aeroelastic stability of the rotor in the low-pressure steam turbine stage. The predictions of a two-dimensional configuration (modified from the tip section of the LP steam turbine stage) reveals up to 144% damping variation with respect to the intr-row gap change from 40% to 140% rotor chord length. The fully three-dimensional study of this low pressure steam turbine stage shows that the existence of the upstream stator blade row leads to a 35% change of the rotor aerodynamic damping in comparison to that of an isolated rotor. Given the presence of upstream fixed blades can significantly change the aeroelastic stability of turbine rotor blades, the conventional isolated rotor predictions may be misleading.

The LP rotor was then studied with a hypothetical tip clearance of 5% tip chord (equivalent to 0.8% blade height at the leading edge). The prediction shows that the

tip clearance flow does reveal considerable bearing both aerodynamically and aeroelastically. In the aeroelastic aspect, the unsteady results reveal that the existence of a tip clearance of 5% tip chord destabilises the blade by 14.2% global damping change.

Part-span shrouds at 75% span location were introduced using the developed simple model. The LP rotor aeroelastic stability is observed to be largely unaffected. Whilst the influence of the part-span shrouds are confined to a local version in which a notable influence on the local unsteady pressure is evident.

## 9.2 Recommendations for Further Work

Based on the finding in Chapter 6 that the presence of upstream fixed blades can significantly change the self-excited aeroelastic stability of turbine rotor blades, there is great interest and value to verify the influence exhibited by the adjacent rows through experimental measurements in a stator-rotor rig.

The investigation into the influence of tip clearance on the oscillating blade flows shows significant variation in the amplitude of first harmonic pressure on the suction surface with respect to the tip clearance. However, the overall aerodynamic damping is largely unaffected by the presence of the tip clearance. The minor change in the aerodynamic damping is partially due to the phase angle of the first harmonic pressure being around 0°, which is a characteristic of the unsteady aerodynamic response to the bending mode shape. Whilst the study of the realistic LP rotor reveals a significant influence of the tip clearance on the aerodynamic damping, where the torsion component has an amplitude of the same order as the bending. These might suggest some dependency of the influence of tip clearance on the vibratory mode shape. To clarify this, it is useful to pursue a study in the tip clearance on the oscillating blade flow with a torsion-dominated mode shape.

It should be noted that the present simple tip clearance modelling can not resolve tip clearance flow in details. More accurate tip clearance modelling (e.g. using multi-block solver with sufficient mesh density in and near the tip clearance) is certainly helpful to enhance our understanding of tip clearance flow, although the implementation of a multi-block solver is more complex and time-consuming.

# Bibliography


Baldwin, B. S. and Lomax, H. (1978). Thin layer approximation and algebraic model for separated turbulent flows. AIAA paper, No. AIAA-78-0257. 4.1

Bell, D. and He, L. (2000). Three-dimensional unsteady flow for an oscillating turbine blade and the influence of tip leakage. *Transactions of the ASME, Journal of Turbomachinery*, 122:93–101. 1.3, 2.1.2.3, 2.1

Bendiksen, O. O. (1990). Aeroelastic problems in turbomachines. AIAA paper, No. AIAA-90-1157-CP. 2.2.2

Bölcs, A. (1983). A test facility for the investigation of steady and unsteady transonic flows in annular cascades. ASME paper, No. 83-GT-34. 2.1.2.2

Buffum, D. H. (1995). Blade row interaction effects on flutter and forced response. *AIAA Journal of Propulsion and Power*, 11(2):205–212. 1.3, 2.2.1, 2.3

Buffum, D. H., Capece, V. R., King, A. J., and El-Aini, Y. M. (1998). Oscillating cascade aerodynamics at large mean incidence. *Transactions of the ASME, Journal of Turbomachinery*, 120:122–130. 2.1.2.3

Buffum, D. H. and Fleeter, S. (1990a). The aerodynamics of an oscillating cascade in a compressible flow field. *Transactions of the ASME, Journal of Turbomachinery*, 112:759–767. 2.1.2.3

Buffum, D. H. and Fleeter, S. (1990b). Oscillating cascade aerodynamics by an experimental influence coefficient technique. *AIAA Journal of Propulsion and Power*, 6(5):612–620. 2.1.2.3, 3.2.3

Buffum, D. H. and Fleeter, S. (1993). Wind tunnel wall effects in a linear oscillating cascade. *Transactions of the ASME, Journal of Turbomachinery*, 115:147–156. 2.1.2.3

Buffum, D. H. and Fleeter, S. (1994). Effect of wind tunnel acoustic modes on linear oscillating cascade aerodynamics. *Transactions of the ASME, Journal of Turbomachinery*, 116:513–524. 2.1.2.3

Carstens, V. and Belz, J. (2000). Investigation of fluid-structure interaction in vibrating cascade using a time-domain method. In Ferrand, P. and Aubert, S., editors, *Proceedings of the 9th International Symposium on Unsteady Aerodynamic, Aeroacoustics and Aeroelasticity*, pages 678–694. 2.2.2

Carta, F. O. (1967). Coupled blade-disk-shroud flutter instability in turbojet engine rotors. *Transactions of the ASME, Journal of Engineering for Power*, 89(3):419–426. 1.2

Carta, F. O. (1983). Unsteady aerodynamics and gapwise periodicity of oscillating cascaded airfoils. *Transactions of the ASME, Journal of Engineering for Power*, 105:565–574. 2.1.2.3

Carta, F. O. and St. Hilaire, A. O. (1978). Experimentally determined stability parameters of a subsonic cascade oscillating near stall. *Transactions of the ASME, Journal of Engineering for Power*, 100:111–120. 2.1.2.3

Carta, F. O. and St. Hilaire, A. O. (1980). Effect of interblade phase angle and incidence angle on cascade pitching stability. *Transactions of the ASME, Journal of Engineering for Power*, 102:391–396. 2.1.2.3

Chen, T., Vansanthakumar, P., and He, L. (2001). Computation of unsteady blade row interaction using nonlinear harmonic approach. *AIAA Journal of Propulsion and Power*, 17(3):601–608. 2.2.1

Collar, A. R. (1946). The expanding domain of aeroelasticity. *The Royal Aeronautical Society*, 50:613–636. 1.1

Crawley, E. F. (1984). Aeroelastic formulations for turbomachines and propellers. In *Proceedings of the 3rd International Symposium on Unsteady Aerodynamics of Turbomachines and Propellers*, pages 13–28, Cambridge, UK. 2.1.1.2

Dawes, W. N. (1987). A numerical analysis of the three-dimensional viscous flow in a transonic compressor rotor and comparison with experiment. *Transactions of the ASME, Journal of Turbomachinery*, 109:83–90. 7.2

Denton, J. D. (1983). An improved time-marching method for turbomachinery flow calculation. *Transactions of the ASME, Journal of Engineering for Power*, 105:514–525. 4.3

Denton, J. D. (1992). The calculation of three-dimmensional visous flow through multistage turbomachines. *Transactions of the ASME, Journal of Turbomachinery*, 114:18–26. 4.3

Denton, J. D. (1993). Loss mechanisms in turbomachines. *Transactions of the ASME, Journal of Turbomachinery*, 115:621–656. 1.3, 7

Doi, H. and Alonso, J. J. (2002). Fluid/structure coupled aeroelastic computations for transonic flows in turbomachinery. ASME paper, No. GT2002-30313. 2.2.2

Erdos, J. I., Alzner, E., and McNally, W. (1977). Numerical solution of periodic transonic flow through a fan stage. *AIAA Journal*, 15(11):1559–1568. 2.2.2

Fleeter, S. and Jay, R. (1987). Unsteady aerodynamic measurements in flutter research. In Platzer, M. F. and Carta, F. O., editors, *AGARD Manual on Aeroelasticity in Axial-Flow Turbomachines, AGARD-AG-298*, volume 1: Unsteady Turbomachinery Aerodynamics, chapter 8. 2.1.2, 2.1.2.3

Fransson, T. H. (1990). Analysis of experimental time-dependent blade surface pressure from an oscillating turbine cascade with the influence coefficient technique. ASME paper, No. 90-GT-225. 2.1.2.2, 3.2.3

Fransson, T. H. and Pandolfi, M. (1986). Numerical investigation of unsteady subsonic compressible flows through an oscillating cascade. ASME Paper, No. 86-GT-304. 2.2.2

Frey, K. K. and Fleeter, S. (2001). Oscillating airfoil aerodynamics of a rotating compressor blade row. *AIAA Journal of Propulsion and Power*, 17(2):232–239. 2.1.2.1

Gallus, H. E. (1987). Unsteady aerodynamic measurements on rotors. In Plater, M. F. and Carta, F. O., editors, *AGARD Manual on Aeroelasticity in Axial-Flow Turbomachines, AGARD-AG-298*, volume 1: Unsteady Turbomachinery Aerodynamics, chapter 11. 2.1.2

Gerolymos, G. A. (1988). Numerical intigration of the blade-to-blade surface Euler equations in vibrating cascades. *AIAA Journal*, 26:1483–1492. 2.2.2

Gerolymos, G. A. (1990). Periodicity, superposition, and 3D effects in supersonic compressor flutter aerodynamics. *International Journal of Turbo and Jet Engines*, 7:143–152. 2.1.1.2

Giles, M. B. (1988). Calculation of unsteady wake rotor interaction. *AIAA Journal of Propulsion and Power*, 4(4):356–362. 2.2.2

Giles, M. B. (1990a). Nonreflecting boundary conditions for Euler equation calculations. *AIAA Journal*, 28(12):2050–2058. 4.3

Giles, M. B. (1990b). Stator/rotor interaction in a transonic turbine. *AIAA Journal of Propulsion and Power*, 6(5):621–627. 2.2.2

Giles, M. B. and Haimes, R. (1993). Validation of a numerical method for unsteady flow calculations. *Transactions of the ASME, Journal of Turbomachinery*, 115:110–117. 2.2.2

Gorlin, S. M. and Slezinger, I. I. (1964). Wind tunnels and their instrumentation. Translated from Russian by the Israel Program for Scientific Translations. 3.1.1

Grüber, B. and Carstens, V. (2001). The impact of viscous effects on the aerodynamic damping of vibrating transoni compressor blades-a numerical study. *Transactions of the ASME, Journal of Turbomachinery*, 123:409–417. 2.2.2

Hall, K. C. and Crawley, E. F. (1989). Calculation of unsteady flows in turbomachinery using the linearised Euler equations. *AIAA Jouanal*, 27(6):777–787. 2.2.1

Hall, K. C. and Lorence, C. B. (1993). Calculation of three-dimensional unsteady flows in turbomachinery using the linearized harmonic Euler equations. *Transactions of the ASME, Journal of Turbomachinery*, 115:800–809. 2.2.1

Hall, K. C. and Silkowski, P. D. (1997). The influence of neighboring blade rows on the unsteady aerodynamic response of cascades. *Transactions of the ASME, Journal of Turbomachinery*, 119:85–93. 1.3, 2.2.1, 2.3

Hall, K. C., Thomas, J. P., and Clark, W. S. (2002). Computation of unsteady nonlinear flows in cascades using a harmonic balance technique. *AIAA Journal*, 40(5):879–886. 2.2.1

Hall, K. C. and Verdon, J. M. (1991). Gust response analysis for cascades operating in nonuniform mean flow. *AIAA Jouanal*, 29(9):633–643. 2.2.1

Hanamura, Y., Tanaka, H., and Yamaguchi, K. (1980). A simplified method to measure unsteady forces actuing on the vibrating blades in a cascade. *Bulletin of the JSME*, 23(180):880–887. 2.1.1.2, 2.1.2.2, 2.1.2.3, 3.2.3

He, L. (1990). An Euler solution for unsteady flows around oscillating blades. *Transactions of the ASME, Journal of Turbomachinery*, 112:714–722. 2.2.2, 4.3

He, L. (1992). Method of simulating unsteady turbomachinery flows with multiple perturbations. *AIAA Journal*, 30(11):2730–2735. 2.2.2, 4.3, 4.3

He, L. (1993). New two-grid acceleration method for unsteady Navier-Stokes calculations. *AIAA Journal of Propulsion and Power*, 9(2):272–280. 2.2.2, 4.2, 4.2

He, L. (1994). Integration of two-dimensional fluid/structure coupled system for calculations of turbomachinery aerodynamic/aeroelastic instabilites. *International Journal of Computational Fluid Dynamics*, 3:217–231. 2.2.2, 1

He, L. (1996). Modelling issues for computation of unsteady turbomachinery flows. VKI Lecture Series: Unsteady Flows in Turbomachines. 2.2.1

He, L. (1997). Computational study of rotating-stall inception in axial compressors. *AIAA Journal of Propulsion and power*, 13(1):31–38. 4.3

He, L. (1998). Unsteady flow in oscillating turbine cascades: Part 1 - linear cascade experiment. *Transactions of the ASME, Journal of Turbomachinery*, 120:262–268. 2.1.2.3, 2.1.2.3, 3.1.2, 3.2.3

He, L. (2000). Three-dimensional unsteady Navier-Stokes analysis of stator-rotor interactions in axial-flow turbines. *IMechE Journal of Power and Energy*, 214:13–22. 2.2.2, 4, 4.2, 6.3.1.1

He, L., Chen, T., Wells, R. G., Li, Y. S., and Ning, W. (2002). Analysis of rotor-rotor and stator-stator interference in multi-stage turbomachines. *Transactions of the ASME, Journal of Turbomachinery*, 124:564–571. 2.2.1

He, L. and Denton, J. D. (1994). Three-dimensional time-marching inviscid and viscous solutions for unsteady flows around vibrating blades. *Transactions of the ASME, Journal of Turbomachinery*, 116:469 475. 2.2.2, 4, 6.3.1.1

He, L. and Ning, W. (1998). Efficient approach for analysis of unsteady viscous flows in turbomachinery. *AIAA Journal*, 36(11):2005–2012. 2.2.1

Hennings, H. and Send, W. (1998). Experimental investigation and theoretical prediction of flutter behavior of a plane cascade in low speed flow. *Transactions of the ASME, Journal of Engineering for Gas Turbines and Power*, 120:766–774. 2.1.1.1

Höhn, W. and Heinig, K. (2000). Numerical and experimental investigation of unsteady flow interaction in a low-pressure multistage turbine. *Transactions of the ASME, Journal of Turbomachinery*, 122:628–633. 2.2.2

Holmes, D. G. and Chuang, H. A. (1993). 2D linearised harmonic Euler flow analysis for flutter and forced response. In Atassi, H. M., editor, *Unsteady Aerodynamics, Aeroacoustics and Aeroelasticity of Turbomachines and Propellers*, pages 213–230. Springer-Verlag. 2.2.1

Holmes, D. G. and Lorence, C. B. (1997). Three-dimensional linearized Navier-Stokes calculations for flutter and forced response. In Fransson, T. H., editor, *Proceedings of the 8th International Symposium on Unsteady Aerodynamics, Aeroacoustics and Aeroelasticity of Turbomachines*, pages 211–224. Kluwer Academic Publisers. 2.2.1

Irwin, H., Cooper, K., and Girard, R. (1979). Correction of distortion effects caused by tubing systems in measurements of fluctuation pressures. *Journal of Industrial Aerodynamics*, 5:93–107. 3.2.2

Isomura, K. and Giles, M. B. (1998). A numerical study of flutter in a transonic fan. *Transactions of the ASME, Journal of Turbomachinery*, 120:500–507. 2.2.2

Jameson, A. (1991). Time-dependent calculations using multi-grid, with application to unsteady flows past airfoil and wings. AIAA Paper, No. AIAA-91-1596. 2.2.2, 4.2

Jameson, A., Schmidt, W., and Turkel, E. (1981). Numerical solutions of the Euler equations by finite volume methods using Runge-Kutta time-stepping schemes. AIAA Paper, No. AIAA-81-1259. 4.2

Ji, S. and Liu, F. (1999). Flutter computation of turbomachinery cascades using a parallel unsteady Navier-Stokes code. *AIAA Journal*, 37(3):320–327. 2.2.2

Jutras, R. R., Stallone, M. J., and Bankhead, H. R. (1981). Experimental investigation of flutter in midstage compressor designs. *AIAA Journal of Aircraft*, 18(10):874–880. 2.1.2.2

Kielb, R. E. (1999). Full scale engine testing. In Fransson, T. H., editor, *Aeroelasitcity in axial flow turbomachines*, VKI Lecture Series 1999-05. Von Karman Institute for fluid dynamics. 2.1.1.1

Kobayashi, H. (1989). Effects of shock waves on aerodynamic instability of annular cascade oscillating in a transonic flow. *Transactions of the ASME, Journal of Turbomachinery*, 111:222–230. 2.1.2.2

Körbächer, H. and Bölcs, A. (1994). Experimental investigation of the unsteady behaviour of a compressor cascade in an annular ring channel. In *Proceedings of 7th International Symposium on Unsteady Aerodynamics and Aeroelasticity of Turbomachinery*, pages 383–400, Fukuoka, Japan. 2.1.2.2

Lane, F. (1956). System mode shapes in the flutter of compressor blade rows. *Journal of the Aeronautical Sciences*, 23(1):54–66. 1.2, 2.1.1.2

Lepicovsky, J., McFarland, E. R., Capece, V. R., and Hayden, J. (2002). Unsteady pressures in a transonic fan cascade due to a single oscillating airfoil. ASME paper, No. GT2002-30312, also NASA/TM-2002-211723. 2.1.2.3

Lepicovsky, J., McFarland, E. R., Chima, R. V., and Wood, J. R. (2001). On flow-field periodicity in the NASA transonic flutter cascade. *Transactions of the ASME, Journal of Turbomachinery*, 123:501–509. 2.1.2.3

Li, H. D. and He, L. (2005a). Blade aerodynamic damping variation with rotor-stator gap: A computational study using single-passage approach. *Transactions of the ASME, Journal of Turbomachinery*, 127:573–579. 1.3, 2.2.2, 2.3, 4

Li, H. D. and He, L. (2005b). Toward intra-row gap optimization for one and half stage transonic compressor. *Transactions of the ASME, Journal of Turbomachinery*, (127):589–598. 1.3, 2.2.2, 2.3, 4.3

Lynn, P. A. and Fuerst, W. (1989). *Introductory Digital Signal Processing with Computer Applications.* John Wiley & Sons. 3.2.1

Manwaring, S. R., Rabe, D. C., Lorence, C. B., and Wadia, A. R. (1997). Inlet distortion generated forced response of a low-aspect-ratio transonic fan. *Transactions of the ASME, Journal of Turbomachinery*, 119:665–676. 2.1.2.1

Manwaring, S. R. and Wisler, D. C. (1993). Unsteady aerodynamics and gust reponse in compressors and turbines. *Transactions of the ASME, Journal of Turbomachinery*, 115:724–740. 2.1.2.1

Marshall, J. G. and Giles, M. B. (1997). Some applications of a time-linearized Euler method to flutter and forced response in turbomachinery. In Fransson, T. H., editor, *Unsteady Aerodynamics and Aeroelasticity of Turbomachines.* Kluwer Academic Publishers. 2.2.2

Mikolajczak, A. A., Arnoldi, R. A., Snyder, L. E., and Stargardter, H. (1975). Advances in fan and compressor blade flutter analysis and predictions. *Journal of Aircraft*, 12(4):325–332. 1.1, 2.1.2.1, 2.1.2.3

Ni, R. H. and Sisto, F. (1976). Numerical computaion of nonstationary aerodynamics of flat plate cascades in compressible flow. *Transactions of ASME, Journal of Engineering for Power*, 98(2):165–170. 2.2.1

Ning, W. and He, L. (1998). Computation of unsteady flows around oscillating blades using linear and non-linear harmonic Euler methods. *Transactions of the ASME, Journal of Turbomachinery*, 120(3):508–514. 2.2.1

Norryd, M. and Bölcs, A. (1997). Experimental investigation of unsteady pressure behaviours in a linear turbine cascade. In *Proceedings of the 8th International Symposium on Unsteady Aerodynamics and Aeroelasticity of Turbomachines*, Stockholm, Sweden. 2.1.2.3

Nowinski, M. and Panovsky, J. (2000). Flutter mechanisms in low pressure turbine blades. *Transactions of the ASME, Journal of Engineering for Gas Turbines and Power*, 122:82–88. 2.1.2.2, 3.2.3

Ott, P., Norryd, M., and Bölcs (1998). The influence of tailboards on unsteady measurements in a linear cascade. ASME paper, No. 98-GT-0572. 2.1.2.3

Queune, O. J. R. and He, L. (2001). Experimental study of 3D unsteady flow around oscillating blade with part-span separation. *Transactions of the ASME, Journal of Turbomachinery*, 123:519–525. 1.3, 2.1.2.3, 2.1

Rai, M. M. (1987). Navier-Stokes simulations of rotor-stator interaction using patched and overlaid grids. *AIAA Journal of Propulsion and Power*, 3(5):387–396. 2.2.2

Rai, M. M. (1989). Three-dimensional Navier-Stokes simulations of turbine rotor-stator interaction; Pt. 1-Methodology, Pt. 2- Results. *AIAA Journal of Propulsion and Power*, 5(3):304–319. 2.2.2

Roberts, W. B. (1999). Extent and computation of the performance abatement due to part-span dampers (shrouds) on transonic axial fan rotors. In *VKI Lecture Series 1999-02 on Turbomachinery Blade Design Systems.* Von Karman Institute for Fluid Dynamics, Belgium. 8

Rothrock, M. D., Jay, R. L., and Riffel, R. E. (1982). Time-variant aerodynamcis of high-turning blade elements. *Transactions of the ASME, Journal of Engineering for Power*, 104:412–419. 2.1.2.3

Saiz, G., Imregun, M., and Sayma, A. I. (2006). A multi blade-row linearised analysis method for flutter and forced response predictions in turbomachinery. Proceeding of GT2006 ASME Turbo Expo 2006: Power for Land, Sea and Air, May 8-11, 2006, Barcelona, Spain. Paper No. GT2006-90789. 2.2.1

Sanders, A. J., Hassan, K. K., and Rade, D. C. (2004). Experimental and numerical study of stall flutter in a transonic low-aspect ratio fan blisk. *Transactions of the ASME, Journal of Turbomachinery*, 126:166–174. 2.1.1.1, 2.1.2.1, 2.2.2

Saxer, A. P. and Giles, M. B. (1993). Quasi-three-dimensional nonreflecting boundary conditions for Euler equations calculations. *AIAA Journal of Propulsion and Power*, 9(2):263–271. 4.3

Sayma, A. I., Vahdati, M., Green, J. S., and Imregun, M. (1998). Whole-assembly flutter analysis of a low pressure turbine blade. *Aeronautical Journal*, 102(1018):459–463. 2.2.2

Sbardella, L. and Imregun, M. (2001). Linearized unsteady viscous turbomachinery flows using hybrid grids. *Transactions of the ASME, Journal of Turbomachinery*, 123:568–582. 2.2.1

Scalzo, A. J., Allen, J. M., and Antos, R. J. (1986). Analysis and solution of a non-synchronous vibration problem in the last row turbine blade of a large industrial combustion turbine. *Transactions of the ASME, Journal of Engineering for Gas Turbines and Power*, 108:591–598. 1.1

Silkowski, P. D. and Hall, K. C. (1998). A coupled mode analysis of unsteady multistage flows in turbomachinery. *Transactions of the ASME, Journal of Turbomachinery*, 120:410–421. 1.3, 2.2.1, 2.3

Silkowski, P. D., Rhie, C. M., Copeland, G. S., Eley, J. A., and Bleeg, J. M. (2001). CFD investigation of aeromechanics. ASME paper, No. 2001-GT-0267. 2.2.2

Sims-Williams, D. B. (2001). *Self-Excited Aerodynamic Unsteadiness Associated with Passenger Cars.* PhD thesis, School of Engineering, University of Durham, U.K. 3.2.2

Sjolander, S. A. (1997). Physics of tip clearance flows I & II. In *VKI Lecture Series 1997-01 on Secondary anf Tip-Clearance Flows in Axial Flow turbomachines.* Von Karman Institute for Fluid Dynamics, Belgium. 1.3, 7

Smith, S. N. (1972). Discrete frequency sound generation in axial flow turbomachines. Reports and Memoranda 3709, Aeronautical Research council, London. 6.1

Snyder, L. E. and Commerford, G. L. (1974). Supersonic unstalled flutter in fan rotor: Analytical and experimental results. *Transactions of the ASME, Journal of Engineering for Power*, 96:379–386. 2.1.1.1, 2.1.2.3

Stargardter, H. (1977). Optical determination of rotating fan blade deflections. *Transactions of the ASME,Journal of Engineering for Power*, 99:204–209. 1.1, 2.1.2.1

Storer, J. A. and Cumpsty, N. A. (1991). Tip leakage flow in axial compressors. *Transactions of the ASME, Journal of Turbomachinery*, 113:252–259. 7.2

Szechenyi, E. (1987). Understanding fan blade flutter through linear cascade aeroelastic testing. In Platzer, M. F. and Carta, F. O., editors, *AGARD Manual on Aeroelasticity in Axial-Flow Turbomachines, AGARD-AG-298*, volume 1: Unsteady Turbomachinery Aerodynamics, chapter 10. 2.1.2.3

Urban, B., Stetter, H., and Vortmeyer, N. (2000). Experimental investigation of shock-induced blade oscillation at an elastically suspended turbine cascade in transonic flow. ASME paper, No. 2000-GT-378. 2.1.1.1

Vahdati, M., Sayma, A. I., Marshall, J. G., and Imregun, M. (2001). Mechanisms and prediction methods for fan blade stall flutter. *AIAA Journal of Propulsion and Power*, 17(5):1100–1108. 2.2.2

Van Zante, D. E., Strazisar, A. J., Wood, J. R., Hathaway, M. D., and Okiishi, T. H. (2000). Recommendations for achieving accurate numerical simulation of tip clear-

ance flows in transonic compressor rotors. *Transactions of the ASME, Journal of Turbomachinery*, 122:733–742. 7.2

Verdon, J. M. and Caspar, J. R. (1982). Development of a linear unsteady aerodynamic analysis for finite-deflection subsonic cascades. *AIAA Journal*, 20(9):1259–1267. 2.2.1

Verdon, J. M. and Caspar, J. R. (1984). A linearised unteady aerodynamic analysis for transonic cascades. *Journal of Fluid Mechanics*, 149:403–429. 2.2.1

Vogt, D. M. (2005). *Experimental Investigation of Three-Dimensional Mechanisms in Low-Pressure Turbine Flutter.* PhD thesis, Royal Institute of Technology, Sweden. 2.1.2.2, 2.1

Vogt, D. M. and Fransson, T. H. (2004). Effect of blade mode shape on the aeroelastic stability of a LPT cascade. Presented at the 9th National Turbine Engine High Cycle Fatigue (HCF) Conference, Pinehurst, North Carolina, USA. 1.3, 2.1.2.2, 2.1

Vogt, D. M. and Fransson, T. H. (2006). Experimental investigation of mode shape sensitivity of an oscillating LPT cascade at design and off-design conditions. Proceeding of GT2006 ASME Turbo Expo 2006: Power for Land, Sea and Air, May 8-11, 2006, Barcelona, Spain. Paper No. GT2006-91196. 2.1.2.2

Von Hoyningen-Huene, M. and Jung, A. R. (2000). Comparison of different acceleration techniques and methods for periodic boundary treatment in unsteady turbine stage flow simulations. *Transactions of the ASME, Journal of Turbomachinery*, 122:234–246. 2.2.2

Walker, M., Gregory-Smith, D., and He, L. (2005). A study of large tip clearance in a row of low speed compressor blades. Presented at 6th European Conference on Turbomachinery, Fluid Dynamics and Thermodynamics, 7-11 March, 2005, Lille, France. 7.2

Whitehead, D. S. (1987). Classical two-dimensional methods. In Plater, M. F. and Carta, F. O., editors, *AGARD Manual on Aeroelasticity in Axial-Flow Turbomachines, AGARD-AG-298*, volume 1: Unsteady Turbomachinery Aerodynamics, chapter 3. 2.2.1

Yang, H. (2004). *3D Unsteady Flow in Oscillating Compressor Cascade.* PhD thesis, School of Engineering, University of Durham, U.K. 3.1.1, 3.2.2, 3.2.3

Yang, H. and He, L. (2004). Experimental study on linear compressor cascade with thress-dimensional blade oscillation. *AIAA Journal of Propulsion and Power*, 20(1):180–188. 1.3, 2.1.2.3, 2.1, 3.1.2

# Appendix: Blade Profile Specification

| $x$(mm) | $y$(mm) | $x$(mm) | $y$(mm) | $x$(mm) | $y$(mm) | $x$(mm) | $y$(mm) |
|---|---|---|---|---|---|---|---|
| 1.4925 | 9.6783 | 60.5052 | 9.7884 | 110.2784 | 99.6255 | 73.1620 | 36.0344 |
| 1.1635 | 9.6219 | 62.3907 | 11.0579 | 110.2113 | 99.8235 | 71.5174 | 34.1606 |
| 0.8535 | 9.4983 | 64.2439 | 12.4087 | 110.1044 | 100.0033 | 69.8378 | 32.3745 |
| 0.5760 | 9.3130 | 66.0636 | 13.8432 | 109.9624 | 100.1569 | 68.1247 | 30.6721 |
| 0.3430 | 9.0740 | 67.8489 | 15.3645 | 109.7918 | 100.2776 | 66.3798 | 29.0499 |
| 0.1649 | 8.7918 | 69.5982 | 16.9757 | 109.5997 | 100.3601 | 64.6041 | 27.5048 |
| 0.0492 | 8.4787 | 71.3100 | 18.6811 | 109.3946 | 100.4010 | 62.7987 | 26.0341 |
| 0.0119 | 8.1485 | 72.9822 | 20.4857 | 109.1855 | 100.3984 | 60.9646 | 24.6357 |
| 0.0230 | 7.8155 | 74.6096 | 22.4031 | 108.9815 | 100.3524 | 59.1023 | 23.3079 |
| 0.1135 | 7.4942 | 76.2080 | 24.3928 | 108.7916 | 100.2648 | 57.2127 | 22.0486 |
| 0.2687 | 7.1988 | 77.7817 | 26.4443 | 108.6240 | 100.1397 | 55.2963 | 20.8566 |
| 0.4821 | 6.9421 | 79.3302 | 28.5596 | 108.4860 | 99.9825 | 53.3534 | 19.7309 |
| 0.7441 | 6.7355 | 80.8526 | 30.7402 | 108.3838 | 99.8001 | 51.3844 | 18.6707 |
| 2.2482 | 5.9449 | 82.3510 | 32.9807 | 107.9876 | 98.6622 | 49.3898 | 17.6750 |
| 5.1982 | 4.5439 | 83.8309 | 35.2681 | 106.8519 | 95.5112 | 47.3696 | 16.7433 |
| 8.0550 | 3.3766 | 85.2918 | 37.6031 | 105.6819 | 92.4469 | 45.3239 | 15.8756 |
| 10.8290 | 2.4173 | 86.7331 | 39.9867 | 104.4787 | 89.4655 | 43.2528 | 15.0716 |
| 13.5286 | 1.6444 | 88.1547 | 42.4204 | 103.2437 | 86.5638 | 40.7692 | 14.2025 |
| 16.1609 | 1.0405 | 89.5559 | 44.9051 | 101.9780 | 83.7393 | 39.0522 | 13.6101 |
| 18.7320 | 0.5903 | 90.9361 | 47.4421 | 100.6828 | 80.9890 | 36.9295 | 12.9356 |
| 21.2468 | 0.2811 | 92.2950 | 50.0331 | 99.3690 | 78.2849 | 34.7792 | 12.3303 |
| 23.7127 | 0.0944 | 93.6319 | 52.6789 | 98.0425 | 75.6130 | 32.6013 | 11.7943 |
| 26.1419 | 0.0000 | 94.9462 | 55.3813 | 96.7039 | 72.9715 | 30.3951 | 11.3291 |
| 28.5329 | 0.0014 | 96.2374 | 58.1421 | 95.3537 | 70.3587 | 28.1603 | 10.9361 |
| 30.8874 | 0.0944 | 97.5046 | 60.9627 | 93.9926 | 67.7735 | 25.8962 | 10.6162 |
| 33.2071 | 0.2748 | 98.7473 | 63.8450 | 92.6212 | 65.2144 | 23.6020 | 10.3719 |
| 35.4929 | 0.5401 | 99.9646 | 66.7910 | 91.2306 | 62.7030 | 21.2769 | 10.2051 |
| 37.7460 | 0.8875 | 101.1557 | 69.8026 | 89.8171 | 60.2495 | 18.9199 | 10.1185 |
| 39.9671 | 1.3150 | 102.3198 | 72.8819 | 88.3811 | 57.8519 | 16.5521 | 10.0589 |
| 42.1570 | 1.8208 | 103.4560 | 76.0315 | 86.9235 | 55.5088 | 14.1843 | 9.9993 |
| 44.3163 | 2.4037 | 104.5633 | 79.2533 | 85.4446 | 53.2192 | 11.8165 | 9.9395 |
| 46.4452 | 3.0626 | 105.6407 | 82.5503 | 83.9451 | 50.9816 | 9.4487 | 9.8799 |
| 48.5440 | 3.7972 | 106.6870 | 85.9254 | 82.4273 | 48.7890 | 7.0810 | 9.8202 |
| 50.6130 | 4.6065 | 107.7010 | 89.3811 | 80.9075 | 46.6021 | 4.7131 | 9.7606 |
| 52.6520 | 5.4909 | 108.6816 | 92.9210 | 79.3876 | 44.4153 | 2.3454 | 9.7009 |
| 54.6610 | 6.4506 | 109.6273 | 96.5484 | 77.8678 | 42.2284 | 1.4925 | 9.6783 |
| 56.6398 | 7.4861 | 110.2837 | 99.2095 | 76.3384 | 40.0652 | | |
| 58.5880 | 8.5983 | 110.3029 | 99.4178 | 74.7697 | 38.0009 | | |